



TECHNISCHE
UNIVERSITÄT
WIEN
Vienna University of Technology

Diese Dissertation haben begutachtet:

Dissertation

Conductivity variations in donor-doped PZT under high-field stress

Leitfähigkeitsvariationen in Nd-dotiertem $\text{Pb}(\text{Zr}_x\text{Ti}_{1-x})\text{O}_3$ unter hohen elektrischen Feldern

ausgeführt zum Zwecke der Erlangung des akademischen Grades eines Doktors der
Naturwissenschaften unter der Leitung von

Univ.Prof. Dipl. Phys. Dr. Jürgen Fleig

164EC, Institut für Chemische Technologien und Analytik - Bereich Elektrochemie

eingereicht an der Technischen Universität Wien,
Fakultät für Technische Chemie
von

Elmar Völkl

Matrikelnummer: 9825638
Jägerhausgasse 50/1; A-1120 Wien

Wien, am 26. September 2011

Elmar Völkl

As soon as questions of will or reason or choice of action arise,
human science is at a loss.

Noam Chomsky

Contents

Abstract	1
Zusammenfassung	3
1 Introduction	5
2 Fundamentals	9
2.1 Defects in solid state ionic materials	9
2.1.1 Thermodynamics	9
2.1.1.1 Basic relations	9
2.1.1.2 From a perfect to a real solid	11
2.1.2 Point defects	12
2.1.3 Intrinsic and extrinsic defects	13
2.1.3.1 Intrinsic defects	13
2.1.3.2 Extrinsic defects - Doping	17
2.1.4 Nonstoichiometry	19
2.1.5 BROUWER diagrams	21
2.1.5.1 Undoped nonstoichiometric metal oxide	22
2.1.5.2 Aliovalent doped metal oxides	23
2.1.6 Frozen-in states	25
2.1.7 Voltage induced defect profiles	26
2.2 Conductivity and impedance	27
2.2.1 Electronic and ionic conduction	27
2.2.1.1 Thermally activated bulk conductivity	30
2.2.1.2 Grain boundaries	33
2.2.1.3 Electrodes	34
2.2.2 Impedance spectroscopy	36

2.3	Lead zirconate titanate $\text{Pb}(\text{Zr}_x\text{Ti}_{1-x})\text{O}_3$ (PZT)	40
2.3.1	The piezoelectric effect	41
2.3.2	The perovskite structure	46
2.3.3	Domain structure and poling	49
2.3.3.1	Domains	49
2.3.3.2	Poling	51
2.3.4	Doping of PZT	54
2.3.5	PbO evaporation	55
2.3.6	Aging, fatigue and degradation	56
3	Experimental	59
3.1	PZT Samples	59
3.2	Conductivity experiments on PZT	62
3.2.1	Hard- and software	62
3.2.2	Conductivity measurement procedure	65
3.2.3	Temperature	67
4	Results and Discussion: Nd:PZT(Cu)	71
4.1	General considerations	71
4.1.1	Typical behavior	71
4.1.2	Fitting	74
4.1.3	Impedance spectra	76
4.1.4	Capacitive effects	80
4.1.5	Zero-field thermal equilibration	81
4.1.6	Conduction path	83
4.1.7	(Non)Linearity	84
4.2	Short-term high field stress and relaxation (Phase 1 & Phase 2)	86
4.2.1	Phase 1: High-field conductivity decrease	86
4.2.1.1	Time constant τ_1	86
4.2.1.2	Magnitude of the conductivity decrease “delta1”	88
4.2.2	Phase 2: Stress-free relaxation	90
4.2.2.1	Time constant τ_2	90
4.2.2.2	Magnitude of the conductivity relaxation “delta2” . . .	91
4.2.3	Relations between Phase 1 and Phase 2	94
4.2.4	Blackening	97
4.2.5	The influence of the experimental atmosphere	100

4.2.6	Stoichiometry polarization: A possible model for short-term conductivity variation	101
4.2.6.1	Comparison with stoichiometry polarization on SrTiO ₃	108
4.2.6.2	Diffusion coefficients	110
4.2.6.3	Further arguments for stoichiometry polarization . .	112
4.3	Long-term high-field stress and breakdowns (Phase 1 & Phase 2LT) .	114
4.3.1	Conductivity variations during Phase 2LT	114
4.3.2	Conductivity variations <i>after</i> Phase 2LT	121
4.3.2.1	Long-term degraded samples <i>without</i> electrical breakdown	121
4.3.2.2	Long-term degraded samples <i>with</i> electrical breakdown	125
4.3.3	Optical and chemical features - Blackening, craters and Cu-precipitates	131
4.3.3.1	Blackening	131
4.3.3.2	Craters	132
4.3.3.3	Cu-precipitates	132
4.3.4	Discussion of Phase 2LT and breakdowns	137
5	Results and Discussion: Nd:PZT(AgPd)	139
5.1	Degradation behavior of Nd:PZT(AgPd) in air	141
5.1.1	High-voltage	141
5.1.1.1	Dendrites	141
5.1.1.2	Blackening	145
5.1.1.3	Current fluctuation	147
5.1.1.4	Cracks	147
5.1.1.5	Breakdown	151
5.1.2	Low-voltage	155
5.2	Degradation behavior of Nd:PZT(AgPd) in Ar	158
5.3	Degradation behavior of Nd:PZT(AgPd) in H ₂	160
5.3.1	Pb-precipitates	163
5.3.2	Long-term recovery	165
5.4	Nd:PZT(AgPd): Comparison and Discussion	167
6	Results and discussion: Other PZT-samples	169
6.1	Macroscopic PZT samples	169
6.1.1	W- and Sr-doped PZT discs (W/Sr:PZT)	169

6.1.2	Nd-doped PZT discs	173
6.2	Complete (full)stacks	175
6.3	PZT samples with microelectrodes	179
6.3.1	High-voltage experiments on microelectrodes	179
6.3.2	Light-effect	185
7	Conclusions	187
	Acknowledgments	191
	Bibliography	193
	Nomenclature	211

Abstract

Lead zirconate titanate, $\text{Pb}(\text{Zr}_x\text{Ti}_{1-x})\text{O}_3$, ($0 \leq x \leq 1$), also known as PZT, is currently one of the most prominent ferroelectric ceramics on the market and is used in actuators, transducers, capacitors, optoelectronics or in memory devices. In modern internal combustion engines PZT-piezostacks open and close the fuel injector nozzles for millions of time. Nevertheless, PZT based devices may suffer from mechanical fatigue and resistance degradation, which finally can cause device failure. Some of these phenomena are often associated with point defects in PZT. However, defect chemistry in PZT is still far from being understood.

In this work, electrochemical impedance spectroscopy and low-voltage resistivity probing was combined with electrostatic high-field stress applied to positively (1.5 % Nd donor) doped PZT actuator stacks with Cu and Ag/Pd inner electrodes, respectively. Changes of the isolation resistance were investigated at temperatures from 350 to 500 °C, at fields between 267 kV/m and 2.67 MV/m and in different gas atmospheres. Measurements on individual ceramic layers ($\sim 75 \mu\text{m}$ thickness) of PZT multilayer stacks allowed numerous experiments on nominally identical material.

On PZT with Cu inner electrodes, the conductivity considerably decreased under high fields on time scales much longer than needed for capacitor charging. At 350 °C, for example, decay times of several 1000 s are found. At 450 °C an accelerated conductivity decrease was observed, followed by a slow increase after reaching a local minimum and a final (apparent) current-breakdown. The time constant of the conductivity decay depends exponentially on temperature with activation energies of about 1.4 eV in air. When the high-field was removed at the conductivity minimum, a much slower, yet thermally activated (~ 1.0 eV), relaxation (conductivity increase) occurred. These phenomena could be attributed to stoichiometry polarization and subsequent chemical backdiffusion due to motion of mobile oxygen vacancies ($\text{V}_{\text{O}}^{\bullet}$). Under voltage load in air, such Nd:PZT(Cu)-layers did show a progressive darkening of the ceramic. When the high-field was not switched-off at the conductivity min-

imum, a final electrical breakdown occurred together with the formation of craters around the interdigit electrodes.

Contrary to the PZT Cu-samples, PZT with Ag/Pd inner electrodes showed a conductivity increase under high-field stress and detectable Ag and Pb precipitation. The Ag precipitates grew from the anode (\oplus) and thus have to follow a different mechanism than that of conventional aqueous electrochemical dendrite growth. However, in Ar and H₂ ambience the conductivity development did not differ from that in air, including a final breakdown, but the superficial Ag-precipitates were almost absent in those reducing atmospheres. Under long-term high-voltage load, the conductivity variations were accompanied by darkening of the Nd:PZT(AgPd) ceramic and subsequent formation of “cracks” and finally ending in mechanical “craters” and electrical breakdowns, which could indicate a superficial or a surface-close conduction path.

Zusammenfassung

Blei-Zirkonat-Titanat, $\text{Pb}(\text{Zr}_x\text{Ti}_{1-x})\text{O}_3$, ($0 \leq x \leq 1$), kurz “PZT”, ist derzeit eine der wichtigsten ferroelektrischen Keramiken am Markt. Es findet Verwendung in Aktuatoren, Signalwandlern, Kondensatoren, optoelektronischen Bauteilen sowie in digitalen Speichern. Millionenfach öffnen und schließen PZT-Piezostacks die Einspritzdüsen in modernen Verbrennungskraftmaschinen. Nichtsdestotrotz zeigt auch PZT mechanische und elektrische Alterungserscheinungen, die letztlich zum Ausfall eines Aktuators führen können. Einige dieser Mechanismen werden Punktdefekten im Kristallgitter von PZT zugeordnet. Bis heute fehlt allerdings ein umfassendes Verständnis der Defektchemie von PZT.

In der vorliegenden Arbeit wurden elektrochemische Impedanzspektroskopie, Kleinsignal-Gleichstrom Widerstandsmessungen und elektrostatische Hochfelder kombiniert auf positiv (1.5 % Nd^{3+} donor) dotierte PZT-Stacks mit Cu bzw. Ag/Pd Innenelektroden angewandt. Leitfähigkeitsänderungen wurden überwiegend im Temperaturbereich zwischen 350 °C und 500 °C, unter Feldstärken von 267 kV/m bis 2.67 MV/m und in verschiedenen Atmosphären untersucht. Durch Messungen einzelner Schichten (a $\sim 75 \mu\text{m}$) in Piezostacks konnten viele Messungen an ein und demselben Stackstück durchgeführt werden.

Unter hohen elektrischen Feldern zeigte PZT mit Cu-Innenelektroden einen (zeitlich weit über bloße Kondensatoraufladung hinausgehenden) Leitfähigkeitsabfall auf ein Minimum. Bei 350 °C betragen die Zeitkonstanten mehrere 1000 s. Bei 450 °C folgte auf einen beschleunigten Leitfähigkeitsabfall allerdings eine deutlich langsamere Leitfähigkeitszunahme, die in einem plötzlichen (scheinbaren) Kurzschluss mündete. Die Zeitkonstante des Leitfähigkeitsabfalls in Luft ist mit ca. 1.4 eV thermisch aktiviert. Wurde die Hochspannung am Leitfähigkeitsminimum abgeschaltet, relaxierte die Leitfähigkeit deutlich langsamer, aber ebenso thermisch aktiviert (~ 1.0 eV) in Richtung ihres ursprünglichen Anfangswertes. Dieses Verhalten konnte mit dem Modell einer stöchiometrischen Polarisierung durch Migration von Sauerstoff-Leerstellen

($V_{\ddot{O}}$) und anschließender chemischer Rückdiffusion erklärt werden. Spannungsbelastete Nd:PZT(Cu)-Stackschichten zeigten eine fortschreitende optische Verdunkelung. Aufrechterhalten des elektrischen Hochfeldes nach Überschreitung des Leitfähigkeitsminimums führte zu elektrischen Durchbrüchen, begleitet von “Kratern” im Bereich der Innenelektroden.

Im Gegensatz zu den Cu-Proben, zeigte PZT mit Ag/Pd-Innenelektroden unter hoher Spannung eine Leitfähigkeitszunahme und einen elektrischen Durchbruch. Ag- und Pb-Ausscheidungen wurden abseits der Elektroden gefunden. In Luft wuchsen Ag-Ausscheidungen von der Anode weg, der Mechanismus muss also ein anderer sein als jener konventioneller elektrochemischer Dendritenbildung. Bei sonst gleichem elektrischen Verhalten wurden allerdings in reduzierenden Atmosphären (Ag, H_2) praktisch keine Ag-Ausscheidungen festgestellt. Auch bei Nd:PZT(AgPd) wurden die spannungsinduzierten Leitfähigkeitsänderungen in Luft oft von einer Schwärzung der betroffenen PZT-Schicht begleitet. Beim elektrischen Durchbruch kam es zu Kratern, die auf oberflächliche oder oberflächen-nahe Leitungspfade schließen lassen.

1 Introduction

Perovskite-type oxides with large band gaps are widely used as electroceramics and play functional roles in numerous devices such as capacitors, piezoelectric actuators and transducers, sound systems, gas igniters, filters, temperature and gas sensors, infrared cameras, etc. Three of the most prominent representatives of the wide range of compositions used in such applications are SrTiO_3 , BaTiO_3 and $\text{Pb}(\text{Zr}_x\text{Ti}_{1-x})\text{O}_3$ ($0 \leq x \leq 1$), the latter one - lead zirconate titanate - is also abbreviated PZT [1, 2].

Subjected to an external voltage, the ferroelectric PZT switches its previously randomly aligned domains parallel to the field. After such a “poling process” all ferroelectric materials show piezoelectric behavior: They change their electrostatical polarization by application of mechanical force (direct piezoeffect) or change their dimensions under an applied electric field (inverse piezoeffect). Origin of this behavior is PZT’s tetragonally distorted perovskite crystal structure (see sec.2.3.2) and the alignment of its polarization vectors along the direction of the electric field (see sec.2.3.3). PZT excels at its electromechanical performance, relatively easy processing and a wide range of achievable properties by changing composition and doping [3].

Nevertheless defect chemistry of PZT is still far from being understood. That is mainly due to the pronounced variability of the defect concentrations, which is caused by aliovalent doping, processing conditions and particularly PbO-evaporation during sintering [4]. The latter can lead to a significant nonstoichiometry.

In case of SrTiO_3 and BaTiO_3 numerous research groups worked on this topic for many years and a very high level of knowledge in bulk defect chemistry and partly also in interfacial defect chemistry has already been achieved [5, 6, 7, 8, 9, 10, 11, 12, 13, 14, 15, 16, 17, 18, 19, 20, 21, 22, 23, 24, 25, 26, 27, 28]. Although a lot of research has also been performed on PZT and related materials, it is still not sufficiently understood under which doping, pressure and temperature conditions ionic or electronic conduction prevails and if grain boundaries are highly resistive

or highly conductive paths for charge transport [4, 29, 30, 31, 32, 33, 34, 35, 36, 37, 38, 39, 40, 41, 42, 43, 44, 45, 46]. Only recently, evidence was found that in donor-doped PZT very pronounced oxygen tracer diffusion along grain boundaries may take place, at least above 600 °C [47, 48].

Aging and fatigue of ferroelectrics *without high electric field stress* is often attributed to migration of defects into the domain walls, the alignment of defect dipoles along the field direction or trapping of electronic species at the domain walls; All of them stabilize the domain walls and hinder domain switching, which is reflected in a decrease of piezoelectric coefficients [4, 49, 50, 51].

Under *high electric field stress*, perovskite-type oxides can show drastic conductivity variations, finally leading to continued increase of leakage current and/or breakdown.

In the case of single- and polycrystalline negatively (acceptor) doped SrTiO₃ and BaTiO₃ drastic conductivity variations under high-voltage load on a longer time scale could be attributed to the motion of oxygen vacancies ($V_{\text{O}}^{\bullet\bullet}$), their accumulation at the cathode (\ominus) and their depletion at the anode (\oplus) [52, 53, 54, 55]. In three papers WASER, BAIATU et al. interpreted their results in terms of a HEBB-WAGNER polarization experiment with two (at least partly) ionically blocking electrodes [56, 57, 58]: Upon high- field stress all mobile charge carriers, i. e. electrons (e^-), holes (h^+) and oxygen vacancies ($V_{\text{O}}^{\bullet\bullet}$) move towards the differently charged electrode. That leads to the accumulation of oxygen vacancies at the cathode (\ominus) and correspondingly to their depletion at the anode (\oplus), while the electronic defects can pass the electrodes (cf. Fig. 1.1a). However, to maintain electroneutrality, the free electronic species adapt to the oxygen vacancy density and also build up a gradient according to Fig. 1.1b. Hence, a corresponding lateral conductivity variation is expected.

The space charge layers adjacent to the grain boundaries act thereby as barriers for $V_{\text{O}}^{\bullet\bullet}$ -motion, retarding the resistance variation process (see sec. 2.2.1). The validity of this model was confirmed by local conductivity measurements on acceptor-doped SrTiO₃ single and polycrystals; the latter one even showed subprofiles within the grain with higher conductivity close to grain boundaries [60, 61]. Donor dopants on the other hand strongly stabilize the high-field resistance of SrTiO₃ and BaTiO₃ [52, 53, 62] and in case of La-donor doped SrTiO₃, for example, even after several hundred hours of high field stress at 350 °C hardly any resistance change was found [52, 53]. This was attributed to the negligible concentration of oxygen vacancies in

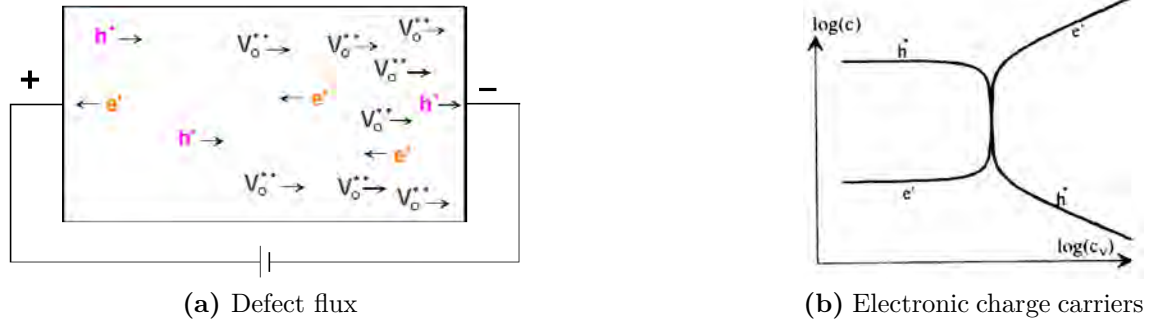


Figure 1.1: (a) Mobile charge carrier flux and (b) concentration dependencies of electronic charge carriers on the oxygen vacancy concentration (c_v) during a HEBB-WAGNER-type polarization experiment with ionically blocking electrodes. Source: [59]

positively (donor) doped materials.

PZT as further representative of the perovskite group, might have a similar defect chemistry as $SrTiO_3$, and phenomena similar to stoichiometry polarization would hardly be surprising in negatively (acceptor) doped PZT.

From bulk and thick-film Pb-containing perovskites a conductivity increase is indeed reported, but mostly under high humidity conditions below $100^\circ C$ [63, 64, 65, 66, 67, 68, 69, 70, 71, 72].

In the presence of water, migration of Ag^+ or other cations dissolving at the anode (\oplus) and precipitating in dendritic structures at the cathode (\ominus) is discussed as a major source of an increase of the leakage current (resistance degradation) [73, 74, 75, 76, 77, 78, 79, 80]. Some studies, conducted under high humidity and temperatures below $100^\circ C$, attributed increased conductivity in ferroelectrics to the formation of metal dendrites along grain boundaries or micro cracks, obviously due to anodic dissolution, electrochemical migration along aqueous surface layers and cathodic deposition of Ag^+ (and other) ions originating from electrode material [63, 65, 64, 73, 74, 75, 77, 78, 79, 80, 76]. See also sec. 2.3.6.

Although the position as well as the exact mechanisms leading to possible metallic discrete conduction paths are still completely unclear, dendrite formation of electrode cations along grain boundaries, in micro-cracks or pores are generally viewed as a highly possible cause.

However, to the best of the author's knowledge little data is available on conductivity variations in bulk-PZT above $200^\circ C$ [35]. More data are available for thin-film

PZT-based ferroelectrics [81, 82, 83], but mechanisms are still heavily discussed. Positively (donor) doped perovskite-type oxides are usually assumed to have virtually no oxygen vacancies, but since the extent of PbO evaporation during sintering is still unquantified, significant V_{O}^{\bullet} -concentrations seem to be still quite reasonable even in positively doped PZT.

Aim of this work The primary focus of this thesis was the investigation of conductivity variations of positively (donor) doped PZT (1.5 % Nd³⁺) at elevated temperatures between 350 °C and 550 °C, upon high fields between 267 kV/m and 2.67 MV/m and in different gas atmospheres. The measurements were carried out on individual layers of multilayer piezoactuator-stacks with Cu- and Ag/Pd- inner electrodes, respectively. As temperatures were > 100 °C, conventional (aqueous) electrochemical migration of electrode material was not to be expected. Temperature and field were systematically varied and the effect of the gas atmosphere was described. Time constants of resistance changes and extent of the conductivity variations were studied as well as the subsequent relaxation behavior after switching-off the electrical field. A possible mechanism causing several observed resistance changes is discussed in the light of previous studies on the stoichiometric polarization of SrTiO₃.

2 Fundamentals

2.1 Defects in solid state ionic materials

Traditionally the education of chemists is mainly focused on liquids and gases. Solids, especially ceramics, are often considered from a naive “outer” point of view as chemically invariant entities, made up of “perfect” crystal structure. However, as MAIER [84] strikingly pointed out, real solids - with all kinds of defects - have to be viewed analogous to gases and liquids: Thermodynamics of gases are determined by the particles which stand out from the empty background space. In solutions of non-charged molecules the dilute ions determine its chemical faith. But also in (ionic) solids the extraordinary particles - the defects - are the ones, which have a dramatic impact on several physical, electrical and chemical properties of one and the same base ceramic. The chemistry and physics of defects - the defect chemistry - plays a key role in this investigation.

In an ideal ceramic crystal the (predominantly ionic) constituents are placed periodically on fixed positions within an infinite three dimensional regular lattice. The smallest repeating unit is called unit cell. It contains every sort of ions present in the material in the characteristic ratio and relative position to the others. In reality already the spatial finiteness of any body, namely its surface, forces deviations from ideality. Besides that, real crystals show defects within their lattice structure, depending of type and composition of the crystal, temperature, atmosphere, pressure and manufacturing process [85, 86, 87, 88].

2.1.1 Thermodynamics

2.1.1.1 Basic relations

The internal energy U of a thermodynamic system is defined as its total energy (E_{tot}) minus its (macroscopic) kinetic (E_{kin}) and minus its (macroscopic) potential (E_{pot})

energy: $U = E_{tot} - E_{kin} - E_{pot}$. Within a closed system, energy can neither be created nor destroyed ($\delta_i U = 0$). Exchange of heat (δq) or mechanical work ($\delta w = -p \cdot dV$; for quasi-static expansion) from outside can lead to a non-zero total differential of the internal energy ($\delta_e U = \delta q + \delta w$). Neglecting surface tension, electrical potential and external material exchange, the *first law of thermodynamics* defines the conservation of internal energy dU as the sum of intrinsic ($\delta_i U$) and extrinsic ($\delta_e U$) energy, hence the sum of exchange of heat (δq) and (constant) pressure (p) times the change of volume (dV):

$$dU = \delta q - p \cdot dV \quad (2.1)$$

However, the concept of energy in the first law does not account for the observation that natural processes have a preferred direction of progress. The introduction of the function of state *entropy* (S) allows a distinction between impossible, reversible and irreversible thermodynamic processes. The entropy distinguishes between dissipated work ($\delta_i S = \frac{\delta W_{diss}}{T} \geq 0$) which stays inside the system and entropy import due to external heat exchange ($\delta_e S = \frac{\delta q}{T} \leq 0$). Obviously entropy “weights” heat production with the absolute temperature T at which the energy transformation takes place. Brought together, the *second law of thermodynamics* becomes

$$dS = \frac{1}{T} \cdot (\delta q + \delta W_{diss}) \geq \frac{1}{T} \cdot \delta q \quad (2.2)$$

Hence, in closed adiabatic ($\delta q = 0$) systems entropy is always increasing ($dS > 0$), only for reversible processes $dS = 0$ by definition. The entropy of an isolated system that is in equilibrium is constant and has reached its maximum value.

Combination of Eq. (2.1) and Eq. (2.2) yields the so called *fundamental thermodynamic relation*

$$-\delta W_{diss} = dU + p \cdot dV - T \cdot dS \leq 0 \quad (2.3)$$

For isobaric ($dp = 0$) and isothermal ($dT = 0$) conditions GIBBS *free enthalpy* G is introduced as

$$G = U + p \cdot V - T \cdot S \quad (2.4)$$

G (also referred to as ΔG) is minimized when a system reaches equilibrium at

constant pressure and temperature: $(dG)_{p,T} = -\delta W_{diss} \leq 0$.

As changes in mole number or defect configuration occur in the irreversibility term $(\delta_i S = \frac{\delta W_{diss}}{T} \geq 0)$ G depends not only on pressure p and temperature T , but also on mole numbers of the constituents n_k .

The total differential of $G(p, T, n_k)$ motivates the definition of μ , the *chemical potential of constituent k* :

$$\mu_k := \left. \frac{\partial G}{\partial n_k} \right|_{p, T, n_{k'} \neq k} \quad (2.5)$$

In the normal case, chemical potentials are dependent on the activity a which is itself a function of the concentration c :

$$\mu_k(c) := \mu_k^0 + RT \cdot \ln(a_k(c_k)) \quad (2.6)$$

with R denoting the ideal gas constant and μ_k^0 denoting the chemical potential under standard conditions for $a_k=1$. With FERMI's definition of partial pressure, the concentration c can be directly converted into the chemical term of *partial pressure p_k of the component k* [89]:

$$p_k = c_k \cdot R \cdot T \quad (2.7)$$

Finally, at constant pressure and constant temperature the fundamental thermodynamic relation becomes

$$dG = \sum_k \mu_k \cdot dn_k \leq 0 \quad (2.8)$$

Hence, at any temperature above 0 K there has to be a finite nonzero kind of disorder or entropy to fulfill Eq. (2.3).

2.1.1.2 From a perfect to a real solid

The way from an ideal perfect crystal to a real electroceramic can be thought in four stages: Starting from the perfect lattice you can think of adding the intrinsic defects, which exist in all pure ionic materials. Introducing external dopants to influence (defect) chemistry of the solid could be a further step (extrinsic defects).

Finally, deliberately or unintentionally a nonstoichiometry within the ceramic could be created, e.g. by freezing-in a high-temperature equilibrium at a lower temperature.

Continuing to follow MAIER [84], defects can be divided into four classes:

0-dimensional defects: Point defects, which are atomic and electronic imperfections,

1-dimensional defects: Line defects, which are essentially dislocations,

2-dimensional defects: Planar defects, i.e. surfaces, stacking faults and internal interfaces like grain boundaries and

3-dimensional defects: Spatial defects, as pores and inclusions.

While one-, two- and three-dimensional defects originate from the manufacturing process, zero-dimensional point defects exist on account of entropy, are reversible and crucial for the charge transfer mechanism in ionic materials. That is why we will take a closer look on the latter one.

2.1.2 Point defects

Point defects are deviations from the perfect crystal at single lattice points. Point defects are the one defect species being responsible for atomic/ionic movement, i.e. charge transfer in solids. They can be characterized as

vacancies, when atoms or ions are missing on their regular lattice points,

interstitials, when atoms or ions situate in between the regular lattice points, or

dopants / impurities, when foreign atoms or ions with the same or different valence state substitute regular ones.

In ionic materials, point defects are usually charged relatively to the regular charge distribution. Hence, charged defects motivate the creation of compensating charges, so that often defect pairs are established. Due to electrostatic reasons, oppositely charged defects often locate together as so-called “*associates*”.

To ease observations on defect chemistry by concentrating on the essential particles alone, KRÖGER and VINK suggested a new kind of defect notation [90]: The

KRÖGER-VINK-notation focuses on the characteristics of a defect, subtracting irrelevant issues of perfect lattice chemistry:

$$\text{Species}_{(\text{Position})}^{(\text{Charge relative to the charge-distribution of the perfect lattice})}$$

The main symbol indicates the species of the defect, either an element such as “Ag” in AgCl or a vacancy “V”. The subscript names the position the defect occupies, which can be a regular lattice point like “Ag” in AgCl or an interstitial site, symbolized by an “i”. The superscript denotes the relative charge of the defect in relation to the regular charge distribution of the imagined perfect lattice: Dots “.” symbolize positive charge units in relation to the defect-free state, dashes “/” denote negative charge units in relation to the charge distribution of the defect free crystal and crosses “×” mean no relative charge difference. Prominent examples are Ag interstitials in AgCl, Ag_i^\cdot , oxygen vacancies in ZrO_2 , V_O^\cdot , free electrons in the conduction band (CB), e' , and electron holes in the valence band (VB), h^\cdot . “*nil*” (or “*null*”) is often used as an entry for a defect-free configuration, e. g. in the KRÖGER-VINK notation of the creation of an Ag interstitial in AgCl: $\text{nil} \rightleftharpoons \text{Ag}_i^\cdot + \text{V}'_{\text{Ag}}$.

2.1.3 Intrinsic and extrinsic defects

2.1.3.1 Intrinsic defects

While *extrinsic defects* are formed only by the addition of impurities or dopants, *intrinsic defects* can already be thermally generated in a previously perfect crystal [88].

There are four basic disorder types of internal ionic defect reactions on a pure monocrystal at finite temperature [84]:

Frenkel disorder (reaction F): Creation of vacancies, after some cations switched from their lattice point to an interstitial. For AgCl the defect chemical reaction and the corresponding mass action law are exemplarily (Brackets “[...]” denote concentrations, \vec{K} is the equilibrium constant for the reaction from left-to-right and for small defect concentrations):



$$\overrightarrow{K_F} = \left[V'_{Ag} \right] \cdot [Ag_i] \quad (2.10)$$

Anti-Frenkel disorder, also “anion-FRENKEL disorder” (reaction \overline{F}): Creation of vacancies, after some (small or polarizable) anions switched from their lattice points to interstitial positions. Exemplarily on CaF_2 the defect chemical reaction and the mass action law are:



$$\overrightarrow{K_{\overline{F}}} = \left[V_F \right] \cdot [F'_i] \quad (2.12)$$

Schottky disorder (reaction S): Creation of a “SCHOTTKY pair”, after a cation and anion switched from their lattice points to the surface (or leaving the crystal). Exemplarily on $NaCl$:



$$\overrightarrow{K_S} = \left[V'_{Na} \right] \cdot \left[V_{Cl} \right] \quad (2.14)$$

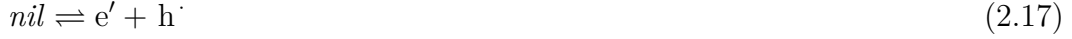
Anti-Schottky disorder (reaction \overline{S}): Creation of an additional monomeric unit (lattice molecule / cation and anion) into interstitial positions. This is definitely not a frequently occurring disorder reaction, one example is yellow PbO :



$$\overrightarrow{K_{\overline{S}}} = [Pb_i \cdot] \cdot [O''_i] \quad (2.16)$$

In addition to the four ionic disorder reactions (acid-base reactions) discussed, there is the fundamental **electronic disorder reaction** (redox reaction) to consider:

In binary ionic crystals ($M^+ X^-$) the valence band (VB) can be associated to the anions (X^-), e.g. oxygen, and the conduction band (CB) to the cations (M^+), usually metals. From a physical point of view, many ionic materials can be seen as semiconductors with large bandgaps, above 3 eV [59]. The electronic disorder reaction can be thought as the excitation of an electron from the valence band to the conduction band, leaving a (free, mobile) electron hole h^\cdot in the valence band behind:



$$\vec{K}_e = [e'] \cdot [h^\cdot] \quad (2.18)$$

The total GIBBS free enthalpy of a real solid G_{real} is given by the G value of the perfect solid $G_{perfect}$ adding the changes that occur on the formation of defects $\Delta_d G$. The GIBBS free enthalpy of the defect formation itself $\Delta_d G$ is additively composed of two local enthalpy terms (static bonding components $\Delta_d G_{bdg}$ and vibrational components $\Delta_d G_{vib}$) and one configurational term $\Delta_d G_{cfg}$. At equilibrium only the concentration-dependent configurational component $\Delta_d G_{cfg}$ is thermodynamically relevant, because both local enthalpy terms ($\Delta_d G_{bdg}$, $\Delta_d G_{vib}$) would afford, instead of produce, free enthalpy at defect introduction [84]. Applying BOLTZMANN's entropy formula to the number of possible micro-states of N_d defects on N regular (lattice) positions yields

$$S_{cfg} = k_B \cdot \ln \left(\frac{N}{N_d} \right) = k_B \cdot \ln \frac{N!}{N_d! \cdot (N - N_d)!} \quad (2.19)$$

By the definition of GIBBS free enthalpy Eq. (2.4) and utilization of the BOLTZMANN (STIRLING-) approximation for small defect concentration ($N_d \ll N$) this leads easily to

$$\Delta_d G_{cfg} \approx N_d \cdot k_B \cdot T \cdot \ln \left(\frac{N_d}{N} \right) \quad (2.20)$$

which is always negative. In total, defect introduction has the following GIBBS free

enthalpy balance:

$$G_{\text{real}} \approx G_{\text{perfect}} + \Delta_d G_{\text{bfg}} + \Delta_d G_{\text{vib}} + N_d \cdot k_B \cdot T \cdot \ln \left(\frac{N_d}{N} \right) \quad (2.21)$$

The local *formation* of intrinsic defects is always endothermic and increases total GIBBS free enthalpy ($\Delta_d G_{\text{bdg}}, \Delta_d G_{\text{vib}} > 0$ in Eq. (2.21)). Only the contribution $\Delta_d G_{\text{cfg}}$ from the increase of configurational entropy is negative (since $N_d < N$). So, up to a certain concentration the effect of entropy driven disorder exceeds the expense of defect formation enthalpy. For *defect pairs* equilibrium is reached at the minimum of the GIBBS free enthalpy, where the number of defect pairs \hat{N}_d is given by [88]:

$$\hat{N}_d = N \cdot \exp \left(-\frac{\Delta g_{\text{local}}}{2 \cdot k_B \cdot T} \right) \quad (2.22)$$

where $\Delta g_{\text{local}} = \frac{1}{N_d} \cdot (\Delta_d G_{\text{bdg}} + \Delta_d G_{\text{vib}})$ abbreviates the specific *local* free formation enthalpies for defect pair formation. Obviously the type of defect pair with the lowest Δg_{local} will be the most prevalent one. Due to Eq. (2.22) the intrinsic defect concentration strongly increases with temperature.

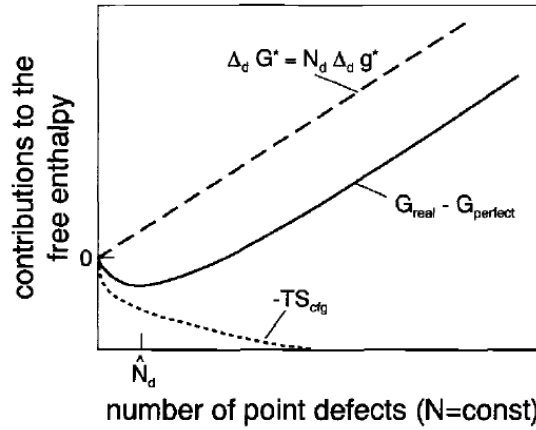
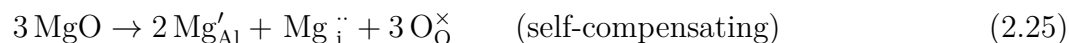
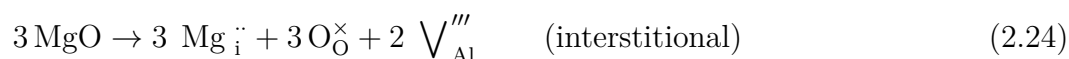
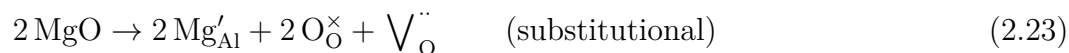


Figure 2.1: Contributions to the GIBBS free enthalpy G_{real} of a solid with a constant number of total sites N by introduction of N_d single defects. $\Delta_d g^*$ is the local free formation enthalpy of a single defect. Source: [84].

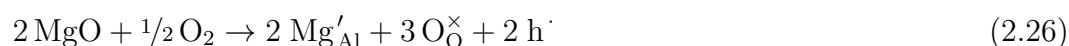
Fig. 2.1 shows a calculated defect-concentration plot of Eq. (2.21) for simple intrinsic point defects. Obviously a finite number of defects is thermodynamically favored to the defect-free “perfect” crystal. Thus, intrinsic point defects in solids are *entropically stabilized*.

2.1.3.2 Extrinsic defects - Doping

Extrinsic defects originate from foreign substances, not represented in the composition of the pure ceramic. Hence, extrinsic defects can be impurities from the manufacturing process, but usually they are triggered intentionally by *doping* the ceramic with other materials. As the introduced dopants usually include aliovalent ions (having a different charge than the host), the created defect will be also charged relative to the undisturbed crystal. To maintain charge neutrality and stoichiometry, some kind of compensating defect with opposite charge has to appear. Not only it's often difficult to predict on which place the dopant will situate, it is equally complicated to predict, which kind of compensating defect will arise. CHIANG et al. illustrated the variability of extrinsic incorporation (and compensation) mechanisms of MgO in Al₂O₃, where the Mg²⁺-ion may enter the solid solution substitutionally, interstitially or self-compensating [88]:



Of course, further doping mechanisms are possible, e.g. combined with intrinsic disorder or particularly with electronic charge compensations effects, e.g.:



MAIER premises the doping ions to be immobile (except for very high temperatures) and their concentration to be constant “*ex situ parameters*”. Further he generalizes one fundamental rule of doping, the “*rule of homogenous doping*” [84]:

If the doping defect introduced is positively charged, than the concentrations of all negatively charged, ionic and electronic defects are increased, while the concentrations of positively charged defects are reduced. The opposite occurs for negatively charged dopants. This applies not only

to a combination of defect concentrations, but to each individual one. In this sense, there are no compensation effects amongst the mobile defects. More concisely: If z_k is the charge number of defect k and c_k its concentration, and z and C the same parameters of the doping defect, then it follows for all k that

$$z_k \cdot \delta c_k < z \cdot \delta C \quad (2.27)$$

with δ denoting a difference operator, e. g. being < 0 for a concentration reduction.

That means that for defect chemistry it is not absolutely necessary to formulate the incorporation reactions, but rather it is merely necessary to know the effective charge (and concentration) of the doping defect introduced.

It has established from semiconductor physics to name electron-donating dopants “*donors*” and hole-creating (electron-accepting) dopants “*acceptors*”, so Mg in Eq. (2.26) would be called an “acceptor”, because it can create (as charge compensating defects) electron-accepting holes. But as this name-giving electronic charge compensation is by far not the only possible mechanism, cf. doping Al_2O_3 with Mg (Equations (2.23), (2.24), (2.25)), MAIER suggests to name the defects by their relative charge [84]: So doping with relatively positive charged ions, e. g. Nd_{pb} , traditionally called “*donors*”, would be more precisely termed *positive doping*; doping with relatively negative charged ions, e. g. Mg'_{Al} , traditionally called “*acceptors*” should be termed *negative doping*.

While intrinsic defect concentrations increase due to Eq. (2.22) with temperature, extrinsic defects remain largely constant in concentration. Thus, at higher temperatures the likelihood of intrinsically dominated behavior increases. However, in some materials the formation energies of intrinsic defects are so high and the resulting concentrations so low, that intrinsic behavior is virtually never encountered [88]. If the intrinsic defect concentration is much lower than the dopant-concentration c_{dop} , simple electroneutrality requires for a single charge compensating defect a defect concentration c_{def} according to

$$c_{\text{def}} = c_{\text{dop}} \cdot \left| \frac{z_{\text{dop}}}{z_{\text{def}}} \right| \quad (2.28)$$

with z_{dop} and z_{def} being the charge numbers of dopant and compensating defect, respectively [59].

2.1.4 Nonstoichiometry

All in sec. 2.1.3 and sec. 2.1.3.1 mentioned internal disorder reactions, Equations (2.9), (2.11), (2.13), (2.15) and Eq. (2.17), leave the strict stoichiometry of the base compound unaltered. But in reality there are nearly always thermodynamically quasi-stable deviations of strict stoichiometry. The most obvious examples are cation (e.g. $\text{Co}_{1-\delta}\text{O}$, $\text{Fe}_{1-\delta}\text{O}$, ...) or anion (e.g. $\text{SnO}_{2-\delta}$, $\text{TiO}_{2-\delta}$, ...) deficient solid oxides. The δ -value quantifies the nonstoichiometry and depends often on the partial pressure of the compounds in the surrounding atmosphere. Again, it is not easy to predict in which way nonstoichiometry is becoming manifest within the compound in question: Incorporated elements could be vacancies or interstitials, inducing (charge compensating) electrons or holes. This issue gains even more complexity, when the considered crystal is not pure, but doped with aliovalent dopants; Then, a competition of many defect reactions of electronic and ionic nature takes place.

As a simple example let's have a look on a pure binary metal oxide with oxygen deficiency, $\text{MO}_{1-\delta}$ ($\delta > 0$): Is it oxidized, oxygen is incorporated and oxygen vacancies are consumed; is it reduced, oxygen is removed and oxygen vacancies are created:



At higher oxygen partial pressure, an oxygen excess may be created ($\delta < 0$). Then, the corresponding oxygen exchange reaction is varying the concentration of cation (metal) vacancies V_M'' and charge compensating with holes h^\cdot :



In any case the intrinsic electronic redox reaction, Eq. (2.17), is superimposed by the additional variation of electronic defects due to nonstoichiometry: Electrons dominate at oxygen deficiency (Eq. (2.29)) and holes dominate at oxygen excess (Eq. (2.30)). Because the electronic mass action law, Eq. (2.18), has still to be valid, the concentration of electrons $[\text{e}']$ has to decrease at high $p(\text{O}_2)$ ($\delta < 0$), while holes

$[h\cdot]$ go down at low $p(\text{O}_2)$ ($\delta > 0$). The corresponding mass action laws for the oxygen removal and oxygen incorporation reactions, Eq. (2.29) and Eq. (2.30), respectively, are

$$\overrightarrow{K_{\delta>0}} = [e']^2 \cdot [V_{\text{O}}^{\bullet\bullet}] \cdot [\text{O}_2(\text{g})]^{\frac{1}{2}} = [e']^2 \cdot [V_{\text{O}}^{\bullet\bullet}] \cdot \sqrt{p(\text{O}_2)} \quad (2.31)$$

or

$$\overrightarrow{K_{\delta<0}} = [h\cdot]^2 \cdot [V_{\text{M}}^{\prime\prime}] \cdot [\text{O}_2(\text{g})]^{-\frac{1}{2}} = [h\cdot]^2 \cdot [V_{\text{M}}^{\prime\prime}] \cdot \frac{1}{\sqrt{p(\text{O}_2)}} \quad (2.32)$$

with $p(\text{O}_2)$ as the partial gas pressure of oxygen in the surrounding gas atmosphere.

While ionic solids with cations of fixed valence and a correspondingly large free enthalpy for reduction or oxidation, like MgO , Al_2O_3 and ZrO_2 , are highly stoichiometric, oxides containing multivalent cations, such as the transition metals, with more than one stable valence state are prone to form nonstoichiometric compounds, e. g. $\text{TiO}_{2-\delta}$, $\text{SrTiO}_{3-\delta}$, $\text{BaTiO}_{3-\delta}$, $\text{Ni}_{1-\delta}\text{O}$, $\text{Fe}_{1-\delta}\text{O}$, $\text{UO}_{2-\delta}$, etc. [88].

If the defect concentration is solely determined by the non-stoichiometry, Eq. (2.31) can be used to calculate the partial pressure dependence of $[V_{\text{O}}^{\bullet\bullet}]$ and $[e']$ for an oxygen deficient $\text{MO}_{1-\delta}$ ($\delta > 0$) [59]; Owing to the electroneutrality equation of Eq. (2.29) $2 \cdot [V_{\text{O}}^{\bullet\bullet}] = [e']$, and hence

$$[V_{\text{O}}^{\bullet\bullet}] = \frac{1}{2} [e'] = \left(\frac{\overrightarrow{K_{\delta>0}}}{4} \right)^{\frac{1}{3}} \cdot (p(\text{O}_2))^{-\frac{1}{6}} \quad (2.33)$$

$$[e'] = 2 [V_{\text{O}}^{\bullet\bullet}] = \left(2 \cdot \overrightarrow{K_{\delta>0}} \right)^{\frac{1}{3}} \cdot (p(\text{O}_2))^{-\frac{1}{6}} \quad (2.34)$$

Since $\overrightarrow{K_{\delta}}$ is constant, and the electronic defect concentration often influences the conductivity (see sec. 2.2.1), a $-1/6$ relationship in conductivity vs. $p(\text{O}_2)$ measurements is a strong hint to oxygen-deficiency; It is often found in experiments, e. g. in BaTiO_3 , SrTiO_3 , SnO_2 or CeO_2 [59]. Similarly a positive slope of $+1/6$ in σ vs. $p(\text{O}_2)$ -diagrams might be a hint to oxygen-excess (cation-deficiency):

$$[h\cdot] \propto (p(\text{O}_2))^{+\frac{1}{6}} \quad (2.35)$$

The final condition we have to consider, is the requirement of overall electroneutrality within the solid. The sum of all (extrinsic and intrinsic, electronic and ionic, positive and negative) defect-charges has to vanish (z ... charge number of defect i ($z \in \mathbb{Z}$), $z > 0$ for positively charged defects, $z < 0$ for negatively charged defects; $[\text{def}_i]$... concentration of defect i):

$$\sum_i z_i \cdot [\text{def}_i] = 0 \quad (2.36)$$

In our example of the binary $\text{MO}_{1-\delta}$ and SCHOTTKY-disorder the electroneutrality condition reads:

$$2 \left[V_M'' \right] + [e'] = 2 \left[V_O^{\bullet\bullet} \right] + [h] \quad (2.37)$$

2.1.5 Brouwer diagrams

For a given solid, with one dominating disorder reaction, e. g. Eqs. (2.10), (2.12), (2.14) or (2.16), the corresponding band-band (electronic) equilibrium, Eq. (2.18), the reaction with the ambient gas phase (nonstoichiometry), e. g. oxygen deficiency, Eq. (2.29), and finally the total electroneutrality condition, Eq. (2.36), build up an equation system of four equations with four unknowns (cationic defect concentration, anionic defect concentration, electronic defect concentration and hole concentration), provided, the mass action law equilibrium constants and the dopant concentration c_{dop} are known.

Graphical plots of the logarithm of the defect concentrations against the logarithm of the gas (oxygen) partial pressure of the surrounding gas are called **BROUWER-diagrams** or **KRÖGER-VINK-diagrams**. For limited partial pressure regimes only two mobile defects or one mobile defect and the dopant dominate the electroneutrality condition, Eq. (2.36). It is possible to divide the full partial pressure range into so-called **BROUWER-regimes**, within which simple partial pressure dependencies lead to power laws of the defect concentrations:

$$c \propto p(\text{O}_2)^n, \quad n \in \mathbb{Q} \quad (2.38)$$

Calculating all possible pairs of majority defects the full BROUWER-diagram can easily be qualitatively constructed. Real BROUWER diagrams show smooth transition instead of sharp bends. [59].

2.1.5.1 Undoped nonstoichiometric metal oxide

For our example of the SCHOTTKY-disordered pure metal oxide $\text{MO}_{1-\delta}$ the corresponding BROUWER-diagram is made up of three regimes, as illustrated in Fig. 2.2:

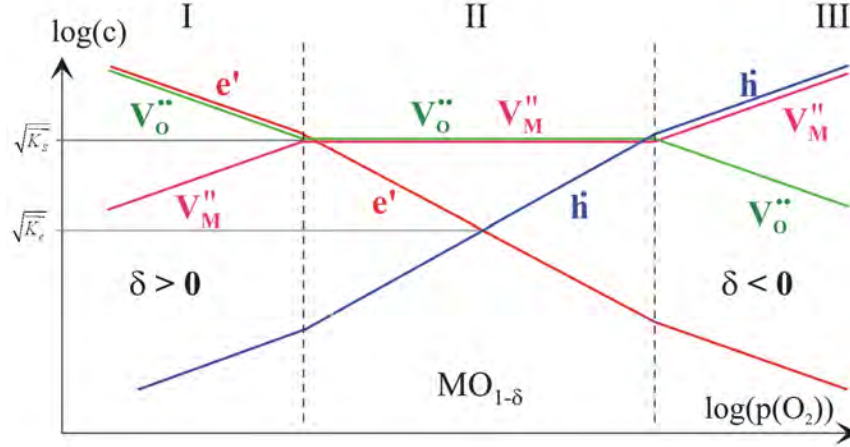


Figure 2.2: Schematic BROUWER-diagram of a pure metal oxide $\text{MO}_{1-\delta}$ with SCHOTTKY-disorder. Regime II is near stoichiometry, hence intrinsic defects dominate. Source: [59].

- I At very low oxygen partial pressure, reduction dominates the electroneutrality condition Eq. (2.37), thus $[e'] \approx 2[V_O^{\bullet\bullet}]$ and the metal oxide $\text{MO}_{1-\delta}$ is oxygen deficient ($\delta > 0$). Hence, Eq. (2.33) and Eq. (2.34) determine the slopes of the concentration of oxygen vacancies $[V_O^{\bullet\bullet}]$ and electrons $[e']$, respectively, which is according to Eqs. (2.33) and (2.34) $-1/6$ for both. The absolute values of the concentrations are slightly shifted by a factor of $\log(2)$ on the ordinate.
- II For medium ambient oxygen partial pressure $p(\text{O}_2)$ the intrinsic SCHOTTKY disorder reaction equivalent to Eq. (2.13) prevails, hence the thermally activated and entropically stabilized intrinsic ionic defects dominate and counterbalance within the electroneutrality condition, Eq. (2.37): $2 \cdot [V_O^{\bullet\bullet}] + [e'] = 2 \cdot [V_M^{\prime\prime}] + [h^{\bullet}]$. The ionic disorder stays almost partial-pressure independent within this regime: The concentrations of the majority defects $[V_O^{\bullet\bullet}]$ and $[V_M^{\prime\prime}]$ are approximately constant. Eqs. (2.31) and (2.32) reveal the slope of $[h^{\bullet}]$ and $[e']$ to be $\pm 1/4$, respectively.
- III At very high oxygen partial pressure the metal oxide $\text{MO}_{1-\delta}$ oxidizes, and it becomes “overfilled” with oxygen, and thus cation (metal) deficient

($\delta < 0$). Metal vacancies and (charge compensating) holes are the major defect species, dominating the electroneutrality condition, Eq. (2.37): $[h^\cdot] \approx 2[V_M'']$. Similar to equations (2.33) and (2.34) the slope of $[h^\cdot]$ and $[V_M'']$ is calculated as $+1/6$, absolute values again slightly shifted by a factor of $\log(2)$ on the ordinate.

Since the intrinsic defect reaction mass action law equilibration constants (ionic Eq. (2.16) and electronic Eq. (2.18)) are valid in all regimes, the concentrations of the corresponding defects proceed symmetric about a horizontal line given by $\sqrt{K_S}$ and $\sqrt{K_e}$, respectively.

2.1.5.2 Aliovalent doped metal oxides

Impurities can have a profound effect on defect chemistry. After clarifying which incorporation mechanism(s) dominates (cf. sec. 2.1.3, sec. 2.1.3.2), a similar model like the one for the undoped oxides (as described in sec. 2.1.5.1) can be constructed.

Extending our example of the SCHOTTKY-disordered metal oxide $MO_{1-\delta}$ by adding a negative (acceptor-type) dopant D_M' , the formerly intrinsic BROUWER-regime (II in Fig. 2.2) splits into one ionically dominated and one electronically dominated section (II and III in Fig. 2.3). In total, four BROUWER-regimes of the defect concentration can be distinguished, each dominated by another majority defect (Fig. 2.3).

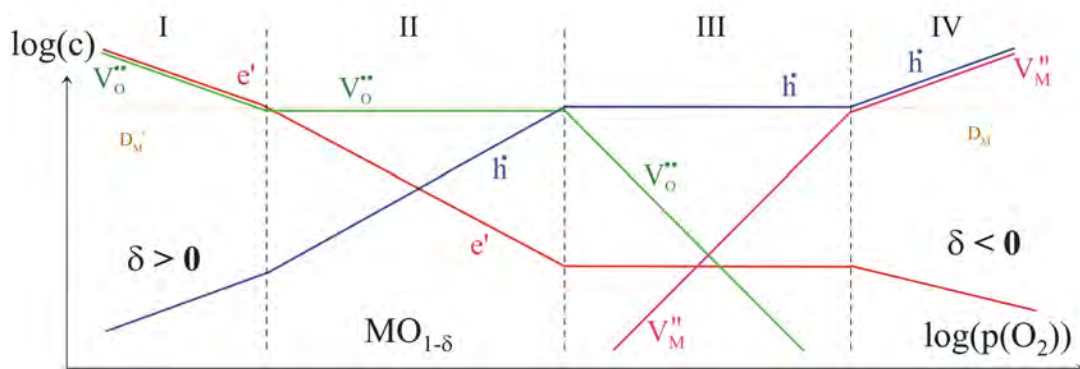


Figure 2.3: Schematic BROUWER-diagram of a SCHOTTKY-disordered, negatively (acceptor-type) doped metal oxide $MO_{1-\delta}$. Between the two nonstoichiometric regimes I and IV two extrinsic regimes (II and III) disclose. Thin yellow line: Constant dopant-concentration D_M' . Source: [59].

Extending the electroneutrality equation for the SCHOTTKY-distorted pure metal

oxide $\text{MO}_{1-\delta}$, Eq. (2.37), with the negative charge introduced by the acceptor leads to the electroneutrality condition for our negatively (D'_M -acceptor) doped metal oxide $\text{MO}_{1-\delta}$:

$$[D'_M] + 2[V''_M] + [e'] = 2[V^\ddot{O}] + [h'] \quad (2.39)$$

This reveals the various distinct compensation mechanisms, leading now to four BROUWER-regimes, illustrated in Fig. 2.3:

- I At very low oxygen partial pressure, like in BROUWER-regime I in Fig. 2.2, nonstoichiometric reduction dominates the extended electroneutrality condition Eq. (2.39). The slope of $[V^\ddot{O}]$ and $[e']$ is again $-1/6$.
- II In this first extrinsically dominated regime at low $p(\text{O}_2)$ oxygen vacancies are charge compensated mainly by the constant dopant concentration $[V^\ddot{O}] \approx \frac{1}{2}[D'_M]$, while intrinsic compensation of electronic defects is the same as already calculated for regime II in the undoped BROUWER-diagram Fig. 2.2: $[e'] \propto (p(\text{O}_2))^{-\frac{1}{4}}$ and $[h'] \propto (p(\text{O}_2))^{\frac{1}{4}}$.
- III At elevated oxygen partial pressure, an increasing $p(\text{O}_2)$ leads to vanishing oxygen vacancies $V^\ddot{O}$ accompanied by a rise of the oxygen excess induced cation (metal) vacancies V''_M . Electronic holes h' predominantly compensate the constant concentration of the negative dopant charge: $[D'_M] \approx [h']$. For an approximately constant hole concentration $[h']$ Eq. (2.32) yields $[V''_M] \propto (p(\text{O}_2))^{\frac{1}{2}}$ and $[V^\ddot{O}] \propto (p(\text{O}_2))^{-\frac{1}{2}}$.
- IV At very high oxygen partial pressure, like in BROUWER-regime III in Fig. 2.2 nonstoichiometric oxidation dominates the extended electroneutrality condition Eq. (2.39). Likewise the slope of the mutual charge-compensating $[h']$ and $[V''_M]$ is $+1/6$.

As the predominant BROUWER-regimes of real materials strongly depend on the concrete sample composition under investigation, it is practically impossible to scan through all four BROUWER-regimes on one and the same ceramic. Within the technically practicable oxygen partial pressure range from about 10^{-25} bar to 1 bar, mostly only one or two BROUWER-regimes of the materials can be experimentally verified [59]. The BROUWER-diagram represents one major research conclusion on the defect chemistry of a compound. However it is rather difficult, to determine the individual defect concentrations, their dependency on the oxygen partial pressure

and equilibrium constants. For many technically important materials, including PZT, BROUWER-diagrams are not available so far [91]. Finally it has to be noted, that the above considerations are simplifications, as small defect concentrations were presupposed, interactions between defects, like creation of associates, precipitations, the use of activities rather than concentrations and effects of higher order defects (dislocations, space charge layers and grain boundaries) were completely ignored. All of them can heavily affect the defect chemistry of a real solid [84, 88].

2.1.6 Frozen-in states

BROUWER-diagrams show defect concentrations in thermodynamic equilibrium at a given temperature and in a given atmosphere. Since the equilibrium defect concentrations depend on temperature (Eq. (2.22)) and surrounding atmosphere (sec. 2.1.4), absolute values in BROUWER-diagrams also change with temperature and partial pressure. A change of equilibrium to different conditions requires diffusion of the defects within the sample, e. g. from the surface to the core. In solids, diffusion coefficients are thermally activated and especially at lower temperature they can be rather small, hence equilibration to changed parameters can take long times or may sometimes never be finished. Therefore, non-equilibrated ionic solids with internal composition gradients can easily occur and often the manufacturing conditions, rather than the actual surroundings determine the defect concentrations. Such non-equilibrated states at lower temperature are called *frozen-in compositions*. While on the one hand high-temperature sintering in a given atmosphere and subsequent quenching to significantly lower temperatures can lead to defect concentrations not expected for the given measurement ambience, on the other hand deliberately “*frozen-in*” high-temperature induced defect concentration profiles enables (spatially resolved) low-temperature measurements of the corresponding conductivity profiles [60, 92, 93].

However, highly mobile defects, like electrons and holes, necessarily equilibrate to the non-equilibrated defect concentrations of a frozen-in reaction, particularly even at room temperature. Such an adjustment of electronic disorder to a frozen-in oxygen vacancy profile in a negatively (acceptor) doped metal oxide is illustrated in Fig. 1.1b.

2.1.7 Voltage induced defect profiles

Applying voltage to an ion-conducting ceramic, usually leads to a steady-state current of ionic charge carriers (e.g. via $\nabla \ddot{O}$) through the crystal from one electrode to the other. However, this is only true if both electrodes allow an ion-electron reaction to convert the external electronic current into the internal ionic transport. Electrodes, which are fully - or at least partly - blocking for ionic exchange, can be used to create defect concentration profiles: Then, for example positively charged mobile defects, like oxygen vacancies, accumulate at the cathode (\ominus), deplete at the anode (\oplus), thus creating an oxygen vacancy (defect) concentration profile decreasing from the cathode (\ominus) to the anode (\oplus), cf. Fig. 1.1a. The concentration of the electronic defects - although themselves involved in the total current - adjust locally to the voltage-triggered oxygen vacancy profile (Fig. 1.1b). This is a kind of a HEBB-WAGNER *stoichiometry polarization* experiment. Both effects lead to significantly different conditions of conductivity within the sample, which have a strong influence on the overall resistance.

For open-circuit cells with the electrode reactions



electrical (cell) voltage U and gas concentrations are coupled by the (modified) NERNST-Equation [94, 95, 84]:

$$U = U^0 + \frac{R \cdot T}{z \cdot F} \cdot \ln \left(\frac{a(\text{O})|_{\text{anode}}}{a(\text{O})|_{\text{cathode}}} \right), \quad (2.41)$$

In Eq. (2.41) U^0 is the standard electromotive force / standard cell voltage (difference of standard electrode potentials of the reduction reaction at the cathode and oxidation reaction at the anode), R is the ideal gas constant, T is the temperature, z is the number of transferred electrons and F the FARADAY-constant and $a(\text{O})$ the chemical activity of neutral oxygen at the anode (\oplus) and the cathode (\ominus), respectively. In our example of *stoichiometric polarization* of an ion conductor between two blocking electrodes (of the same material, $U^0 = 0$) the steady-state current is predominantly carried by electronic charge carriers. However, MAIER has calculated that even in such a case a direct (NERNST'ian) relation between applied voltage U

and the $p(\text{O}_2)$ -axis in the BROUWER-diagram is given by [84]:

$$U = \frac{R \cdot T}{4 \cdot F} \cdot \ln \left(\frac{p(\text{O}_2)|_{\text{anode}}}{p(\text{O}_2)|_{\text{cathode}}} \right) \quad (2.42)$$

Hence, cell voltage U and state of nonstoichiometry (oxygen vacancy concentration $\propto p(\text{O}_2)$) can be transformed into each other and vice versa. The low $p(\text{O}_2)$ -limit in the BROUWER-diagram (left side end of the $p(\text{O}_2)$ -axis) corresponds to the O^{2-} -dispelling ($\text{V}_{\text{O}}^{\bullet}$ attracting) negatively charged cathode (\ominus). The high $p(\text{O}_2)$ -limit in the BROUWER-diagram (right side end of the $p(\text{O}_2)$ -axis) can be viewed as the O^{2-} -attracting ($\text{V}_{\text{O}}^{\bullet}$ repelling) positively charged anode (\oplus).

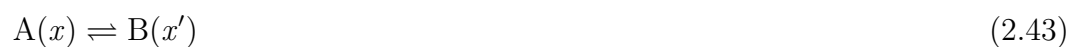
Stoichiometry polarization plays an important role in degradation phenomena of electroceramics like YSZ, SrTiO_3 , BaTiO_3 and possibly also $\text{Pb}(\text{Zr}_x\text{Ti}_{1-x})\text{O}_3$. On some of them laterally resolving microelectrode impedance spectroscopy measurements, have already proven spatial conductivity variations due to high-field induced stoichiometry polarization [59, 60, 96].

2.2 Conductivity and impedance

Considering the relevant (defect) particles, transport and reaction phenomena in ionic solids in principle can be described like electronic and ionic conduction in semiconductor physics and liquid electrochemistry. Hence the approach to transport phenomena in electroceramics in the next two subsections will resemble to otherwise well-known formulas and methods.

2.2.1 Electronic and ionic conduction

While a “typical” chemical reaction $\text{nil} \rightleftharpoons \sum_k \nu_k \cdot A_k$ ($k \dots$ component index; $\nu \dots$ stoichiometric index; $A \dots$ component) is expected to happen on one and the same place x , but changing the reactants from A to B (homogeneous chemical reaction), a change of the chemical situation can also be a transport of one and the same reactant ($A = B$) from the former location x to a final destination x' (heterogeneous transport step). Hence, a chemical reaction of one reactant in general can be described as



Extending the traditional chemical potential μ (Eq. (2.6)) for one mole of z -charged particles by considering its electrical potential ϕ (within an electrical field $E = -\nabla\phi$), leads to the definition of the electrochemical potential $\tilde{\mu}$ (F... FARADAY constant, $F = 96.485 \text{ } ^kC/mol$; R... ideal gas constant, $R = 8.314 \frac{\text{J}}{\text{mol}\cdot\text{K}}$):

$$\tilde{\mu} = \mu + z \cdot F \cdot \phi = \mu^0 + R \cdot T \cdot \ln(a(c)) + z \cdot F \cdot \phi \quad (2.44)$$

The electrochemical potential $\tilde{\mu}$ can be understood as kind of pressure onto the particle, which forces the particle to the conditions, where $\tilde{\mu} \rightarrow \min$.

The corresponding general equilibrium condition for Eq. (2.43) is

$$\tilde{\mu}_A(x) = \tilde{\mu}_B(x') \quad (2.45)$$

Whatever may be the reason for a difference between the electrochemical potentials within a system, if the potentials in Eq. (2.45) deviate from each other, fluxes \mathbf{J} or reaction rates \mathbf{R} appear, trying to counterbalance any electrochemical potential gradient $\nabla\tilde{\mu}$. The continuity equation governs the change of particle concentration:

$$\frac{\partial c}{\partial t} = -\nabla \mathbf{J} + \nu \cdot \mathbf{R} \quad (2.46)$$

For heterogeneous transport steps of one and the same particle ($A=B$), linear flux-force relationships, like FICK's diffusion law or FOURIER's heat conduction law are expected. Hence the field driven charged-particle flux \mathbf{J} is described with the linear *fundamental transport equation*:

$$\mathbf{J} = -\frac{\sigma}{z^2 \cdot F^2} \cdot \nabla \tilde{\mu} \quad (2.47)$$

Hereby, the electrical conductivity σ (the inverse of the specific electrical resistance ρ) was introduced as

$$\sigma = 1/\rho = |z| \cdot F \cdot u \cdot c \quad (2.48)$$

For the boundary condition $\nabla\mu = 0$ (constant chemical potential) only the electrical field gradient $\nabla\phi$ remains as the driving force in the gradient of Eq. (2.44). Then, Eq. (2.47) leads to OHM's law (expressed in terms of electrical charge current density

$\mathbf{i} = z \cdot F \cdot \mathbf{J}$, rather than particle flux density \mathbf{J}):

$$\mathbf{i} = -\sigma \cdot \nabla \phi \quad \text{Migration - Self-diffusion} \quad (2.49)$$

The (NERNST-) EINSTEIN *relation* enables a transformation of the electrical terms mobility u and conductivity σ into the chemical expression of the **self-diffusion coefficient** D^σ (in “thermal units”) [84]:

$$\frac{D^\sigma}{R \cdot T} = \frac{u}{|z| \cdot F} = \frac{\sigma}{z^2 \cdot F^2 \cdot c} \quad (2.50)$$

For the boundary conditions of $\nabla \phi = 0$ (no electric field) and $\nabla \mu^0 = 0$ (hence $\nabla \tilde{\mu} = \nabla \mu$: pure diffusion) the fundamental transport equation Eq. (2.47) yields FICK’s *first law of diffusion* (D^δ ... **chemical diffusion coefficient**):

$$\mathbf{J} = -D^\delta \cdot \nabla c \quad \text{Chemical diffusion} \quad (2.51)$$

Obviously different transport tasks (experiments) lead to different diffusion coefficients: While the chemical diffusion coefficient D^δ describes a diffusion of neutral components, thus ambipolar diffusion of at least two oppositely charged chemically different particles, the self-diffusion coefficient D^σ is the result of migration of *one* charged defect in a (solid) solution. In addition, diffusion of radionuclide isotopes in tracer exchange experiments is described by the **tracer diffusion coefficient** D^* [84].

Eqs. (2.47)-(2.48) are valid for ionic (vacancies, interstitials) and electronic (electrons, holes) mobile charge carriers, thus the total conductivity of a (mixed conducting) ionic solid is the sum of all contributions [59]:

$$\sigma = \sum_m \left| z_m^{\text{ionic}} \right| F \cdot u_m^{\text{ionic}} \cdot c_m^{\text{ionic}} + \sum_n \left| z_n^{\text{electronic}} \right| F \cdot u_n^{\text{electronic}} \cdot c_n^{\text{electronic}} \quad (2.52)$$

Since the conductivity σ_k is proportional to the concentration c_k of an individual species k (Eq. (2.48)), the oxygen pressure dependency of the total conductivity σ can easily be calculated into a transformed “BROUWER diagram” by weighting the concentration c with the factor $|z| \cdot F \cdot u$ as defined in Eq. (2.48). The corresponding σ vs. $p(\text{O}_2)$ -plot of the BROUWER-diagram of our negatively (acceptor) doped metal oxide $\text{MO}_{1-\delta}$ is illustrated in Fig. 2.4.

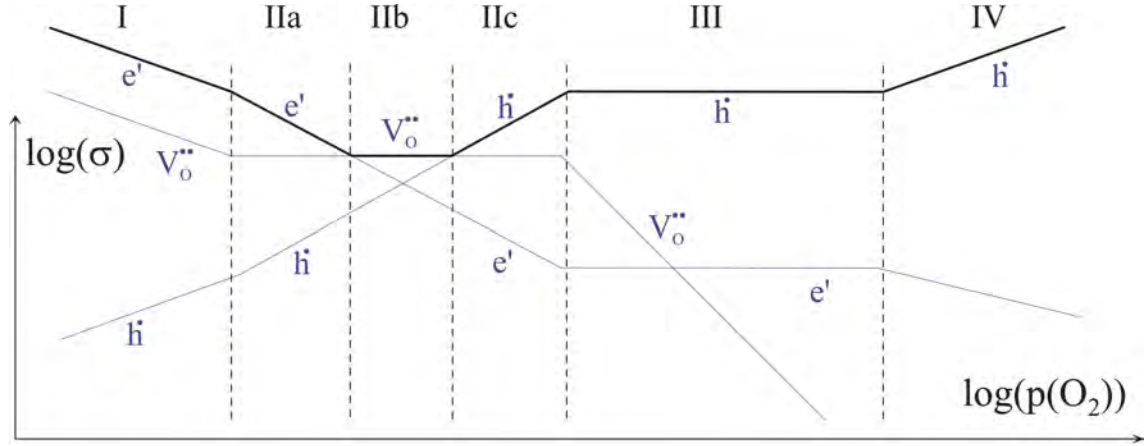


Figure 2.4: Partial pressure dependency of σ , corresponding to the BROUWER-diagram of a negatively (acceptor) doped metal oxide $\text{MO}_{1-\delta}$ (Fig. 2.3). Source: [59]

Although in BROUWER-regime II in Fig. 2.3 the concentrations of the dopant $[D'_M]$ and of (its charge compensating) oxygen vacancies $[V_{\text{O}}^{\bullet\bullet}]$ are higher than both electronic charge carrier concentrations, due to the much higher mobility u of the electronic species, the conductivity within this regime is partly dominated by electrons or holes: In the regimes IIa and IIc in Fig. 2.4, a smaller number of electronic charge carriers determine the overall conductivity due to their higher mobility, although the dopant is mainly compensated by a higher number of ionic defects. Analog considerations employed about BROUWER-regime II in Fig. 2.3 lead also for the conductivity σ to a slope of $\pm 1/4$ in a σ vs. $\log(p(\text{O}_2))$ -plot. Only in between, where both electronic charge carrier concentrations are concurrently at low concentrations, the constant oxygen vacancy concentration might dominate the total conductivity (regime IIb in Fig. 2.4) [59].

2.2.1.1 Thermally activated bulk conductivity

In contrast to common electronic conductivity in metals (i. e. scattering determined movement) or in semiconductors (i. e. transport within a conduction band), the thermally activated hopping process of charged defects from one defect site to the next one is the rate determining step for migration in ionic solids. In the case of a homogeneous electrochemical reaction ($\text{A}(x) \rightleftharpoons \text{A}(x')$) - neglecting concentrations changes and without any electric field - the chemical barrier (in terms of GIBBS free-enthalpy) between two sites is symmetrically, leading to identical reaction rates

for both directions of site-exchange.

An external field ($\mathbf{E} = -\nabla\phi$) however, induces a local potential drop between two defect sites: $\eta := \phi(x) - \phi(x')$, which modulates the GIBBS free-enthalpy \tilde{G} on one side of the barrier (x')

$$\overrightarrow{\tilde{G}} = G^0 - \alpha \cdot z \cdot F \cdot \eta \quad (2.53)$$

and on the other side (x)

$$\overleftarrow{\tilde{G}} = G^0 + (1 - \alpha) \cdot z \cdot F \cdot \eta \quad (2.54)$$

with G^0 denoting the GIBBS free-enthalpy without any field and a ($0 \leq a \leq 1$) being a symmetry factor. These different reaction enthalpies are reflected in different rate constants, leading to different current densities, for opposing transport directions [84]:

$$\overrightarrow{\mathbf{i}} = z \cdot F \cdot k_0 \cdot \exp\left(-\frac{\overrightarrow{\tilde{\Delta G}}}{R \cdot T}\right) = \mathbf{i}_0 \cdot \exp\left(\frac{\alpha \cdot z \cdot F}{R \cdot T} \cdot \eta\right) \quad (2.55)$$

$$\overleftarrow{\mathbf{i}} = z \cdot F \cdot k_0 \cdot \exp\left(-\frac{\overleftarrow{\tilde{\Delta G}}}{R \cdot T}\right) = \mathbf{i}_0 \cdot \exp\left(-\frac{(1 - \alpha) \cdot z \cdot F}{R \cdot T} \cdot \eta\right) \quad (2.56)$$

Here, the exponential BOLTZMANN-terms correspond to the *probability* of successfully passing the barrier and k_0 corresponds to the hopping *attempt* frequency. The *exchange current density* \mathbf{i}_0 is an abbreviation for

$$\mathbf{i}_0 := z \cdot F \cdot k_0 \cdot \exp\left(-\frac{G^0}{R \cdot T}\right) \quad (2.57)$$

Thus, the resulting current density \mathbf{i} can be calculated as

$$\begin{aligned} \mathbf{i} &= \overrightarrow{\mathbf{i}} - \overleftarrow{\mathbf{i}} = \\ &= \mathbf{i}_0 \cdot \left\{ \exp\left(\frac{\alpha \cdot z \cdot F}{R \cdot T} \cdot \eta\right) - \exp\left(-\frac{(1 - \alpha) \cdot z \cdot F}{R \cdot T} \cdot \eta\right) \right\} \end{aligned} \quad (2.58)$$

Eq. (2.58) complies with the BUTLER-VOLMER equation for the current-voltage be-

havior of a metallic electrode in a liquid electrolyte [94], for $\alpha = 1/2$ it corresponds a hyperbolic-sine behavior. For potential drops $|\eta| \gg \frac{R \cdot T}{|z| \cdot F}$, either the anodic ($\vec{\mathbf{i}}$) or the cathodic ($\overleftarrow{\mathbf{i}}$) exponential term in Eq. (2.58) dominates the reaction, so that the other one can be neglected. Then a single exponential function can be used to describe the current/voltage behavior, e. g. for the anodic ($\vec{\mathbf{i}}$) branch of Eq. (2.58):

$$\vec{\mathbf{i}} = \mathbf{i}_0 \cdot \exp\left(\frac{1}{2} \cdot \frac{z \cdot F}{R \cdot T} \cdot \eta\right) \quad (2.59)$$

This exponential relationship between voltage η and current \mathbf{i} is termed TAFEL-law [59, 84, 94].

For small potential drops $|\eta| \ll \frac{R \cdot T}{|z| \cdot F}$ however, the BUTLER-VOLMER relation, Eq. (2.58), can be approximated by its first linear terms ($e^x = 1 + x + \dots$), establishing an *ohmic* current-voltage dependency:

$$\vec{\mathbf{i}} = \mathbf{i}_0 \cdot \frac{z \cdot F}{R \cdot T} \cdot \eta = \sigma \cdot \eta \quad (2.60)$$

Since the exchange current density \mathbf{i}_0 (Eq. (2.57)) is in any case strongly temperature dependent, also the conductivity σ is thermally activated, and for the assumption of temperature independent charge numbers ($z \neq z(T)$) we get

$$\sigma = \sigma_0 \cdot \exp\left(-\frac{G^0}{R \cdot T}\right) = \sigma_0 \cdot \exp\left(-\frac{E_a}{k_B \cdot T}\right) \quad (2.61)$$

with G^0 and E_a being hereby defined as the activation energies per mol and per particle, respectively. σ_0 is proportional to the frequency of hopping attempts. The temperature dependent BOLTZMANN-factor ($1/k_B T$) however, determines the *successful* site-swaps. In $\log(\sigma)$ vs. $1/T$ diagrams (ARRHENIUS-plots) such an activated behavior is displayed as a descending straight line with a slope of E_a .

When the dependence of conductivity with respect to temperature, partial pressure and dopant concentration is known, the mathematical tools presented in this subsection enable at least a qualified guess, to what extent ionic, electronic or mixed conduction dominates in a given ionic material. For a detailed discussion of various mass and charge transport models (ionic conductivity, tracer exchange and chemical diffusion) see [84].

2.2.1.2 Grain boundaries

Ceramic materials are frequently polycrystalline, like PZT. By definition grain boundaries always represent a thin (typically 0.5- 2 nm) breaking line between two ordered crystal structures. Within this grain boundary core, strong crystallographic and chemical differences can exist compared to the bulk. Such modified lattice distances, enhanced disorder and defect concentrations, amorphous phases, segregated impurities or even thin films of second phases can lead to highly resistive *or* highly conductive behavior of the core region [88, 27, 97, 59, 98, 99, 100]. Actually, from an electrical point of view, a grain boundary consists not only of its core: Owing to the different chemical conditions, hence different chemical potentials, in the grain and in the grain boundary core, mobile charge carriers move in the direction of lower chemical potential μ . This separation of positive and negative charge carriers between grain and grain boundary simultaneously creates an electrical field ($\mathbf{E} = -\nabla\phi$), counterbalancing the charge accumulation until - in equilibrium - the electrochemical potential $\tilde{\mu}$ over the polycrystalline solid is constant again. The exact charge distribution in the space-charge region ρ_{scr} in the presence of a given electrical field \mathbf{E} , is ruled by the first MAXWELL-equation (GAUSS's law)

$$\nabla\mathbf{E} = \frac{1}{\epsilon_{scr}} \cdot \rho_{scr} \quad (2.62)$$

with ϵ_{scr} denoting the permittivity in the space-charge region.

If a charged grain boundary core leads to a *depletion* of mobile charge carriers (defects) within the adjacent space charge zone, perpendicular highly resistive space charge layers will result; However, grain-boundary cores enriched with highly mobile defects can still lead to parallel highly conductive grain boundaries [101, 102, 93]. If the charge distribution in the grain boundary core leads to an *enrichment* of mobile charge carriers in the adjacent space charge region, perpendicular highly conductive space charge layers will result; However, mobile defect depleted grain boundary cores lead to parallel highly resistive grain boundaries [103, 104]. If one majority defect species or the dopant is “frozen-in”, i. e. immobile at the temperature at question, one speaks of the MOTT-SCHOTTKY-case. If all majority defects are mobile and thus free to deplete or enrich, this is the GOUY-CHAPMAN-case [84].

Although all charge carriers are in thermodynamic equilibrium, the majority charge carrier determines the electrical potential profile in a space charge zone, forcing the

minority charge carriers to adapt to the given electrical potential distribution. In the oxygen deficient regime of our example of the negatively (acceptor) doped metal oxide $\text{MO}_{1-\delta}$ ($\delta > 0$; BROUWER-regime II in Fig. 2.3), the positively charged oxygen vacancies V_{O}^{\bullet} are the predominant defects often depleted in the space charge zone, but then holes are depleted as well. On the other hand the electron concentration in the space charge region is accordingly enhanced. Due to their poor mobility, the dopants D_{M}' themselves don't contribute to the ionic current, but nevertheless, they may equilibrate and show concentration profiles at grain boundaries. If the major mobile charge carrier is depleted, the dopant concentration is enhanced in the space charge layer, what is often referred to as “*precipitation of the dopant*” [59].

However, it is not trivial to determine whether the conduction occurs in the core of the grain boundary or in the adjacent space charge layers. Furthermore, external applied fields lead to a deformation of the space charge zone, which is utilized in prominent nonlinear electroceramics, namely in high-capacity capacitors, like SrTiO_3 and BaTiO_3 , and varistors (variable resistors) or PTC-resistors mostly based on ZnO and BaTiO_3 , respectively [88]. Exemplarily, for negatively (acceptor) doped SrTiO_3 the space charge layers and the adjacent defect concentrations are illustrated in Fig. 2.5.

2.2.1.3 Electrodes

In space charge layers *within* an ionic conductor, electronic (e' , h') and ionic (V_{O}^{\bullet} , D_{M}' , ...) charge carriers behave *in principle* the same. At the exchange step on the outer borders of the solid, this changes:

Electron transfer Is an electrode metal attached to a mixed conducting electroceramic, both FERMI levels (in other words, the electrochemical potentials) of the electrons must be equal in thermodynamic equilibrium. For negligible interface states, two situations can be distinguished:

- For highly doped (electronic charge-carrier rich) semiconductors or in the case of similar work functions (energy for removing an electron from FERMI-level to the outside vacuum) of metal and electroceramic, theoretically a symmetric transfer of electrons is possible, the current-voltage relationship displays a linear behavior and the contact is termed “*ohmic*”.

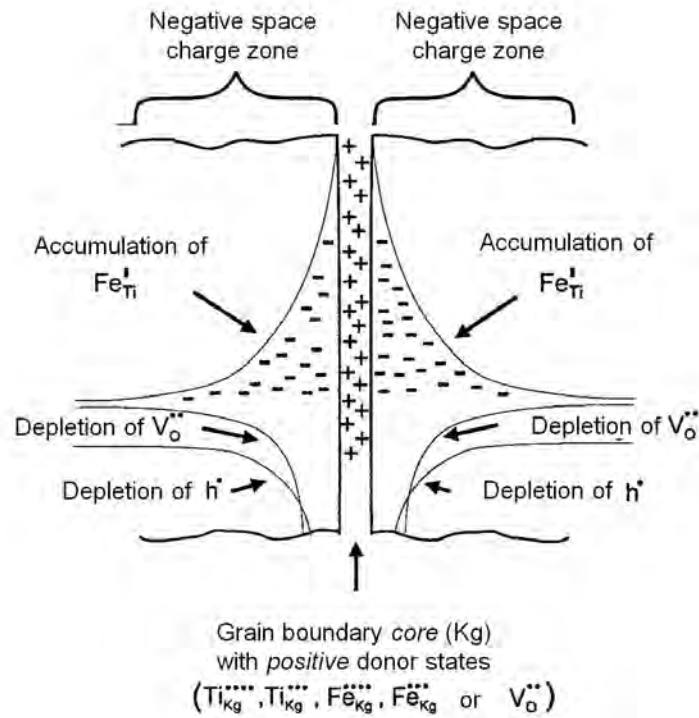


Figure 2.5: Negatively charged space charge layers due to a positively charged grain boundary core and corresponding defect concentrations in negatively (Fe'_{Ti} -acceptor) doped SrTiO_3 . Modified from [92].

- If the work functions of metal and electroceramic differ, electrons in the border area are exchanged, until the resulting electric field counterbalances this transport process. This leads to a bending of the conduction band and the valence band in the interface region of the (semiconducting) electroceramic. While in the metal due to the high electron concentration the resulting space charge layer is quite thin, in the mixed conductor pronounced depletion or accumulation areas can be created, which hinder a free current flow of the charge carriers. An external field affects the magnitude of the band-bending and the extension of the space charge region. Then this SCHOTTKY-*barrier* is the dominating hindrance to current flow and a highly non-linear and strongly temperature dependent current-voltage relationship will result, like in the SCHOTTKY diode:

$$I = I_0 \cdot \left(\exp \left(\frac{e \cdot U}{k_B \cdot T} \right) - 1 \right) \quad (2.63)$$

(I_0 ... saturation current; e ... elementary charge). However, since the SCHOT-

TKY barrier gets smaller for higher dopant concentrations, *quantum tunneling* can then diminish SCHOTTKY-like behavior. [105].

Ionic transfer For the mobile ionic species the electrochemical redox reactions at the electrode/electroceramic interface are of prime interest. A prominent example is the cathodic oxygen reduction reaction of the incorporation of O^{2-} in solid oxide fuel cells (SOFC):



Depending on material and morphology of the electrode, three reaction paths are discussed: (I) Adsorption and diffusion of oxygen species along the electrode surface to the (1-dimensional) three phase boundary and subsequent incorporation step, (II) dissolution and transport of oxygen within the electrode and incorporation at the (2-dimensional) electrode/electrolyte contact area or (III) direct ionization and incorporation of oxygen directly at the electrolyte surface, without the use of electrode supplied electrons. Further modifications of these paths are also possible. Plenty of research is still required, to solve this complex problem. Some promising studies were performed by utilization of geometrically defined microelectrodes [61, 106, 107, 108].

If an electrochemical electrode reaction, e. g. Eq. (2.64), displays a negligible resistance, the corresponding electrode is called a “*reversible electrode*”. The “electrode resistance” denotes the electrical resistance due to the electrochemical reaction or to the transfer step through the space charge layer, rather than the resistance of the electrode material itself [59].

2.2.2 Impedance spectroscopy

Electrochemical impedance spectroscopy (EIS), in which the voltage (current) response to an alternating current (voltage) signal is analyzed as a function of frequency, is an extremely important electrochemical method for determining kinetic parameters. In contrast to electrochemical *dc* measurement methods, EIS replaces the inconvenient measurement of time dependence by a simple measurement of amplitude and phase shift of a sinusoidal signal [84]. While conventional two- or even

four-point *dc* measurements allow at most the exclusion of electrode resistance, the EIS *ac* method allows - under certain conditions - a differentiation between bulk, grain boundary and electrode resistance, diffusion, induction and capacitive effects [59].

If a system is linear, the response to a sinusoidal input signal is also sinusoidal with the same frequency but with a different phase and amplitude. The (frequency dependent) response to the input will be termed transfer function. For the full frequency range, the transfer function - mathematically a convolution of the response with the input signal - describes entirely the dynamic properties of the system. The general tool for transformations from the time-domain into the frequency-domain is the LAPLACE-transformation \mathcal{L} , which converts the convolution in a simple multiplication. If the system is in a steady state, the response to harmonic input is also harmonic; then the LAPLACE function can be replaced by the simpler FOURIER-transformation [109, 84]:

$$\mathcal{F}[f(t)] := \int_0^{\infty} f(t) \cdot \exp(-j\omega t) dt \quad (2.65)$$

j denotes the imaginary unit ($j^2 := -1$), ω the angular frequency ($\omega := 2\pi f$) and t denotes the time.

In general, electrochemical systems are by far not linear. So the direct application of the classical transfer function method is impossible due to their non-linear behavior. The solution of this problem is based on the theory of FREDHOLM-VOLTERRA and lies in the local application of the theory of linear systems. It enables an approximation of a non-linear system with linear terms, if the equivalent linear equations are known at every point of its steady state non-linear characteristic. In electrochemical systems the locally linear analysis is implemented by measuring the transfer function at **very small amplitude of the perturbation (input) signal**, taking into account only the linear part of the response [109].

In terms of such an electrical input-output situation, the LAPLACE transform can be identified with the complex impedance Z , $Z \in \mathbb{C}$, that is the complex *ac* resistance. It is defined as the ratio of time-dependent voltage $u(t)$ and time-dependent current

$i(t)$ [84, 110]:

$$\frac{u(t)}{i(t)} = Z = \Re(Z) + \Im(Z) = R + jX = Z' + jZ'' = |Z| \cdot \exp(j\vartheta) \quad (2.66)$$

$$|Z| = \sqrt{R^2 + X^2} \quad |Z| \in \mathbb{R} \quad (2.67)$$

The complex impedance Z is constituted of a real part $\Re(Z)$ - the resistance R (or Z') - and an imaginary part $\Im(Z)$ - the reactance X (or Z''). The phase factor ϑ tells us that the current lags the voltage by a phase of ϑ .

Electrical circuits as well as empirical relationships of electrochemical systems can often be modeled with networks of *constant phase elements* (CPE):

$$Z_{CPE} = \frac{1}{(j\omega)^n \cdot A} \quad (2.68)$$

Obviously for $n=0$ an ideal resistance R is modeled with $A = R^{-1}$; For $n=0 \pm \epsilon$ ($0 < \epsilon \leq 0.2$) the CPE describes a distorted resistance, e.g. of ion clouds. For $n=1$ the impedance of an ideal capacity C is created with $A = C$; For $n=1 - \epsilon$ ($0 < \epsilon \leq 0.2$) the CPE models a distorted “real” capacitor, accounting losses like electrode surface roughness, charge carrier densities at double layers and accumulation of charge carriers. For $n=-1$ Z_{CPE} describes the behavior of an ideal inductance L with $A = L^{-1}$; For $n=-1 + \epsilon$ ($0 < \epsilon \leq 0.2$) the element describes a distorted inductance, e.g. inductive accumulation of electromagnetic energy. A WARBURG element, $n=0.5$, is often used for a semi-infinite diffusion process, which obeys the second FICK’s law; then $A = \sigma$, which is known as WARBURG coefficient. Diffusion within a finite layer is described by the bounded WARBURG element (BWE), which has a more complicated formula than that of the CPE. Small deviations of this (mostly integer) values of n can be used to describe “distorted” elements, deviating from the ideal electrical behavior. More modeling elements are described e.g. by MACDONALD [111], FLEIG et al. [98] and STOYNOV et al. [109].

If the problem can be mapped by means of an equivalent circuit, then the problem is solved by application of KIRCHHOFF’s rules:

$$Z = \sum_i Z_i \quad \text{for series connections} \quad (2.69)$$

$$\frac{1}{Z} = \sum_i \frac{1}{Z_i} \quad \text{for parallel connections} \quad (2.70)$$

Different kinds of plots based on impedance Z , admittance Z^{-1} , modulus $i\omega Z$ or complex capacitance $(i\omega Z)^{-1}$ can be used to display impedance data. In solid state ionics particularly NYQUIST- (or COLE-COLE-) plots (Z' vs Z'') or BODE-plots ($\log(Z)$ vs. $\log(\omega)$) are common.

For a simple parallel R//C circuit, equations (2.68) and (2.70) yield a semicircle in the impedance complex plane (Z'' vs. Z'). For $\omega = 0$ (*dc*-voltage), the capacitor is completely blocking, $Z = R \in \mathbb{R}$ and only the real part of Z , the resistance R , is measured. For finite and increasing ω (*ac*-voltage) the capacitor “opens” and for $\omega \rightarrow \infty$ finally R is capacitively short-circuited: $Z = \frac{1}{j\omega \cdot C} \in \mathbb{C}$.

When the currents through the resistor and through the capacitor are equal, the imaginary part of the impedance Z (Z'') reaches its minimum. The corresponding frequency is called the characteristic *relaxation frequency* ω_r of an R//C element. In the time period $\tau = \frac{1}{\omega_r} = R \cdot C$ the voltage of the capacitor has changed by a factor $1/e$. For an R//C equivalent circuit with conductivity σ and permittivity $\epsilon = \epsilon_r \cdot \epsilon_0$ it can be calculated, that [59]:

$$\frac{1}{\tau} = \omega_r = \frac{1}{R \cdot C} = \frac{\sigma}{\epsilon} \quad (2.71)$$

Simplifying a polycrystalline electrolyte to a so called brick-layer model, the Faradaic current within the grains can be modeled as a resistance R_{bulk} , while the dielectric displacement current within the grains is described by a capacitor C_{bulk} . The same is true for the resistance of the grain boundaries R_{gb} , where the adjacent space charge layer represents capacitive behavior C_{gb} . Depending on the rate-determining step, also the electrode can be modeled as a parallel $R_{\text{el}}//C_{\text{el}}$ circuit [59].

In the case of highly resistive grain boundaries these considerations can be extended to a so-called “VOIGT’s model” of a connection of bulk ($R_{\text{bulk}}//C_{\text{bulk}}$), grain boundary ($R_{\text{gb}}//C_{\text{gb}}$) and electrode ($R_{\text{el}}//C_{\text{el}}$) as illustrated in Fig. 2.6a. The impedance $Z(j\omega)$ for a series of n R//C elements is calculated as:

$$Z(j\omega) = \sum_{k=1}^n \left(R_k^{-1} + j \cdot \omega \cdot C_k \right)^{-1} \quad (2.72)$$

For $n=3$ Eq. (2.72) leads to three (not necessarily separated!) semicircles, like exemplarily illustrated in Fig. 2.6b.

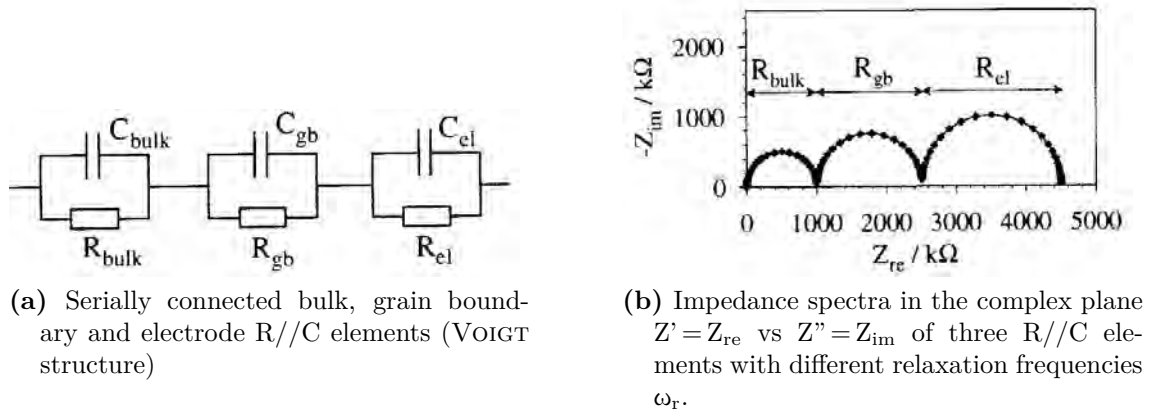


Figure 2.6: Equivalent circuit model of a polycrystalline electrolyte with distinguishable grain boundary and electrode effects. Source: [59]

Usually computer software such as Scribner's zView2[®] is used, to fit the parameters of a modeled equivalent circuit to the empirical data. As “with enough parameters one can fit an elephant”, minimal, experienced and deliberate use of equivalent elements is highly decisive for a realistic interpretation of the EIS data.

However, real electrochemical objects behave as large statistical systems with distributed parameters on macro- and micro-scale. Highly conducting grain boundaries may “shortcut” the bulk resistance in the EIS analysis. During experimentation, processes of mass- and energy-transfer or structural changes could take place. Thus, the system can show non-linear, non steady-state behavior and memory properties, all of which can heavily complicate EIS analysis. A KRAMERS-KRONIG transformation test can be used for verification of a valid interdependency between real and imaginary part of the measured and calculated impedance and thus validation of the assumed working hypothesis [109, 112].

2.3 Lead zirconate titanate $\text{Pb}(\text{Zr}_x\text{Ti}_{1-x})\text{O}_3$ (PZT)

$\text{Pb}(\text{Zr}_x\text{Ti}_{1-x})\text{O}_3$ ($0 \leq x \leq 1$) is a solid solution of the ferroelectric PbTiO_3 and the antiferroelectric PbZrO_3 , developed and described in the early 1950s by SHIRANE et al. [113] and JAFFE et al. [114]. Preparation usually occurs by dissolving the two ceramic powders in a solvent, adding binder and additives, shaping and finally sintering. Mostly the perovskite-type structure of PZT is realized with a Zr/Ti ratio close to the morphotropic phase boundary of two co-existing - tetragonal and

rhombohedral - ferroelectric phases. Depending on the electrode metals used in piezoelectric actuator applications of PZT, the sintering temperatures in the manufacturing process of PZT are about 1000 °C (Cu), 1100 °C (AgPd) and 1300 °C (Pd, Pt) [115].

From an application point of view, PZT largely replaced its predecessor BaTiO_3 : The higher CURIE-temperature T_C of up to more than ~ 350 °C (120 °C for BaTiO_3) allows higher working temperatures for the ferroelectric devices (above T_C PZT turns paraelectric), higher planar electromechanical coupling factors (up to $k_p = 0.65$; BaTiO_3 : 0.35) and piezoelectric constants (up to $d_{33} = 593 \times 10^{-12}$ C/N; BaTiO_3 : 190×10^{-12} C/N) allow better piezoelectric performance. Furthermore, a wide range of properties can be achieved by compositional variations and doping [3, 91].

Piezoelectric transducers are the most important application for PZT. Compared to other actuator systems (motors, magnets, hydraulics, ...) piezoelectrics are very fast, precise and powerful, but show only small displacements [116]. Considering a value for the piezoelectric charge constant d_{33} of 500×10^{-12} m/V a 1 mm thick disk would produce a displacement of only 0.5 μm at 1000 V. Stacking of several hundred, rather thin layers of PZT with interdigit electrodes in between, multiplies the performance of a single element in such so-called multilayer stacks to forces up to 10 kN and deflections up to 130 μm [91, 117].

2.3.1 The piezoelectric effect

There are five types of dielectric response of a dielectric material to an external electric field [118]:

- Polarization of the electronic cloud around the atoms (Electronic response of solids)
- Motion of the charged ions (Polarization of ionic crystals)
- Rotation of molecules with permanent dipole moments (Thermal deflection of field-aligned molecular dipoles in liquids and gases)
- Dielectric screening of a quasi-free electron gas (Many-body COULOMB-interaction of electrons in metals)
- Metastable remaining of polarization in electrets (Frozen-in disorder in organic waxes)

Since for PZT as an ionic solid only the motion of charged ions is relevant for the investigation at hand, we will focus in the following on the classical polarization of ionic crystals.

Electrostriction Owing to the electric force an electric field exerts on differently charged particles, all dielectric solids experience a small change in dimension [51]. The field-triggered deflection of charged particles leads to a net charge difference between two opposed sides of the - even centrosymmetric - unit cells, resulting in attraction and shrinking of the material in direction of the field. Inversion of the field does *not* reverse the strain in the opposite direction, as well as mechanical force alone does *not* trigger elementary electrical separation, i.e. charging of the material. For pure electrostriction the strain S is proportional to the square of the polarization P ($S \propto P^2$) and thus proportional to the square of the electric field E : $S \propto E^2$ [116].

Piezoelectricity Πιέζειν (piezein) is the greek expression for “squeeze” or “press”, ἤλεκτρον (electron) is greek for amber, an ancient source of electric charge. Thus, the electrical polarization of mechanically squeezed materials is called the (*direct*) *piezoelectric effect*. This linear relationship between strain S and electrical field E is completely reversible: The deformation of a material subjected to an electrical field is called the *inverse piezoelectric effect* [116]. The most famous piezoelectric material is quartz, SiO_2 , which resonant crystal oscillations are utilized to stabilize the periodic voltage in so-called “quartz clocks”.

With symmetry operations (rotation, mirroring at a plane, inversion and combinations of these) a periodic lattice structure can be constructed by means of exactly 32 crystallographic (point) classes. Of these 32 crystal classes 21 are not centrosymmetric, i.e. they exhibit a potentially (di)polar structure. With the exception of the cubic class 432 (for reasons of other combined symmetry elements) all of these crystals show piezoelectrical behavior: Upon mechanical stress (compression or tension) a dipole moment can be induced, because the centers of positive and negative charge do no longer coincide. The single contributions of the unit cells accumulate over the whole crystal to an overall polarization, i.e. a net charge separation (voltage difference) between two sides of the macroscopic solid. Inverting the mechanical stress, e.g. from push to pull, also inverts the piezo-voltage. The other way round, an electrical voltage applied to a piezoelectric makes the lattice changing its structure,

hence making the whole solid changing its dimension [1, 115, 119]. An exemplarily illustration of quartz, SiO_2 , is depicted in Fig. 2.7.

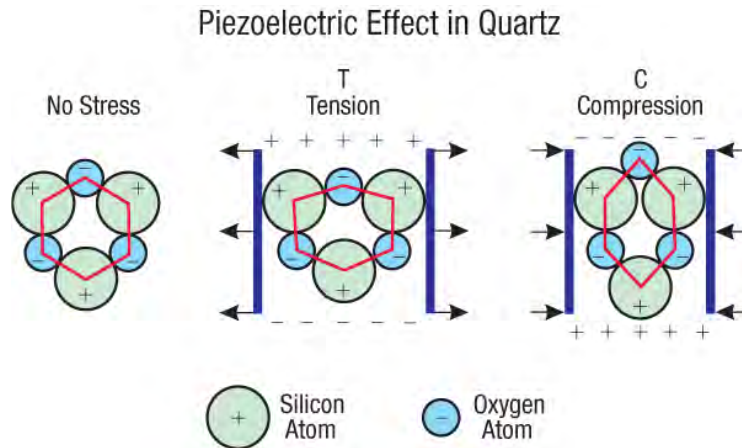


Figure 2.7: Piezoelectric effect in SiO_2 . Source: [120]

Some of the 20 piezoelectric crystal classes are *nonpolar*, i. e. without spontaneous polarization. Examples are α - and β -quartz (SiO_2), Rochelle salt ($\text{KNaC}_4\text{H}_4\text{O}_6 \cdot 4\text{H}_2\text{O}$) and gallium arsenide (GaAs). 10 piezoelectric crystal classes own a single polar axis and thus show spontaneous polarization, i. e. the elementary cells (and hence the domains) have an electrical dipole already without external force, because of different centers of positive and negative charge, respectively. As the length (and orientation) of such polar crystals changes already at isotropic thermal expansion, they are called *pyroelectrics* and are used in motion detectors, temperature sensing, etc. A subset of the pyroelectrics are the so-called *ferroelectrics*¹, which are probably the most important electroceramics: Their (single) polar axis can be inverted by an external electric field. Similar to the magnetic domains in a ferromagnetic, ferroelectrics show a polarization vs. electric-field hysteresis loop and loose their pyroelectric behavior above the so-called CURIE-temperature [1, 3, 115, 121]. See also sec. 2.3.3.

Piezoelectricity is the combined effect of the electrical behavior of the material and HOOKE's law. The dielectric charge displacement vector \vec{D} describes the polarization effects of a dielectric material (with the relative permittivity ϵ_r) in an external electric field \vec{E} :

$$\vec{D} = \epsilon_0 \cdot \vec{E} + \vec{P} = \epsilon_0 \cdot (1 + \chi_e) \cdot \vec{E} = \epsilon \cdot \vec{E} \quad (2.73)$$

¹Although iron has nothing to do with it, the term “ferro” is used due to some characteristic analogies to ferromagnetism.

Here, ϵ_0 is the electric constant ($\epsilon_0 = 8.854 \times 10^{-12} \text{ F/m}$), \vec{P} is the polarization, χ_e is the electric susceptibility, $\epsilon = \epsilon_0 \cdot \epsilon_r$ is the absolute permittivity and the dimensionless entity ϵ_r is the frequency-dependent relative permittivity of the material (called “dielectric constant” only for a frequency of zero).

HOOKE’s law describes the *linear* relationship between the strain tensor \mathbf{S} and stress tensor \mathbf{T} of a material with the stiffness (compliance) s (for one dimension: $s := F/\Delta x$; F ... force, Δx ... displacement):

$$\mathbf{S} = s \cdot \mathbf{T} \quad (2.74)$$

Utilization of equations (2.73) and (2.74), elimination of the polarization \vec{P} , and introduction of *piezoelectric charge constant* d leads to two coupled equations describing linear piezoelectric behavior:

$$D_k = \{d_{kmn}\} \cdot T_{mn} + \{\epsilon_{kl}\}^{T=const} \cdot E_l \quad \text{direct piezoelectric effect} \quad (2.75)$$

$$S_{mn} = \{s_{mnpq}\}^{E=const} \cdot T_{pq} + \{d_{mnl}^\top\} \cdot E_l \quad \text{inverse piezoelectric effect} \quad (2.76)$$

The subscripts indicate that electric displacement D_i and electric field E_i are vectors (1st-order-tensors), strain S_{ij} and stress T_{ij} matrices (2nd-order-tensors). Accordingly, the corresponding material properties are tensors of 2nd order (electric permittivity ϵ_{ij}), of 3rd order (piezoelectric charge constant d_{ijk}) and of 4th order (stiffness tensor s_{ijkl}), respectively. ϵ_{ij} and s_{ijkl} refer to their values at constant (or zero) strain ($T=const$) and electric field ($E=const$), respectively. That d_{ijk}^\top is just the transposed version of the otherwise identical tensor of d_{ijk} is proved in references [1] and [51].

As orientated (poled) piezoceramics show rotational symmetry along their polar axis, in this cases the tensors of higher order reduce to simple matrices. Usually the direct piezoelectric effect is exploited without application of an additional electric field E . The same is true for common applications of the inverse piezoelectric effect, where normally no additional mechanical stress T is applied [116]. For such a simplified situation the piezoelectric effect is described by these two formulas:

The *direct piezoelectric effect* is the change of electric displacement \vec{D} , due to me-

chanical stress \mathbf{T} , coupled by the piezoelectric charge constant matrix d :

$$D_i = d_{ijk} \cdot T_{jk} \quad (2.77)$$

The *inverse piezoelectric effect* is the change of dimension (strain) \mathbf{S} due to an electric field \vec{E} , equally linked by the same (transposed) piezoelectric charge constant matrix d :

$$S_{ij} = d_{ijk}^\top \cdot E_k \quad (2.78)$$

For switching between dielectric displacement D and electric field E , the piezoelectric charge constant d is sometimes substituted by the piezoelectric voltage constant g , $g := \frac{1}{\epsilon} \cdot d$.

For the direct piezoelectric effect, only a part of the mechanical energy density input $w_{\text{mech}} = \frac{1}{2} \cdot S \cdot T$ is converted into an electrical power output $w_{\text{el}} = \frac{1}{2} \cdot E \cdot D$, the rest dissipates into lattice reorganization. The same is true for the inverse piezoelectric effect, where only a fraction of the electric energy density input $w_{\text{el}} = \frac{1}{2} \cdot E \cdot D$ is converted into the desired mechanical work $w_{\text{mech}} = \frac{1}{2} \cdot S \cdot T$. The *electromechanical coupling factor* k quantifies the relationship between converted energy and total energy input [91, 115]:

$$k = \sqrt{\frac{w_{\text{el}}}{w_{\text{mech}}}} \quad \text{direct piezoelectric effect} \quad (2.79)$$

$$k = \sqrt{\frac{w_{\text{mech}}}{w_{\text{el}}}} \quad \text{inverse piezoelectric effect} \quad (2.80)$$

Because piezoelectrics are anisotropic materials, the piezoelectric constants are tensors, as we have seen. Hence, subscript indices are used to identify a definite tensor entry: The first subscript denotes the direction along which the electrodes and the electric field are applied; the second subscript denotes the direction along which the mechanical energy is performed. An example is the d_{33} value for the piezoelectric charge constant, already mentioned in the introduction to sec. 2.3: As the first subscript for the direction of the electric field and the second subscript for the mechanical performance are the same, electrical field and mechanical strain go along the same direction 3.

2.3.2 The perovskite structure

PZT, $\text{Pb}(\text{Zr}_x\text{Ti}_{1-x})\text{O}_3$ ($0 \leq x \leq 1$), is a solid solution of the ferroelectric PbTiO_3 ($T_C = 495^\circ\text{C}$) and the antiferroelectric PbZrO_3 ($T_C = 234^\circ\text{C}$). Both materials as well as the mixed system crystallize in the perovskite structure ABO_3 , as do many ferroelectrics and other oxides and halogenides [51, 86, 115]. In its **paraelectric state** (above the CURIE-temperature T_C) the perovskite structure is cubic, with the large A-cations (Pb^{2+}) on the corner, the oxygen anions at the center of the faces, and the small B-cation (Zr^{4+} , Ti^{4+}) in the center of the elementary cell, cf. Fig. 2.8a. The structure can also be described as corner linked $(\text{Ti,Zr})\text{O}_6$ octaeders, with the Pb^{2+} cations in the dodecahedral empty spaces between them, similar as Sr^{2+} in SrTiO_3 , see Fig. 2.8b [86, 116, 122]. In this state the structure of PZT is centrosymmetric and paraelectric, hence no piezoelectric behavior is shown, cf. illustration (1) in Fig. 2.8c.

The electric susceptibility χ_e in Eq. (2.73) couples polarization \vec{P} and electric field \vec{E} within a material, $\vec{P} = \chi_e \cdot \vec{E}$. In the paraelectric regime (above T_C) the electric susceptibility χ_e is determined by a CURIE-WEISS behavior ($\beta_C \dots$ constant, $T_C \dots$ CURIE-temperature) [118]:

$$\chi_e(T) = \frac{1}{\beta_C \cdot (T - T_C)} \quad (2.81)$$

Depending on the Zr/Ti ratio in PZT two different ferroelectric structures are possible below the CURIE temperature T_C : A so-called *morphotropic phase boundary* (MPB) separates the rhombohedral (Zr-rich) structure from the tetragonal (Ti-rich) structure, cf. the phase diagram of PZT in Fig. 2.10:

In the **tetragonal phase** the fourfold $[001]$ axis of the unit cell (usually called c -axis) elongates for 2-6 % and the Ti^{4+} and Zr^{4+} cations leave their initial central position and move in one (of two possible) direction(s) along this axis. This shift of the (positive) center of charge with respect to the negligible displacement of the (negative) center of charge creates a non-zero electrical dipole in either the positive or negative direction of the c -axis (cf. Fig. 2.9 and illustration (2) in Fig. 2.8c). For three unit cell axis this yields in total six polarization possibilities. In the **rhombohedral phase** of PZT the length of all unit cell axis stay the same, but all 90° -angles from the cubic system change slightly to $\alpha = 89.75^\circ$ and the Ti^{4+} and Zr^{4+} cations is moving along the new polar threefold $[111]$ axis, which is the

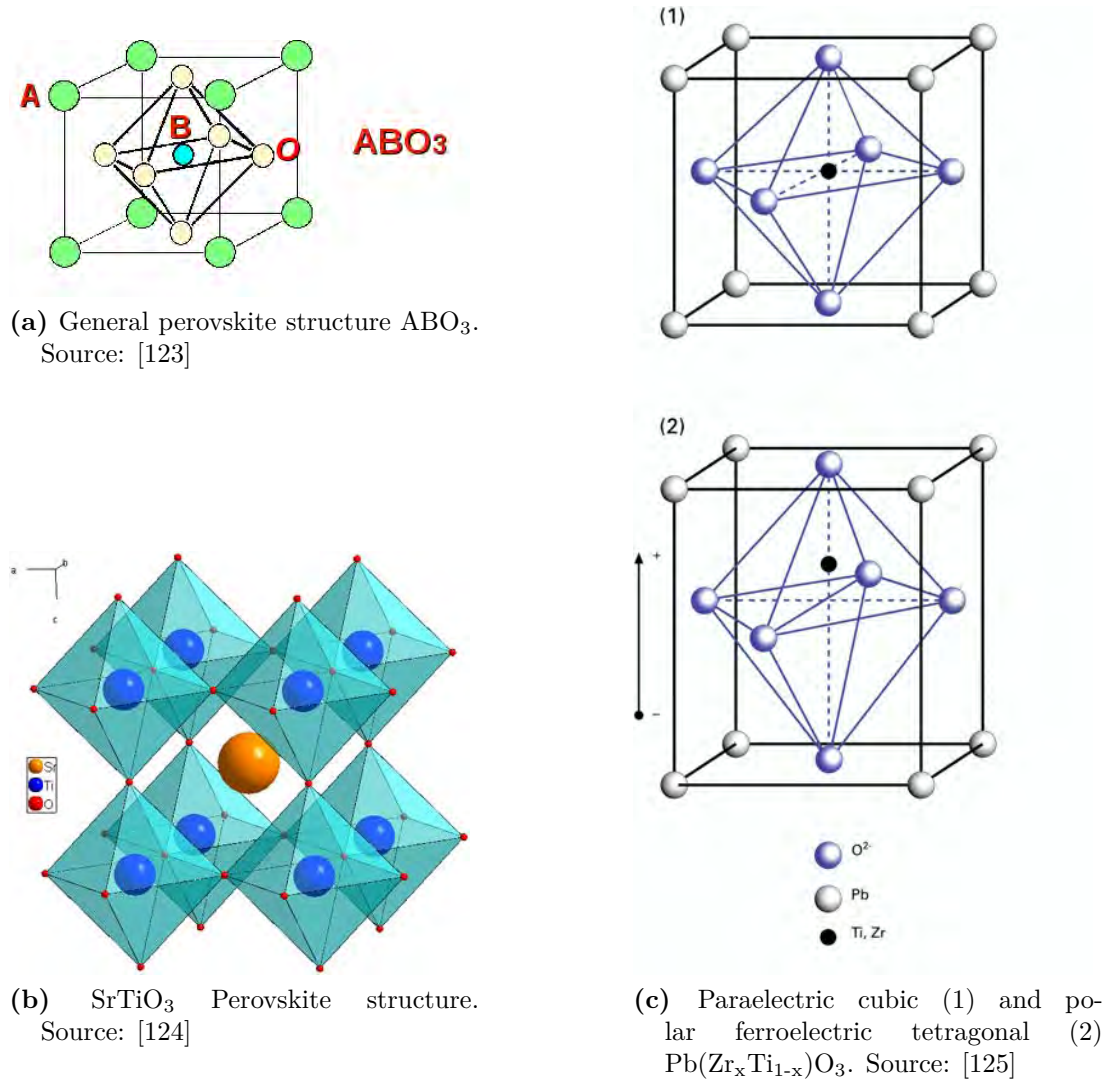


Figure 2.8: ABO_3 Perovskite structure of PZT, $\text{Pb}(\text{Zr}_x\text{Ti}_{1-x})\text{O}_3$ ($0 \leq x \leq 1$)

unit cell diagonal, hence eight polarization directions can be distinguished [115, 91]. In the **orthorhombic phase**, at low temperature and very low Ti content, PZT displays antiferroelectrics behavior, that is due to antiparallel dipole orientation of neighboring unit cells.

According to the phase diagram of $\text{Pb}(\text{Zr}_x\text{Ti}_{1-x})\text{O}_3$ ($0 \leq x \leq 1$), Fig. 2.10, at room temperature the morphotropic phase transition between the rhombohedral ferroelectric and tetragonal ferroelectric phase happens at a composition of about 53 mol% PbZrO_3 and 47 mol% PbTiO_3 , hence $x \approx 0.53$. As close to the morphotropic phase boundary (MPB) both ferroelectric phases exist simultaneously together, the number of possible crystal structures, hence dipole orientations, increases (6 tetragonal

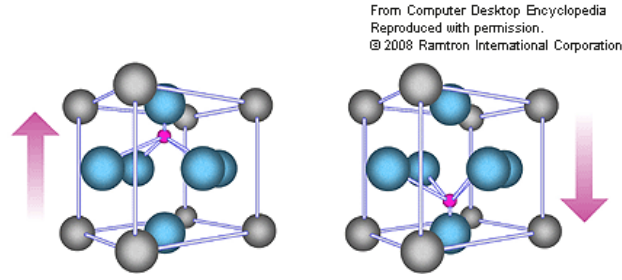


Figure 2.9: Energetically favored positions of the formerly central Ti^{4+} or Zr^{4+} cations in tetragonal (Ti-rich) PZT, creating spontaneous polarization. Source: [126]

+ 8 rhombohedral = 14). This reduces mechanical stress and enables the polar domains to orientate along an external field more easily. Hence, dielectric constant ϵ_r and electromechanical coupling factors d reach their maximum in the vicinity of the (by the way approximately temperature-independent) MPB (peak of relative permittivity, $\epsilon_r > 1500$). At the MPB of PZT about $1/3$ of the unit cells deform tetragonally and $2/3$ switch into the rhombohedral phase [127]. The CURIE temperature T_C depends on the Zr/Ti ratio of PZT, ranging from 230°C to 490°C with increasing Ti proportion (declining x) and $T_C \approx 360^\circ\text{C}$ at the morphotropic phase boundary [128, 115].

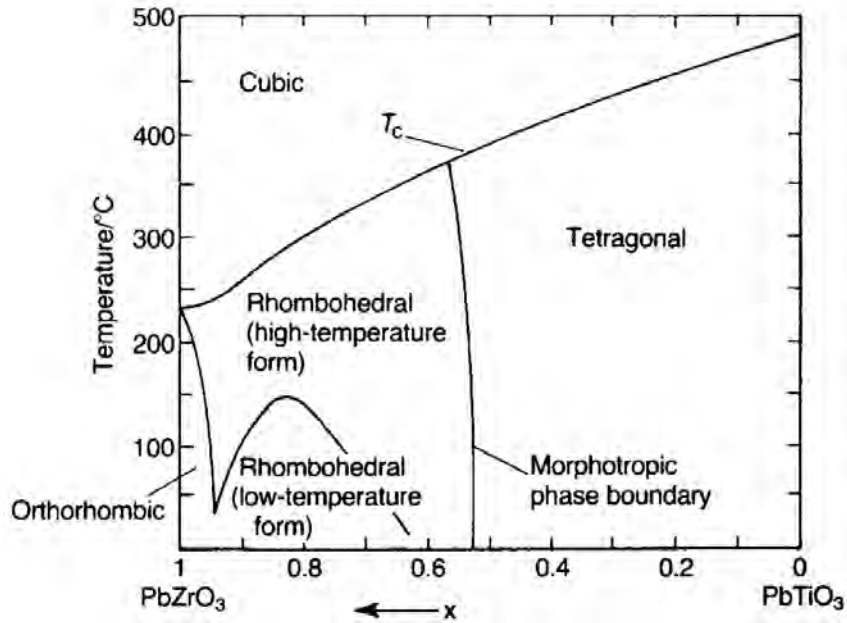


Figure 2.10: Phase diagram of PZT: $\text{Pb}(\text{Zr}_x\text{Ti}_{1-x})\text{O}_3$ ($0 \leq x \leq 1$). Source: [51]

2.3.3 Domain structure and poling

2.3.3.1 Domains

Just as for ferromagnets, a ferroelectric crystal undergoes a phase transition from the paraelectric phase to the ferroelectric phase when the temperature is lowered below the CURIE-temperature T_C . The transition can be either first order (discontinuous, with a latent heat, e. g. BaTiO_3) or second order (continuous, without latent heat, e. g. LiTaO_3). Just as for ferromagnets, ferroelectrics typically split into *domains* of varying size and orientation of polarization. Ferroelectric domains are regions (with a typical size of $\sim 10^{-5}$ m or even more) where the electric dipoles of all included unit cells are orientated in the same direction [86, 116, 87]. Ferroelectrics show polarization \vec{P} vs. \vec{E} -field hysteresis just like ferromagnets display magnetization \vec{M} vs. \vec{H} -field hysteresis. Usually a ferroelectric material consists of many randomly orientated domains, to keep the electric field inside and to minimize flux losses to the outside world. However, within a single-crystal (grain) only discrete directions are possible due to the restrictions of unit-cell and lattice structure. Thus, the minimization of external flux creates an upper limit to the size of domains, but one may wonder, why already only two electric dipoles align parallel, although the electrostatic repulsion (COULOMB-law) would suggest otherwise (e. g. antiparallel). The reason for the existence of domains greater than one unit cell is a “frozen-in” lattice vibrations mode:

The y -component \vec{P}_y of a polarization wave traveling in x -direction can be set as (\vec{q} ... wave vector; ω ... wave number):

$$P_y = P_y^0 \cdot \exp(j(\vec{q} \cdot \vec{x} - \omega t)) \quad (2.82)$$

The solutions for $\omega(q)$ of Eq. (2.82) represent coupled electromagnetic and mechanical waves and are called *polaritons*.

In the centrosymmetric paraelectric state above the CURIE temperature T_C electric dislocations (e. g. dipoles) are only created due to thermally activated lattice vibrations. As those lattice vibrations propagate periodically through the crystal, their integral over time (or space) normally vanishes (paraelectric state). However, the electrodynamic influence of the very dipole in question and neighboring ions (local field) leads to a reduction of the frequency of the transverse normal mode when approaching T_C from higher temperatures. Immediately at the CURIE temperature

T_C of a continuous ferroelectric transition (as in the case of PZT [115]) the crystal spontaneously and continuously distorts to a polarized state, hence the dielectric constant ϵ_r peaks (“*Polarization catastrophe*” of the CLAUSIUS-MOSSOTTI equation $\epsilon_r \rightarrow \infty$) .

A way of viewing the ferroelectric transition is by the LYDDANE-SACHS-TELLER (LST) relation: Here an infinite dielectric constant ϵ_r implies a zero-frequency optical mode. This leads to COCHRAN’s theory of ferroelectricity arising from zero-frequency soft optical modes. COCHRAN has pioneered the approach to a microscopic theory of the onset of spontaneous polarization by the *soft mode* or “freezing out” (wave number $\omega(q)$ going to zero) of an optic mode of zero wave vector q . The vanishing frequency $\omega(q)$ appears to result from a canceling of short-range and long-range (COULOMB) forces between ions: For sufficiently large effective charges, high electronic polarizabilities and/or relatively weak coupling to the nearest neighbors, the transverse frequency $\omega(q)$ can even become zero [129, 121, 118].

Especially for PZT, the covalent (homopolar) part of the Ti-O bonding of the TiO_6 octahedra may be a further explanation for the parallel (and not antiparallel) alignment of the dipoles of adjacent unit cells below T_C , and thus leading to ferroelectric (instead of antiferroelectric) behavior: This homopolar contribution involves also the tendency of oxygen towards angled valencies, like the 109 °C angle between hydrogen in water molecules. It favors the parallel orientation of the polarization in neighboring lattice cells and it causes the transition to ferroelectricity instead of antiferroelectricity below the CURIE-temperature T_C [130].

In individual grains of polycrystalline PZT multiple domains are established of the size of about 1 μm [128]. At the morphotropic phase boundary the domains can be arranged in angles of 90° and 180° (tetragonal phase) and in angles of 71°, 109° and 180° (rhombohedral phase) [1]. Up to 25 unit cell wide *domain walls* with continuously changing dipole orientation separate two adjacent ferroelectric domains. In a macroscopic piece of ferroelectric PZT the polarization directions of different domains are after fabrication randomly distributed. In total they cancel each other out, hence a macroscopic polarization of zero results and disables any macroscopic piezoelectric effect.

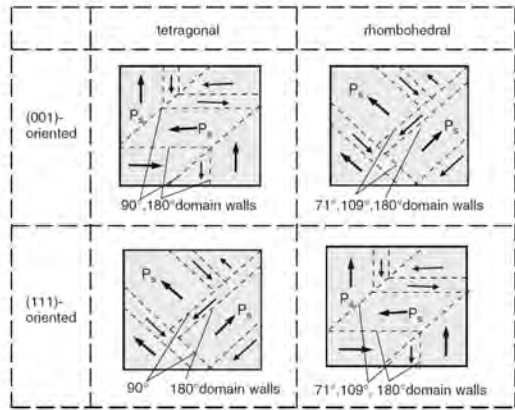
2.3.3.2 Poling

To evoke macroscopic piezoelectric effects, the sample has to be poled. Often at increased temperatures, but anyway below the CURIE temperature, the spontaneously poled ceramic (Fig. 2.11a) is subjected to a high external electric field (for PZT ranging from 25 °C / 2 MV/m up to ca. 150 °C / 30 kV/m for several seconds to minutes [91, 131]), but also “hot-poling” above T_C and subsequent cooling under applied field (ca. 0.5 MV/m) is used.

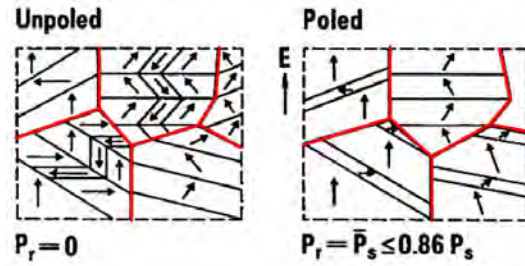
The domain structure realigns by growth of domains with compatibly oriented spontaneous polarization \vec{P}_s and domain switching of domains not fitting to the external electric field \vec{E} . As saturation is an asymptotic process, the so-called *saturation polarization* \vec{P}_{sat} is defined as linear extrapolation of the slope of \vec{P} at maximum \vec{E} -field \vec{E}_{sat} to the \vec{P} -axis; cf. Fig. 2.11b. Logically, domain switching by 180° has virtually no effect on the strain, but 90° (tetragonal) and 71° and 109° domain flips create internal stress, which is partly converted into an elongation of the crystal in field direction and slight contraction perpendicular to \vec{E} . Switching off the poling field leads only to a slight reversal relaxation of the dipoles, leaving a *remanent polarization* \vec{P}_r (at $\vec{E} = 0$). Fig. 2.11c schematically illustrates the unpoled and remanent poled state at $\vec{E} = 0$ and the growth of domains aligned parallel to the poling field \vec{E} at the cost of domains with different polar orientation. But as the grains (and with them the unit cells) are arranged in an irregular random, but fixed, orientation, by far not all domains can align exactly along the external field. Consequently the maximum level of remanent polarization \vec{P}_r of a whole polycrystalline PZT ceramic reaches only up to 83 % (tetragonal) and 86 % (rhombohedral) if compared to a single domain. Still, the electromechanical response in polycrystals is much greater than in single crystals [1, 3, 116].

Like in ferromagnetics inversion of the external field in the negative direction, reduces the polarization by the same domain reorientation mechanisms but in the other direction. At the coercive field strength \vec{E}_C the overall macroscopic polarization is expunged ($\vec{P} = 0$). Further increase of the \vec{E} -field in the opposite (negative) direction leads to the corresponding negative saturation polarization. Changing the \vec{E} -field back in positive directions, the polarization is also drawn back to the saturation polarization \vec{P}_{sat} , but on a different hysteresis loop, which is characteristic for ferroelectrics, cf. Fig. 2.11b. The corresponding plot of mechanical strain vs poling field \vec{E} yields so-called *butterfly-loops*, as illustrated in Fig. 2.11d.

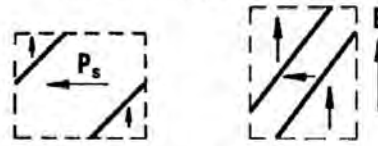
Strong mechanical load as well as elevated temperature destabilize a remanent polarization, thermal depolarization can be expected to start already at $\approx 1/2 \cdot (T_C [^\circ\text{C}])$. Actuator applications are operated in a high-field regime (e. g. 2 MV/m), thus the piezoceramic is completely poled all the time [115]. Complete depolarization can only be achieved by heating (temporarily) above the CURIE temperature T_C .



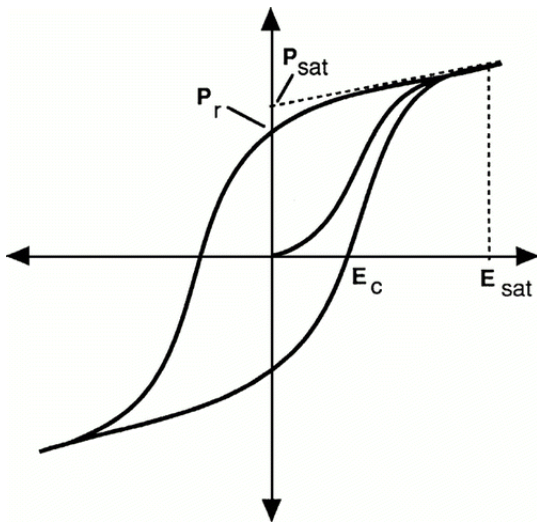
(a) Spontaneously poled domains in tetragonal and rhombohedral crystallites with selected orientations. Source: [130]



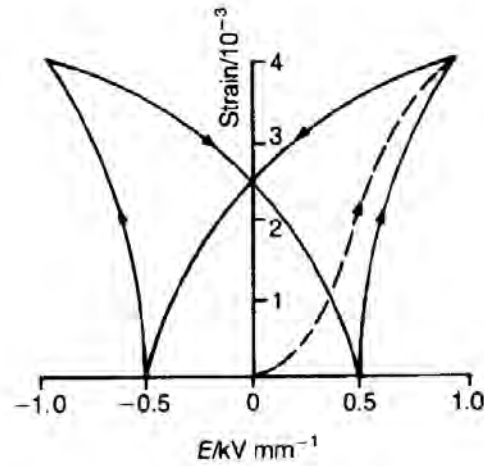
Polarization and strain due to moving domain walls



(c) Microstructure before and after poling Red lines: Grain boundaries. Source: [130]



(b) Polarization \vec{P} vs. electrical field \vec{E} plot. The curve starting from the origin is the so-called “virgin curve”, when the ferroelectric is poled for the first time. Source: [132]



(d) Butterfly-loop: Mechanical strain vs. electric field plot. Source: [51]

Figure 2.11: Spontaneous polarized (\vec{P}_s) domains (a), domains before and after poling by an external electrical field \vec{E} (c), polarization (\vec{P}) vs. field (\vec{E}) hysteresis (b) and strain-field relationship (d) of a typical ferroelectric material.

2.3.4 Doping of PZT

Undoped PZT is believed to be p- (h⁻) conducting due to the (e⁻) acceptor properties of the common negatively charged impurities: Fe³⁺, Al³⁺ and Mg²⁺ replacing Zr⁴⁺ or Ti⁴⁺ on the B-site, e. g. $(\text{Fe}^{3+})'_{\text{Zr}^{4+}}$, $(\text{Al}^{3+})'_{\text{Ti}^{4+}}$, $(\text{Mg}^{2+})''_{\text{Zr}^{4+}}$ and Na⁺ replacing Pb²⁺ on the A-site, $(\text{Na}^+)_{\text{Pb}^{2+}}$ [4]. Depending on the stoichiometry also ionic oxygen conductivity is reported for PZT between 250 °C and 700 °C [133].

As already mentioned in sec. 2.1.3.2, three types of doping are possible:

Isovalent doping: Additives with the same valence state (and approximately the same size) replace the host ion, e. g. $((\text{Sr}, \text{Ba}, \text{Ca})^{2+})^\times_{\text{Pb}^{2+}}$ or $((\text{Sn})^{4+})^\times_{(\text{Zr}, \text{Ti})^{4+}}$. The primary effect of isovalent doping is a stabilization of the ferroelectric domain walls, leading to a decreased piezoelectric response. Furthermore the CURIE-temperature T_C and the dielectric loss (dissipated energy of an *ac*-field within a dielectric) are decreased and the aging rate is accelerated. Isovalent doped PZT is used in high-power applications [1, 3, 134].

Positive doping - Donors: As member of the class of (relatively) charged defects, positive dopants (donors) necessarily introduce simultaneously a charge-compensating defect, as mentioned in sec. 2.1.3.2. To maintain electroneutrality positively charged dopants (traditionally termed *donors*), like $((\text{La}, \text{Nd}, \text{Bi}, \text{Sb})^{3+})'_{\text{Pb}^{2+}}$ or $((\text{Nb}, \text{Ta}, \text{Sb})^{5+})'_{\text{Zr}, \text{Ti}^{4+}}$, are mostly compensated by an increase of cation vacancies on the A-site (V''_{Pb}), but also B-site vacancies have been considered ($V'''_{\text{Zr}, \text{Ti}}$). If oxygen vacancies ($V\ddot{\text{O}}$) are (for nonstoichiometric reasons) available, a decrease of them is a primary mechanism to maintain electroneutrality. In any case, positive doping can strongly influence overall conductivity. Furthermore, domain reorientation is enhanced, leading to increased piezoelectric coefficients d , low coercive fields \vec{E}_C and high electromechanical coupling factors k . Aging is suppressed, but the dielectric loss increases due to internal friction. Positively (donor) doped (“*soft*”) PZT has a wide field of high sensitive acoustic applications but also for some actuators and direct fuel injection systems it is used [31, 115, 122].

Negative doping - Acceptors: Dopants with smaller valence as their host ion, like $((\text{Ag}, \text{K}, \text{Rb}, \text{Na})^+)_{\text{Pb}^{2+}}$, $((\text{Fe}, \text{Co}, \text{Mn}, \text{Ni}, \text{Cu})^{2+})''_{\text{Ti}, \text{Zr}^{4+}}$ or $((\text{Fe}, \text{Co}, \text{Mn}, \text{Mg}, \text{Sc}, \text{Ga}, \text{Cr})^{3+})'_{\text{Ti}, \text{Zr}^{4+}}$ are accordingly called *acceptors*. Dominant charge compensating defect reactions (to maintain defect electroneu-

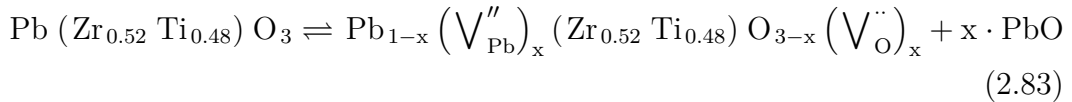
trality) are removal of oxygen (i. e. creation of oxygen vacancies ($\text{V}_{\text{O}}^{\bullet\bullet}$)) or the increase of electronic holes (h^{\bullet}), both possibly leading to enhanced conductivities. Owing to the interaction with oxygen vacancies, the mobility of the domain walls and the piezoelectric coefficients d are reduced and strain and coercive field \vec{E}_C are increased. Hence, negatively (acceptor) doped PZT is called “*hard*”. Due to its small dielectric (heat) loss it is used for high-power applications, like ultra-sonic transducers [1, 3, 115, 130].

Dopants are usually added in concentrations ~ 3 at.% [130], additives in larger amounts are called *modifiers*, e. g. La^{3+} in $(\text{Pb},\text{La})(\text{Zr},\text{Ti})\text{O}_3$ (PLZT) [91].

Although doping levels of PZT are known, a quantification of the extrinsic defect concentrations (and corresponding conductivities) is difficult. With electrochemical impedance spectroscopy (EIS, sec. 2.2.2) it is not necessarily possible to distinguish between distinct conductivity contributions, especially if only one semi-circle appears in the NYQUIST-plot. Usually, conductivity is attributed to electronic charge carriers (e' , h^{\bullet}) and oxygen vacancies ($\text{V}_{\text{O}}^{\bullet\bullet}$), with the holes being partly trapped at immobile lead vacancies. Whether electrons, holes or oxygen vacancies are dominating overall conductivity depends on oxygen partial pressure, temperature and preparation conditions [29, 31, 46, 47].

2.3.5 PbO evaporation

In contrast to the extensively understood BaTiO_3 and SrTiO_3 , the high volatility of lead(II)-oxide (PbO) during sintering of PZT leads to a significant, but usually unknown non-stoichiometry [29, 55, 135]. This uncertainty is one major reason for the incomplete understanding of the defect chemistry of PZT. For undoped PZT with a Zr/Ti ratio of $52/48$ the PbO removal reaction and its corresponding mass action law can be written [29, 115, 122]:



$$\overrightarrow{K_{\text{PbO}}} = [\text{V}_{\text{Pb}}^{\bullet\bullet}] \cdot [\text{V}_{\text{O}}^{\bullet\bullet}] \cdot p(\text{PbO}) \quad (2.84)$$

For PZT, composed at the MPB, losses up to 2.5 mol% PbO are reported [34]. Such a large nonstoichiometry certainly affects defect chemical properties of a compound, so that a qualitative extrapolation from BaTiO₃ and SrTiO₃ to PZT is not directly possible. As the PbO evaporation creates A-site vacancies (V''_{Pb}), incorporation of positive (donor) dopants is evidently facilitated. A high PbO deficiency anyway leads to oxygen vacancies (V_{O}), especially if the PZT is sintered in reducing atmosphere. In practice, PZT precursor powders are often enriched with ~1.5 mol% PbO and the sintering process is done in oxygen-rich and PbO saturated atmosphere to minimize PbO loss. In PbTiO₃ PbO creates an eutectical liquid phase, inhibiting grain growth, improving grain-grain contact and densification, but also dissolving TiO₂, and thus shifting the Zr:Ti ratio away from morphotropic phase transition [115].

2.3.6 Aging, fatigue and degradation

Intrinsic and extrinsic factors determine the stability of piezoelectric properties against aging and different types of external stress [130]. This will be discussed in the following paragraphs.

Electromechanical aging and fatigue mechanisms Many authors investigated thermal aging mechanisms which - even without further external stress - all diminish the piezoelectrical (polarization) response of ferroelectric materials [49, 136, 55, 50]. For PZT some models suggest that oxygen vacancies (induced by PbO evaporation during sintering) may be responsible for *domain wall stabilization*, which lower the electromechanical response, by defect precipitation to grain boundaries like in negatively (acceptor) doped (“hard”) PZT [137, 138, 139, 140, 141, 142] or by creation of defect pair (associates) dipoles and clusters [143, 144]. The same is true for an increased number of locally trapped electronic charge carriers “pinning” domain walls, hence impeding polarization switching [4]. Also positive (donor) dopant driven cation vacancies form defect associates, but due to their low mobility there is no effect expected on domain switching [51]. Due to the mechanical stress at interfaces in piezoelectric actuators *microcracks* are created, which further impede subsequent domain switching [145, 146]. For ferroelectric thin films LOU et al. [136, 141, 147, 148] suggest an (alternative) third polarization degradation model, the so-called *local phase decomposition - switching-induced charge injection* model for bipolar electrical *ac*-load: At the very beginning (and the very end) of a single

domain switching process, extremely high electric fields occur due to the small distance between the unscreened poles of the growing inverted domain (up to 1 GV/m). Correspondingly high currents lead to a decomposition of the PZT phase (partly due to heat-induced evaporation of PbO) in every half-wave of the external depolarization field (< 10 MV/m). Hence ϵ_r of the decomposed fraction of the PZT is stepwise dramatically changed by each load cycle. Mixed (electronic-ionic) conducting electrodes made from LSC, lanthanum strontium cobaltate $(\text{La,Sr})\text{CoO}_{3-\delta}$ turned out to reduce fatigue in PZT films. Since nonstoichiometric LSC is discussed to be a sink for oxygen vacancies from PZT, this could be interpreted as a further hint to V_{O} -contribution in PZT fatigue [149, 150]. Fig. 2.12 schematically illustrates some polarization fatigue models for PZT films.

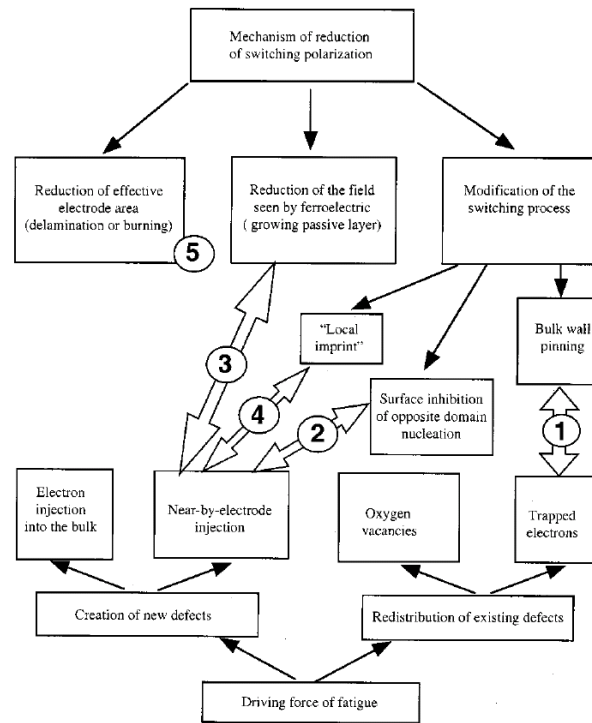


Figure 2.12: Relationship between the phenomena associated with polarization fatigue according to different fatigue models. Source: [149]

Resistance degradation In contrast to the (bipolar) polarization degradation mentioned in sec. 2.3.6, the term resistance degradation is usually applied for piezoelectrics operated *unipolarly* at high voltages. As actuator applications rely strongly on isolation resistance and stable polarizability, resistance degradation is regularly

quantified in terms of an increasing leakage current [151, 64, 65, 63]. Many parameters influence conductivity and degradation (doping, nonstoichiometry, magnitude and frequency of electric field, electrode materials) and comparison of different resistance degradation results is complicated [136]. In contrast to oxide electrodes (like LSC) , regular employed silver based electrodes seem to have a negative effect on piezoelectric properties (e.g. increase of leakage current by grain boundary conductivity) [152], which might be attributed to the high mobility of Ag within PZT [153], possibly leading to a further doping effect [152]. Of course, a different behavior between various electrode materials might also result from the type of the electrochemical contact. So are many metal electrodes known for creating SCHOTTKY-contacts with PZT instead of ohmic contacts like some oxides [154, 155, 156].

This thesis discusses a resistance variation mechanism for positively (Nd-donor) doped PZT with Ag/Pd and Cu electrodes, respectively, and compares it to the stoichiometry polarization model already suggested for negatively (acceptor) doped SrTiO_3 and mentioned in chapter 1 or in [35, 52, 53, 54, 55, 56, 57, 58, 81, 82, 83, 157].

3 Experimental

3.1 PZT Samples

Different types of lead zirconate titanate samples were analyzed in this study, all based on $\text{Pb}(\text{Zr}_{0.525}\text{Ti}_{0.475})\text{O}_3$ (PZT), hence being a composition close to the morphotropic phase boundary. One undoped PZT sample series (referred to as “pure:PZT”) and one sample series doped with varying proportions of Sr^{2+} (isovalently on A-site and acceptor-like on B-site) and B-site donor W^{6+} (referred to as “Sr/W:PZT”) were delivered by the research group of Prof. KLAUS REICHMANN, Graz University of Technology [158]. All other samples of this study were positively (donor) doped with 1.5 mol% Nd^{3+} (referred to as “Nd:PZT”) and supplied by TDK-EPC Corporation, Deutschlandsberg, Austria. While REICHMANN’s PZT samples (approximately $\varnothing 10 \text{ mm} \times 1 \text{ mm}$) were sintered at 1100°C directly from powder to discs (hence without tape casting process and interdigit electrodes), the Nd-doped PZT samples from TDK-EPC originated from the mass production of commercial PZT actuator stacks (hence tape casted and sintered together with metallic interdigit electrodes). A complete stack of TDK-EPC ($\sim 6.8 \times 6.8 \times 28 \text{ mm}^3 \dots \sim 10 \times 10 \times 30 \text{ mm}^3$) consists of about 350 approximately ca. $75 \mu\text{m}$ thick layers of Nd:PZT, separated by metallic interdigit electrodes which are alternately connected to zero potential on the one edge and the working voltage on the other edge by current collectors (contact stripes). An inactive layer of electrode-free PZT is situated as “top-face cover plates” (german: *Deckplatten*) on the very top and the very bottom of such a multilayer piezoactuator element. Some illustrations of Nd:PZT multilayer piezoactuator stacks used in this work are depicted in Fig. 3.1.

The Nd:PZT stacks can be distinguished by the metal used for the interdigit electrodes: The samples with interdigit electrodes made of an $\text{Ag}_{0.75}\text{Pd}_{0.25}$ alloy of 75 % Ag and 25 % Pd are sintered in air and are referred to as “Nd:PZT(AgPd)”. The samples with copper interdigit electrodes are sintered at about 1000°C in a

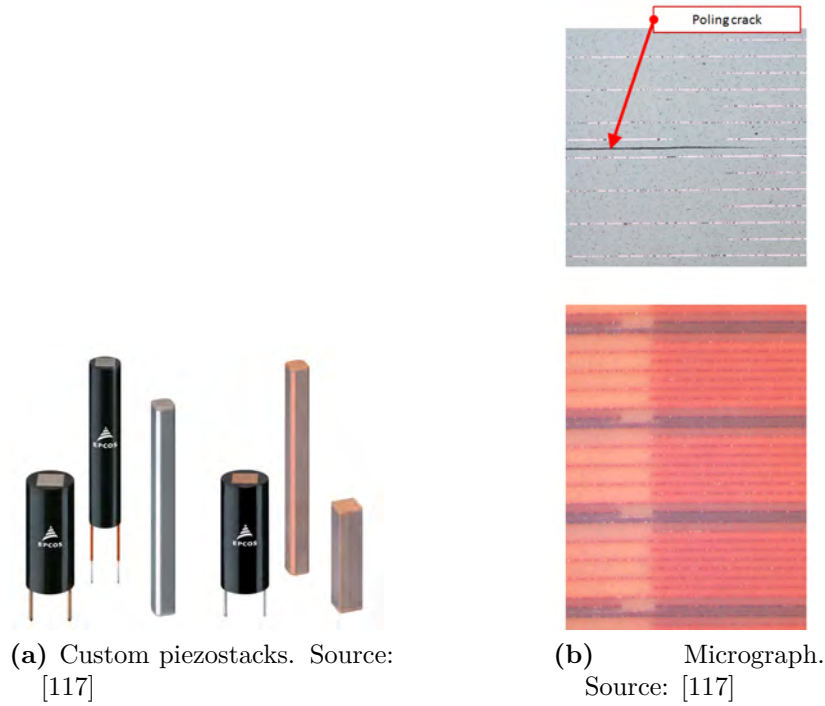


Figure 3.1: Design of a multilayer piezoactuator stack:

reduced oxygen partial pressure range from about 10^{-6} Pa to 10^{-4} Pa according to [115] and will be referred to as “Nd:PZT(Cu)”. Hence at least for one of the two electrode systems a nonstoichiometric PZT is expected during measurements at intermediate temperatures in air. Utilizing the existing current collectors (contact stripes) complete stacks (“fullstacks”) were used for some measurements. For experiments without the need of interdigit electrodes (e.g. self-made sputtered Pt/Au-microelectrodes) the electrode-free top and bottom segments (“top-face cover plates”) of the multilayer stacks were used. However, most experiments were done on stack-segments ($\sim 6 \times 7 \times 1.5 \text{ mm}^3$... $\sim 10 \times 10 \times 1.5 \text{ mm}^3$), which were cut out from the complete stacks. FRÖMLING has measured the average grain size as $4 \mu\text{m}$ for the Nd:PZT(AgPd) stack [47]. The Nd:PZT(AgPd) stacks are completely regularly divided by interdigit electrode pairs. The Nd:PZT(Cu) stacks feature predetermined breaking layers each sixth interdigit electrode pair. These guide poling cracks (which occur unavoidable under high load) in a controlled direction, namely parallel to the electrodes, to minimize their damage on piezoelectric performance. A schematic sketch of such a Nd:PZT(Cu) stack segment is depicted in Fig. 3.2.

For application of voltage only between two interdigit electrodes of stack segments

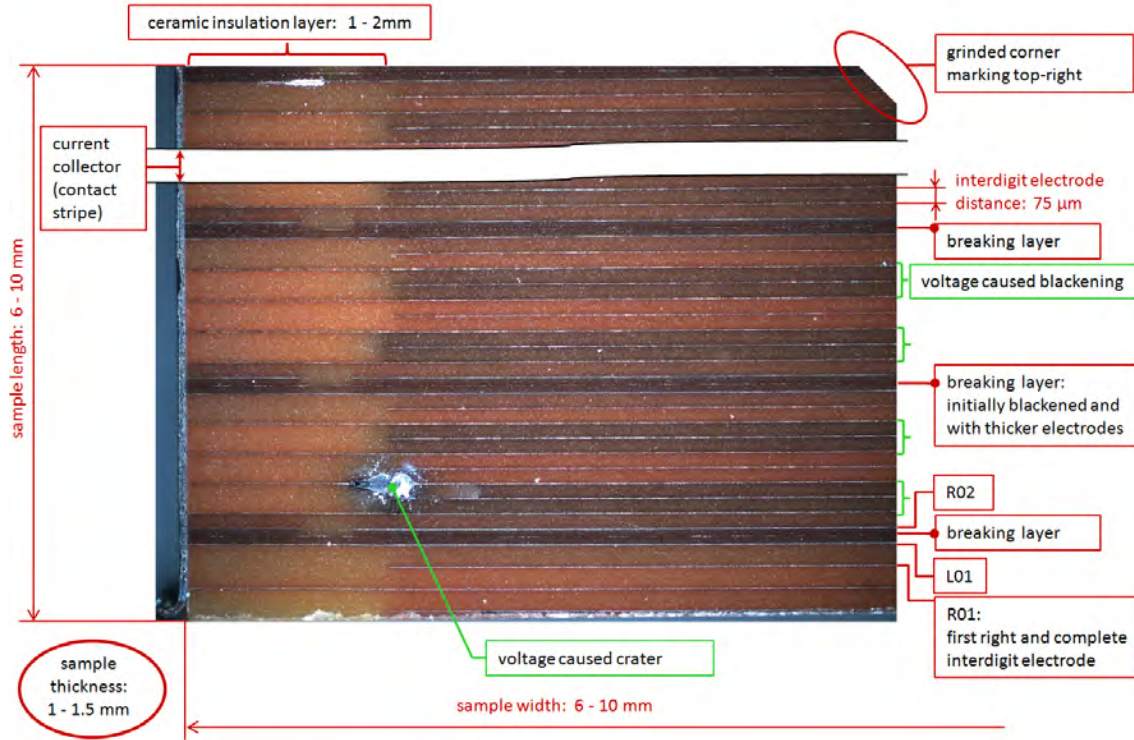


Figure 3.2: Sketch of a Nd:PZT(Cu) stack segment. Depending on the dimensions both, only one (as depicted) or none of the electrode comb structures in the ceramic insulation layer areas are conserved in the cut out sample.

(as depicted in Fig. 3.2), each interdigit electrode was numbered, starting with the first complete electrode “R01” at the down right hand side corner. The upper next electrode - originating from the left electrode comb - was accordingly numbered “L01”. The next pair “R02” and “L02”, etc. If single electrodes have been contacted by tungsten (W) or tungsten carbide (WC) tips, usually the referring voltage is that of the right needle, thus, the applied voltage (up to ± 200 V) is always the potential difference between the right electrode and the left electrode, while the latter one was virtually always at zero potential $U = 0$ V.

Besides to the integrated interdigit electrodes in Nd:PZT stacks also self-made microelectrodes were sputtered on various PZT samples: Mostly 20 - 200 μm circles of 200 nm Au followed 20 nm Cr or Ti (as adhesive layer), which were deposited by a standard photo lithography route (micro resist technology, Germany and ROSE Fotomasken, Germany).

The CURIE-temperature T_C for both types of the Nd:PZT samples is approximately between 340 °C [117] and 360 °C [47].

3.2 Conductivity experiments on PZT

3.2.1 Hard- and software

Depending on the sample geometry (complete stacks, macroscopic discs or microscopic interdigit electrode experiments), different measurement setups were employed:

For measurements of complete stacks (so-called “*fullstacks*”) and macroscopic samples self-made tubular furnaces and glass sample holders were used to heat the samples. For microscopic measurements the sample was heated on a furnace (Linkam, UK), clamped between a sapphire (Al_2O_3) isolation plate and a small piece of insulating YSZ (Yttrium doped ZrO_2), to ensure a good and constant heat transfer from the hot stage to the sample, see Fig. 3.3.

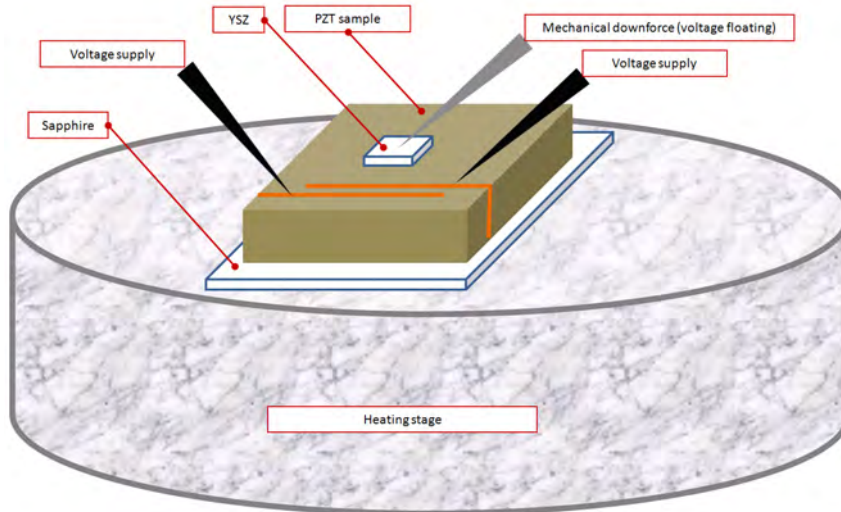


Figure 3.3: Schematic “sandwich” setup for microelectrode measurements. The third (gray) needle is only used to stabilize the Al_2O_3 -PZT-YSZ “sandwich” by pressing it towards the furnace. Only one pair of interdigit electrodes is drawn.

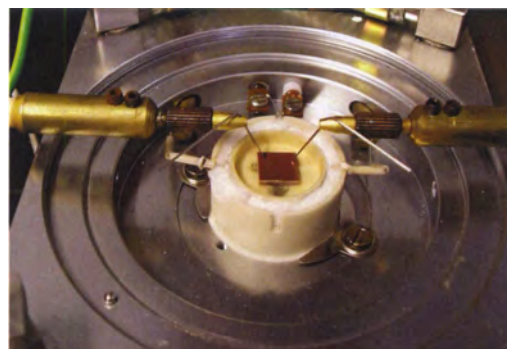
For “live” observation of the hot sample under voltage a reflecting light microscope with dark-field and light-polarization options (Mitutoyo, Japan) was used. Optical investigations of the “cold” samples were done on a Zeiss AxioImager M1m microscope (Zeiss, Germany), equipped with dark-field and light-polarization options, but also an AxioCam MRc 5 ccd-camera. Scanning electron microscopy (SEM) was done on a FEI Quanta 200 MK II with an EDX Detector AMETEK Super UTW.

If grinding/polishing of samples was necessary, this was performed either manually with SiC grinding paper 600, 1000, 2400 and 4000 (Struers, Denmark) or automatically with diamond suspensions (DiaPro 9 μm and 3 μm , Struers, Germany) on MD-Largo discs (Struers, Denmark) on a Pedemax, Planopol-3 polishing machine (Struers, Denmark).

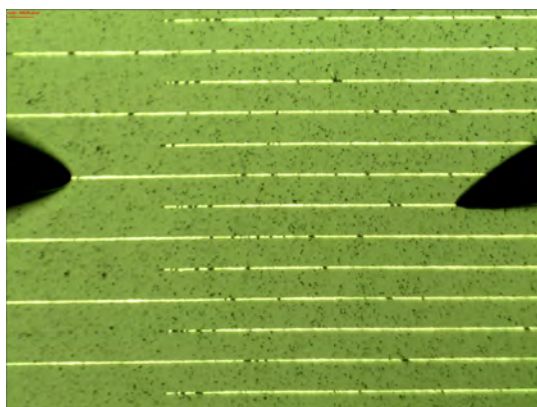
Contacting of microelectrodes was done by tungsten (W) or tungsten carbide tips (WC), supplied by American Probe & Technologies Inc., USA, with 1, 2 or 7 μm tip radius. Some photographs and a sketch of the experimental setup for microelectrode measurements are depicted in Fig. 3.4.



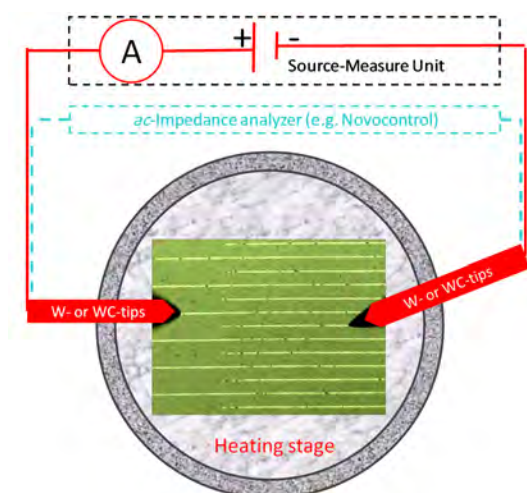
(a) Photograph of microscope and gas-tight chamber including hot stage. Source: [91]



(b) Close-up of a Nd:PZT(Cu) sample on the hot stage. Source: [91]



(c) Microscope view of a Nd:PZT(AgPd) stack segment sample surface. Two needle-tips contacting two single interdigit electrodes.



(d) The sample electrodes are *alternatively* probed either by *dc*- or *ac*-voltage.

Figure 3.4: Hardware setup for measurements on microelectrodes

The electrical behavior of the sample was investigated either by *ac* electrochemical impedance spectroscopy (EIS) or by *dc* measurements. Experiments with *direct*-

current (up to ± 200 V) were carried out with a Source-Meter-Unit 2611A (Keithley, USA) with a special high capacity mode, or with a Source-Meter-Unit 2611 (Keithley, USA) with a self made antiparallel diode circuit in the current output line to minimize instabilities at elevated sample capacities (>20 nF), e. g. *fullstack*-measurements, see sec. 6.2. Most EIS *ac*-measurements were carried out with a Novocontrol Alpha-A High-Performance Analyzer connected to a ZG2 Impedance Interface (both: Novocontrol, Germany). Some measurements were conducted on a Newtons4th Ltd (N4L, UK) PSM1735 Frequency Response Analyzer connected to a Femto DHCPA-100 Variable Gain High-Speed Current Amplifier (Femto, Germany). Impedance was analyzed in the frequency range from 10^{-2} Hz to 10^6 Hz, normally with a probing voltage between 0.3 VAC and 1 VAC (for zero *dc*-bias). In some cases the “live” observation of the high-voltage behavior was not investigated with pure *dc*, but with *ac*-EIS on an underlying high voltage *dc*-bias: This was done by exchanging the Novocontrol ZG2 Impedance Interface with a Novocontrol High Voltage Booster. Thus *dc*-offsets up to ± 150 V could be spectroscopically observed, of course only with increasing the superimposed *ac*-probing signal up to 15 VAC due to the increased signal/noise ratio.

Most measurements were carried out in air, but some experiments on Nd:PZT(AgPd) were conducted at a reduced oxygen partial pressure. For this purpose the self-made gas-tight chamber around the hot stage was sealed and a flow of either 2.5 vol% H_2 (in Ar) or 99.999 % Ar (both: AirLiquide, Austria) was used to obtain oxygen partial pressures of 1×10^{-15} ppm O_2 (H_2) and 35 ppm O_2 (Ar), respectively, controlled by a lambda sensor (Rapidox, Germany).

EIS measurement data were evaluated by *complex non-linear least square fitting* (CNLS) of equivalent circuits with the software zView2 (Scribner, USA).

In the following, voltages greater than 15 V will be termed “high-voltage” and sometimes abbreviated by “HV”. Voltages smaller than 15 V will be termed “low-voltage” and sometimes abbreviated “LV”. The term “small-signal” will mostly refer to *ac*-voltages smaller than 1 V. Alternating current will be indicated by an “*ac*” prefix or the extension of the voltage unit V to “VAC”. Direct current is accordingly indicated by “*dc*” or “VDC”. Remember that a high-voltage U alone, does not necessarily lead to a high electric field E . Owing to

$$U = \int E \cdot ds \quad \text{for planar geometry} \quad E = \frac{U}{d} \quad (3.1)$$

the field E depends on the distance d between the electrodes which are subjected to the potential difference U . Nevertheless in this work voltage instead of field strength is mostly given for practical reasons.

3.2.2 Conductivity measurement procedure

While for some samples only the small-signal resistance ($U \leq 10$ V) was measured at various temperatures, most samples were also subjected to high electric field stress: After the sample was kept some time on the set-temperature (to equilibrate thermally), a triple of three low-voltage conductivity measurements were carried out, e. g. ± 1 V and one *ac*-EIS-measurement. Then a constant high-voltage (10-200 VDC) was applied to the sample for different periods of time, recording the current value at a rate of one measurement per second to one per minute (depending on temperature and velocity of the conductivity change). Either the high voltage was switched-off, after a pseudo-constant value was reached and subsequent relaxation was monitored by a small probing voltage or the high-voltage was kept switched-on (e. g. until breakdown). In any case, a small-signal resistance measurement was carried out finally. *ac*-impedance spectroscopy turned out to be a helpful tool for investigating the quality of the contact between the tungsten tip and the sample electrodes, because only EIS was able to separate undesired additional resistivities e. g. due to bad contacting or oxidation layers.

For all samples the resistance R was calculated from the applied voltage U and the measured current I by OHM's law (cf. Eq. (2.49)):

$$R = \frac{U}{I} \quad (3.2)$$

The specific conductivity σ (reciprocal of the specific resistivity ρ) was calculated considering current cross section A and sample length l :

$$\sigma = \frac{1}{\rho} = \frac{1}{R} \cdot \frac{l}{A} \quad (3.3)$$

For macroscopic disc samples with diameter D the current cross section area $A = 1/4 \cdot D^2 \cdot \pi$ and l equals the sample thickness. For circular microelectrodes (diameter d_{ME}) on the sample surface with a pseudo-infinite counterelectrode (e. g. at the sample bottom) the bulk conductivity can be calculated from the measured spreading

resistance R_{spr} of such a surface-microelectrode [159, 160, 161]:

$$\sigma_{bulk} = \frac{1}{2 \cdot d_{ME} \cdot R_{spr}} \quad (3.4)$$

For conductivity measurements involving interdigit electrodes the current cross section A was (in a simplification) identified with the overlapping area of the alternating interdigit electrodes. For fully contacted complete stacks (“fullstacks”) that is the sample cross section minus the ceramic insulation layer area without overlapping interdigit electrodes, cf. Fig. 3.2. If n piezoactive layers are simultaneously contacted by alternating interdigit electrodes, the conductivity calculates as a parallel chain of n PZT-layers with a thickness of $l=75\text{ }\mu\text{m}$ each:

$$\sigma = \frac{1}{R} \cdot \frac{l}{n \cdot A} \quad (3.5)$$

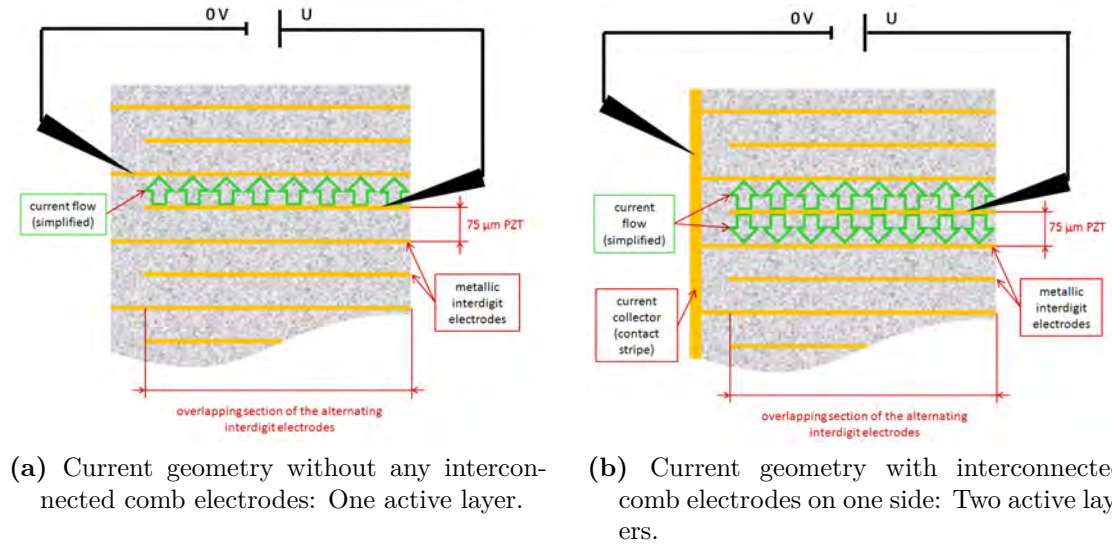


Figure 3.5: Contacting with or without utilizing one current collector (contact strip).

For stack-segments different contacting modes have to be considered: If the remains of both current collector (contact stripes) are preserved, Eq. (3.5) is still valid. If one or both current collectors are cut off or grinded away, only three or two distinct interdigit electrodes (two or one 75 μm thick PZT layers) are active, respectively (cf.

Fig. 3.5). Hence the conductivity is calculated as:

$$\sigma = \frac{1}{R} \cdot \frac{l}{A} \quad \text{One active layer, Fig. 3.5a} \quad (3.6)$$

$$\sigma = \frac{1}{R} \cdot \frac{l}{2 \cdot A} \quad \text{Two active layers, Fig. 3.5b} \quad (3.7)$$

U [V]	E for a 75 μm layer
0.3	4.00 kV/m
1	13.3 kV/m
10	133 kV/m
20	267 kV/m
50	667 kV/m
100	1.33 MV/m
150	2.00 MV/m
180	2.40 MV/m
200	2.67 MV/m

Table 3.1: Applied voltages U and their corresponding electric field strength E on 75 μm multilayer elements.

Due to Eq. (3.1), voltages between 0.3 V and 200 V applied on 75 μm thick layers lead to the electric fields as listed in Tab. 3.1.

3.2.3 Temperature

All measurements were carried out at set-temperatures of the hot stage between 350 °C and 500 °C. As the CURIE-temperature T_C of the PZT samples in question is about 350 °C and depolarization starts already at $\approx T_C/2$ [115], it can be expected, that in all experiments the samples are either in the paraelectric state or (at

the lowest temperature, $T_{set} = 350^\circ\text{C}$) in the ferroelectric state. Although the commercial use of PZT is virtually always below T_C in the ferroelectric / piezoelectric regime, measurements at lower temperatures turned out to be not very reasonable, because of the strong temperature dependence of the conductivity of PZT. Some measurements at 350°C already needed more than 12 hours, so further reduction of temperature would render experiments with systematic parameter variations almost impossible.

In contrast to samples investigated in tube furnaces (providing homogeneously heated compartments), samples on the top of the Linkam hot stage suffer heat loss not only because of undefined heat transfer between hot stage and sample but, even more important, due to radiation and convection losses into the upper hemisphere. Due to the open setup of the Linkam hot stage, in all microscopic measurements not only a reduced average sample temperature but even a temperature gradient from the (hotter) sample bottom to the (cooler) sample upside is expected. Furthermore OPITZ has demonstrated on YSZ, that already the contacting of a ceramic sample with a metallic needle can extract a significant amount of heat from the contacted area [106].

To determine the true average sample temperature two methods were employed. In one experiment a metallic Ni dummy sample of approximately the size of the Nd:PZT samples used in this thesis was put on the hot stage. A thermocouple was inserted into a hole in the middle of this metal dummy sample and the measured temperature vs. the set-temperature was recorded, cf. Fig. 3.6. At any temperature, the maximum temperature offset of the metal dummy sample did not exceed 25 K.

The other method employed to determine the real temperature of contacted PZT samples, was a comparison of the conductivities of the same Nd:PZT material measured in the standard tubular furnaces, at which the sample temperature was expected to be the same as for a nearby installed thermocouple, see Fig. 3.7. For all temperatures, the maximum temperature difference between the same conductivity values of *micro*- and *macro*-measurements of Nd:PZT(Cu) or Nd:PZT(AgPd) samples did not exceed 40 K.

These experiments indicate, that the temperature difference between real temperature of the sample and set-temperature of the Linkam hot stage is at most 40 K. The advantage of the possibility of subsequently contacting numerous individual electrodes of a single stack segment and observing optical phenomena “live” dur-

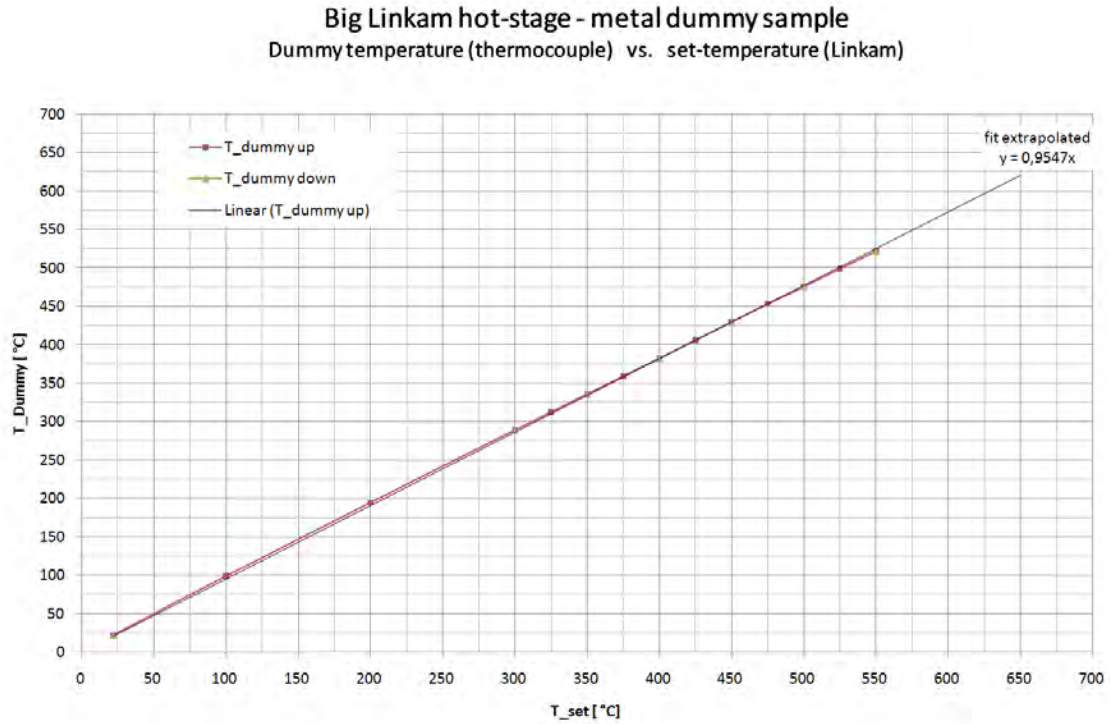


Figure 3.6: Temperature offset of the Linkam hot stage, measured with a metallic sample of approximately the same size as the Nd:PZT samples used in this thesis.

ing the degradation process by far counter-balances the disadvantage of the minor temperature uncertainty unavoidable in the microscopic (Linkam) setup. Moreover, for identical set-temperatures a direct comparison between various samples in the Linkam setup is of course possible.

In the following will be always referred to the set-temperatures of the furnace and the hot stage, respectively. So one has to keep in mind that the intermediate sample temperature is slightly lower than the set temperature.

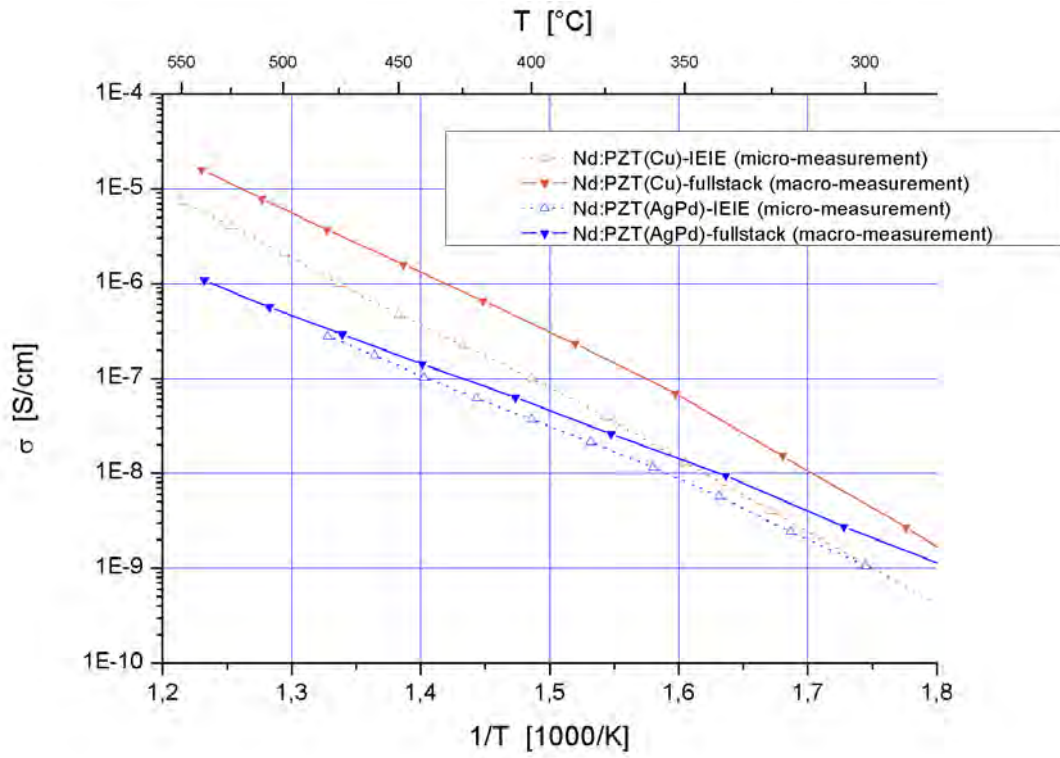


Figure 3.7: Comparison of temperature-dependent conductivities of Nd:PZT samples on the Linkam hot stage (single interdigit electrode measurements “IEIE / micro”) and samples in the standard furnace (“fullstack / macro”).

4 Results and Discussion:

Nd:PZT(Cu)

In this chapter the measurements on single (Fig. 3.5a) or double (Fig. 3.5b) inter-digit electrode layers of Nd:PZT(Cu) are discussed. However, in the first section some general considerations about the evaluation process will be given.

4.1 General considerations

4.1.1 Typical behavior

In general, stressing Nd:PZT(Cu) with high electric fields (up to 2.67 MV/m) by applying high electric voltage (up to 200 V) to 75 μm Nd:PZT(Cu) layers leads to the characteristic conductivity variation as illustrated in Fig. 4.1, which can be divided into three different types:

Short-term high-field stress (Phase 1) After a small-signal EIS verification of the resistance and contact quality (first two points ($t=0$, $U=0$ / $\sigma \approx 3.5 \times 10^{-7} \text{ S/cm}$) in Fig. 4.1), immediately as 200 VDC was applied, in a first phase, the conductivity started to *decrease* from its initial high-voltage value, which is significantly larger than the corresponding small-signal value due to nonlinear U - I behavior. Usually the conductivity decrease was accompanied with a “*blackening*” of the stressed PZT layer, visible in the dark-field mode of the optical microscope. The fast and drastic conductivity decrease ends in a conductivity minimum. This first phase will be referred to as “*short-term high-field*”, sometimes as “*Phase 1*” and will be occasionally indexed by “1”.

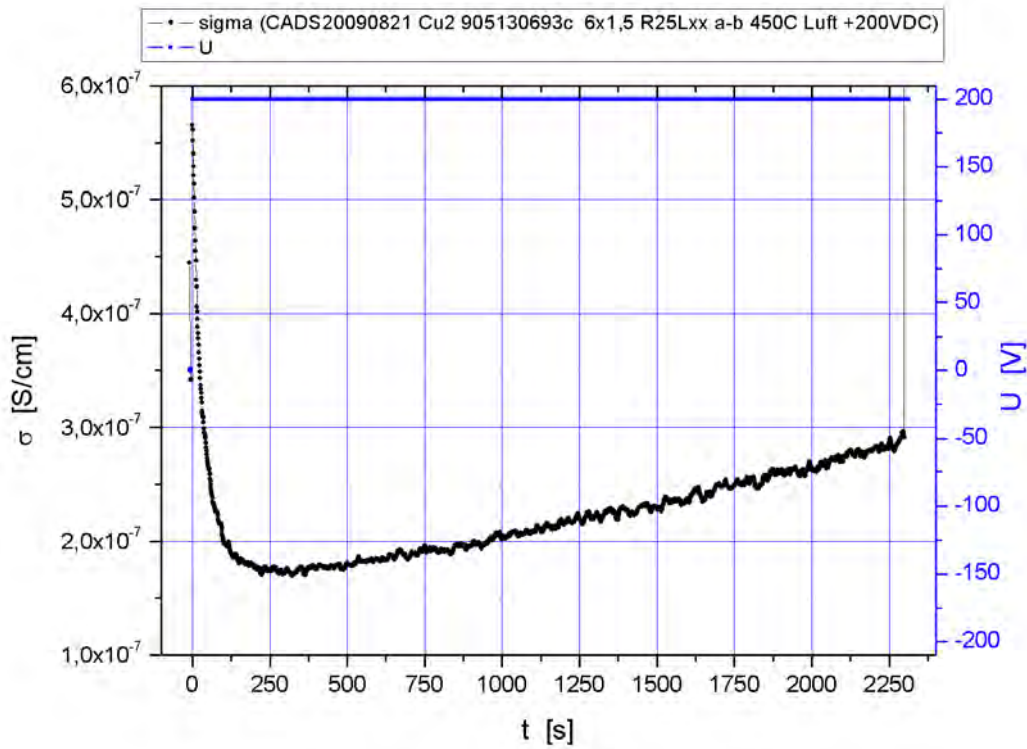


Figure 4.1: Uninterrupted long-term conductivity behavior of a 75 μm Nd:PZT(Cu) layer stressed with 200 VDC at 450 $^{\circ}\text{C}$. The difference between the first two points at $t=0$ / $U=0$ and the first σ -values for 200 VDC, indicate a nonlinear I - U -behavior. The minimum of the σ -curve denotes the separation of “Phase 1” and “Phase 2LT”.

Long-term degradation (Phase 2LT) Keeping the high-voltage turned on after the conductivity minimum was reached, the conductivity *increased* until sooner or later a breakdown (electrical breakthrough) occurred. The breakdown was defined by a sudden jump of the measured current to the current limit of the Source-Measure-Unit (Keithley 2611(A): 100 mA for 200 VDC-range), mostly accompanied by visible creation of “craters” at the stressed interdigit electrode pair. This complete high-voltage degradation behavior will be termed “*long-term degradation*”. The second part of a high-voltage long-term experiment - after the initial *Phase 1* which is of course identical to Phase 1 of short-term behavior - will be referred to as “*Phase 2LT*” and will be occasionally indexed by “*2LT*”.

Conductivity Recovery / Relaxation (Phase 2) If the high-voltage was switched-off at the minimum of the conductivity-time curve, for almost any temperature

greater than 350 °C a *relaxation* behavior of the conductivity could be monitored by small-signal *ac*-EIS or low-voltage *dc*-measurements: The conductivity again increased on a much longer time-scale. Often conductivity values were reached which were close to the initial conductivity starting value before the degradation experiment. This relaxation behavior at small or zero voltage after a short-term high-field stress will be referred to as “*Phase 2*” and will be occasionally indexed by “2”. Fig. 4.2 illustrates the conductivity increase after switching off the HV degradation field. A similar relaxation behavior was observed in H₂-atmosphere [91].

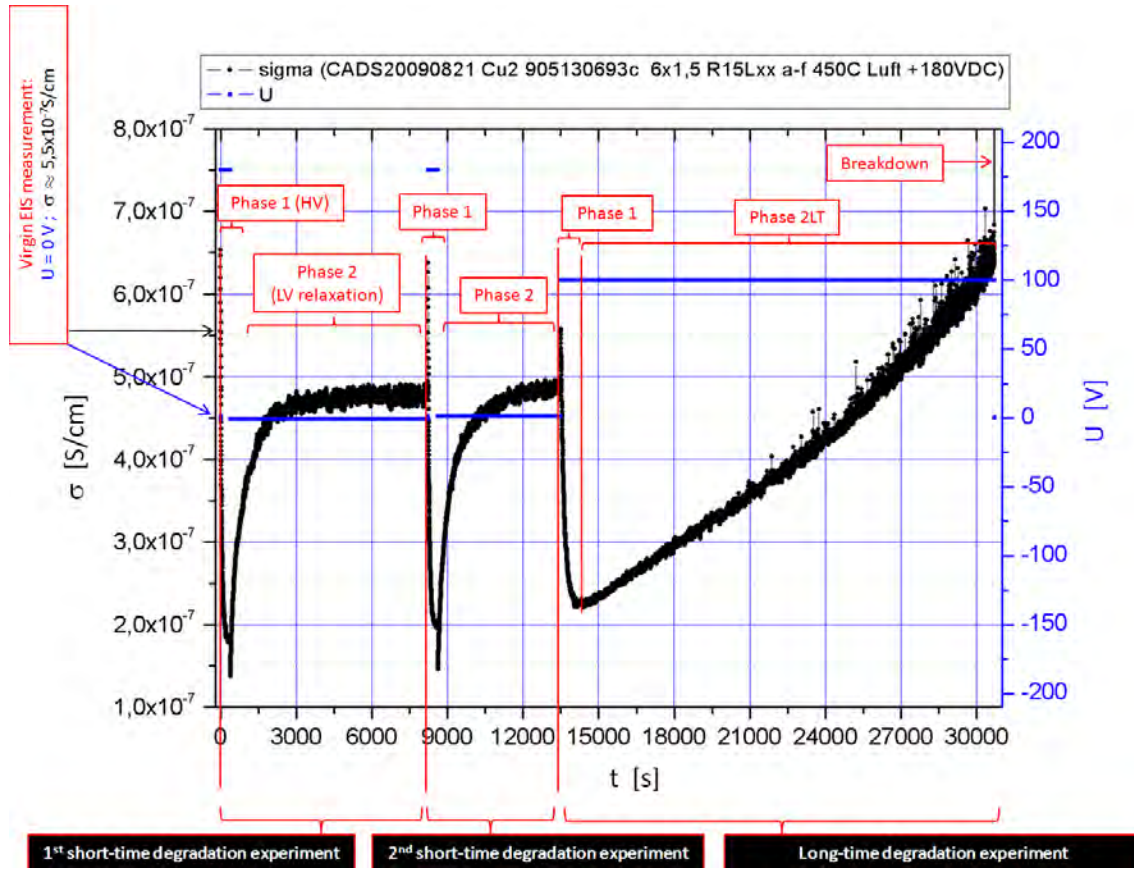


Figure 4.2: Two subsequent short-term experiments and one final long-term degradation experiment on one and the same 75 μm Nd:PZT(Cu) layer at 450 °C and 200 V and 100 V, respectively. Note the (hardly visible) initial small signal conductivity values ($\sigma \approx 5.5 \times 10^{-7} \text{ S/cm}$ at $t = 0$, $U = 0$), which are nearly reached at the end of the two relaxation processes and even exceeded during the final long-term degradation. Black: Conductivity; Blue: Voltage.

In the experiment series illustrated in Fig. 4.2, after the conductivity has relaxed to a new apparently constant value close to the initial LV starting value, another

subsequent experiment was conducted on the very same 75 μm Nd:PZT(Cu) layer: A similar short-term high-field Phase 1 and relaxation Phase 2 was repeated. Finally a long-term degradation Phase 2LT was conducted still on the same PZT-layer, but in the experiment depicted in Fig. 4.2, only at 100 V. With half the voltage the breakdown occurred later, so that the high-voltage conductivity within Phase 2LT exceeded the initial low-voltage starting value significantly, in contrast to Fig. 4.1 (which shows an experiment at 200 V *dc*-load). *Prima facie* at least the short-term conductivity variations (Phase 1 and Phase 2) seem to display some kind of reversibility.

4.1.2 Fitting

For reasons of better quantification and comparability both parts of the short-term variation (Phase 1 & Phase 2 (relaxation)) and Phase 1 of the long-term degradation experiments were fitted with applicable analytical functions (but without any physical or chemical model behind). Simple exponential functions of the form

$$\sigma_1(t) = \sigma_1^\infty + (\sigma_1^0 - \sigma_1^\infty) \cdot \exp\left(-\frac{t - t_1^0}{\tau_1}\right) \quad (\text{HV-Phase 1}) \quad (4.1)$$

$$\sigma_2(t) = \sigma_2^\infty + (\sigma_2^0 - \sigma_2^\infty) \cdot \exp\left(-\frac{t - t_2^0}{\tau_2}\right) \quad (\text{LV-Phase 2}) \quad (4.2)$$

turned out to fit well to the measured conductivity data of the high-voltage conductivity decrease phase and the subsequent low-voltage relaxation phase. σ^∞ denotes the (asymptotic) conductivity end-value for $\sigma(t \rightarrow \infty)$, σ^0 is the conductivity at $t = t^0$; t^0 is the temporal offset from $t = 0$ on the x -axis and the beginning of the exponential conductivity decay. Finally, τ is the time constant ($\sigma(\tau + t^0) = \sigma^\infty + 1/e \cdot (\sigma^0 - \sigma^\infty)$). The subscript indices 1 and 2 refer to the high-field and subsequent relaxation processes, Phase 1 and Phase 2, respectively.

According to the indexing system already mentioned, e.g. the time constant of Phase 1 will be termed τ_1 (occasionally “tau1”), the probing-voltage of the relaxation phase (Phase 2) U_2 , etc. Irrespective of the non-linearity mentioned in sec. 4.1.7, the extent of conductivity changes were all referred to the first high-voltage conductivity value ($\sigma_1^0(\text{HV})$): The absolute magnitude of the first conductivity change under high-

voltage (Phase 1) was defined as the difference between this first HV-conductivity starting value of the fit function $\sigma_1^0(\text{HV})$ and the asymptotic end-value of the fit function Eq. (4.1) $\sigma_1^\infty(\text{HV})$:

$$\text{magnitude1} = \sigma_1^0(\text{HV}) - \sigma_1^\infty(\text{HV}) \quad (\text{Phase 1}) \quad (4.3)$$

The absolute magnitude of the (purely low-voltage) relaxation process was nevertheless referred to the first HV starting value of the conductivity $\sigma_1^\infty(\text{HV})$:

$$\text{magnitude2} = \sigma_1^0(\text{HV}) - \sigma_2^\infty(\text{LV}) \quad (\text{Phase 2}) \quad (4.4)$$

with $\sigma_2^\infty(\text{LV})$ being the asymptotic end-value of the fitting function Eq. (4.1) for the relaxation phase (Phase 2).

For comparison of conductivity changes at different temperatures, both magnitude-values were normalized by setting $\sigma_1^0(\text{HV})$ to 100 % and referring any conductivity change to this very first (high-voltage) conductivity-value:

$$\text{delta1} = \frac{\sigma_1^\infty(\text{HV})}{\sigma_1^0(\text{HV})} \cdot 100\% \quad (\text{Phase 1}) \quad (4.5)$$

$$\text{delta2} = \frac{\sigma_2^\infty(\text{LV})}{\sigma_1^0(\text{HV})} \cdot 100\% \quad (\text{Phase 2}) \quad (4.6)$$

One would expect for reasons of symmetry, that “magnitude2” in Eq. (4.4) and “delta2” in Eq. (4.6) refer to $\sigma_2^0(\text{LV})$ rather than $\sigma_1^0(\text{HV})$. However, since the conductivity variations with respect to one and the same starting value should be emphasized, it was decided to refer both parameters to the high-voltage starting value $\sigma_1^0(\text{HV})$.

Starred (“*”) values will be used to indicate averaged mean values. For reasons of symmetry, tables and diagrams will often refer only to the absolute value of an applied voltage, neglecting the direction (+/-) of the current flux. Due to the symmetrical geometry of the setup this is assumed to be a reasonable simplification.

A fitting example for different degradation phases of the experiment depicted in Fig. 4.2 is illustrated in Fig. 4.3. Due to the unpredictable progress (breakdown),

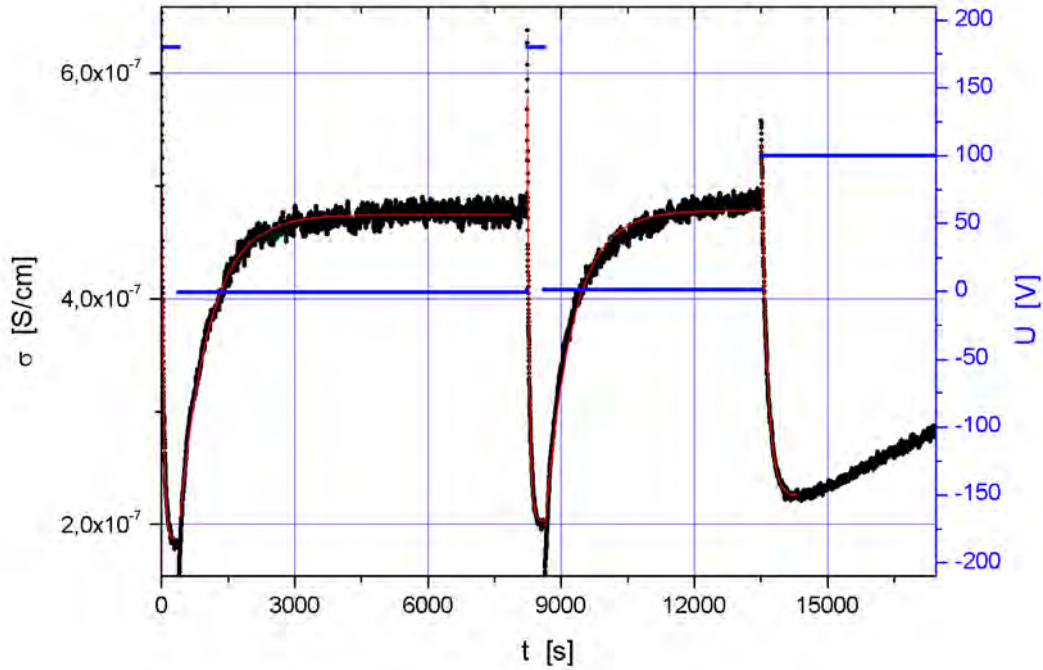


Figure 4.3: Detail of Fig. 4.2 with five fitted exponential functions (red lines) according to Eq. (4.1). First fit: Phase 1 of the short-term (HV) conductivity decrease; Second fit: subsequent (LV) relaxation Phase 2 of the first experiment; Third fit: Phase 1 of the (second) short-term (HV) conductivity decrease; Fourth fit: Subsequent (LV) relaxation (Phase 2); Fifth fit: Phase 1 of a long-term degradation experiment; Phase 2LT is not fitted.

the last part (Phase 2LT) of the long-term degradation experiments was not fitted with any analytical function. Only the conductivity changes with respect to the conductivity minimum and the time until breakdown were recorded.

4.1.3 Impedance spectra

At all temperatures between 350 °C and 500 °C impedance spectra of PZT without any high field stress show a single quasi semi-circle in the complex impedance plane (NYQUIST-plot), cf. Fig. 4.4.

Obviously the slightly deformed semi-circles in Fig. 4.4 can perfectly be simulated by a *complex non-linear least square* (CNLS) *fitting* of a parallel R//CPE equivalent circuit, consisting of a single resistance R and a non-ideal capacitor (CPE) with

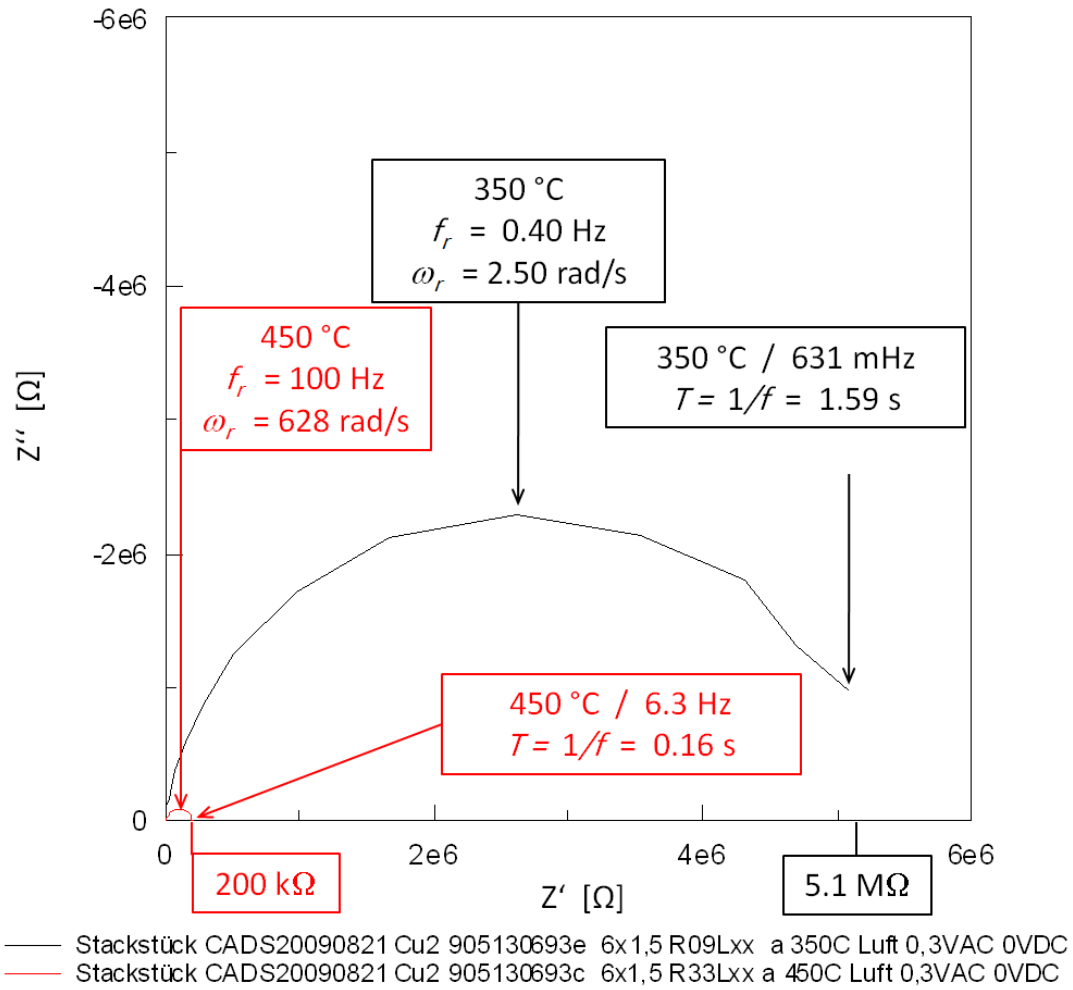


Figure 4.4: NYQUIST-plot of a 75 μm thick Nd:PZT(Cu) layer at 350 $^{\circ}\text{C}$ (black line) and 450 $^{\circ}\text{C}$ (red line). Note the different relaxation angular frequencies ω_r for the different temperatures and the different frequencies f and periods T for approaching the real axis. Impedance $Z = Z' + j \cdot Z''$.

$0.9 \leq n \leq 1$ in Eq. 2.68. Variations of different (surface and interdigit) electrode materials (Cu, cf. Fig. 4.4; Ag/Pd, see chapter 5; Ag, Cr-Au and Ti-Au bilayer, see sec. 6.3) have shown, that electrode effects are *not* visible within the frequency range of the NYQUIST-plots under the experimental conditions at this work.

Even EIS measurements with high *dc*-bias voltage display nearly perfect semicircles. Fig. 4.5 shows an impedance spectrum (NYQUIST-plot) of a 75 μm Nd:PZT(Cu) layer at 350 $^{\circ}\text{C}$ measured with a 5 VAC probing voltage while *simultaneously* stressed with 140 VDC bias.

Due to the simple behavior of the Nd:PZT(Cu) layers in the NYQUIST-plots, all

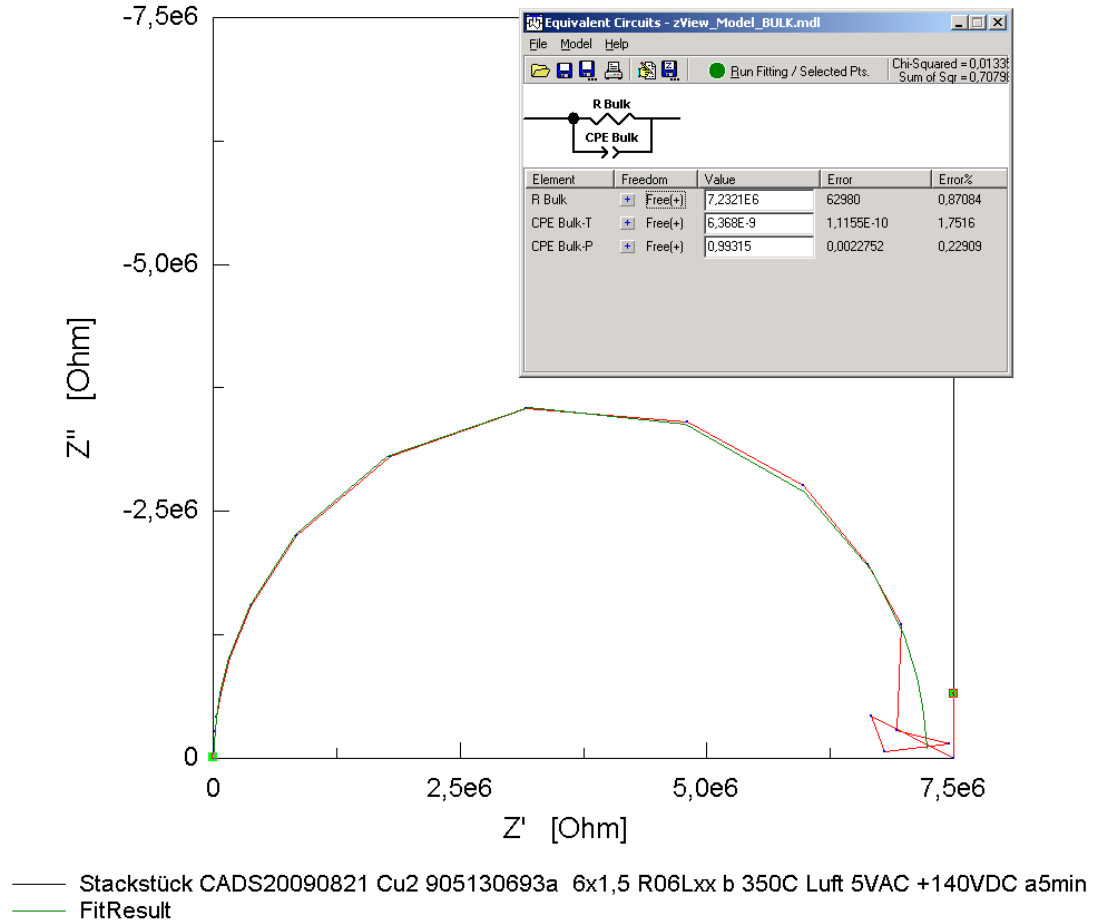


Figure 4.5: *ac*-EIS measurement of a 75 μm Nd:PZT(Cu) layer at 350 $^{\circ}\text{C}$ and underlying 140 VDC bias voltage. The red line refers to the measurement, while the green line is a complex non-linear least square fitting (CNLS) of the impedance spectra of the R//CPE equivalent circuit of the inset.

corresponding resistance values R have been derived by a complex non-linear least square fitting (CNLS) of a parallel R//CPE equivalent circuit.

There are three possibilities to explain the single-arc conductivity of the PZT under investigation: Either the entire resistance of the PZT is determined by bulk conductivity of PZT (1), by highly conducting grain boundaries (2) [99, 104, 162] or grain-size extended space-charge layers at grain boundaries dominate the overall conductivity (3) while the capacitance is still that of the bulk. Due to the relatively large grain sizes of PZT (avg. $\sim 4 \mu\text{m}$) the latter case is expected to be quite unlikely, and was only verified for nanocrystalline SrTiO_3 [163, 164].

It is quite surprising to find only one semicircle in a material, which is expected

to be a mixed conductor. Especially as DONNELLY and RANDALL repeatedly have separated ionic and electronic conduction in PZT by means of EIS, as also observed in SrTiO_3 for example. However in these publications, [46, 135], a Nb^{5+} positively (donor) doped PZT was investigated after a long-term equilibration phase in air at 700°C , which of course could have strongly influenced defect concentrations and conductivity ratios. Although ^{18}O tracer diffusion experiments of FRÖMLING et al. [165] could indicate an enhanced O^{2-} conductivity at grain boundaries for $\text{Nd:PZT}(\text{AgPd})$ at $T \geq 650^\circ\text{C}$, it is still to be clarified, whether electronic or ionic conductivity prevails at lower temperatures and in $\text{Nd:PZT}(\text{Cu})$. In a close up of Fig. 4.4 and other NYQUIST-plots of the PZT under investigation, sometimes a very small offset on the real axis of some few OHMS could be observed. This was attributed to the contact resistance at the W-needle tip / interdigit electrode interface. Especially for longer times and/or elevated temperatures, growth of a CuO oxidation layer can be expected at the unshielded top edge of the Cu electrodes, which has to be penetrated by the W-tip. The EIS-separable resistance offset turned out to be an important indicator of the quality of the contact.

FRÖMLING has roughly estimated the CURIE-temperature of the $\text{Nd:PZT}(\text{Cu})$ and the $\text{Nd:PZT}(\text{AgPd})$ samples to be approximately 360°C [47]. For undoped PZT it turned out to be $\sim 380^\circ\text{C}$, see sec. 6.1.1.

From the temperature dependent impedance measurements ARRHENIUS-plots (conductivity vs. inverse temperature) can be deduced: In Fig. 4.6 $\text{Nd:PZT}(\text{Cu})$ samples contacted at interdigit electrodes (“IEIE”) in the “micro” setup (Linkam hot stage) are compared with $\text{Nd:PZT}(\text{Cu})$ -fullstacks in the “macro” setup (normal furnace). ARRHENIUS-plots of $\text{Nd:PZT}(\text{AgPd})$ samples are given in Fig. 3.7. The *slope* of the conductivities below the CURIE-temperature ($T_C \approx 360^\circ\text{C}$) is slightly higher than above T_C , although the bend at T_C is not very pronounced, which is in accordance with previous results for PZT [29, 47, 158]: The activation enthalpies E_a according to Eq. (2.61) for $\text{Nd:PZT}(\text{Cu})$ are 1.46 eV ... 1.57 eV in the ferroelectric regime below T_C , 1.26 eV ... 1.37 eV in the paraelectric phase above T_C and 1.39 eV averaged over the whole temperature range, neglecting the hardly visible kink at T_C . Compared with the $\text{Nd:PZT}(\text{AgPd})$ -samples from Fig. 3.7, the conductivity of $\text{Nd:PZT}(\text{Cu})$ is about half an order of a magnitude higher at 500°C , which could be related to the probably higher oxygen vacancy concentration due to decreased oxygen partial pressure during sintering. However, the activation enthalpy E_a of $\text{Nd:PZT}(\text{Cu})$ in the ferroelectric and paraelectric regime is higher than that of $\text{Nd:PZT}(\text{AgPd})$ (1.24 eV

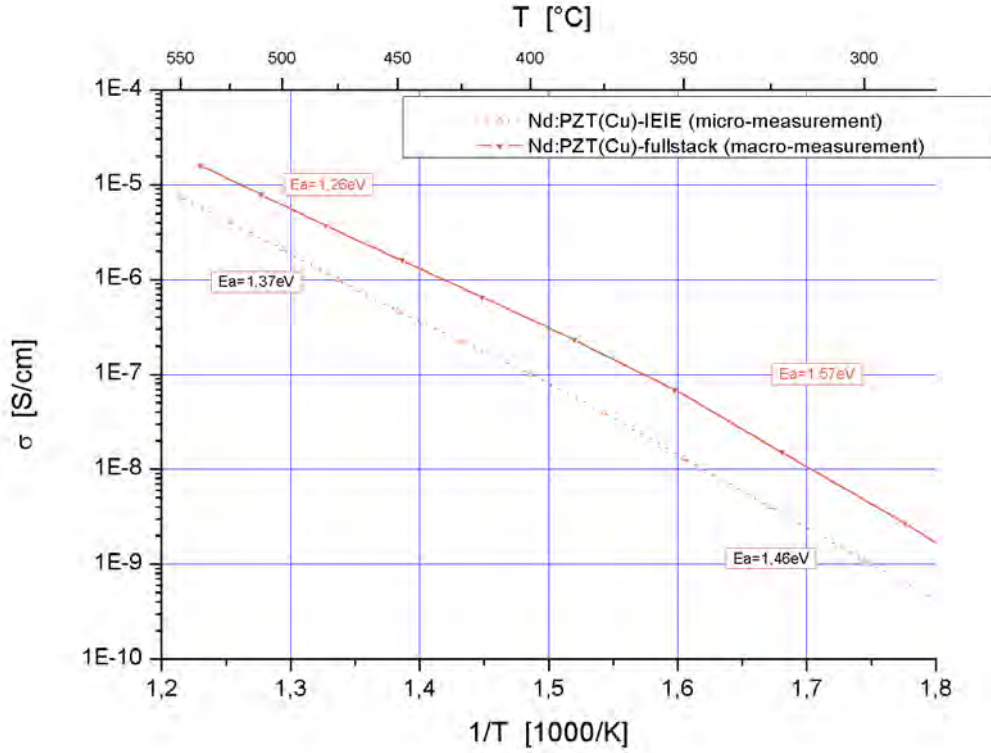


Figure 4.6: ARRHENIUS-plot of various Nd:PZT samples.

and 0.99 eV, respectively). Activation enthalpies E_a of about 1 eV are often found for oxygen vacancy bulk conductivity [84, 88] which has also been assumed for PZT [36, 48, 166]. For undoped PZT thin films KHODOROV et al. [166] and CHAUDHARI et al. [167] observed higher E_a above T_C than below and accordingly suggest temperature dependent conduction mechanisms¹. However, it is not recommended to draw any final conclusions on conductivity mechanisms from the temperature dependency of PZT solely.

4.1.4 Capacitive effects

Anticipating the *dc*-high voltage experiments discussions beginning with sec. 4.2, it is worth to mention that the relaxation frequencies ($f_r = \frac{1}{2\pi} \cdot \omega_r = \frac{1}{2\pi \cdot R \cdot C}$), Eq. (2.71), of the impedance measurements range from highest values of several kHz at 500 °C to lowest values of about 0.4 Hz at 350 °C, cf. Fig. 4.4. Under *dc*-voltage, charging

¹In contrast to this work, both authors calculated their ARRHENIUS plots *not* with the values from (extrapolated) *dc*-resistance ($R_{dc} = \Re(Z'(\omega) + jZ''(\omega))|_{\omega \rightarrow 0}$), Eq. (2.71), but with *ac*-conductivities at arbitrarily chosen *constant* frequencies (ω_{ac}): $R_{ac} = \Re(Z'(\omega_{ac}) + jZ''(\omega_{ac}))$.

of the capacitive part of the PZT-sample is expected to take place on the time scale of $1/\omega_r$, hence ~ 0.4 s at 350°C and a few microseconds at 500°C . Accordingly, dc -conductivity changes for times $t \gg 1/\omega_r$ can not be attributed to any conventional capacitive effect.

4.1.5 Zero-field thermal equilibration

Another very important effect, which should be mentioned before discussing any voltage-induced time-resolved conductivity variation on PZT was primarily discovered by HILLEBRAND on Nd:PZT(Cu) [91]: At elevated temperatures, even without any electric field stress, the conductivity of Nd:PZT(Cu) decreases with time.

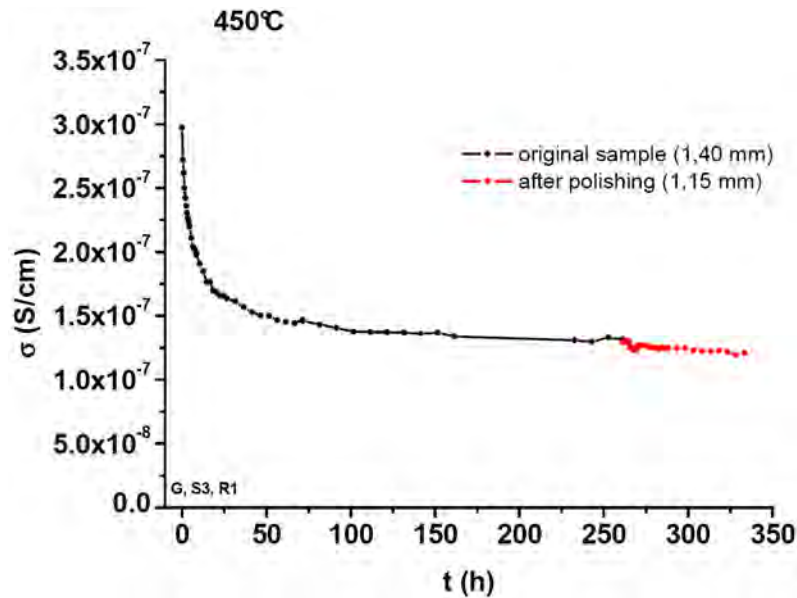
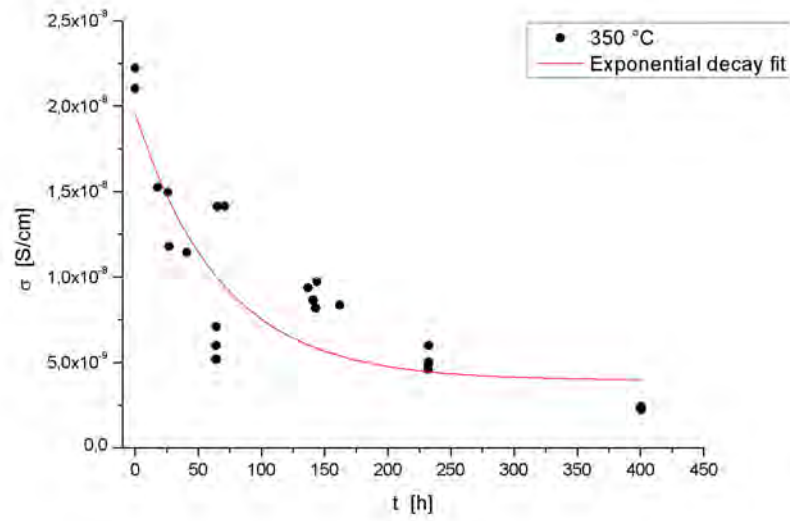


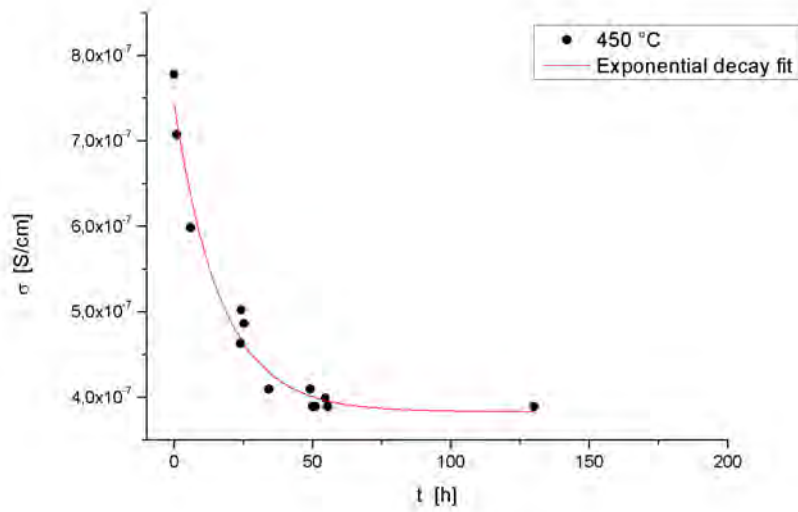
Figure 4.7: Thermal equilibration of Nd:PZT(Cu) without high electric field stress at 450°C for 350 h, observed by [91].

HILLEBRAND investigated the conductivity without external high-field stress at 450°C for 350 h, cf. Fig. 4.7, and also excluded superficial effects by grinding off $125\ \mu\text{m}$ on both sides.

The purely thermal decrease of conductivity with time was verified on the Nd:PZT(Cu) samples investigated in this thesis for 350°C and 450°C . The field-free starting-values of small-signal conductivity of different layers after different periods of time at constant temperature are plotted in Fig. 4.8.



(a) 350 °C



(b) 450 °C

Figure 4.8: Pure thermal equilibration of Nd:PZT(Cu) without any constant electric field. Every data point is from a different layer. Exponential fit functions determined according to Eq. (4.1).

While HILLEBRAND analyzed one and the same interdigit electrode pair over 350 h, the diagrams in Fig. 4.8 rely on the initial conductivity values of different Nd:PZT(Cu)-layers just before high-voltage experiments were started after a certain time at 350 °C and 450 °C, respectively. This may explain the greater scattering of the values, but also conductivity variations from one PZT sample to the other may have contributed to the scattering.

The PbO volatility of PZT is generally known, cf. sec. 2.3.5, and as the Nd:PZT(Cu) stacks are fabricated in a reducing atmosphere (just with a simple PZT-powder buffer), an increased oxygen vacancy concentration corresponding to the oxygen partial pressure during sintering is expected. In subsequent experiments in air and at elevated temperatures the PZT tends to equilibrate with this new oxygen partial pressure by ambipolar diffusion of oxygen. It is assumed that this rather slow changes in stoichiometry are responsible for the conductivity changes shown in Fig. 4.8. The change of conductivity due to pure thermal equilibration of Nd:PZT(Cu) without any external high-voltage stress is in fact dramatic, but on a long time scale. Finally, due to the presumably asymptotic nature of such an equilibration process, suggested by Fig. 4.7 and Fig. 4.8, no further significant changes are expected after ~50 h at 450 °C and ~200 h at 350 °C, respectively.

4.1.6 Conduction path

Another important aspect, also primarily shown by HILLEBRAND [91], is the fact, that (at least small-signal) conductivity in Nd:PZT(Cu) takes place within the sample and not on its surface. This was simply deduced by stepwise reducing sample thickness and observing the resistance. As the calculated conductivity stayed constant after each grinding step, it was concluded, that (at least small-signal) conduction in Nd:PZT(Cu) is predominantly occurring within the material and not on its surface. FRÖMLING [47], ANDREJS [168] and AYRANCIOGLU [169] made further extensive investigations on that point.

Whether electrons, holes or oxygen vacancies are the primarily conducting defects is a matter of stoichiometry (see sec. 2.1.4), however, there is some evidence, that in Nd:PZT oxygen conduction is enhanced at grain boundaries, at least above 600 °C [47].

4.1.7 (Non)Linearity

As the small-signal probing voltage in EIS measurements has to be within the linear current-voltage regime, the I - U relationship of Nd:PZT(Cu) was evaluated.

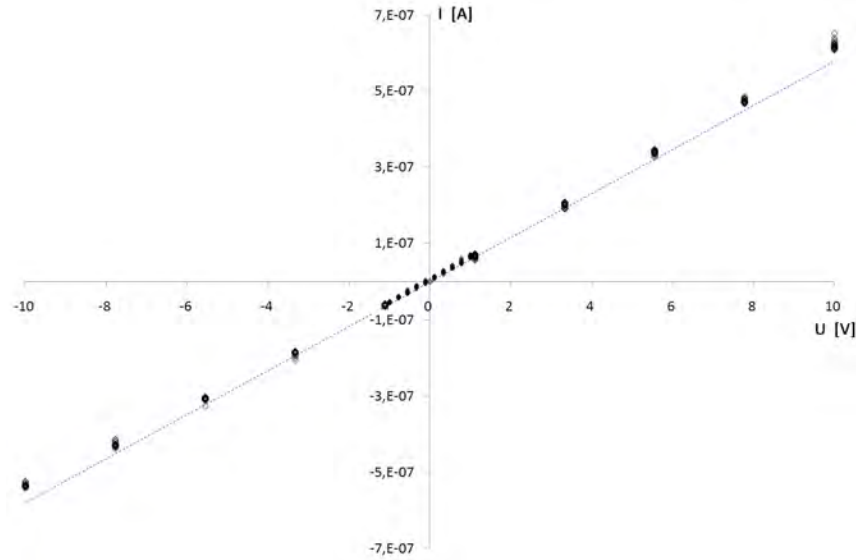


Figure 4.9: Virtually linear dc -current (I) vs. dc -voltage (U) plot for a Nd:PZT(Cu) interdigit electrode layer between -10 VDC and +10 VDC.

Fig. 4.9 displays a good linear current-voltage relationship in the range between -10 VDC and $+10$ VDC. For EIS small-signal measurements without dc -bias or for small-signal dc -conductivity probing, always signals smaller than 1 VAC were applied, which is by far in the linear regime.

However, the linear I - U -relationship, depicted in Fig. 4.9, is not maintained for higher dc -voltages: The ratio between the first measured high-voltage conductivity ($\sigma_1^0(\text{HV})$) and the small-signal EIS conductivity value ($\sigma_1^0(\text{LV})$) should equal 1 at any voltage for a true linear system. The deviations of this ratio from the value of 1 are depicted in Fig. 4.10 for different temperatures. The Nd:PZT(Cu) layers averaged for this plot show deviations from linearity up to 50 % in the voltage range up to 200 VDC. At least for higher temperatures an increased nonlinearity is found when increasing the voltage. Reasons for the larger scattering at lower temperatures (without any trend) are not known.

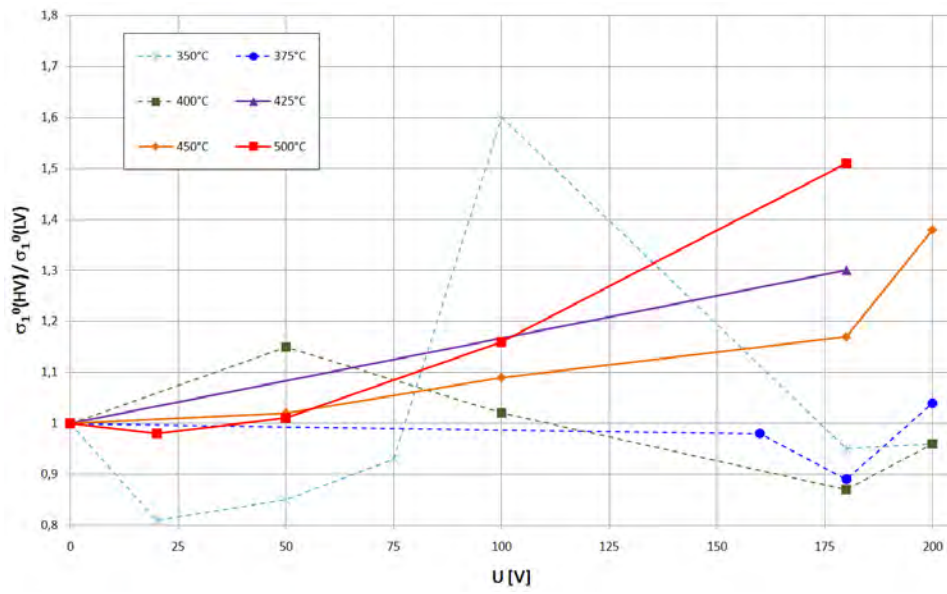


Figure 4.10: Deviations from linearity for higher electric fields on Nd:PZT(Cu) layers. The y -axis is the ratio of high- dc -voltage conductivity at $t = 0$ and small- ac -voltage conductivity.

4.2 Short-term high field stress and relaxation (Phase 1 & Phase 2)

Immediately after the application of high-voltages up to 200 VDC to a 75 μm Nd:PZT(Cu) layer, the conductivity *decreased* exponentially. After switching-off the high electric field, an exponential relaxation behavior of the conductivity was found in the opposite direction (conductivity *increase*).

4.2.1 Phase 1: High-field conductivity decrease

4.2.1.1 Time constant τ_1

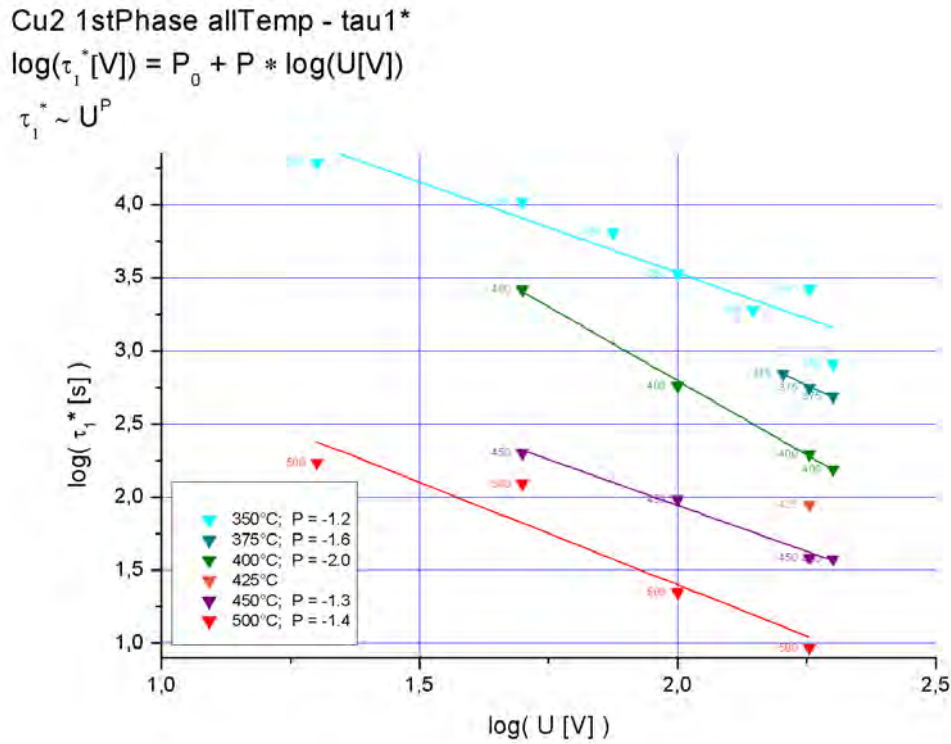


Figure 4.11: Phase 1: log-log plot of the HV conductivity decrease time constants τ_1 vs. the absolute value of the high-field voltage U_1 for different temperatures, parameterized by temperature T . Straight lines are linear fit functions.

The time constant τ_1 of the high-voltage phase (Phase 1) turned out to be strongly voltage-dependent: The higher the degradation voltage U_1 , the faster the conductivity minimum was reached. A double-logarithmic τ_1 vs. degradation-voltage U_1

plot in Fig. 4.11 visualizes that τ_1 follows a power-law relationship

$$\tau_1 \propto (U_1)^P \quad (4.7)$$

Fitting with this power-law function revealed the power-law exponent P to be in the range of $-1.2 \dots -1.6$ for temperatures between 350°C and 500°C (with one exception of $P = -2.0$ at 400°C). That means, that an increase of the high-field voltage U_1 by one order of a magnitude leads to an increase of the *rate* of field-driven conductivity variation ($1/\tau$) approximately by a factor of ~ 14 .

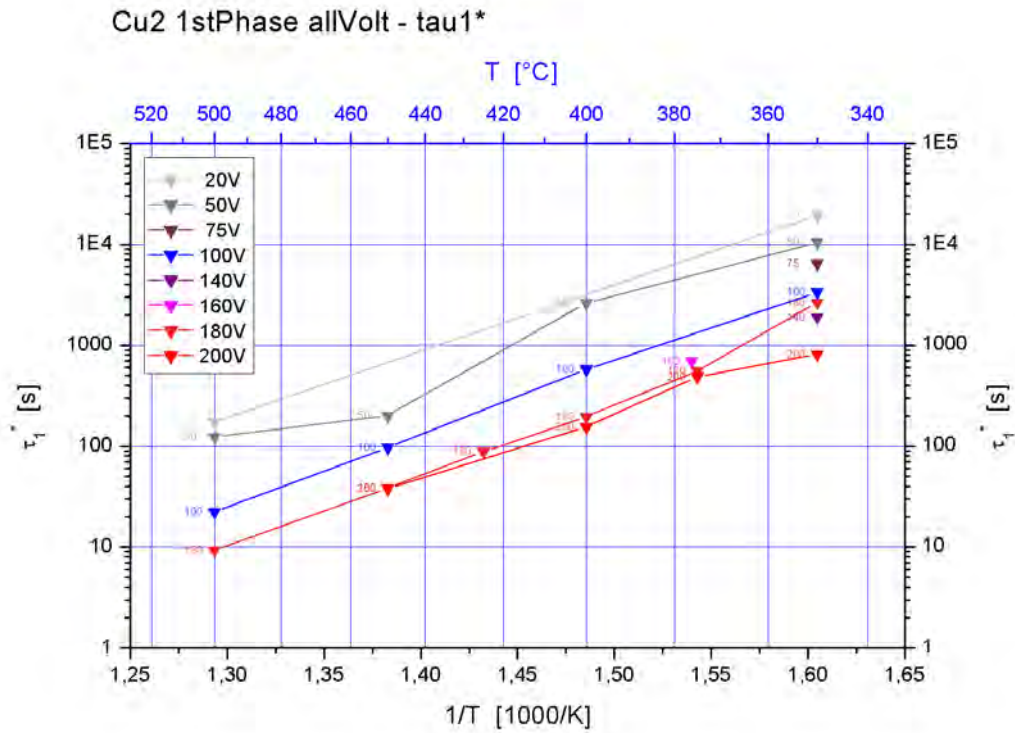


Figure 4.12: Time constants of Phase 1 vs. reciprocal temperature of short-term high-field conductivity decrease. Parameterized by high-field voltage U_1 . Lines are only connecting data points.

In Fig. 4.12 the time constants of the high-field Phase 1 (τ_1) are shown in an ARRHENIUS-like manner versus the reciprocal temperature $1/T$, parameterized by the high-field voltage U_1 (20 V ... 200 V).

Clearly, a thermally activated *rate* ($1/\tau$) of the conductivity decrease during high-field Phase 1 is identifiable. The analysis of the corresponding activation enthalpies is given in sec. 4.2.3.

4.2.1.2 Magnitude of the conductivity decrease “delta1”

Cu2 1stPhase allTemp - delta1*

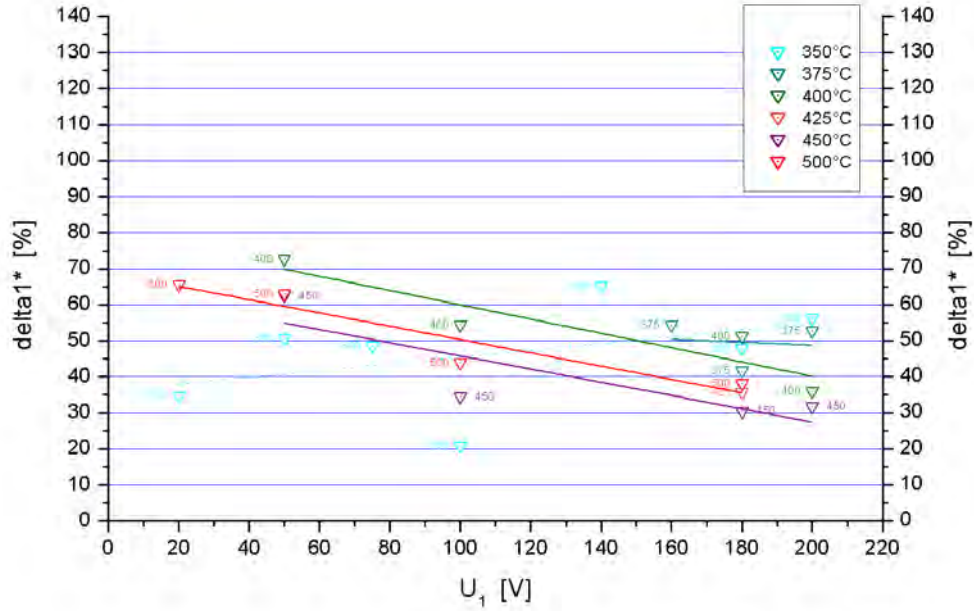


Figure 4.13: Relative change of the high-voltage conductivity (“delta1*”) during Phase 1 vs. high-field load U_1 . All experiments above $T_{set} > 350^\circ\text{C}$ show a clear proportionality between the magnitude of the conductivity decrease (“delta1*”) and the simultaneously applied voltage load U_1 . Straight lines are linear fit functions.

The extent (magnitude) of the conductivity changes was calculated according to Eq. (4.5) for “delta1” and Eq. (4.6) for “delta2”, corresponding to the change in conductivity during Phase 1 and Phase 2, respectively. A plot of the averaged magnitude of the conductivity change during the high-voltage Phase 1 is depicted in Fig. 4.13.

Above 375°C the relative change of conductivity during Phase 1 (“delta1”) shows a clear trend: Larger high-field voltage loads (U_1) lead to a more pronounced conductivity decrease. For example at 450°C the conductivity drops under 20 V *dc*-load to 60 % of its initial value which is $\approx \frac{2}{3} \cdot \sigma_1^0(\text{HV})$; under 200 V σ drops to 30 %, which is $< \frac{1}{3} \cdot \sigma_1^0(\text{HV})$. The voltage dependency however, is almost independent of temperature.

The relative change of conductivity during the high-voltage Phase 1 (“delta1”) did

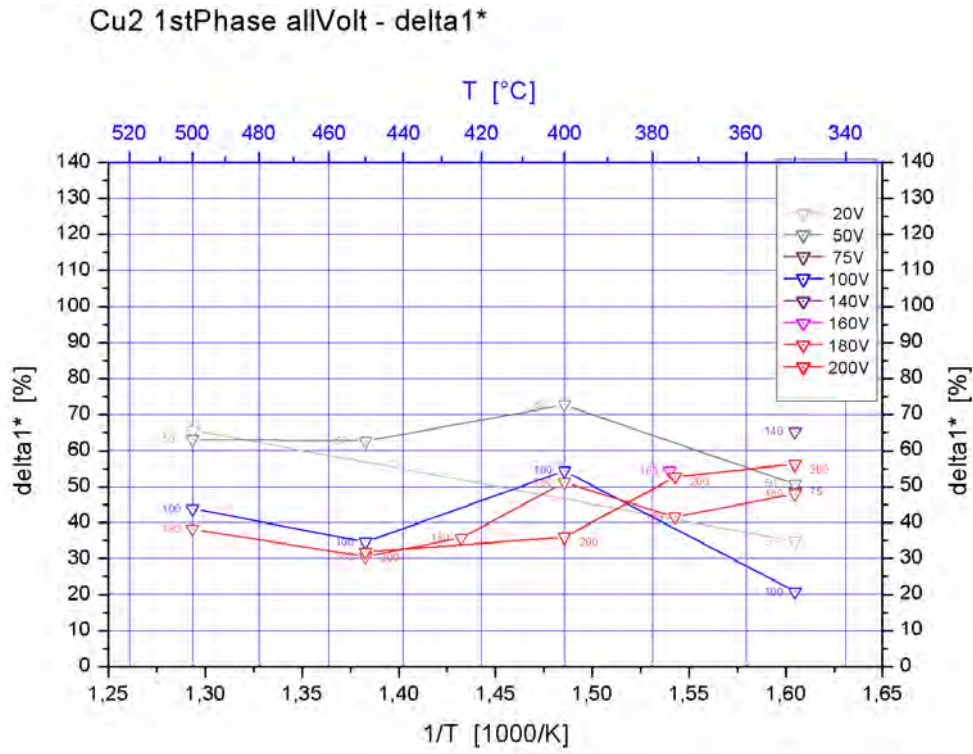


Figure 4.14: Relative decrease of the high-voltage conductivity during Phase 1 (“delta1*”) vs. reciprocal temperature $1/T$. No clear temperature dependency is found for any voltage load U_1 . Lines are only connecting data points.

not show any ARRHENIUS-like activation behavior, as can be seen in the plot of “delta1*” vs. reciprocal temperature $1/T$ in Fig. 4.14.

4.2.2 Phase 2: Stress-free relaxation

4.2.2.1 Time constant τ_2

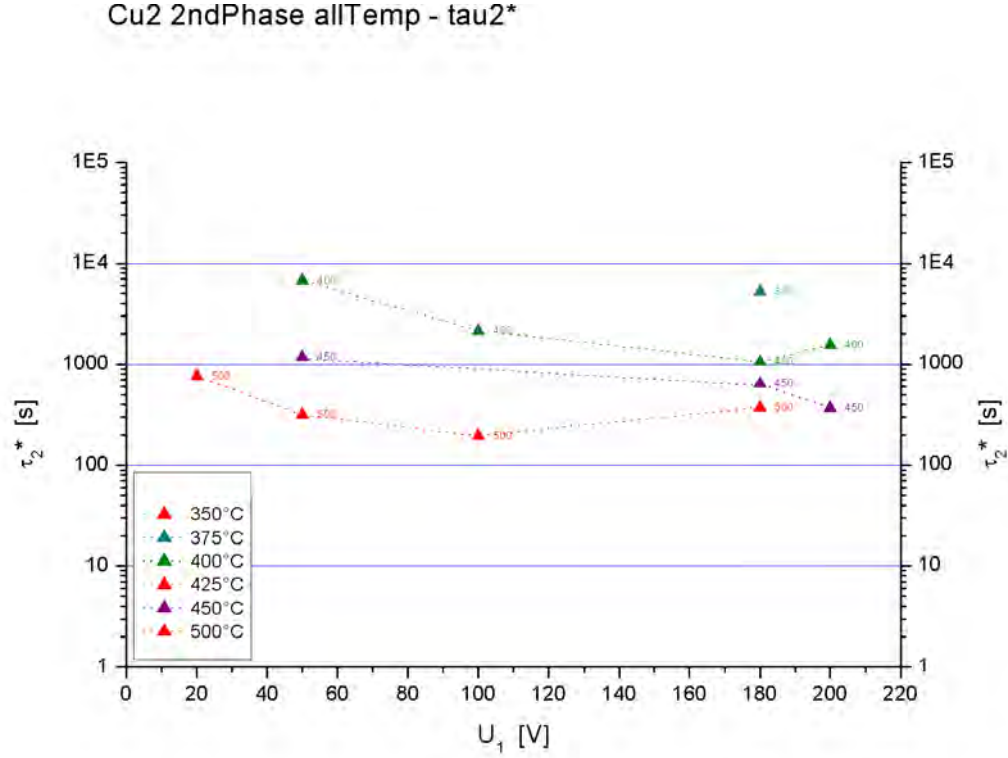


Figure 4.15: Phase2: Logarithmic plot of the relaxation time constant τ_2 vs. the absolute value of high-field voltage U_1 , parameterized by temperature. Lines are only connecting data points.

Clearly, the time constants of the low-voltage relaxation process (Phase2 / conductivity recovery) Phase2 (τ_2) are greater than those of Phase1 (τ_1). This means, the rate of conductivity recovery ($1/\tau_2$) is slower than that of high-field conductivity decrease in Phase1 ($1/\tau_1$). However, τ_2 does not seem to depend on the high-field voltage U_1 (which was applied only in the previous Phase1), cf. Fig. 4.15.

In Fig. 4.16 the time constants of the relaxation phase (Phase2: τ_2) are shown in an ARRHENIUS-like manner versus the reciprocal temperature $1/T$, parameterized by the high-field voltage U_1 (50 V ... 200 V). A thermal activation of τ_2 can clearly be recognized. The analysis of activation enthalpies will be described in sec. 4.2.3.

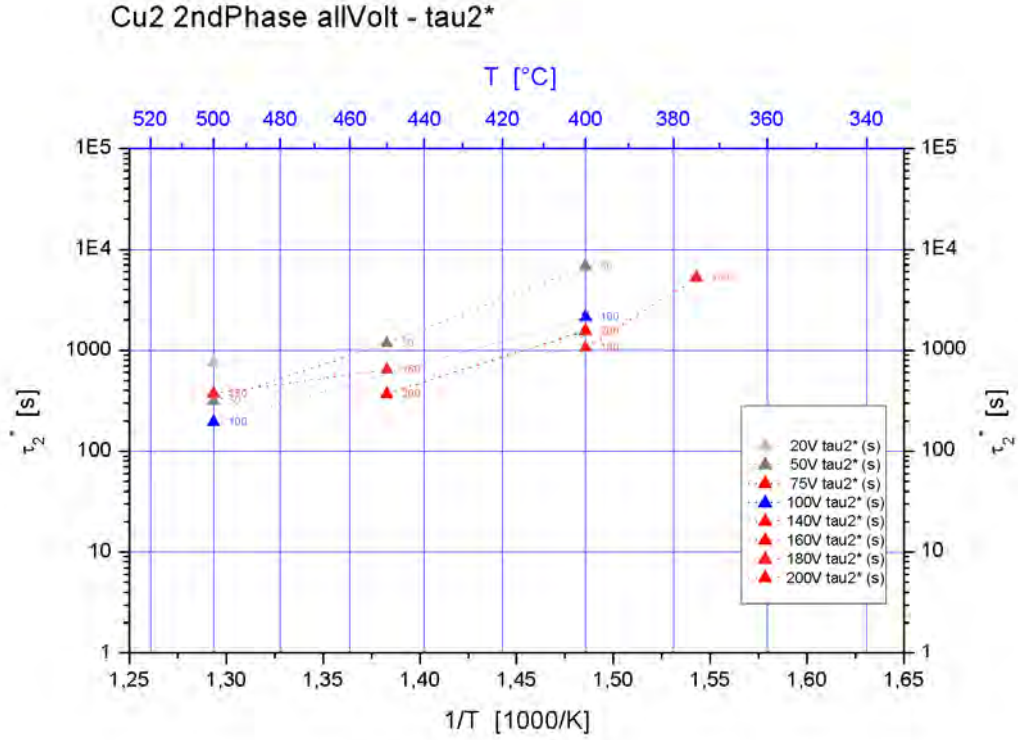


Figure 4.16: Recovery time constants of Phase 2 (τ_2) of short-term experiments vs. reciprocal temperature, parameterized by high-field voltage U_1 . Lines are only connecting data points.

4.2.2.2 Magnitude of the conductivity relaxation “delta2”

After the minimum of the conductivity was reached within the high-field Phase 1 and the high-voltage was switched-off (Phase 2), the relative magnitude of the subsequent field-free conductivity recovery (“delta2^{*}”) scattered significantly, as can be seen in Fig. 4.17. No clear dependency on the value of U_1 could be found.

A plot of the identical values of the relative change of conductivity during the relaxation Phase 2 (“delta2^{*}”) vs. reciprocal temperature shows the same indefinite result in Fig. 4.18. A clear dependency on temperature can not be recognized. For most high-field voltages ($U_1 \geq 100$ V) the final conductivity value ($\sigma_2^\infty(\text{LV})$) recovered approximately to 80 % of the initial high-voltage starting value ($\sigma_1^0(\text{HV})$).

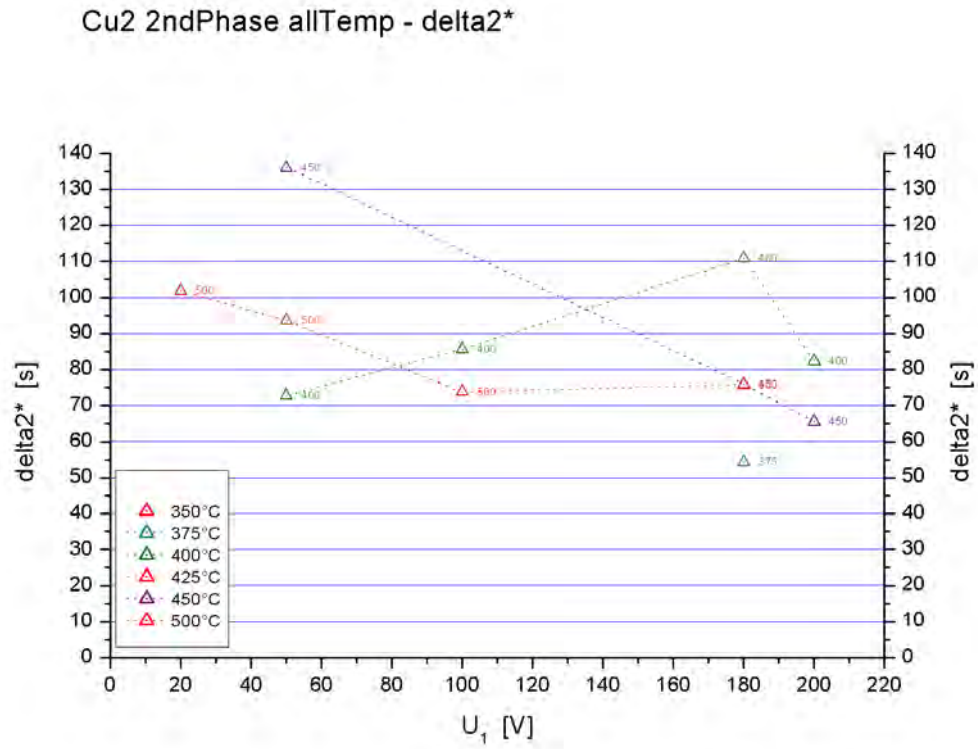


Figure 4.17: Magnitude of the conductivity recovery during relaxation Phase2 ($\delta a2^*$) vs. absolute value of the previous degradation voltage U_1 , parameterized by temperature. Lines are only connecting data points.

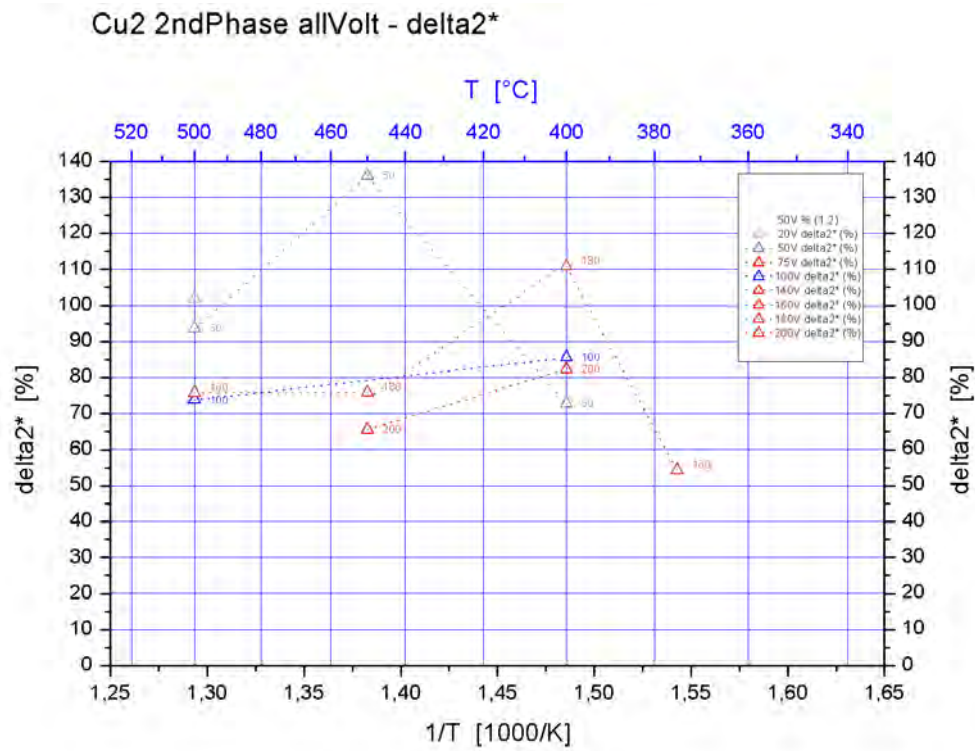


Figure 4.18: Magnitude of the conductivity recovery during relaxation Phase 2 ($\delta 2^*$) vs. reciprocal set-temperature, parameterized by high-field stress voltage U_1 . Lines are only connecting data points.

4.2.3 Relations between Phase 1 and Phase 2

Logarithmic plots of Fig. 4.12 and Fig. 4.16 visualize the ARRHENIUS-like activation character for the time constants τ_1 and τ_2 , cf. Fig. 4.19.

The linear fit-functions in Fig. 4.19 allow the calculations of activation enthalpies for $E_a(\tau)$ according to

$$\tau \propto \exp\left(\frac{E_a}{k_B \cdot T}\right) \quad (4.8)$$

The results $E_a(\tau_1)$ and $E_a(\tau_2)$ are listed for different voltage values (U_1) during the high-field stress Phase 1 in Tab. 4.1.

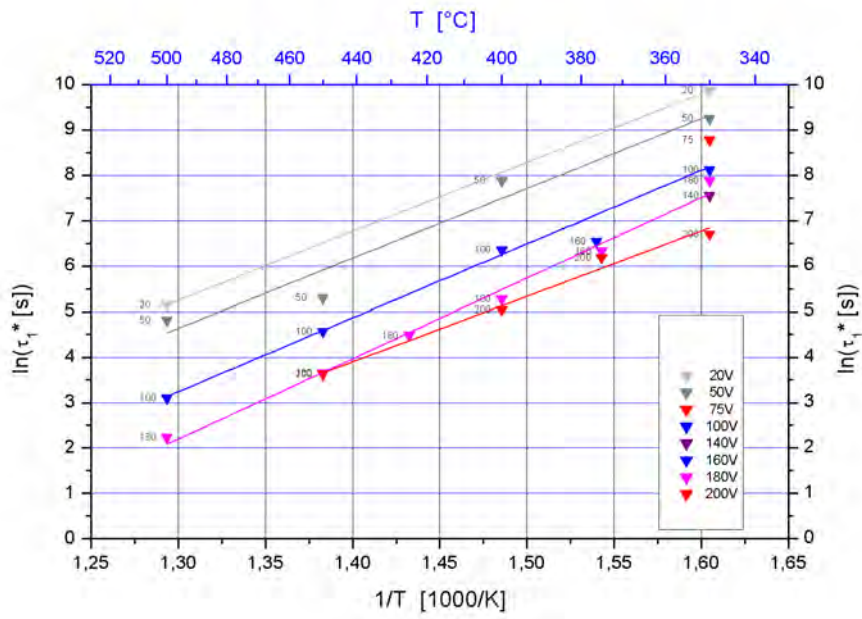
(a) Activation enthalpies E_a of τ_1 .		(b) Activation enthalpies E_a of τ_2 .	
U_1 [V]	$E_a(\tau_1)$ [eV]	U_1 [V]	$E_a(\tau_2)$ [eV]
20	1.31	20	-
50	1.32	50	1.38
100	1.39	100	1.07
180	1.52	180	0.82
200	1.24	200	1.20

Table 4.1: ARRHENIUS-like activation enthalpies E_a of time constants for Phase 1 (τ_1) and Phase 2 (τ_2) of a short-time high-field experiment, according to Eq. (2.61).

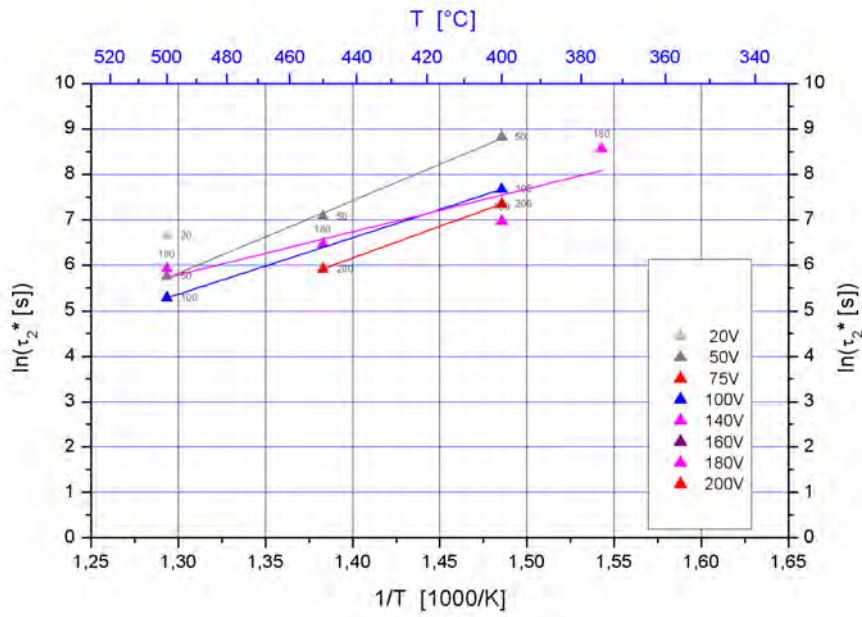
To summarize, the activation enthalpies of the time constants for the high-field conductivity decrease process (Phase 1), $E_a(\tau_1)$, range from 1.2 eV to 1.5 eV. The corresponding values for the low-voltage relaxation process $E_a(\tau_2)$, range from 0.8 eV to 1.4 eV.

The *ratio* of the relaxation time constant τ_2 and the degradation time constant τ_1 vs. $1/T$ is depicted in Fig. 4.20.

The time constant of conductivity recovery after high-field stress (τ_2) is ranging from $3\times$ (for low U_1) to $40\times$ (for high U_1) the time constant of the high-field induced conductivity decrease (τ_1).



(a) Phase 1: Logarithmic plot of τ_1 vs. $1/T$.



(b) Phase 2: Logarithmic plot of τ_2 vs. $1/T$.

Figure 4.19: Logarithmic plot of the time constants τ_1 (Phase 1: conductivity decrease) and τ_2 (Phase 2: conductivity recovery) versus $1/T$ and linear fit functions according to Eqs. (4.1) and (4.2).

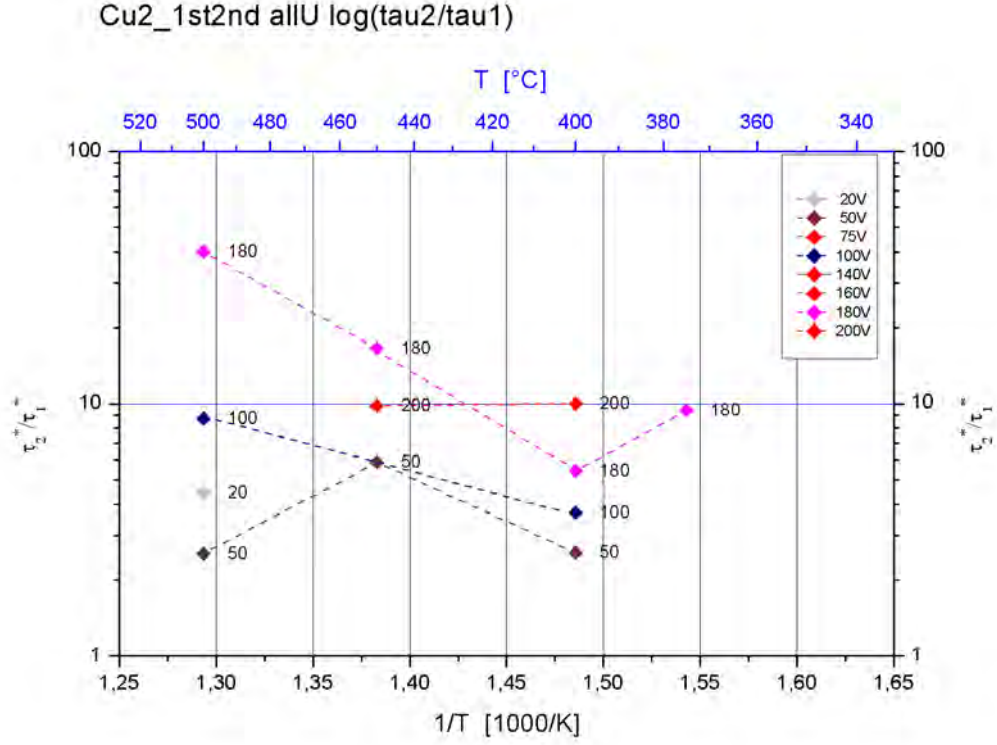


Figure 4.20: Logarithmic ratio of the relaxation time constant τ_2 and the conductivity decrease time constant τ_1 vs. $1/T$. Curve parameter is the high-field voltage U_1 .

As the relaxation time constant τ_2 shows only a slight dependency on degradation voltage U_1 (cf. Fig. 4.15), but the degradation time constant τ_1 is strongly dependent on U_1 (cf. Fig. 4.11), the ratio τ_2/τ_1 displays an increased value for higher voltage and higher temperature. For $U_1 = 180$ V and higher temperatures the conductivity relaxation (τ_2) requires more than the ten-fold time of the high-field conductivity decrease (τ_1).

4.2.4 Blackening

In parallel to the high-field induced decrease in conductivity, all 75 μm Nd:PZT(Cu) layers, subjected to high-voltage stress showed an optically observable color change: This darkening of the bulk PZT material layer, visible in the optical microscope will be called in the following “*blackening*”. Pictures of some Nd:PZT(Cu) layers stressed with different voltages can be seen in Fig. 3.2 and in Fig. 4.21. A close-up of two blackened layers is given in Fig. 4.22.

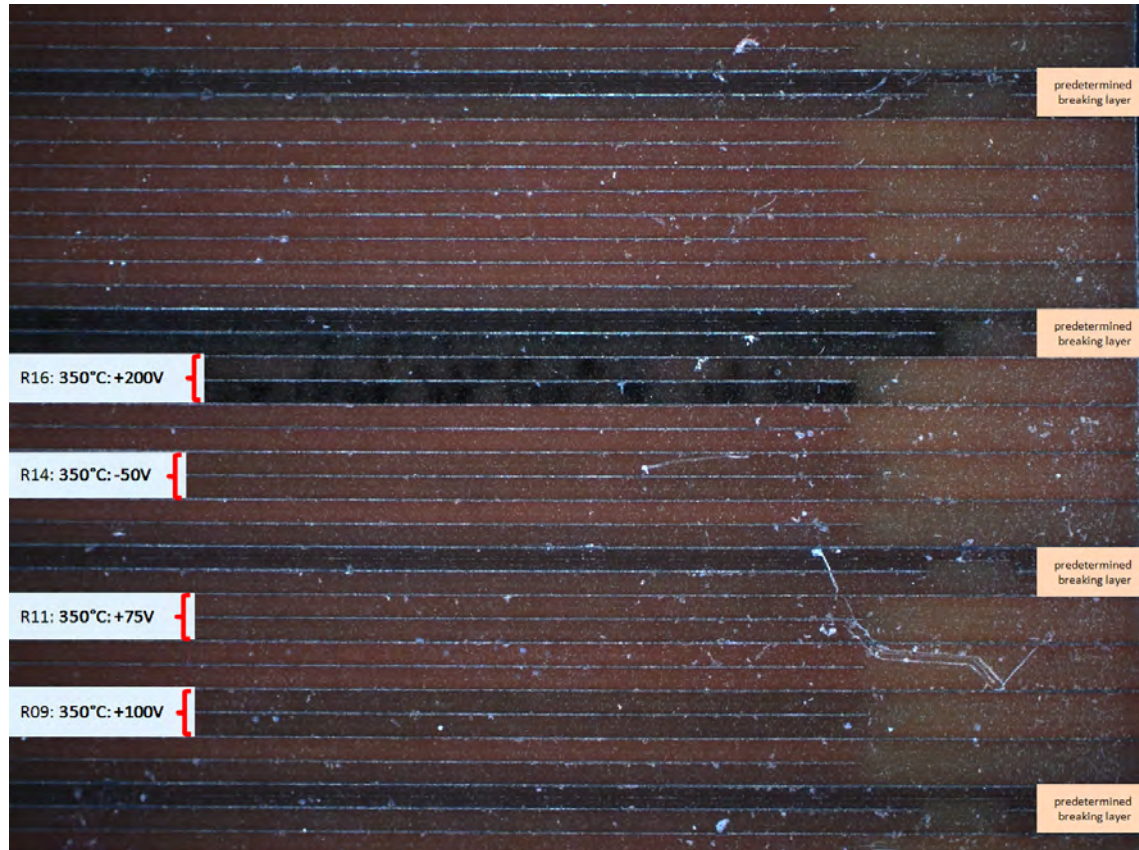


Figure 4.21: Dark-field micrograph of blackened layers on a Nd:PZT(Cu) sample degraded at 350 °C. Note the different intensity of the blackening with respect to the applied voltage. The predetermined breaking layers (with slightly thicker interdigit electrodes) are also blackened, but already after sintering and not due to an external electric field.

As *in-situ* observation of the blackening process was only possible in a limited quality, detailed investigation was difficult and limited to general statements:

- Blackening became gradually visible at all temperatures and degradation voltages (U_1) within the first third of the high-voltage Phase 1 before the conduc-

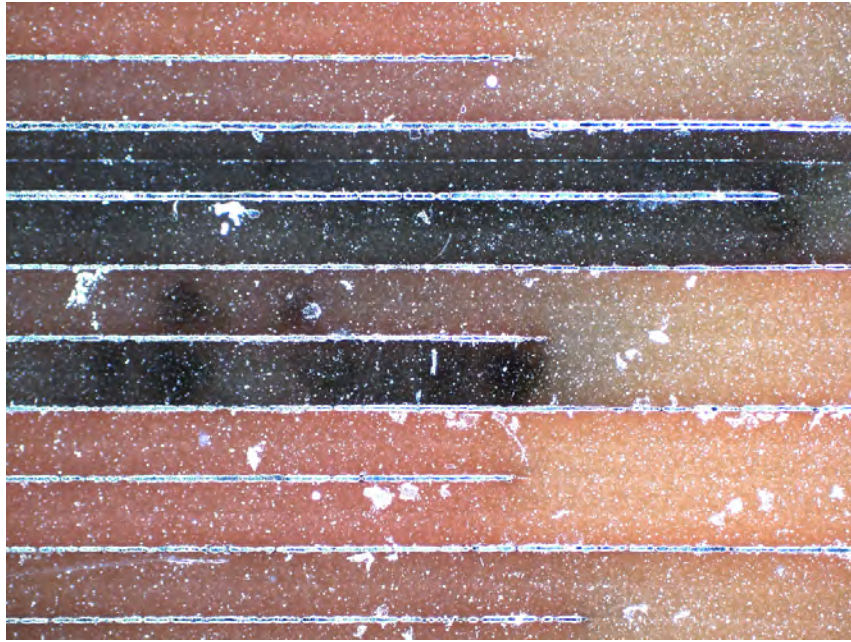


Figure 4.22: Close up of two blackened double-layers; dark-field micrograph. The upper blackened one is a predetermined breaking layer. The lower layer pair darkened due to 200 VDC high-field load at 350 °C. Note the relatively sharp color change at the end of the interdigit electrode.

tivity minimum was reached. It seemed to be a gradually growing process, as it first appeared as a slight darkening with respect to the neighboring (field-free) Nd:PZT(Cu) layers, intensifying with progressing time of voltage load.

- A movement of a blackened front from one electrode to the other could not be identified. Always the full length and width of the Nd:PZT(Cu) layer under electric field stress seemed to darken relatively homogeneously.
- After switching-off any high-voltage applied at temperatures below 400 °C, annealing at 550 °C for at least 1 hour is necessary to weaken or clear the blackening of the formerly stressed Nd:PZT(Cu) layers.
- After switching-off any high-voltage applied at temperatures above 425 °C, the high-voltage induced blackening weakens or clears within the recovery (relaxation) Phase 2 at the same temperature.
- A conductivity recovery at 350 °C could never be observed and the same is true with the optical recovery at this temperature: The blackened areas did not bleach even within some days at 350 °C. However, all blackened layers recovered optically and electrically after annealing at 550 °C.

- Qualitatively, blackening intensifies also with time, not only with voltage. Some intermediate-voltage (e. g. 20 VDC) long-term stressed layers showed the most intensive blackening, because the blackening process was not stopped by a breakdown. However, blackening does not directly correlate with the value of conductivity.

It is an open question whether the blackening is associated with Phase 1 or the second long-term degradation process Phase 2LT, already mentioned in sec. 4.1.1 and discussed in more detail in sec. 4.3. However, the phenomena of voltage-induced color change is well known for mixed conductors as YSZ and SrTiO_3 under high fields, see Refs. [96, 60].

Already new fabricated samples, without being ever subjected to any voltage-load show a similar dark appearance at the predetermined breaking layers, visible in Fig. 4.21 and Fig. 4.22. However, this phenomenon was not further investigated in this work.

4.2.5 The influence of the experimental atmosphere

Within this work no special measurements with Nd:PZT(Cu) samples have been conducted in atmospheres other than air. However, HILLEBRAND [91] investigated some of the very same Nd:PZT(Cu) samples in a reducing Ar atmosphere with 2.5 % H₂. This did not lead to a qualitative change of the conductivity behavior under high-field stress, cf. Fig. 4.23. However, the magnitude ($\Delta 1$) and the time constant (τ_1) of the conductivity change under high-voltage load (Phase 1) increased in H₂-atmosphere: τ_1 increased by a factor of 1.4 and the magnitude of the high-voltage degradation phase ($\Delta 1$, in the nomenclature of this thesis) increased by a factor of 1.3 compared to HILLEBRAND's data of Nd:PZT(Cu) in air.

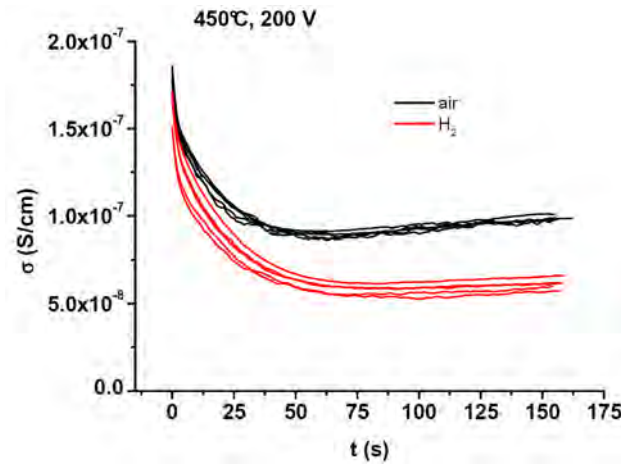


Figure 4.23: Conductivity decrease of Nd:PZT(Cu) layers at 450 °C in air (black) and 2.5 vol% H₂ (in Ar). Source: [91]

4.2.6 Stoichiometry polarization: A possible model for short-term conductivity variation

As already discussed in chapter 2, two processes are well known candidates for conductivity variations of PZT under high electric fields:

1. Build-up of stoichiometry variations and spatially varying defect concentrations, due to (partially) blocking electrodes, like in HEBB-WAGNER-type polarization experiments, and
2. conventional electrochemical migration of electrode material cations with formation of conducting paths/dendrites.

The same two models are also assumed to govern the resistance changes in thin films of resistive switching random access memory (RRAM) devices [170, 171, 172, 173]. Also already mentioned in chapter 2, the second process of dendrite growth at the electrodes was often reported for low temperatures ($< 100\text{ }^{\circ}\text{C}$) and highly humid conditions. Taking account of the temperatures employed in this study ($350\text{ }^{\circ}\text{C}$ - $500\text{ }^{\circ}\text{C}$) and the rare identification of highly conductive (metallic) precipitates within (or at the surface of) the resistive bulk, the conventional electrochemical cation migration model was considered to be improbable. Moreover, as conducting dendrites increase the active electrode surface and reduce the distance to the opposite electrode, the conductivity should increase from the very first moment, rather than decrease as observed in our experiments at Nd:PZT(Cu). Hence, in the following the stoichiometry polarization model as an explanation of the short-term conductivity variations of $75\text{ }\mu\text{m}$ Nd:PZT(Cu) layers under high electric field will be employed.

1st objection: No oxygen vacancies in positively (donor) doped Nd:PZT(Cu)

Stoichiometry polarization can either be carried by cation (e. g. A-site: $V''_{\text{Pb}2+}$) or anion ($V\ddot{\text{O}}$) vacancies. In the perovskite structures of the mixed conducting SrTiO_3 and BaTiO_3 , the A-site cation is comparatively immobile with high activation energies, at least below $500\text{ }^{\circ}\text{C}$ [17, 174, 175, 176, 177]. Certainly, this does not necessarily allow a final conclusion about the Pb mobility in PZT. However, in the model presented in this chapter, oxygen vacancies ($V\ddot{\text{O}}$) will be assumed to be the defect species causing the internal defect concentration changes leading to the conductivity variations described in sec. 4.2 - sec. 4.2.5. This model of stoichiometry polarization was proposed and experimentally validated for negatively (Fe^{3+} -acceptor) doped

SrTiO₃ [52, 53, 54, 60]. Nevertheless in Refs. [52, 53, 54] it was simultaneously argued (and also verified for positively (La³⁺-donor) doped SrTiO₃) that stoichiometry polarization by oxygen vacancies is highly unlikely for donor-doped perovskites such as SrTiO₃ and BaTiO₃: A positive donor ion (La_{Pb}) should rather boost negative cation vacancies and strongly suppress creation of (positive) oxygen vacancies. However, as discussed in detail in sec. 2.3.5, the pronounced PbO volatility at the (low $p(\text{O}_2)$) sintering process of our Nd:PZT(Cu) might still cause a significant oxygen vacancy concentration even in positively (donor) doped PZT, despite protection-means to avoid pronounced PbO evaporation, as burying the samples into PZT-powder. As long as neither BROUWER-diagrams nor oxygen partial-pressure dependent conductivity measurements are available for positively (donor) doped PZT, a significant amount of V_{O} cannot be excluded. The ¹⁸O isotope exchange experiments and subsequent *ToF-SIMS* analysis by FRÖMLING on Nd:PZT(AgPd) samples sintered even in air [165], already mentioned in sec. 4.1.3, showed very pronounced oxygen grain boundary diffusion at least at temperatures above 600 °C, indicating a substantial amount of oxygen vacancies at least in the grain boundary region, cf. sec. 2.2.1.2.

2nd objection: Conductivity decrease instead of conductivity increase In negatively (Fe³⁺-acceptor) doped SrTiO₃ and BaTiO₃ a conductivity increase of several orders of magnitude was observed under high electric field stress [52, 53, 54, 60]. So *prima facie* it seems quite implausible, that the very same stoichiometry polarization mechanism could display the very opposite conductivity behavior (decrease of σ) in our case of positively (Nd³⁺-donor) doped Nd:PZT(Cu). For single-crystal SrTiO₃ with partially ion-blocking electrodes at different electric potential, oxygen vacancies V_{O} are depleted at the positively charged anode (\oplus) and enriched at the negatively charged cathode (\ominus). For reasons of charge neutrality the low (anode \oplus) and high (cathode \ominus) V_{O} concentrations are charge compensated by enhanced hole (anode \oplus) and electron (cathode \ominus) concentrations, respectively [59].

As the chemical potential of oxygen $\mu(\text{O}_2)$ is due to Eq. (2.6) and Eq. (2.7) proportional to the natural logarithm of the oxygen partial pressure $p(\text{O}_2)$, a stoichiometry polarization experiment can be displayed in the slightly modified BROUWER-diagram from sec. 2.2.1 of a negatively (acceptor) doped metal oxide $\text{MO}_{1-\delta}$. With the NERNST-Equation (2.42) the $\log(p(\text{O}_2))$ x -axis can be directly converted to an axis of electric potential U and the effects of a HEBB-WAGNER like stoichiometry polarization on conductivity can be illustrated in the modified BROUWER-diagram

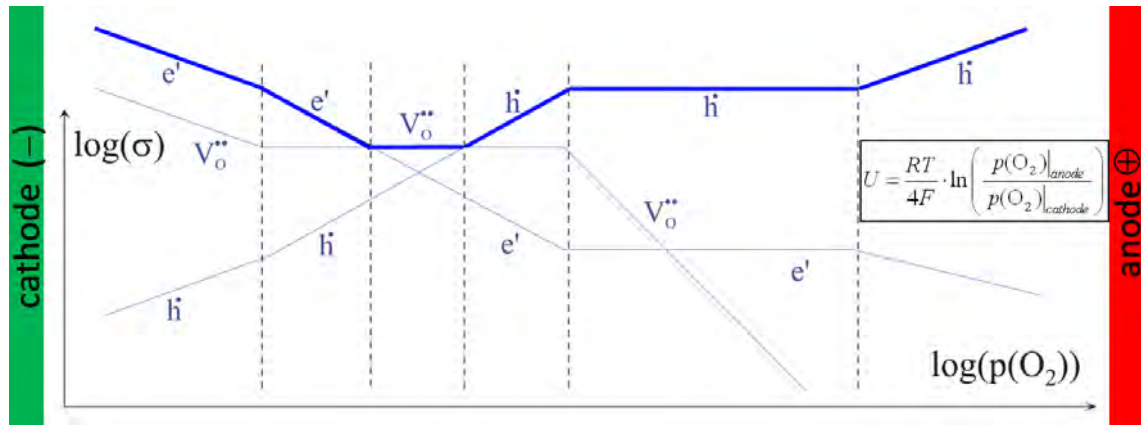


Figure 4.24: Modified BROUWER-diagram of a negatively (acceptor) doped metal oxide $\text{MO}_{1-\delta}$: Due to the NERNST-relation (Eq. (2.42), inset) the $\log(p(\text{O}_2))$ axis can be thought as an axis of electrical potential U . As the electrical potential drops (in a nonlinear way) from the anode(\oplus) to the cathode(\ominus), the x -axis also represents a not-to-scale spatial dependency. The thick blue line is the total conductivity σ_{total} . Note the NERNST proportionality between U and $\ln(p(\text{O}_2))$ and the characteristic minimum of σ_{total} . Source: [59].

in Fig. 4.24. Hence a stoichiometry polarization experiment can be alternatively illustrated in chemical terms as a shift of the chemical potential $\mu(\text{O}_2)$ between two regimes of different oxygen partial pressure $p(\text{O}_2)$, or in electrical terms as a shift of the electrochemical potential $\tilde{\mu}(\text{O}^{2-})$ between two regimes of different voltage U .

Without being subjected to an electric field, a certain composition is - depending on doping and nonstoichiometry - situated on a certain point of the x -axis in Fig. 4.24. Applying a field is the very same as to change the oxygen partial pressure in opposite direction at both sides of the sample. Hence, the composition within the stressed sample will adapt to the different boundary conditions and will show spatial deviations. Depending on the position of the field-free stoichiometry in the BROUWER-diagram and on the magnitude of the stoichiometry distortion, the spatially resolved total conductivity will show a monotonic gradient or exhibit a local minimum between the electrodes [18, 54, 60].

In fact, RODEWALD et al. have actually measured a spatially resolved conductivity profile of polycrystalline negatively (Fe^{3+} -acceptor) doped SrTiO_3 [60], with a pronounced conductivity minimum, see Fig. 4.25. Without electric field stress, RODEWALD's $\text{Fe}:\text{SrTiO}_3$ was obviously in a stoichiometric regime already close to the conductivity minimum (of Fig. 4.24). The application of positive voltage on the anode shifted this side of the sample into a regime with enhanced (hole) conductivity.

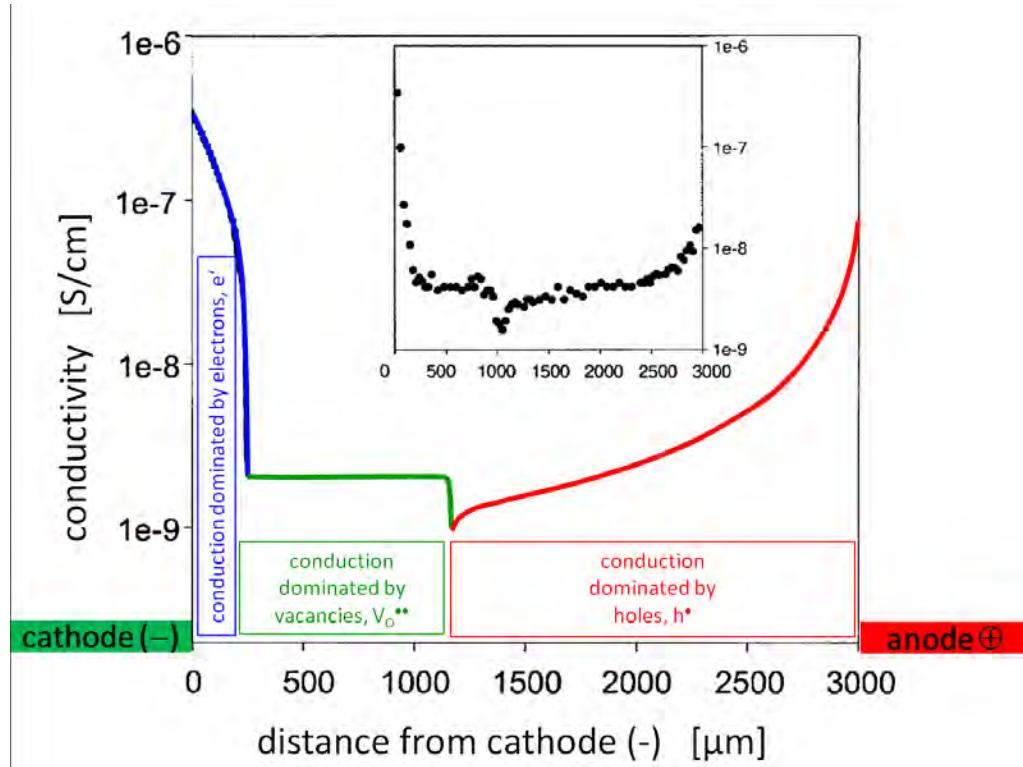


Figure 4.25: RODEWALD's experimental data (inset) and calculated conductivity profile for negatively (acceptor) doped PZT (0.2 % Fe^{3+}) frozen-in after 100 kV/m high-field “coloration” (Obviously referring to a blackening effect, similar at the Nd:PZT investigated in this work). Regions of predominant hole h^+ (red), vacancy $V_O^{\cdot\cdot}$ (green) and excess electron e^- (blue) conduction and the spatial arrangement of the electrodes are indicated. Note the similarity to the characteristic conductivity minimum in the BROUWER-diagram Fig. 4.24. Source: Modified from [60].

The (negative) cathodic part of the sample also suffered an increase of conductivity, but due to electron conductivity. Together this lead to an overall conductivity increase of stoichiometrically polarized $\text{Fe}:\text{SrTiO}_3$.

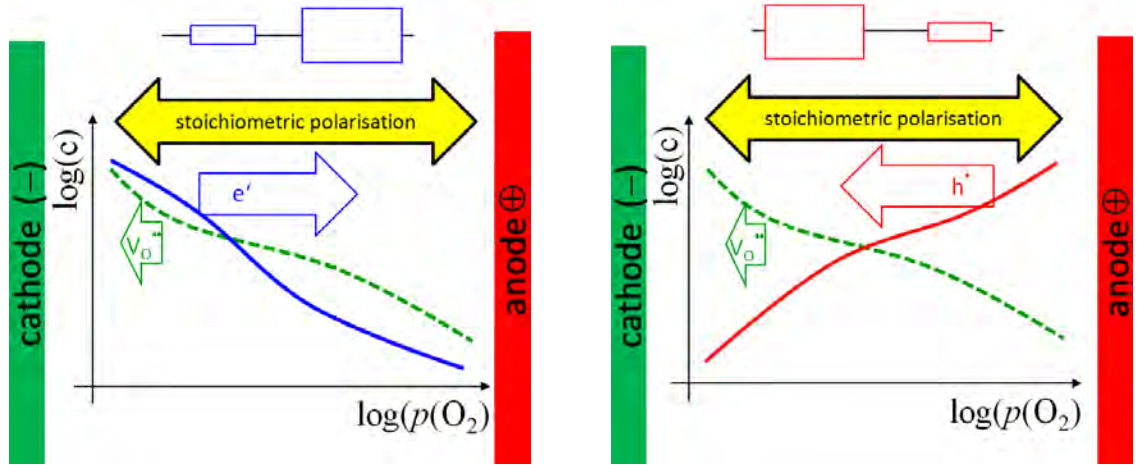
For positively (donor) doped PZT, BROUWER-diagrams - and thus σ vs. $p(\text{O}_2)$ plots - have to differ significantly from those of negatively (acceptor) doped SrTiO_3 , even though quantitative information is not available so far.

To explain the different direction of the conductivity change of positively doped Nd:PZT(Cu) in Phase 1 of short-term experiments, simply a starting stoichiometry ratio beyond the conductivity minima plateau of Fig. 4.24 might be sufficient: If a sample of such a stoichiometric ratio is subjected to an electric field, one part of the sample could suffer a *conductivity decrease*, which may or may not be counterbal-

anced by a possible *conductivity increase* in the opposite part of the sample. Even though this example is based on a negatively (acceptor) doped metal oxide $\text{MO}_{1-\delta}$ (Fig. 4.24) and may thus not be valid for positively (donor) doped PZT, other, similar, scenarios leading to monotonic conductivity changes along the sample are easily conceivable, see below.

This model is supported by a further consideration on the electrodes: For ideal stoichiometry polarization experiments, the electrodes (and theoretically even the sample surface / three phase boundary) should be totally tight and blocking for oxygen (gas) exchange with the atmosphere. However, complete ion blocking at the electrodes is not required in order to obtain variations of local defect concentration upon high field [54, 61]. Such a strongly (but not completely) blocking scenario is realistic within a multilayer stack of the ceramic-insulated type, Fig. 3.1. Especially the three phase boundary at which the electrode edge and PZT intersect with atmosphere, a limited oxygen reaction is conceivable. In fact, HILLEBRAND [91] found on the very same Nd:PZT(Cu) samples a significant increase of the magnitude of conductivity change by a factor of about 1.3 and an increase of τ_1 by a factor of about 1.4 in 2 vol% H_2 -atmosphere, cf. Fig. 4.23. As - compared to oxygen - hydrogen strongly modifies cathodic as well as anodic reaction kinetics and especially hinders any oxygen incorporation at the cathode, an effect of H_2 on degradation behavior can be interpreted as result of a finite transfer reaction at the electrodes of our Nd:PZT(Cu) under high fields.

If real (partially ion-blocking) anodes and cathodes are limiting the ion exchange differently, the stoichiometric polarization will also be influenced. If, for example, the oxygen release at the anode (\oplus) occurs faster than the oxygen incorporation at the cathode (\ominus), oxygen vacancy creation is virtually unlimited (due to the faster removal reaction) at the anode (\oplus). Simultaneously oxygen vacancy concentration $[\text{V}_{\text{O}}^{\bullet\bullet}]$ is enhanced also at the cathode (\ominus) (due to the hindered oxygen incorporation reaction). However, any voltage induced $[\text{V}_{\text{O}}^{\bullet\bullet}]$ -gradient between two electrodes can be assumed to be compensated predominantly by electronic defects. Depending on the stoichiometric position in the BROUWER-diagram (yet unknown for our PZT), this can be done *either* by electrons e' *or* by holes h' , cf. Fig. 4.26: To maintain local charge neutrality, Eq. (2.39), negatively charged electrons e' compensate the gradient of the positively charged oxygen vacancies $\text{V}_{\text{O}}^{\bullet\bullet}$ by displaying a gradient of the same slope (Case (a), Fig. 4.26a). Positively charged holes h' compensate the gradient of $\text{V}_{\text{O}}^{\bullet\bullet}$ by displaying a similar gradient but with a slope of opposite sign



(a) Case (a): Predominant electron compensation of a \ddot{V}_O gradient, with holes playing no role leads in a rough simplification to a serial connection of a small (cathode) and a big (anode) resistor: Overall conductivity decreases.

(b) Case (b): Predominant hole compensation of a \ddot{V}_O gradient, with electrons playing no role, leads to a serial connection of a small (anode) and a big (cathode) resistor: Overall conductivity decreases.

Figure 4.26: Stoichiometric polarization of two different stoichiometric compositions leading to similar conductivity decrease. Remember, that electronic charge carriers (e' , h') dominate the conductivity due to their higher number and greater mobility.

(Case (b), Fig. 4.26b):

- (a) The voltage induced spatial \ddot{V}_O -gradient is predominantly compensated by electrons e' ($\frac{\partial}{\partial x} [e'] \approx \frac{\partial}{\partial x} (\ddot{V}_O)$). Since the mobility of electronic charge carriers is much greater than that of ionic defects ($u(e') \gg u(\ddot{V}_O)$) and the (partially) blocked oxygen vacancies are not available for charge transport, the resulting conductivity σ is dominated by electrons e' . The cathodic section of the sample shows increased electronic conductivity, while the anodic region suffers a conductivity loss, cf. Fig. 4.26a. Due to the serial connection character of two different resistors, the bigger one limits the overall conductivity; A *decrease* of overall conductivity is a highly possible result of such a situation.
- (b) The voltage induced spatial \ddot{V}_O -gradient is predominantly compensated by holes h' ($\frac{\partial}{\partial x} [h'] \approx -\frac{\partial}{\partial x} (\ddot{V}_O)$). Since $u(h') \gg u(\ddot{V}_O)$, and the \ddot{V}_O are moreover (partially) blocked, the resulting conductivity σ is dominated by holes h' . The cathodic section of the sample shows decreased

hole conductivity, while the anodic region suffers a conductivity rise, cf. Fig. 4.26b. Due to the serial connection character of two different resistors, the smaller one limits the overall conductivity; A *decrease* of overall conductivity is a highly possible result of such a situation.

To summarize: Because of the serial connection of the differently stoichiometrically polarized parts of a PZT-layer under voltage and the unknown BROUWER-diagrams of PZT in general, high-voltage stress does not necessarily lead to an *increase* in conductivity. For Nd:PZT(Cu) we suggest, that the very same stoichiometry polarization mechanisms, actually leads to the *decrease* of overall conductivity, which was actually observed during Phase 1 of the short-term experiments, mentioned in sec. 4.2.

Qualitatively a BROUWER-diagram for the conductivity of a positively (donor) doped metal oxide $\text{MO}_{1-\delta}$, like Nd:PZT, should look like that in Fig. 4.27.

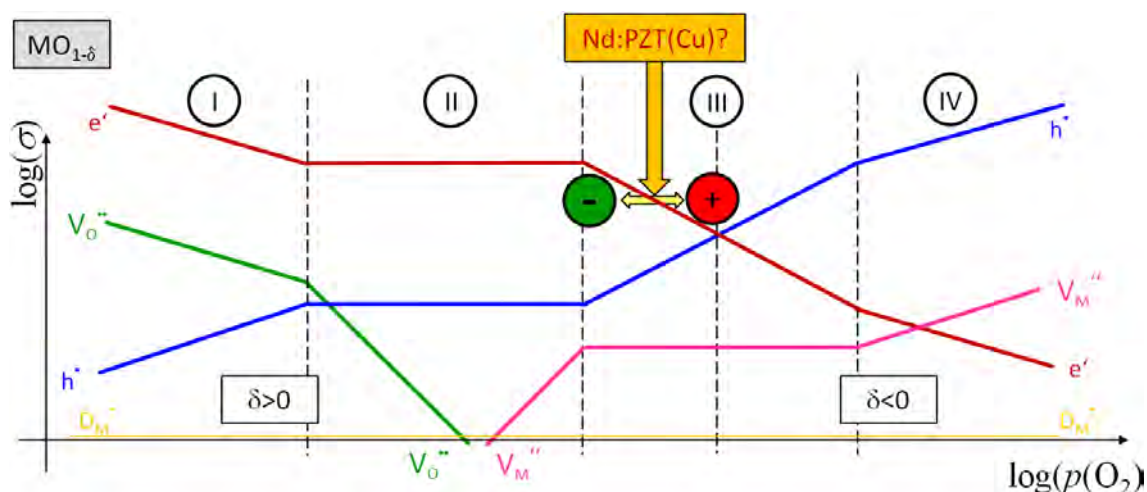


Figure 4.27: BROUWER-like plot of the conductivity contribution of different defects in positively (donor) doped metal oxide $\text{MO}_{1-\delta}$. Overall conductivity is determined by the upper envelope: e' -dominated at oxygen deficiency and h' -dominated at oxygen excess. Nd:PZT(Cu), which is sintered in reducing atmosphere, is expected to be situated as indicated. Thin yellow line: Acceptor dopant $\text{D}_M^{\bullet-}$.

Even at the elevated temperatures (350 °C ... 500 °C) our Nd:PZT(Cu) is not a good conductor. Hence, it is not expected to show such high electronic conductivities as in the regimes I, II and IV of Fig. 4.27. Moreover, since our Nd:PZT(Cu)-samples are sintered under reduced oxygen partial pressure, it is reasonable to assume its stoichiometry to be situated in regime III as indicated in Fig. 4.27. This stoichio-

metric situation would correspond to an electron dominated conductivity, as already considered in Fig. 4.26a. So, voltage-triggered stoichiometry polarization and subsequent field-free relaxation could easily lead to the conductivity decrease under *dc*-load and subsequent purely thermal conductivity recovery.

However, it is not easy to *quantify* the $p(\text{O}_2)$ -axis and the voltage-triggered shift of stoichiometry for the electric fields used in this study. In addition, one has to keep in mind, that the distribution of the ionic charge carriers, namely the cation vacancies (V_{M}'') and anion vacancies ($V_{\text{O}}\cdot$), is plotted in Fig. 4.27 for a fully equilibrated state. But equilibration of *all* ionic defects is most probably far from being completed within even several days below 500 °C. But rather the ionic defect distribution has to be described as a frozen-in state from the sintering conditions. However, a consideration of the far more complex freeze-in process of ionic defects and subsequent equilibration of electronic defect species would go beyond the scope of this work.

Nevertheless, in the following section a quantitative comparison with the stoichiometry polarization model for SrTiO_3 will be given.

4.2.6.1 Comparison with stoichiometry polarization on SrTiO_3

In the following table the experimental features of voltage-induced conductivity variations of SrTiO_3 (1st column) are compared to our results on Nd:PZT(Cu) (2nd column). For SrTiO_3 a stoichiometry polarization model was already numerically calculated and experimentally supported [52, 53, 54, 60, 157]. This comparison of the data of SrTiO_3 with the data of our Nd:PZT(Cu) supports our hypothesis of stoichiometry polarization in Nd:PZT(Cu).

SrTiO_3	Nd:PZT(Cu)
Phase 1: Activation energy of the high-field time constant τ_1 close to oxygen vacancy transport activation	
In negatively (acceptor) doped SrTiO_3 (0.2 % Fe^{3+}) the degradation time constant τ_1 is thermally activated by 0.6 eV ... 0.9 eV in single crystals [53] and ca. 1.2 eV in polycrystals [52]. This is similar to the value predicted by calculations on stoichiometry polarization, where - to a first approximation - the thermal activation is supposed to reflect the activation enthalpy of the oxygen vacancy mobility [54], which is ca. 0.9 eV for slightly Fe-doped SrTiO_3 .	The corresponding time constant τ_1 of the polycrystalline Nd:PZT(Cu) investigated in this chapter is also thermally activated in the range of 1.2 eV ... 1.5 eV. These somewhat higher values might be attributed to the enhanced defect interaction in our samples. However, the thermal activation of oxygen vacancy transport may indeed be the cause of the activation energy of τ_1 .

4.2 Short-term high field stress and relaxation (Phase 1 & Phase 2)

Phase 1: Power-law dependency of the high-field time constant τ_1 on the high-field voltage U_1 : Exponent P

In monocrystalline, negatively (Ni-acceptor) doped SrTiO₃ the degradation time constant τ_1 is depending on the degradation voltage U_1 by the power-law relationship Eq. (4.7) $\tau_1 \propto (U_1)^P$ with an exponent $P = -1.1$ at 180 °C [53]. According to the model calculated by BAIATU et al. a linear inverse relation between τ_1 and field-strength E is expected. $\tau_1 \propto 1/E$ ($P = -1$) [54].

In polycrystalline negatively (acceptor) doped SrTiO₃ the power-law exponents P are somewhat larger, $P = -2.45$ [52], which can be attributed to strongly blocking grain boundaries in SrTiO₃, as depletion of positive charge-carriers at grain-boundary space-charge layers hinder oxide ions to pass.

In our positively (donor) doped Nd:PZT(Cu) samples the exponent P in the power-law relation between U_1 and τ_1 , Eq. (4.7), was found to be approximately in the range of $-1.2 \dots -1.6$ for temperatures between 350 °C and 500 °C, cf. Fig. 4.11. This is not surprising, since in contrast to negatively (acceptor) doped perovskites space-charges at grain boundaries of positively (donor) doped material more likely exhibit a depletion of negative charge-carriers [97, 178, 179, 180]. Hence, our polycrystalline Nd:PZT(Cu) might either behave almost like a single crystal in terms of oxygen conduction (if grain-boundary space-charges are negligible) or fast vacancy conduction via grain boundaries is present (if enhanced \ddot{V}_O concentration at grain boundaries dominates ionic migration under load). Due to BAIATU's model [54], the first case (negligible grain-boundary effects) would lead to an exponent P close to -1 . For the second case (fast ionic grain boundaries) to the best of the authors knowledge model calculations do not exist.

Phase 2: Relaxation time constant τ_2 complies with ambipolar chemical diffusion of oxygen (D_O^δ)

In negatively (acceptor) doped SrTiO₃ the relaxation time turned out to be much slower than the field-driven change of conductivity ($\tau_2 > \tau_1$). The reason for that is, that the conductivity relaxation (Phase 2) is caused by chemical (ambipolar) diffusion of oxygen (D_O^δ) back to a homogeneous stoichiometry, after the oxygen stoichiometry was heavily distorted by the electric field during Phase 1 [60]. Hence, relaxation (τ_2) is thermally activated in accordance with the chemical diffusion coefficient.

Also in our Nd:PZT(Cu) samples, the relaxation time constants of Phase 2, τ_2 , are significantly (3...40 times) larger than the degradation time constants of phase 1, τ_1 , cf. Fig. 4.20.

According to Tab. 4.1 the activation energies $E_a(\tau_2)$, for our Nd:PZT(Cu) range from 0.8 eV to 1.4 eV, which agrees perfectly with the activation energy of D_O^δ reported for a similar positively (Nb-doped) PZT: $E_a(D_O^\delta) = 1.2$ eV [46].

Blackening

In negatively (acceptor) doped SrTiO₃ voltage driven conductivity variations are accompanied by color changes which disappear during or after the relaxation of the sample, particularly at enhanced temperature [53, 60].

The Nd:PZT(Cu) layers investigated for this work also darkened while subjected to an electric field and recovered (optically) at least at elevated temperatures ("blackening", cf. sec. 4.2.4).

4.2.6.2 Diffusion coefficients

Self-diffusion coefficient of oxygen vacancies During the high-voltage (conductivity decreasing) Phase 1 a distorted $V_{\ddot{O}}$ -concentration front is assumed to move through the stressed Nd:PZT(Cu) layer of thickness L . Assuming that the time constant of the high-field Phase 1, τ_1 , indicates that the concentration front has passed the entire layer, the velocity v is given by $v = L/\tau_1$. BAIATU has shown in his model for SrTiO₃ stoichiometry polarization [54], that to a first approximation the mobility of oxygen vacancies $u_{V_{\ddot{O}}}$ is related to the velocity v of migrating concentration fronts moving under high-fields (E) by

$$u_{V_{\ddot{O}}} = \frac{v}{E} = \frac{L}{\tau_1 \cdot E} \quad (4.9)$$

With an adaption of the (NERNST-)EINSTEIN relation from Eq. (2.50),

$$D^\sigma = \frac{R \cdot T}{|z| \cdot F} \cdot u \rightarrow D_{V_{\ddot{O}}}^\sigma = \frac{k_B \cdot T}{2 \cdot e} \cdot u_{V_{\ddot{O}}} = \frac{k_B \cdot T}{2 \cdot e} \cdot \frac{L}{\tau_1 \cdot E} \quad (4.10)$$

it is possible to estimate the *oxygen vacancy self-diffusion coefficient* $D_{V_{\ddot{O}}}^\sigma$ ($|z| = 2$): For 200 V *dc*-load ($E = 2.67$ MV/m), a hot stage set-temperature of 400 °C (assumed average sample temperature $T \approx 380$ °C) and $\tau_1 = 170$ s an $V_{\ddot{O}}$ -self-diffusion coefficient of $D_{V_{\ddot{O}}}^\sigma \approx 4.7 \times 10^{-11}$ cm²/s can be calculated. For $T_{set} = 450$ °C ($T \approx 410$ °C) and $\tau_1 = 30$ s, the same calculation with otherwise identical parameters leads to an $V_{\ddot{O}}$ -self-diffusion coefficient of $D_{V_{\ddot{O}}}^\sigma \approx 2.8 \times 10^{-10}$ cm²/s .

Chemical diffusion coefficient of oxygen In the relaxation Phase 2 the voltage is switched-off after the high-field stress and during the recovery process the conductivity increases exponentially into the direction of the initial starting value with the time constant τ_2 . Assuming that the relaxation time constant τ_2 represents a chemical (back)diffusion of oxygen to restore the initial homogeneous $V_{\ddot{O}}$ -distribution, the *chemical (ambipolar) diffusion coefficient of (neutral) oxygen* D_O^δ can be estimated from the definition of the diffusion length L_{D^δ} (inflection points of a GAUSS'ian diffusion distribution) [84]:

$$L_{D^\delta} = \sqrt{2 \cdot D^\delta \cdot t} \rightarrow D_O^\delta = \frac{(L_{D^\delta})^2}{2 \cdot \tau_2} \quad (4.11)$$

For full recovery of the complete layer ($L_{D^s} = L = 75 \mu\text{m}$) the *chemical diffusion coefficient* D_O^δ can be calculated for a set-temperature of 400°C ($\tau_2 = 2000 \text{ s}$) to be approximately $D_O^\delta \approx 1.4 \times 10^{-8} \text{ cm}^2/\text{s}$ and for $T = 450^\circ\text{C}$ ($\tau_2 = 400 \text{ s}$) to be $D_O^\delta \approx 7.0 \times 10^{-8} \text{ cm}^2/\text{s}$.

The calculated value for D_O^δ at 450°C is supported by a similar consideration utilizing the long-term thermal equilibration of a Nd:PZT(Cu)-layer, observed by HILLEBRAND in Fig. 4.7 [91]: From Fig. 4.7 it is possible to estimate a time constant of $\tau_{\text{eq}} \approx 20 \text{ h} \approx 72000 \text{ s}$ for the purely thermal defect-equilibration of the complete layer with the surrounding atmosphere (air). Since the stoichiometric change in this case is not perpendicular to the interdigit electrodes, but rather parallel to them, we have to replace L_{D^s} in Eq. 4.11 with the sample thickness ($d \approx 1.5 \text{ mm}$) and the factor 2 with the factor π^2 due to Ref. [84, 24]:

$$D_O^\delta = \frac{d^2}{\pi^2 \cdot \tau_{\text{eq}}} \quad (4.12)$$

This formula yields a *chemical diffusion coefficient of oxygen* $D_O^\delta = 3.2 \times 10^{-8} \text{ cm}^2/\text{s}$, which is well comparable to the value of $D_O^\delta \approx 7.0 \times 10^{-8} \text{ cm}^2/\text{s}$, calculated from the relaxation Phase 2.

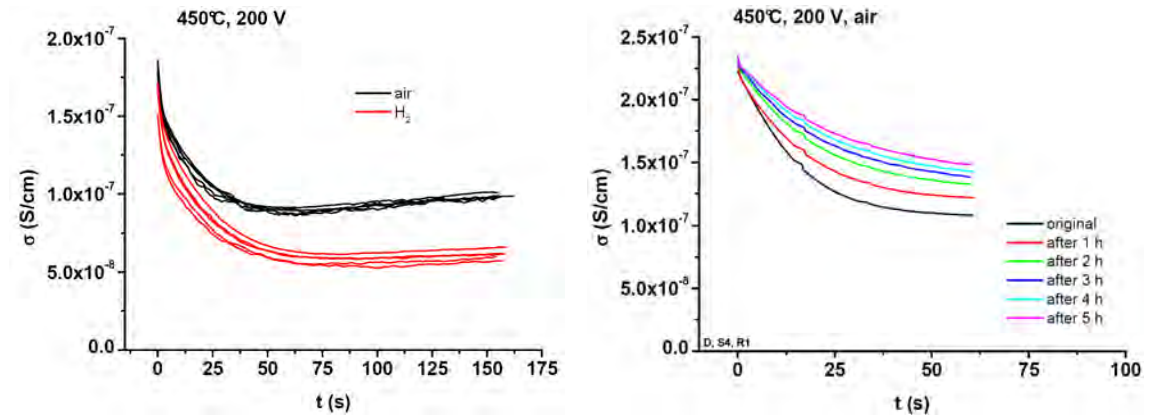
Comparison of diffusion coefficients Our calculated *chemical diffusion coefficients of oxygen* at 450°C ($D_O^\delta = 7.0 \times 10^{-8} \text{ cm}^2/\text{s}$ and $D_O^\delta = 3.2 \times 10^{-8} \text{ cm}^2/\text{s}$) are close to the extrapolated range of chemical diffusion coefficients reported in Ref. [46], which is $D_O^\delta \approx 1 \times 10^{-6} \text{ cm}^2/\text{s}$ for a similarly (positively donor) doped, but differently prepared (*air-fired* after sintering for 30 min at 850°C) Nb:PZT. So the smaller oxygen diffusion coefficients (higher $\text{V}_O^{\bullet\bullet}$ -concentration) in our (H_2 -sintered) Nd:PZT(Cu) might be due to the missing annealing step in air.

Even though our *self-diffusion coefficients of oxygen vacancies* ($D_{\text{V}_O^{\bullet\bullet}}^\sigma$) are more than two orders of magnitude smaller than our *chemical diffusion coefficients of oxygen* (D_O^δ), even *prima facie* both values are still feasible, since smaller values of $D_{\text{V}_O^{\bullet\bullet}}^\sigma$ than those of D_O^δ are a matter of fact and quite common in oxides [84]. But our calculated $\text{V}_O^{\bullet\bullet}$ -*self-diffusion coefficients* for 380°C ($D_{\text{V}_O^{\bullet\bullet}}^\sigma \approx 4.7 \times 10^{-11} \text{ cm}^2/\text{s}$) and for 410°C ($D_{\text{V}_O^{\bullet\bullet}}^\sigma \approx 2.8 \times 10^{-10} \text{ cm}^2/\text{s}$) are much smaller than those of slightly negatively (Fe-acceptor) doped SrTiO_3 ($\approx 1.5 \times 10^{-7} \text{ cm}^2/\text{s}$) and ($\approx 2.9 \times 10^{-7} \text{ cm}^2/\text{s}$),

respectively [5]. Maybe Eq. (4.10) might not be appropriate for calculation of $D_{V_O}^\sigma$, particularly, if fast oxygen transport mechanisms occur in or along grain boundaries.

4.2.6.3 Further arguments for stoichiometry polarization

Our model of stoichiometry polarization is further supported by the experimental observation of decreasing magnitude of the conductivity decrease at *repeated* high-field stress (Phase1) on one and the same Nd:PZT(Cu)-layer, cf. Fig. 4.28b and the stronger pronounced conductivity variations in H₂-atmosphere compared to air, cf. Fig. 4.28a, both observed by HILLEBRAND [91].



(a) Compared to air (black lines) the conductivity decrease during Phase1 is significantly more pronounced in H₂-atmosphere. (b) Six successive high-voltage experiments with one relaxation hour in between. The magnitude of the conductivity variation during Phase1 decreases with increasing number of repeated high-field load & relaxation cycles.

Figure 4.28: Phase 1 of short-term high-field conductivity experiments in air and H₂-atmosphere (a) and for repeated high-voltage stress (b). Source of both diagrams: [91].

In a multilayer PZT-stack strongly ion-blocking electrodes are certainly realistic, but complete oxygen blocking is not expected: At least close to the three phase boundary between atmosphere, PZT and electrode material, e. g. where Cu pores intersect with PZT, some oxygen exchange should be possible. Since a H₂-atmosphere is tantamount to a blocked cathodic oxygen reduction reaction (blocked O₂-incorporation), voltage application in reducing atmospheres may thus intensify the conductivity variation response, what actually was observed by HILLEBRAND cf. Fig. 4.28a. Moreover, the reaction rates of oxygen exchange at the anode and the cathode can easily differ also in air. Hence, the total amount of V_O^σ in the sample may vary during a

polarization experiment. In such a case, a subsequent polarization experiment (after a sufficient relaxation period) can be expected, to lead to a different conductivity development. Is, for example, the cathodic oxygen incorporation faster than the anodic oxygen release, than the total amount of V_{O} in the stressed layer would sustainably decrease during each polarization step. Such a situation might have been the cause for the diminishing magnitude of conductivity decrease observed for repeated Phase 1 high-field stress periods, observed by HILLEBRAND, cf. Fig. 4.28b.

To sum up, almost all experimental phenomena described in sec. 4.2 support our model of field-driven stoichiometry polarization of Nd:PZT(Cu), i. e. V_{O} migration and accumulation near the cathode (\ominus) and/or depletion near the anode (\oplus), leading to a conductivity decrease during high-field stress Phase 1. After switching-off the voltage a chemical diffusion relaxation process leads to a recovery of the conductivity during field-free Phase 2. Whether the assumed motion of oxygen vacancies V_{O} is predominantly in the grain interior (bulk) or along grain boundaries (e. g. in space charge layers) cannot be decided from these measurements. At least, there is evidence of enhanced oxygen diffusion along Nd:PZT grain boundaries in ^{18}O tracer exchange experiments above 600 °C [165]. However, also field-driven motion of lead vacancies, V_{Pb}'' , either in the bulk or at grain boundaries could lead to stoichiometry polarization and resulting conductivity variations. For reasons of the lower cation mobilities reported for related materials such as SrTiO_3 and BaTiO_3 [181], this alternative model was regarded as 2nd choice, although it could not have been excluded.

4.3 Long-term high-field stress and breakdowns (Phase 1 & Phase 2LT)

The typical behavior of the conductivity during a long-term degradation experiment (with high-voltage kept switched-on until electrical breakdown / breakthrough “BT”) was already illustrated for 450 °C and 200 V in Fig. 4.1. More than 70 % of long-term degradation experiments with high-voltages greater than 50 V showed a very similar behavior at temperatures between 350 °C and 500 °C: 42 of 60 experiments with various voltages ended with an electrical breakdown, meaning that suddenly the measured current increased to values higher than the current-limit of the Keithley Source-Measure-Unit (which is 100 mA in the voltage range to 200 V). *ac*-impedance or small-signal *dc*-measurements revealed post-breakdown resistances of $< 1 \text{ k}\Omega$, corresponding to extraordinarily high conductivities of $> 10^{-4} \text{ S/cm}$. Three long-term experiments ended with an electrical breakdown immediately after switching-on the high-voltage. 15 long-term experiments did not show an electrical breakdown during the duration of the experiment. This was observed especially at lower temperatures: At 350 °C not a single breakdown could have been provoked within the finite course of the measurements (up to 28 hours). Despite the missing breakdown, the measurements were aborted after displaying conductivity variations otherwise similar to Fig. 4.1. Since some of the 60 long-term experiments were conducted after relaxations (Phase 2) from previous high-field stress (Phase 1), most evaluation has been done on 42 explicit long-term degradation experiments on virgin Nd:PZT(Cu)-layers without any previous voltage stress.

4.3.1 Conductivity variations during Phase 2LT

As the long-term degradation behavior of the conductivity was *not* fitted with an analytical (e. g. exponential) function like the short-term conductivity variations in Phase 1 and Phase 2 (Eqs. (4.1)-(4.2)), an alternative characterization of the conductivity curves had to be defined: The time, when the conductivity minimum was reached will be termed t_{MIN} (related to τ_1 , but without analytical fitting); The time after which the experiment was stopped without any breakdown occurring is termed t_{FINAL} ; The time to a final breakdown is referred to as t_{BT} ; The conductivity values $\sigma_{LT}^0(\text{HV})$, $\sigma_{LT}^{MIN}(\text{HV})$, $\sigma_{LT}^{final}(\text{HV})$, $\sigma_{LT}^{BT}(\text{HV})$ refer to the first measured high-voltage conductivity value, the conductivity value at its minimum, the last mea-

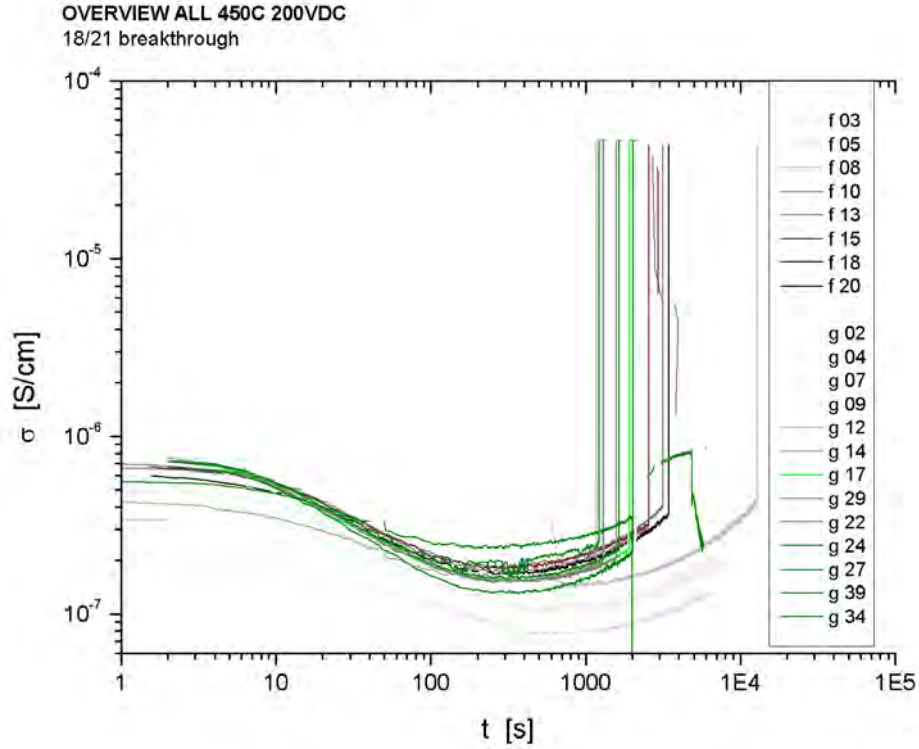


Figure 4.29: Selection of relevant long-term degradation experiments: Conductivity vs. time. All curves were recorded at 450 °C and under 200 V *dc*-load. The short non-continuous data segments represent low-voltage conductivity measurements. Green and gray colored curves represent different samples, the brightness within the curves of one sample represents the time at 450 °C (brighter = longer).

sured HV-conductivity before a measurement was aborted without breakdown, and the HV-conductivity value measured immediately before breakdown, respectively. In analogy to Eqs. (4.5)-(4.6) the magnitude of the overall conductivity change during long-term degradation experiments was defined as the ratio between the last measured (valid) conductivity value and the first measured conductivity value:

$$\text{delta2LT_final} = \frac{\sigma_{LT}^{\text{final}}(\text{HV})}{\sigma_{LT}^0(\text{HV})} \quad (\text{without breakthrough}) \quad (4.13)$$

$$\text{delta2LT_BT} = \frac{\sigma_{LT}^{\text{BT}}(\text{HV})}{\sigma_{LT}^0(\text{HV})} \cdot 100\% \quad (\text{breakthrough}) \quad (4.14)$$

Accordingly σ_{LT}^0 (LV), σ_{LT}^{MIN} (LV), σ_{LT}^{final} (LV), σ_{LT}^{BT} (LV) are the corresponding conductivities of small-signal (low-voltage) measurements, before and after high-voltage was applied, respectively.

Since the first conductivity decrease (Phase 1) of long-term degradation experiments is quite fast compared to the slower conductivity increase in Phase 2LT a logarithmic plot of time on the x -axis was chosen. A selection of 21 long-term degradation experiments at 450 °C under 200 V is illustrated in Fig. 4.29.

Obviously the conductivity minima were reached within the first 220 ... 800 s (t_{MIN}). At 450 °C and 200 V 18 of the 21 long-term degraded samples in Fig. 4.29 showed a breakdown within ~6 hours. The breakdown mostly occurred in the time range between 1 200 s and 3 000 s (t_{BT}). The ratio “delta2LT_BT” (Eq. (4.14)), indicating the extent (magnitude) of the conductivity change from the very beginning of the long-term high-voltage degradation (σ_{LT}^0 (HV)) until shortly before breakdown (σ_{LT}^{BT} (HV)) is scattering between 0.29 and 0.78.

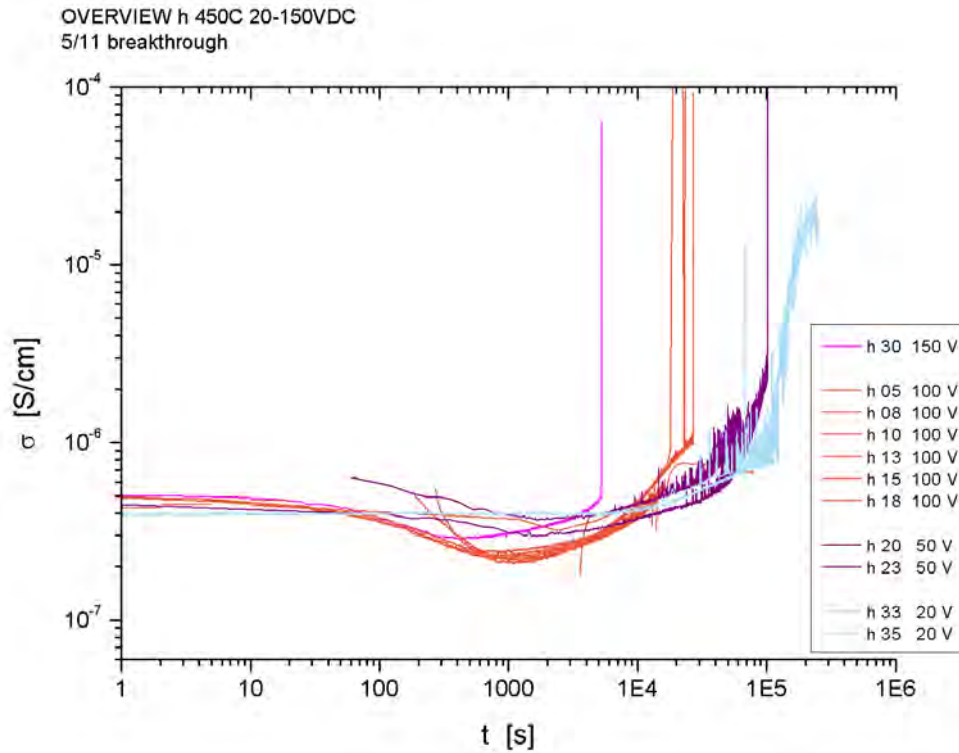


Figure 4.30: Long-term conductivity degradation at 450 °C. Influence of voltage: 150 V (pink); 100 V (orange); 50 V (violet); 20 V (cyan).

The influence of voltage on the conductivity in long-term degradation experiments

at 450 °C is illustrated for one sample in Fig. 4.30:

While the 150 V curve ($t_{BT} \approx 5\,300$ s; $\Delta 2LT_BT = 1.07$) is still close to the 180 V (not shown) and 200 V (Fig. 4.29) curves, the tendency to later (and less) breakdowns and increased magnitudes “ $\Delta 2LT_BT$ ” for decreasing voltage is obvious: At $U = 100$ V only four of eight experiments ended in a breakdown (average breakdown time $t_{BT} \approx 17\,000$ s). Only one of two experiments at 50 V ($t_{BT} = 102\,540$ s) and none at 20 V showed a breakdown. The magnitude of the overall conductivity change (without breakthrough) “ $\Delta 2LT_final$ ” turns to values > 1 (corresponding to an overall conductivity gain, rather than loss); for 50 V and 20 V “ $\Delta 2LT_final$ ” values are in the range of 1.59 up to 46.8.

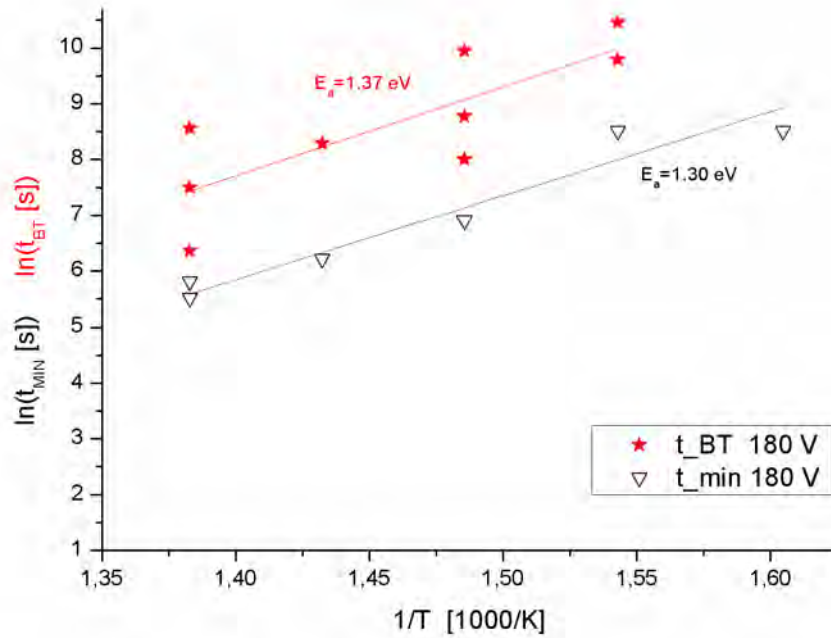


Figure 4.31: t_{MIN} (black) and t_{BT} (red) vs. $1/T$ for the 180 V series of long-term degradation experiments. Straight lines are linear fit functions.

In Fig. 4.31 t_{MIN} and t_{BT} for the 180 V series are plotted against the inverse temperature $1/T$. The time period until the conductivity minimum is reached (t_{MIN}) displays an activation energy of $E_a = 1.30$ eV. The time period until breakdown (t_{BT}) is similarly activated with $E_a = 1.37$ eV. Both are close to the ARRHENIUS-activated behavior of τ_1 which was 1.52 eV for 180 V; The activation energy of the recovery time constant (Phase 2) τ_2 was only 0.82 eV for 180 V and thus significantly smaller,

see Tab. 4.1.

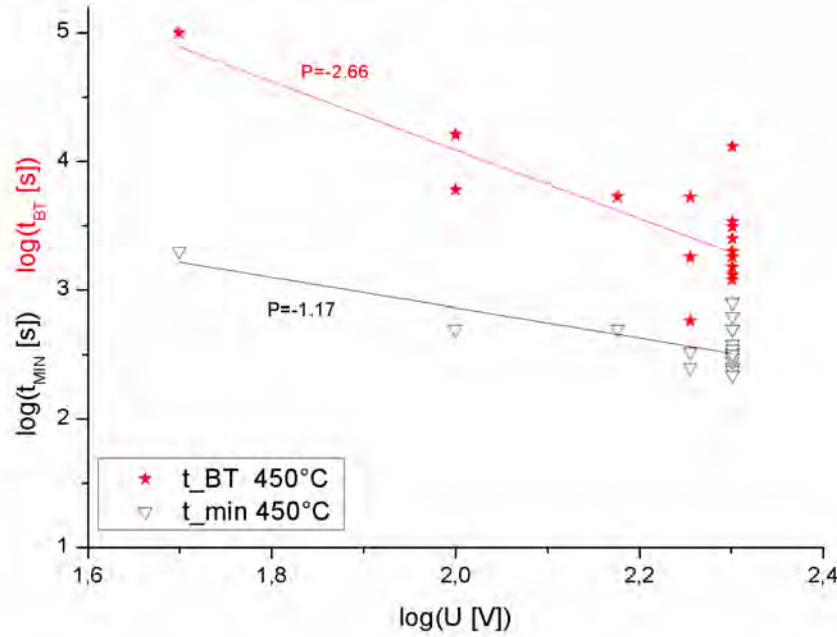


Figure 4.32: $\log(t_{MIN})$ (black) and $\log(t_{BT})$ (red) vs. $\log(U)$ at 450 °C. U varies from 50 V to 200 V. Straight lines are linear fit functions.

In Fig. 4.32 the values of t_{MIN} and t_{BT} for 450 °C are exemplarily plotted against the values of the degradation voltage U in a double-logarithmic plot. Analog to Fig. 4.11 t_{MIN} and t_{BT} were fitted with a power law functions $t \propto (U)^P$, cf. Eq. (4.7). The power-law exponent P of t_{MIN} is $P = -1.17$ which is close to that of τ_1 ($P = -1.26$ for 450 °C). The power-law exponent of the time until breakdown t_{BT} is $P = -2.66$ and leads to a much steeper dependency of t_{BT} with respect to U .

Similar to the results for the short-term experiments, the trends became much less clear at lower temperatures: Neither an unambiguous ARRHENIUS-activation energy, nor the power-law voltage-dependencies of t_{MIN} and t_{BT} could be determined at lower temperatures, cf. Fig. 4.33a.

Long-term experiments on previously short-term stressed layers Long-term degradation experiments conducted even after one (or more) previous short-term high-field experiments showed the same behavior: Reduced long-term degradation voltage increases the magnitude of the overall conductivity gain up to 289%

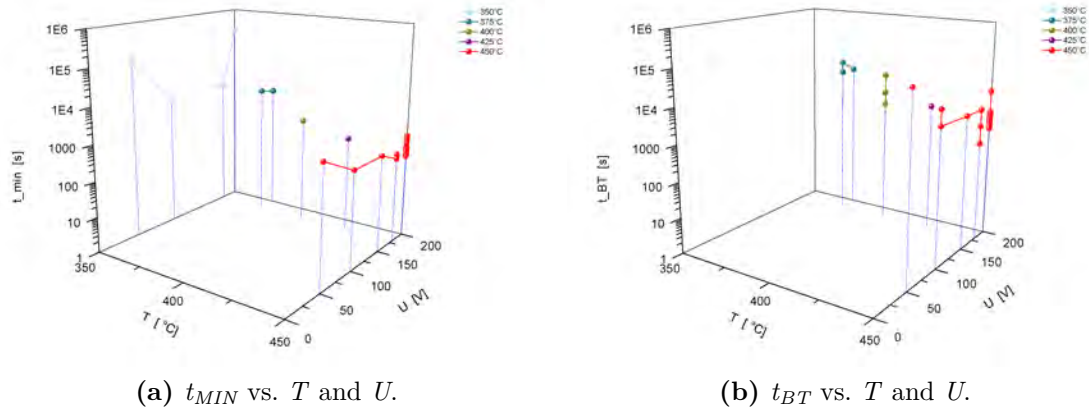


Figure 4.33: Long-term degradation: Dependencies of t_{MIN} and t_{BT} on temperature T and degradation voltage U .

($\Delta_{2LT_BT} = 2.89$, for 100 V, Fig. 4.2; $\Delta_{2LT_BT} = 2.06$, for 50 V, Fig. 4.34b), also in other respects no significant differences seem to appear at long-term degradation experiments after previous short-term high-field experiments on one and the same layer (Fig. 4.34).

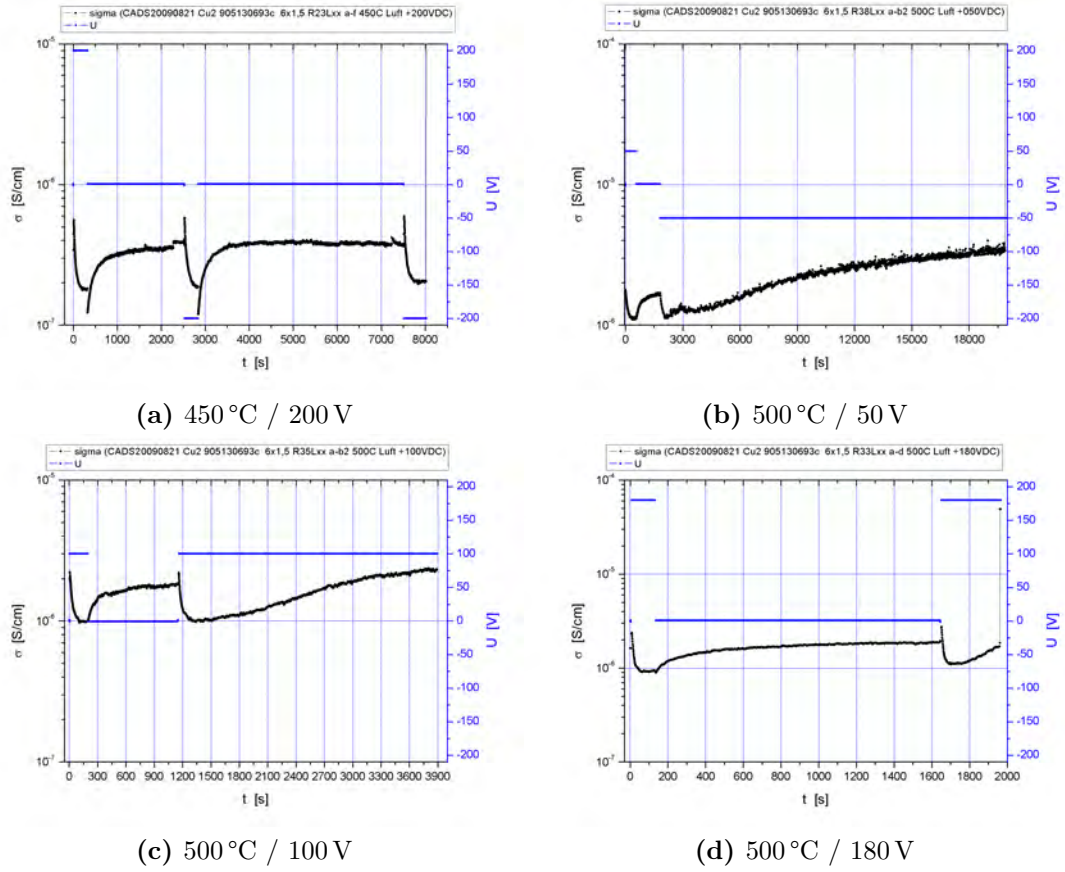


Figure 4.34: Examples of long-term degradation experiments after one or two previous short-term high-field experiments on one and the same layer. Note the linear time-scale on the x -axis.

4.3.2 Conductivity variations *after* Phase 2LT

On some long-term degraded samples *post*-Phase 2LT measurements were conducted at 450 °C: Immediately after each single long-term degradation experiment a small-signal (low-voltage) conductivity was measured. Also after several Nd:PZT(Cu) layers have been subjected to long-term degradation experiments, all of the previously stressed layers were measured again at the same temperature. Since re-contacting of the (crater- and CuO-) damaged surface of the interdigit electrodes turned out to be difficult, some few micrometers ($< 50 \mu\text{m}$) were polished off, to enable a recontacting of the electrodes.

4.3.2.1 Long-term degraded samples *without* electrical breakdown

A smaller number of long-term degradation experiments (15 of 60) did not end up in an electrical breakdown. This experiments were aborted by switching-off the high-voltage after time-periods within which other samples already had displayed electrical breakdowns. Of course, that does not mean, that those layers would have never shown a breakdown; The experiments were aborted for reasons of time-efficiency. Subsequent small-signal (low-voltage) conductivity measurements (EIS and/or *dc*) revealed, that the conductivity value immediately after the high-field stress $\sigma_{\text{LT}}^{\text{final}}(\text{LV})$ was close to the final high-voltage conductivity value $\sigma_{\text{LT}}^{\text{final}}(\text{HV})$ (with a small offset to lower values due to non-linearity already mentioned in sec. 4.1.7).

Most impedance plots showed good agreement with R//CPE equivalent-circuit fitting, cf. Fig. 4.35 and acceptable deviations from ideality ($n > 0.8$ in Eq. (2.68)). The reason for the strange shape of the red impedance “semicircle” (immediately after switching-off the previously applied 200 V) in Fig. 4.35 might be a first hint to a purely thermal recovery from the long-term conductivity variation: Since the small frequencies probe predominantly the ohmic fraction of the impedance, temporal variations of the resistance during impedance recording may be most reflected at the lowest frequencies. For that reason the red semicircle in Fig. 4.35 is heavily distorted and even bends at 1 Hz, reflecting a relatively rapid increase of conductivity. The thermal recovery of the previously distorted conductivity was also verified by small-signal *dc*-measurements and will be discussed in the following paragraph.

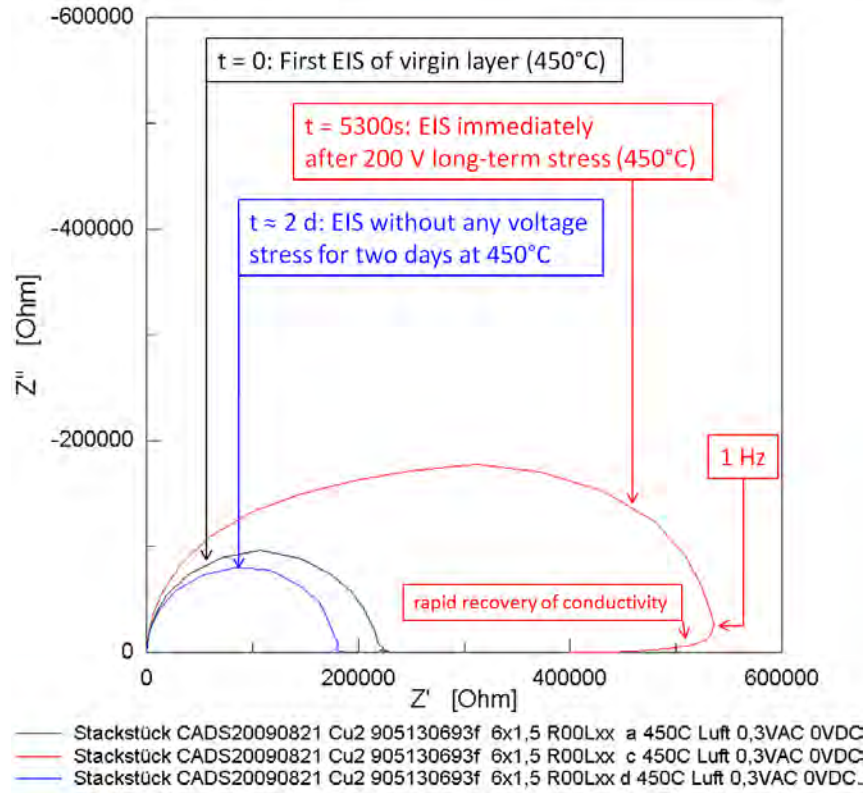


Figure 4.35: Impedance spectra (NYQUIST-plot) of a long-term degraded Nd:PZT(Cu) layer, which did not show any breakdown (measurement aborted). Black: Impedance of virgin layer ; Red: Immediately after long-term high-voltage stress (5300 s); Blue: After two days at 450 °C without any voltage stress.

Reversibility After switching-off the high-voltage before any breakdown a purely thermal relaxation in the direction of the initial conductivity starting value before any high-field stress σ_{LT}^0 (LV) was observed. This relaxation took place even without any polishing process, which might have removed any superficial layer with a different conductivity.

In Fig. 4.36 the high-field was switched-off at ≈ 8000 s without any breakdown occurring ($T = 450^\circ\text{C}$). The small-signal *ac*-conductivity seems to recover from its distorted value immediately after breakdown to a value close to the initial starting conductivity of the virgin layer after approximately 30 000 s at 450 °C.

In Fig. 4.37 the conductivity relaxation of an interrupted long-term degradation experiment at 450 °C (without breakdown) is resolved even better: After ≈ 14000 s of 100 V long-term degradation the high-field stress was switched-off and an immediate subsequent conductivity relaxation under small *dc*-signal was monitored for

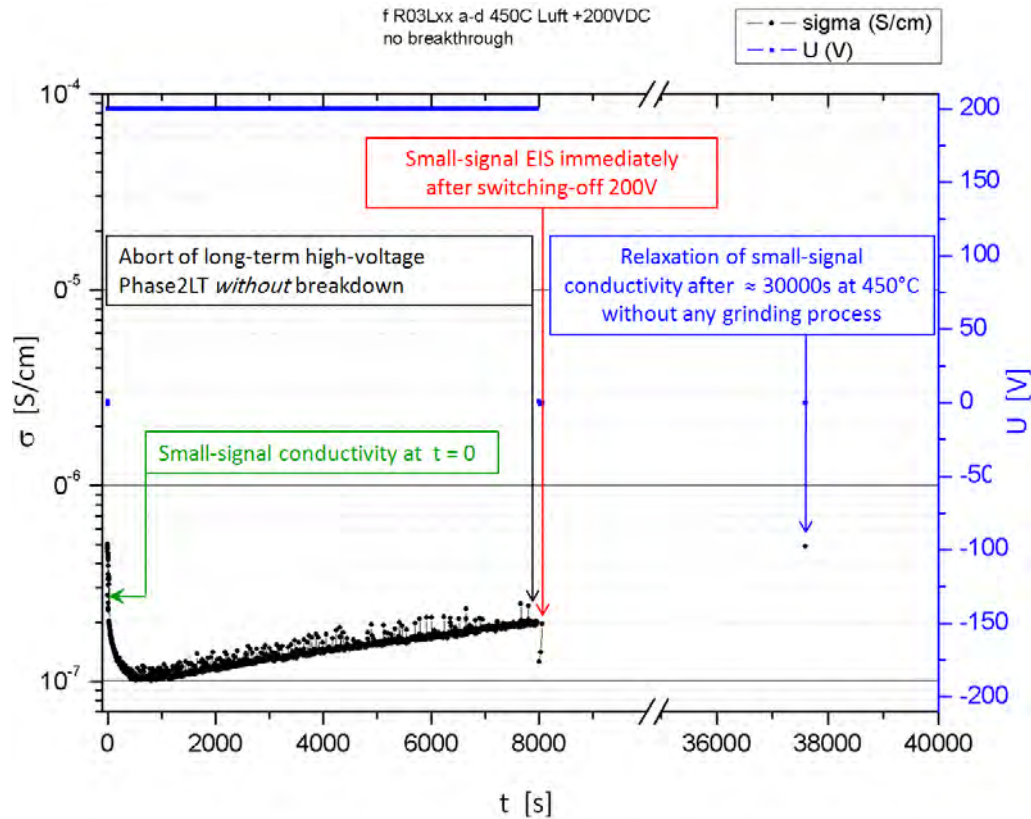
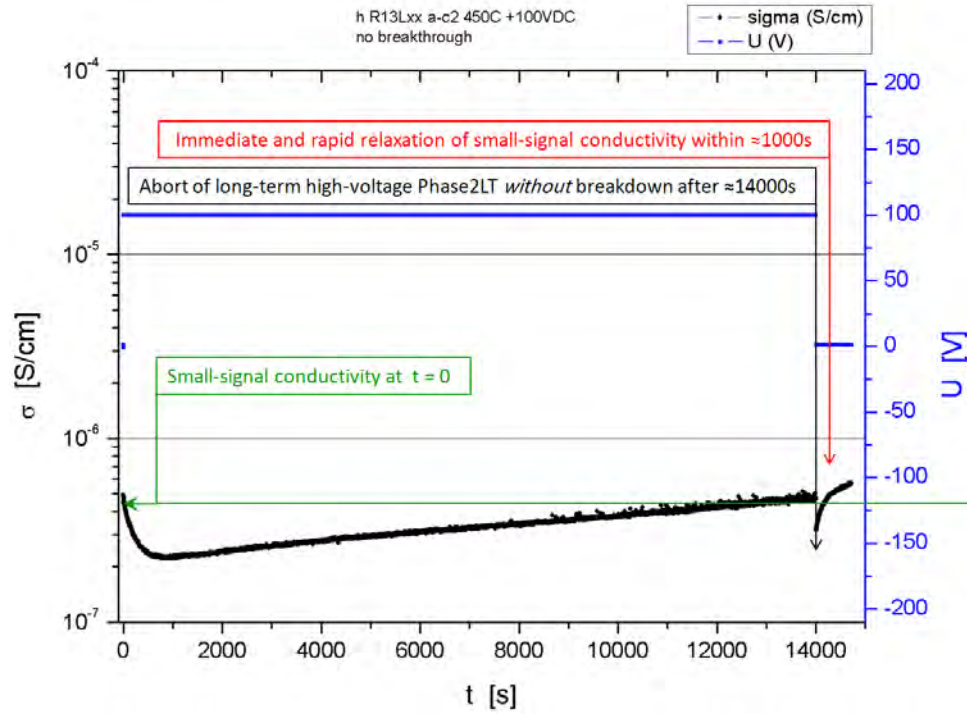
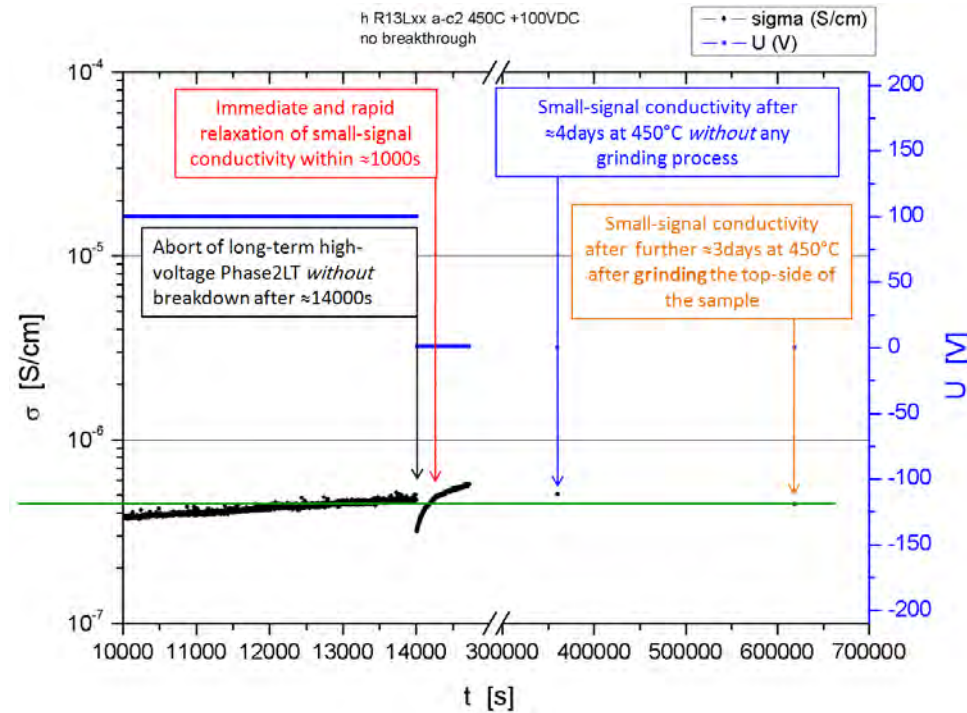


Figure 4.36: Relaxation of non-breakdown long-term degradation. - A relatively low conductivity $\sigma_{LT}^{final}(HV)$ at the end of the high-field stress relax to a higher value after ca. 30000 s.

≈ 1000 s, cf. Fig. 4.37a. After this, other layers on the same sample were investigated, so the next check of *ac*-conductivity was done after ≈ 4 days (sustained at 450°C), which showed only a slight conductivity deviation compared to the last *ac*-conductivity value of the monitored relaxation process. Further ≈ 3 days later (sustained at 450°C) and after grinding-off some μm from the top-side of the sample a final *ac*-conductivity measurement at 450°C yielded a slightly further decreased conductivity, incidentally exactly equal to the *ac*-conductivity starting value of the virgin layer before any high-field load was applied, cf. Fig. 4.37b.



(a) After switching-off the high-field, the small-signal conductivity increases from its nonlinear offset value to a value close to the conductivity of the virgin layer σ_{LT}^0 (LV).



(b) Continuation of Fig. 4.37a. The relaxed post-breakdown conductivity stays constant after some days and even after grinding off a superficial layer.

Figure 4.37: Long-term experiment interrupted before any breakdown and subsequent relaxation behavior.

4.3.2.2 Long-term degraded samples *with* electrical breakdown

42 of 60 long-term degradation experiments on Nd:PZT(Cu) layers ended in an electrical breakdown. Since the electrical breakthrough was detected (and defined) by a sudden increase of current into the *current limit* of the Source-Measure-Unit, a subsequent low-voltage conductivity measurement was necessary, to determine the true conductivity $\sigma_{LT}^{BT}(LV)$. Only on 26 samples the *post-breakdown* behavior was further analyzed. However, two classes of such *post-breakdown* conductivities could be identified:

a) Temperature dependent short-circuits: Most samples with an electrical breakdown (22 of 26) showed extraordinarily high (small-signal) conductivity values in the range of $\sim 3 \times 10^{-4} \text{ S/cm}$ ($\sim 280 \Omega$) up to $\sim 1 \times 10^{-2} \text{ S/cm}$ ($\sim 10 \Omega$) immediately after breakdown at 450°C , measured by the very same contacting setup as used for high-field stress (i.e. with one and the same needle-pair still contacting the sample). However, in a later re-measurement series of these Nd:PZT(Cu)-layers new needles were used, hence a recontacting of the interdigit electrodes took place. In these measurements (small-signal) conductivity values in the range of $\sim 4 \times 10^{-7} \text{ S/cm}$ ($\sim 200 \text{ k}\Omega$) to $\sim 2 \times 10^{-6} \text{ S/cm}$ ($\sim 40 \text{ k}\Omega$) were found at the same temperature (450°C). Obviously a certain relaxation had taken place, while the samples were kept at 450°C for several hours between these two measurements. Although the initial current breakthrough supposedly indicates an irreversible electrical short-circuit, this kind of post-breakdown conductivities turned out to be rather temperature dependent: Those Nd:PZT(Cu)-layers which exhibited a resistance in the order of $\text{k}\Omega$ after recontacting at 450°C had at room temperature ($\sim 22^\circ\text{C}$) immeasurably high resistances ($> 10^8 \text{ k}\Omega$ / $> 10^{-11} \text{ S/cm}$), see Fig. 4.38:

The first post-breakdown impedance spectrum (Fig. 4.38b) shows almost pure inductive behavior (most probably from the cables). However, the impedance spectra before (Fig. 4.38c) and after (Fig. 4.38e and Fig. 4.38f) polishing-off $40 \mu\text{m}$ and further $50 \mu\text{m}$, respectively, again correspond to quite similar R//CPE equivalent circuits. A thermal activation of this post-breakdown conductivity was concluded from the immeasurable small conductivity at room temperature, cf. Fig. 4.38d.

Reversibility Strong indications of a thermal relaxation of the post-breakdown high conductivity values were found: While the first measurement immediately af-

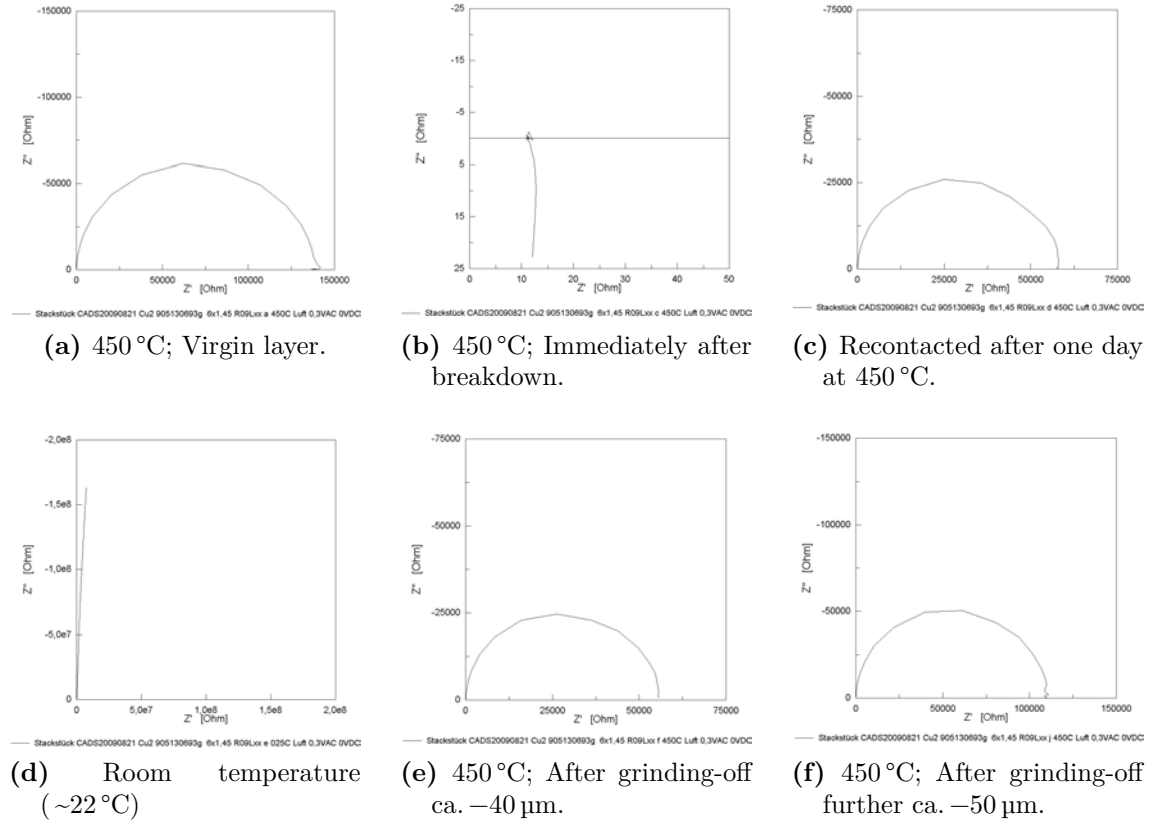


Figure 4.38: Thermally activated post-breakdown conductivity: NYQUIST-plots of a Nd:PZT(Cu) layer at 450 °C.

ter the breakdown (with the originally contacted needle-tips) showed true short-circuit conductivities ($\leq 10^{-4}\ \text{S/cm}$), cf. Fig. 4.38b, subsequent measurements by recontacting with new W-tips after about one day later at 450 °C showed strongly decreased conductivity values close to the initial starting value of the virgin layer ($\sim 10^{-6}\ \text{S/cm}$), cf. Fig. 4.38c. At room temperature, however, the conductivity was immeasurably small ($R \gg 10^9\ \Omega$, $\sigma \ll 10^{-11}\ \text{S/cm}$), cf. Fig. 4.38d. A (first) polishing step (ca. $-40\ \mu\text{m}$) did not change the conductivity significantly, cf. Fig. 4.38e. After a second polishing step (ca. $-50\ \mu\text{m}$) a further reduction of conductivity still closer to the virgin starting-value $\sigma_{\text{LT}}^0(\text{LV})$ (Fig. 4.38a) was observed, cf. Fig. 4.38f. Since no continuous thermal relaxation measurements on post-breakdown layers have been conducted, it can not be definitely decided, whether this final conductivity drop was due to the second polishing step or due to the further progressing relaxation process. However, as the first polishing step did not influence the conductivity anyhow, a purely thermal relaxation behavior of this type of breakdowns

seems to be more likely. This idea is also supported by HILLEBRAND, who did regular EIS-measurements during such a relaxation of a post-breakdown Nd:PZT(Cu) layer [91].

A typical development of conductivities of this breakdown-type is illustrated in Fig. 4.39.

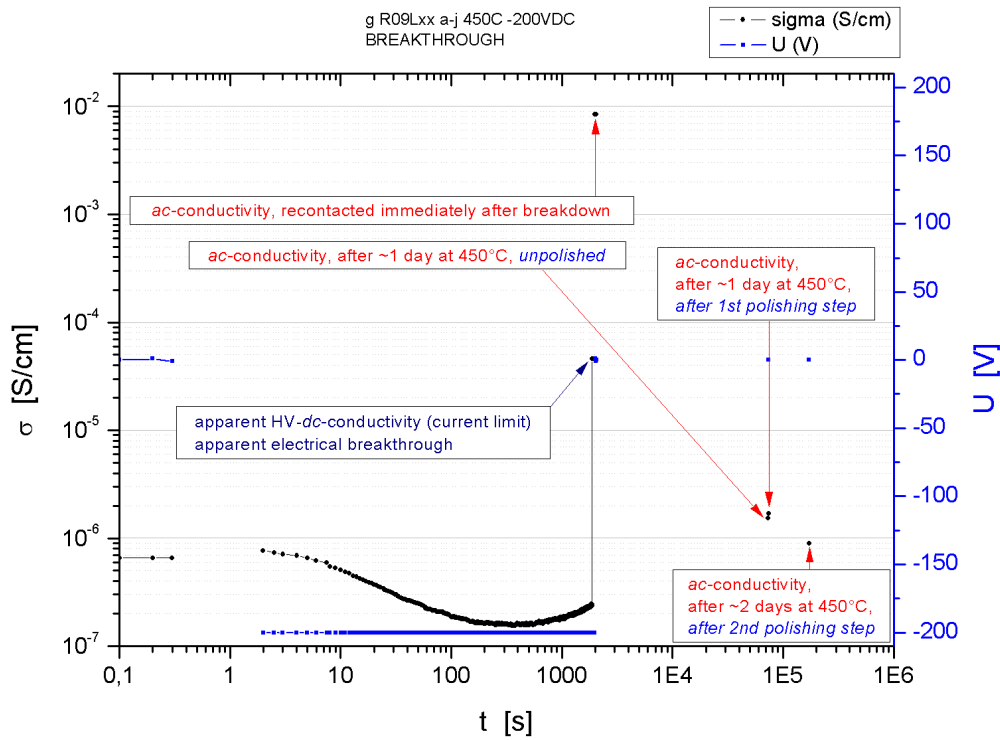


Figure 4.39: Thermally activated post-breakdown conductivity: Conductivity behavior of a 75 μm Nd:PZT(Cu)-layer before, during and after high-field stress (200 V, 450 $^{\circ}\text{C}$).

A rare exception from this type of post-breakdown behavior will be mentioned in the following paragraph.

b) Temperature independent short-circuits: Only 4 of 26 post-breakdown Nd:PZT(Cu) layers showed extraordinarily high conductivities in the range of $>10^{-4}$ S/cm ($20\ \Omega$ to $60\ \Omega$) not only immediately after breakdown, but *still after approximately one hour at 450 $^{\circ}\text{C}$ and even at room temperature.*

The corresponding impedance spectroscopy NYQUIST-plots did no longer show semi-circles, but rather a purely ohmic offset and some small inductive deviations (most

probably from the cables) at all temperatures, see Fig. 4.40.

Reversibility The (small-signal) *ac*-conductivity values of this type of post-breakdown short-circuits virtually did *not* change by simple holding the temperature (450 °C). Even a first grinding step (−30 μm, −50 μm, respectively) did not change the conductivity. However, after further 50 μm were polished-off in the next grinding step, the short-circuit has vanished and the conductivity is suddenly restored close to its virgin value before any high-field stress.

The typical development of post-breakdown behavior of this second type is illustrated in Fig. 4.41.

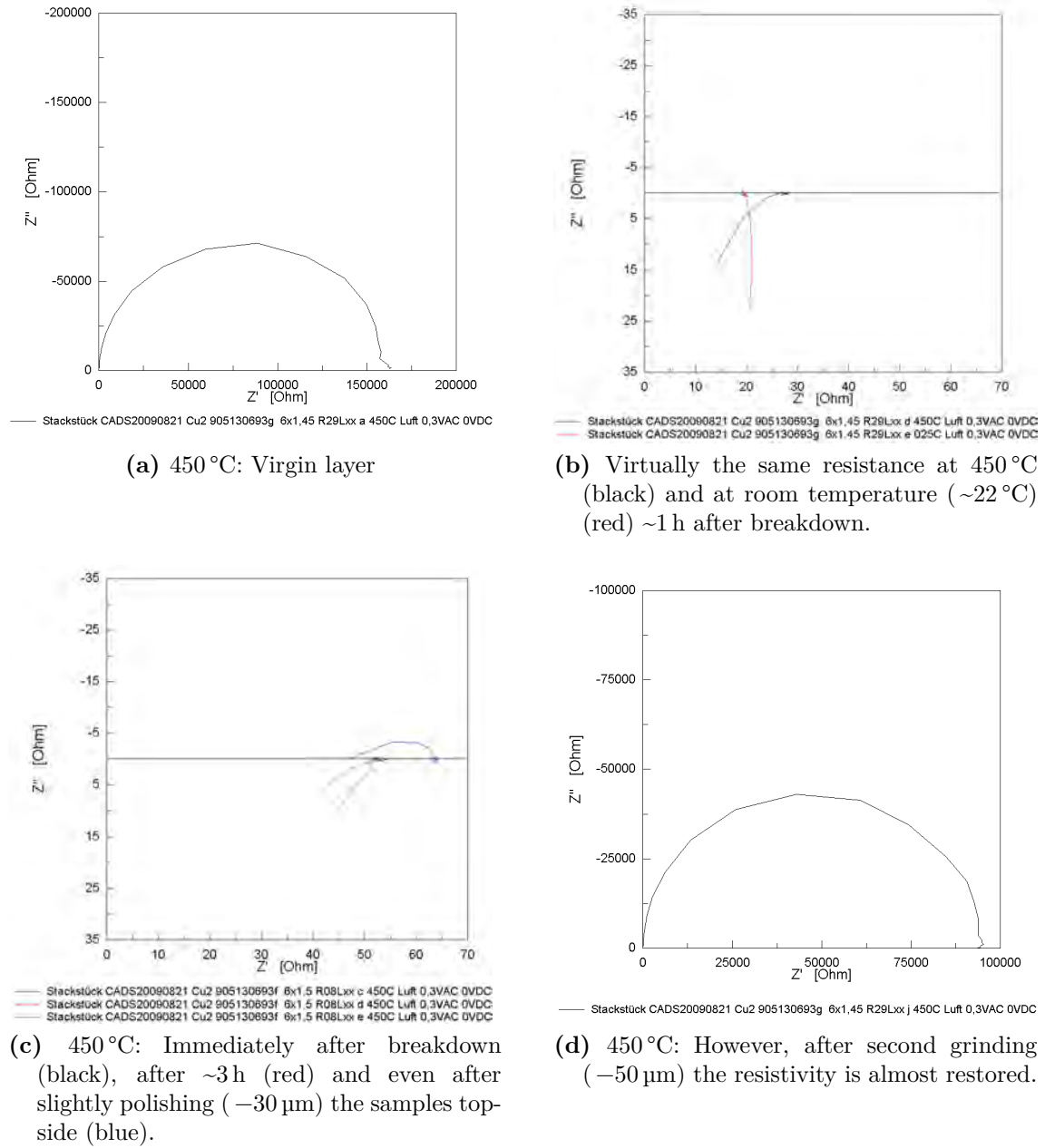


Figure 4.40: Temperature independent post-breakdown conductivity: NYQUIST-plots of a Nd:PZT(Cu) layer at 450 °C and at room temperature.

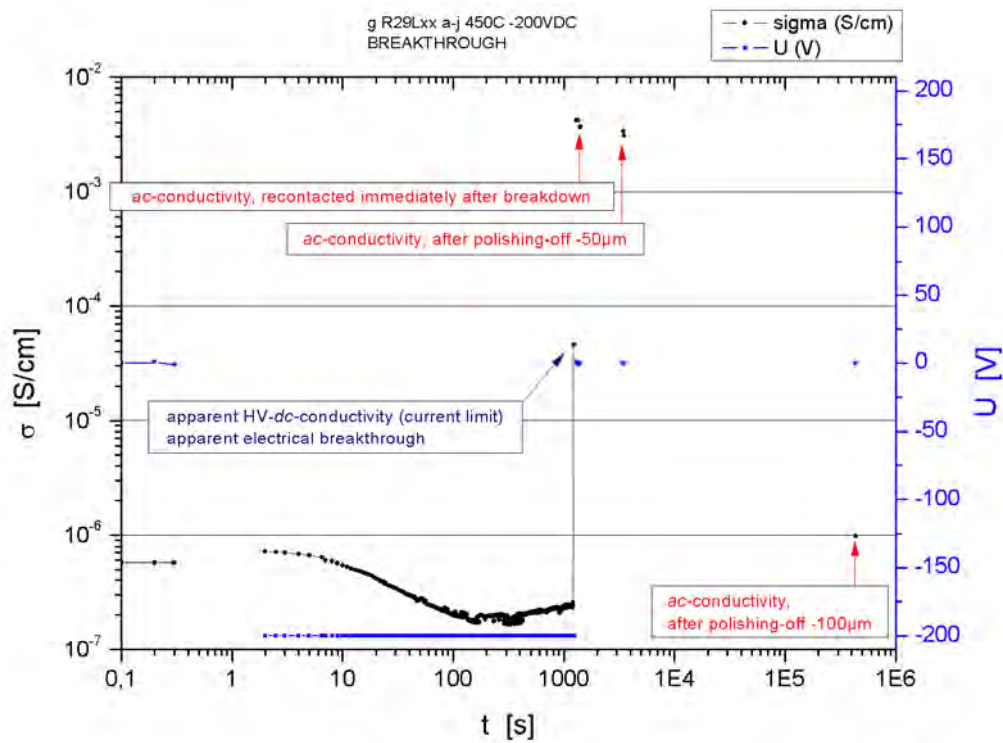


Figure 4.41: Dependency of a highly conducting temperature independent post-breakdown conductivity on superficial grinding processes: After the first 50 μ m being grinded-off no significant conductivity change could be observed, but after removing further 50 μ m, the conductivity is suddenly restored to a value close to its virgin conductivity before any high-field stress.

4.3.3 Optical and chemical features - Blackening, craters and Cu-precipitates

The optical darkening phenomenon of *blackening* continues during Phase 2LT after already having started in Phase 1 (cf. sec. 4.2.4). Investigation through the (dark-field) microscope seems to indicate a further intensification of the blackening during long-term degradation Phase 2LT, although the initially decreasing conductivity starts to increase again in Phase 2LT. Another phenomenon, actually indicating the end of Phase 2LT of long-term degradation experiments, is the creation of *craters*: If an electrical breakdown occurred, it was (with only five exceptions in more than 60 experiments) accompanied by smaller or bigger craters, mostly on the sample surface at the contact point of the W-tips or on any other surface region of the stressed Nd:PZT(Cu)-layer, on the top-side or (less often) on the bottom-side of the sample. An extensive investigation of craters on Nd:PZT(Cu) can be found in [91]. Some impressions of long-term triggered blackening and craters are given in Fig. 4.42.

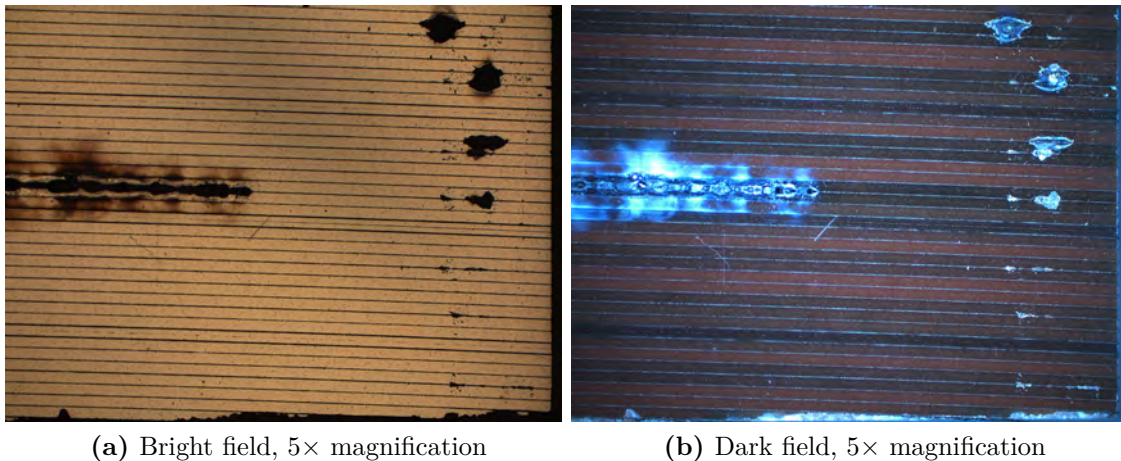


Figure 4.42: Micrographs of the top face of an unpolished Nd:PZT(Cu) sample after long-term degradation experiments. Interestingly “blackening” seems to be visible only in the dark field mode (b).

4.3.3.1 Blackening

Although the blackening effect is excellently visible in the dark-field mode of the microscope but hardly identifiable in bright-field, blackened piezolayers can also be recognized with the bare eye.

Since the most intensive blackening was found on the Nd:PZT(Cu) layers subjected to voltage for the longest time (e. g. for only 20 V and ~61 h ($\sim 220\,000$ s) at 450 °C), and not on layers subjected to the greatest voltage, it is concluded, that blackening is more likely to be related to the long-term Phase 2LT than to the stoichiometry polarization found during short-term degradation Phase 1. Blackening intensified continuously and usually very homogeneously along the stressed layer with time under *dc*-voltage load. Any kind of moving front of a blackened region from one electrode to the other was never observed. Also with respect to the depth, it was not found that blackening was reduced within the first ~100 μm grinded-off from the sample. However, HILLEBRAND found, that thermally weakened blackening (e. g. after 65 h at 450 °C) turned out to appear again after grinding-off 90 μm of the sample's surface [91].

4.3.3.2 Craters

The craters appeared simultaneously with the electrical breakdown. Most craters occurred at the contact interface of W-tip and interdigit electrode. This is illustrated in Fig. 4.43 for the unpolished top-side of a Nd:PZT(Cu) sample after some long-term degradation experiments.

Obviously the point of contact between W-tip and interdigit electrode seems to be a likely starting position for craters. Other (additional or unique) craters were sometimes observed in some distance from the needle-tip contacting point.

Some breakdowns were accompanied by (additional or unique) craters on the downward back-side of the sample. The bottom-side of the sample in Fig. 4.43 is shown in Fig. 4.44.

Usually a single crater did not only spread along the directly contacted interdigit electrode, but the crater mostly included parts of one or both oppositely charged counter-electrodes. However, some (electrical) breakdowns did not result in any visible crater at all.

4.3.3.3 Cu-precipitates

Since the surface of long-term degraded Nd:PZT(Cu) samples was heavily distorted by craters, some 30 μm ... 50 μm were occasionally polished-off for further investiga-



Figure 4.43: Long-term high-voltage induced craters on the upper top-side of a Nd:PZT(Cu) sample. Note that most craters are close to the contact point between W-tip and electrode (pink ellipses).

tion. Precipitates of Cu were found in the regions of some craters, but in any case *offside* the interdigit electrode line, cf. Fig. 4.45.

The Cu precipitates were verified by energy-dispersive X-ray spectroscopy (EDX) during scanning electrode microscopy (SEM) investigations, cf. Fig. 4.46.

By the very same SEM/EDX method, no measurable difference in the composition of a high-field blackened and a virgin Nd:PZT(Cu) layer was found (offside crater regions), cf. Fig. 4.47.

By multiple polishing procedures HILLEBRAND investigated the development of the craters along the z -direction, meaning into the depth of the samples. He found, that some craters have obviously melted through the complete sample thickness, being connected with a crater on the other (bottom) side of the very same Nd:PZT(Cu) layer. Further HILLEBRAND stated, that in air most craters are created at the upper top-side of the sample, while in H_2/Ar atmosphere many craters also arose on the downwarded bottom-side of the samples [91].

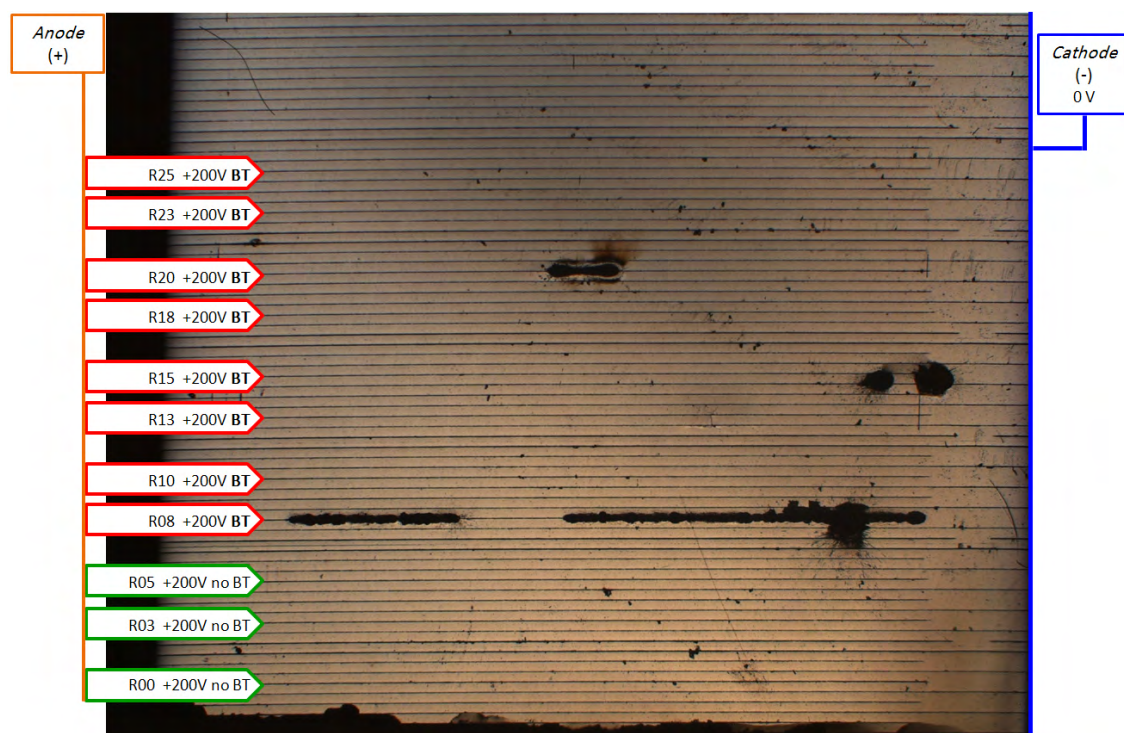
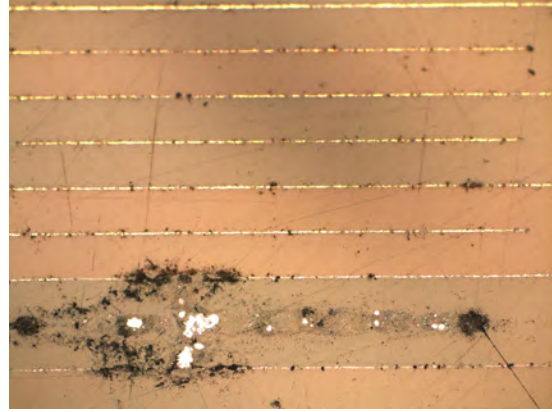


Figure 4.44: Long-term high-voltage induced craters on the downwarded bottom-side of a Nd:PZT(Cu) sample.



(a) Microsection of crater centered around an anodically (+200 V) polarized interdigit Cu-electrode. Polished top-side of the sample. Breakdown after 12 170 s.



(b) Microsection of another crater centered around an anodic (+200 V) interdigit. Polished bottom-side of the sample.

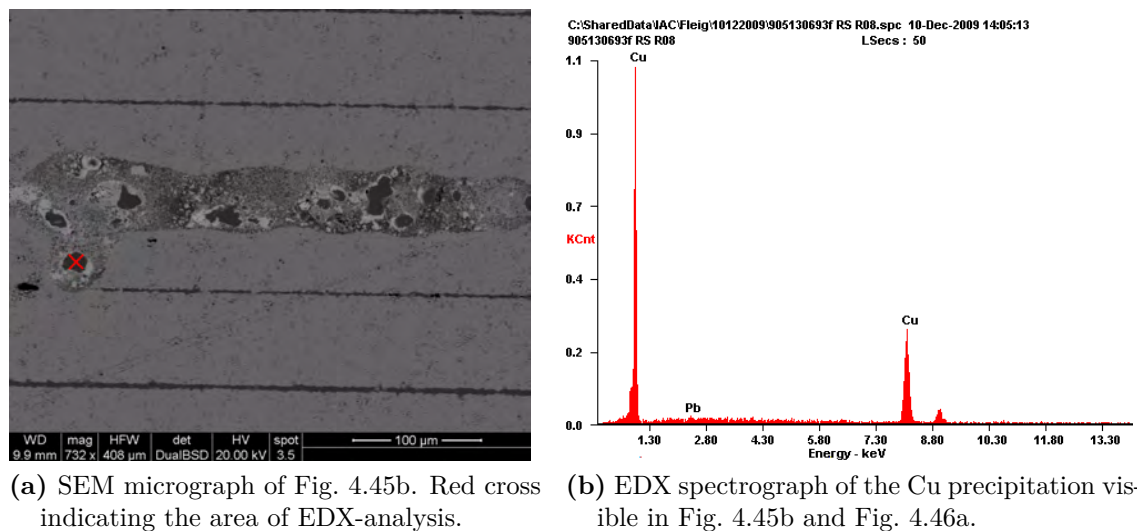


(c) Microsection of crater: The contact tip was previously attached on the lower Cu interdigit electrode, where an cathodic voltage (-200 V) was applied. Polished top-side of the sample. Breakdown after 1 300 s.



(d) Microsection of crater: The contact tip was previously attached on the lower Cu interdigit electrode, where a cathodic voltage (-200 V) was applied. Polished top-side of the sample. Breakdown after 1 640 s.

Figure 4.45: Four different Cu precipitates offside the Cu interdigit electrodes on three different Nd:PZT(Cu) layers. All breakdowns occurred at 450 °C and $|U| = 200$ V.



(a) SEM micrograph of Fig. 4.45b. Red cross indicating the area of EDX-analysis. (b) EDX spectrograph of the Cu precipitation visible in Fig. 4.45b and Fig. 4.46a.

Figure 4.46: Analysis of the Cu precipitates in one crater by means of (a) scanning electrode microscope (SEM) and (b) energy dispersive X-ray spectrography (EDX).

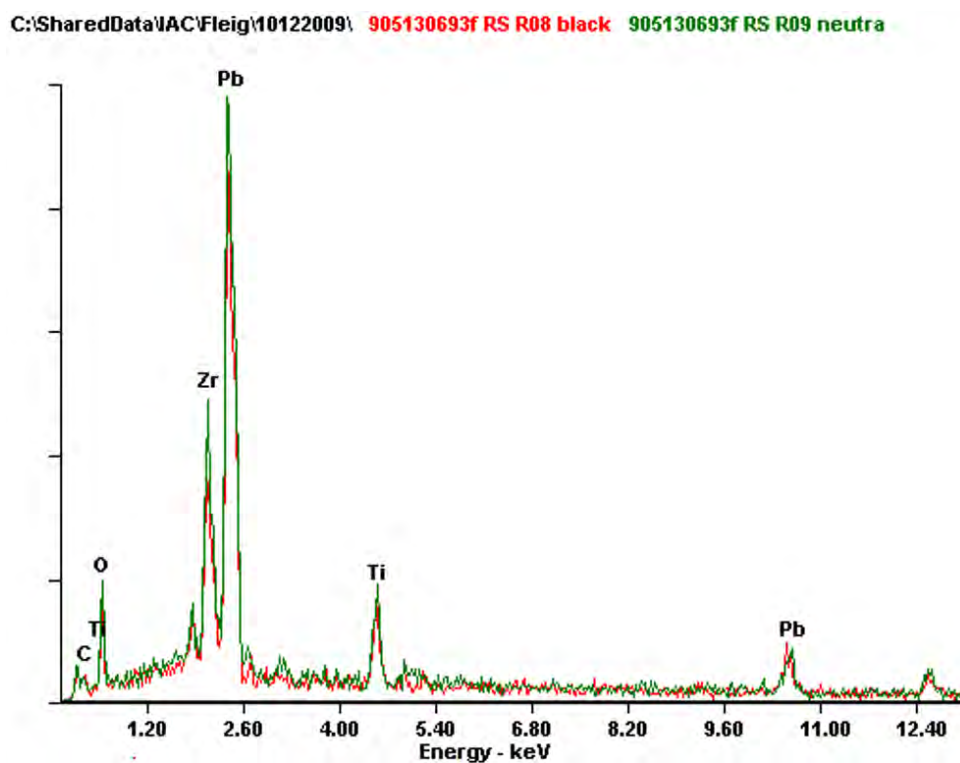


Figure 4.47: EDX spectra of a voltage-blackened (red) and a virgin (green) Nd:PZT(Cu) layer.

4.3.4 Discussion of Phase 2LT and breakdowns

To the best of the authors knowledge, there is no theoretical model for the long-term degradation behavior and the post-breakdown conductivity variations, described in sec. 4.3, available.

The Cu precipitates found after breakdowns might indicate some kind of metallic short-circuiting, especially for the temperature-independent type of breakdowns. However, it is difficult to use this explanation for the temperature-dependent breakdown type, as it is not expected for a metallic path to be destroyed continuously at 450 °C and to show a strong temperature dependency. Hence, for the temperature-dependent breakdown type (sec. 4.3.2.2-a) a model has to be found, which explains the continuous “self-healing” behavior shown in Fig. 4.39. Maybe another type of stoichiometric change, e. g. V''_{Pb} -migration, might play a role. At least for Nd:PZT(AgPd) Pb precipitates were found within long-term degraded layers, cf. chapter 5.

For the temperature-independent breakdown type (sec. 4.3.2.2-b), also a model is completely missing up to now. Possibly a meltdown of the interdigit-electrodes due to local current overload plays a role with respect to crater creation and Cu-precipitates.

5 Results and Discussion:

Nd:PZT(AgPd)

Another important sample type used for this thesis, was the Nd:PZT(AgPd) multilayer stack. In this composition $\sim 75\mu\text{m}$ thick Nd:PZT layers are separated by interdigit electrodes made of a metallic alloy of 80 % Ag and 20 % Pd. Since the noble metals Ag and Pd are in contrast to Cu less prone to oxidation, Nd:PZT(AgPd) multilayer stacks are sintered in air. Hence, the Nd:PZT(AgPd) composition will show a different stoichiometry than the Nd:PZT(Cu) stacks.

All measurements on Nd:PZT(AgPd) were done on multilayer stack segments with one interconnected electrode comb, as illustrated in Fig. 3.5b. Hence, always two layers of Nd:PZT(AgPd) were subjected to the voltage applied to the insulated electrode in between.

Before any *dc*-experiment was conducted, impedance spectra of the layer under investigation were recorded. NYQUIST-plots of Nd:PZT(AgPd) did yield good semi-circles, appropriate for a CNLS-fitting with an R//CPE equivalent circuit model, cf. Fig. 5.1. CNLS-fitting for the vast majority of R//CPE equivalent circuits yielded a non-ideality exponent n in Eq. (2.68) between 0.8 and 1.0.

However, it turned out, that under voltage load the Nd:PZT(AgPd) samples were much less stable (in air) than the Nd:PZT(Cu) samples at the same conditions. Due to very early breakdowns it was decided, to reduce temperature and voltage of the degradation experiments on Nd:PZT(AgPd): Most experiments were conducted at $T_{set} = 400\text{ }^{\circ}\text{C}$ and $U \leq 100\text{ V}$.

The most significant difference between Nd:PZT(AgPd) and Nd:PZT(Cu) samples was, that on a short-time scale the former showed a *conductivity increase* under high-field stress, rather than a conductivity decrease, which was found for Nd:PZT(Cu) samples under high-voltage load.

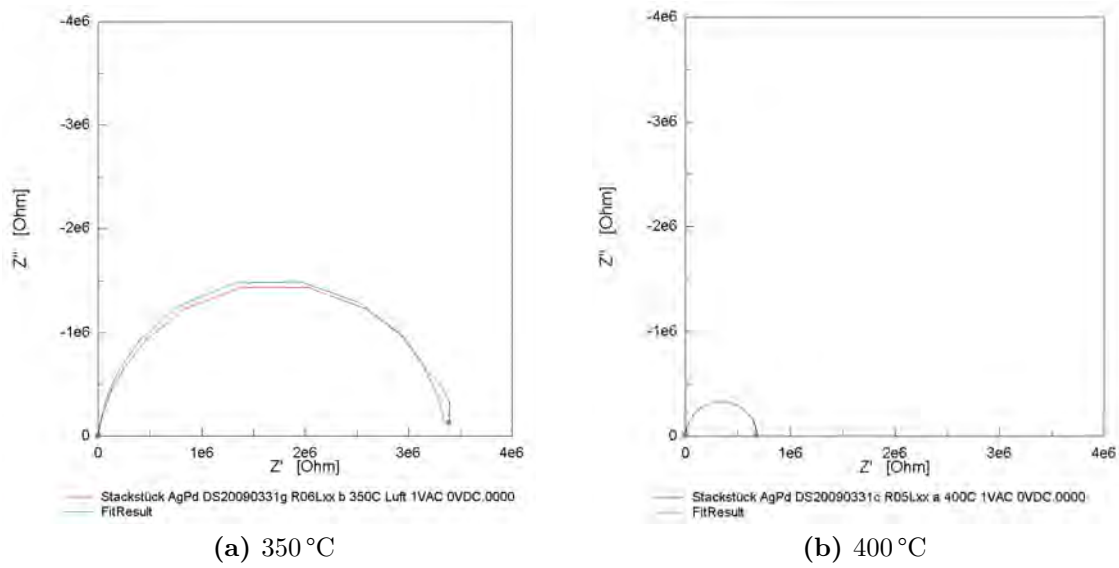


Figure 5.1: Impedance spectra (NYQUIST-plot) of a Nd:PZT(AgPd)-layer at $350\text{ }^{\circ}\text{C}$ (a) and $400\text{ }^{\circ}\text{C}$ (b) before any *dc*-experiment (black) and corresponding R//CPE fit (green).

5.1 Degradation behavior of Nd:PZT(AgPd) in air

In this section the experiments on Nd:PZT(AgPd)-layers in air will be described.

5.1.1 High-voltage

In air, all five high-voltage stressed 75 μm Nd:PZT(AgPd)-layers showed a behavior as illustrated in Fig. 5.2 (400 °C; 100 VDC).

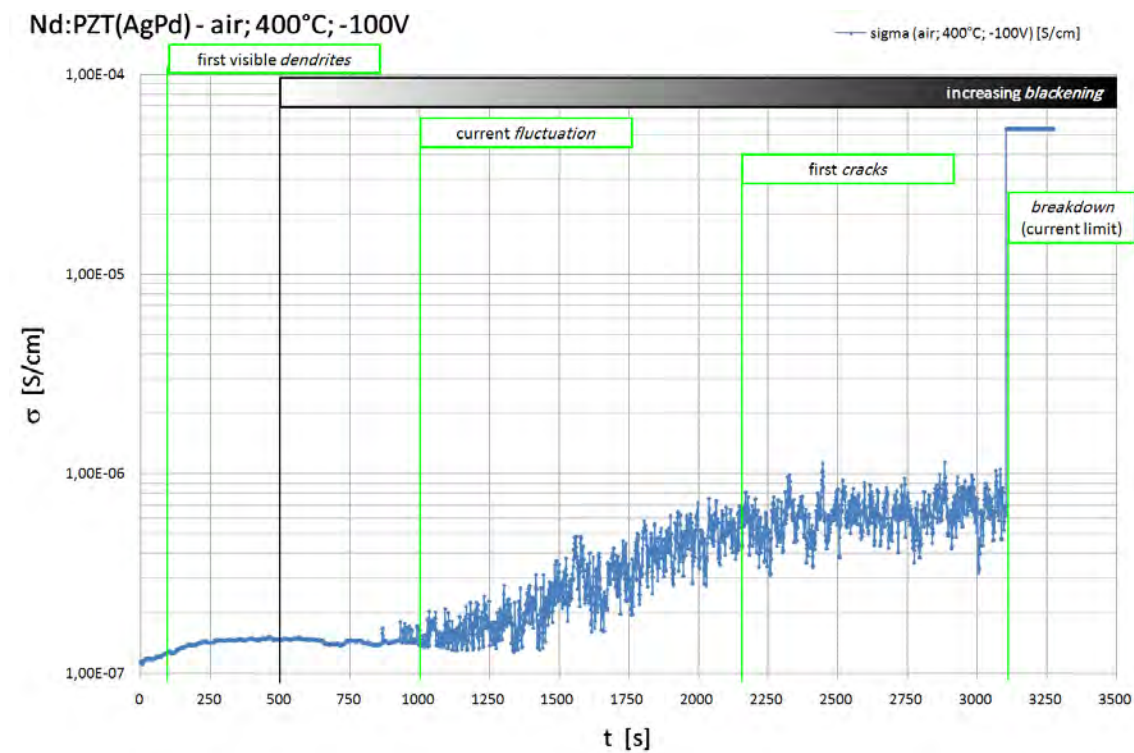
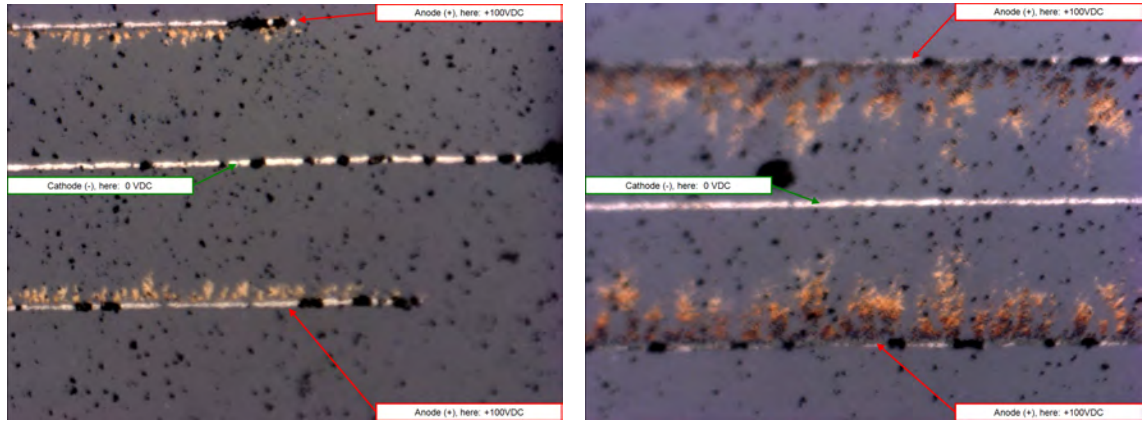


Figure 5.2: Typical behavior of a 75 μm Nd:PZT(AgPd)-layer under 100 V at 400 °C.

Between switching-on the high-voltage and breakdown several features were observed, which will be discussed in the following subsections (sec. 5.1.1.1-sec. 5.1.1.5):

5.1.1.1 Dendrites

During *in-situ* observation of the “hot” sample (on the hot stage, under voltage) within the first 60 s... 120 s golden colored *dendrites* became visible. Astonishingly



(a) Very first moment of perceptible dendrites

(b) Shortly before breakdown

Figure 5.3: *In-situ* micrographs of dendrites growing on the “hot” sample. 400 °C; 100 V.

the dendrites started growing from the anodic interdigit electrode (\oplus) in the direction of the cathodic interdigit electrode (\ominus).

For reasons of air convection and an unstable mounting of the hot stage microscope, the “live” micrographs in Fig. 5.3 of dendrite-growth are slightly blurred.

The dendrites are randomly distributed within the segment of the stressed layer where the interdigit electrodes overlap, cf. Fig. 5.15. A close-up of dendrites after the final breakdown is given in Fig. 5.4.

A scanning electron microscope (SEM) picture of the dendrites is given in Fig. 5.5. This inspection revealed, that the dendrites actually consisted of individually separated droplets.

These dendrite-constituting *droplets* were analyzed by SEM/EDX-microprobing. All abnormal objects (droplets, cubes, etc.) in the dendritic area turned out to be silver (Ag), cf. Fig. 5.6.



Figure 5.4: Detailed micrograph of dendrites after breakdown of the layer.

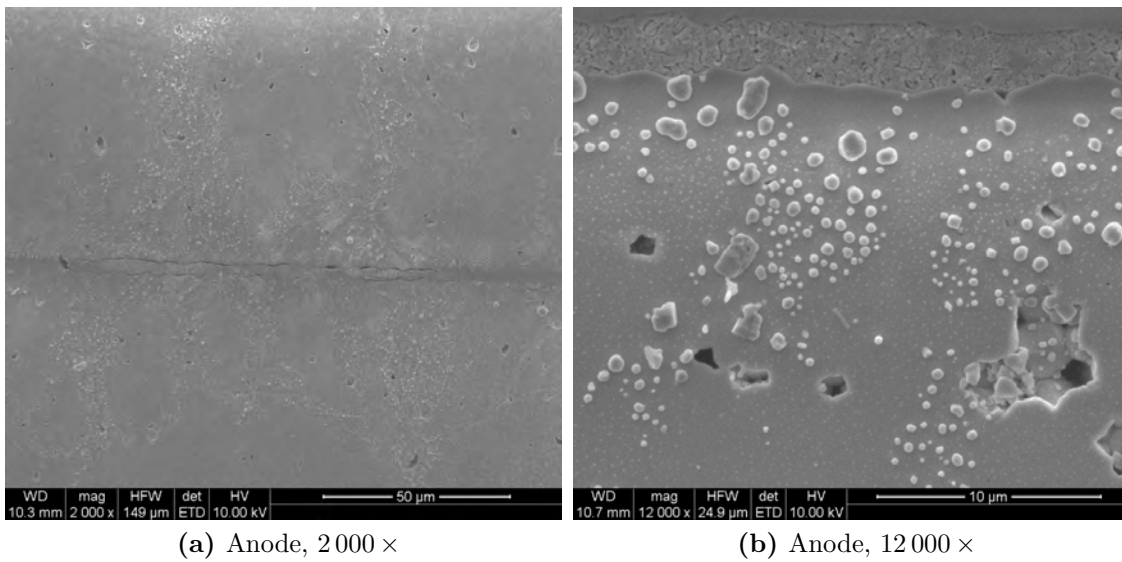


Figure 5.5: Secondary electron pictures of a dendrite structure

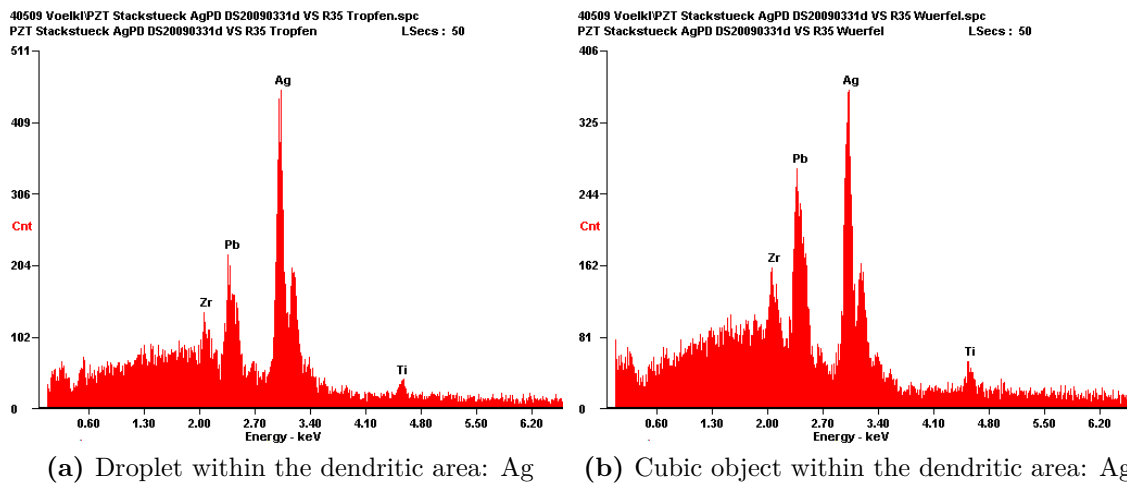


Figure 5.6: EDX spectrographs of objects within the dendritic area. Pb, Zr and Ti peaks result from the PZT background close to the analyzed object.

5.1.1.2 Blackening

Similar to voltage-stressed Nd:PZT(Cu) also Nd:PZT(AgPd)-layers under electrical load did show a progressive *darkening* with increasing degradation time: At 450 °C this “*blackening*” became visible in the dark field mode of the optical microscope after 5 to 8 minutes of applied high-field stress. An *in-situ* snapshot of blackening on a Nd:PZT(AgPd)-layer at 450 °C and under 100 V is depicted in Fig. 5.7.

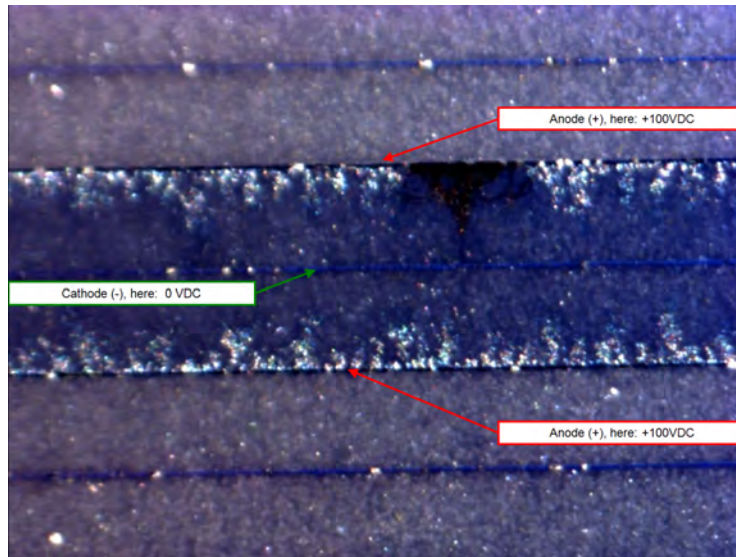


Figure 5.7: Dark field micrograph during the *in-situ* observation of blackening on a Nd:PZT(AgPd)-layer. 450 °C; 100 V.

During the scanning electron microscopy (SEM), EDX-microprobing was used to investigate the chemical composition of voltage-blackened vs. virgin Nd:PZT(AgPd)-layers. EDX spectrographs of virgin Nd:PZT(AgPd) and of dendrite-free areas of darkened layers are illustrated in Fig. 5.8. Both show original PZT-composition and any differences could not be identified.

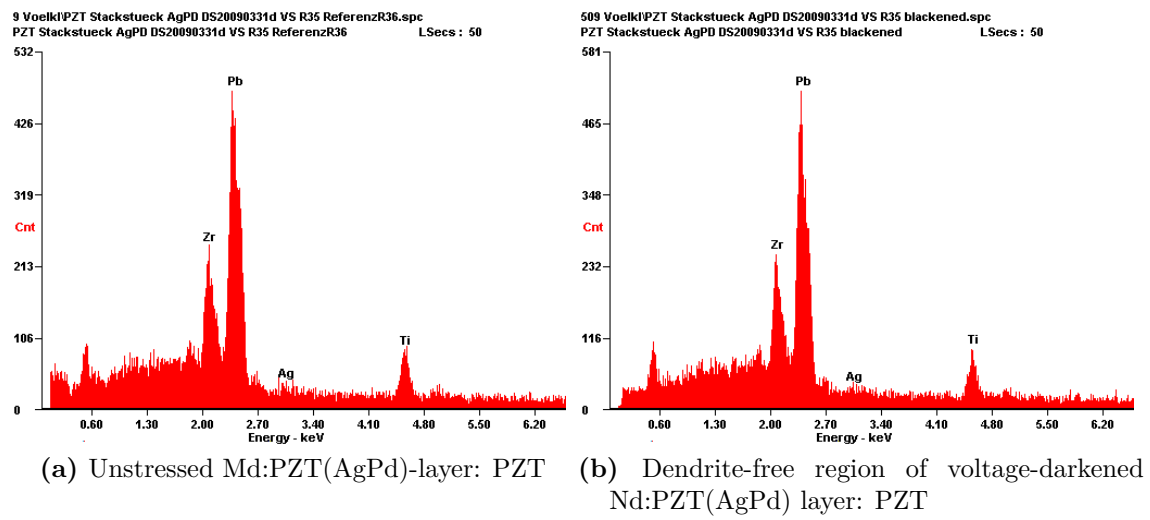


Figure 5.8: EDX spectrographs of a virgin Nd:PZT(AgPd)-layer (a) vs. a blackened one (b).

5.1.1.3 Current fluctuation

The first part of the conductivity curve in Fig. 5.2 is relatively smooth. After ~ 600 s ... 1 000 s, however, a heavily *dithering current* changes the character of the conductivity progress significantly: Accordingly, the conductivity shows strong fluctuations. Optically, no corresponding visible counterpart to this change of behavior was observed *in-situ* through the microscope.

5.1.1.4 Cracks

After $\sim 2\,000$ s of 100 V stress some of the dendritic areas transformed suddenly into apparent “*cracks*”, cf. Fig. 5.9.

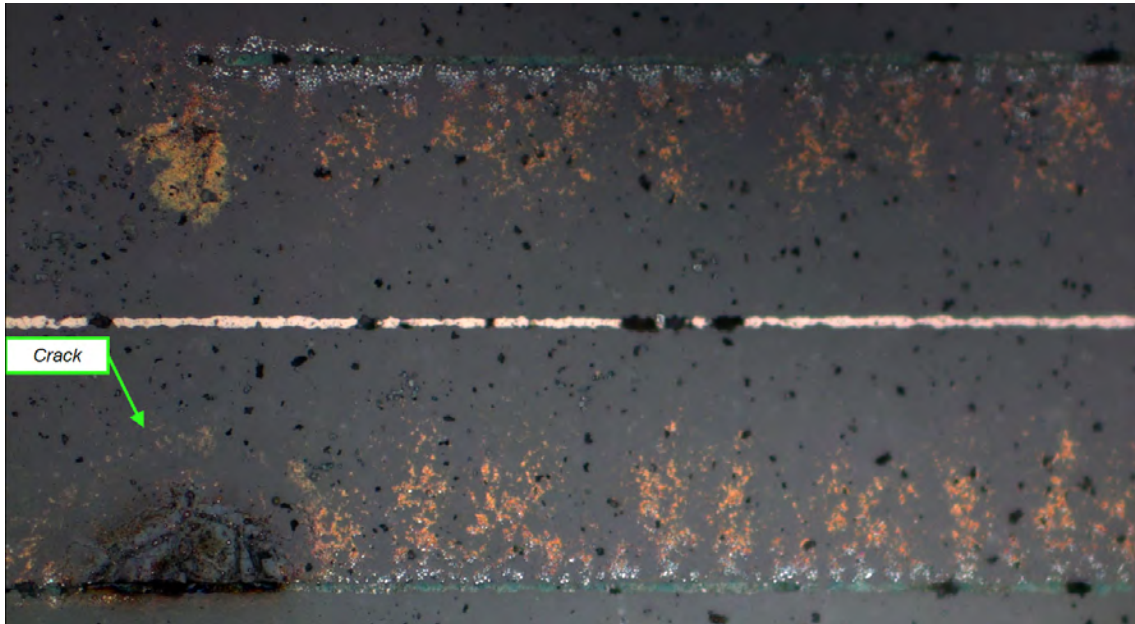


Figure 5.9: Post-breakdown micrograph of a crack, formed during the degradation process. Air, 400 °C, 100 V.

Also the crack structures were investigated by scanning electrode microscopy (SEM) and energy-dispersive X-ray spectroscopy (EDX) microprobing. A SEM micrograph of a post-breakdown dendrite/crack structure on the *unpolished* sample is depicted in Fig. 5.10.

The crack-termed structure turned out to be constituted of planar offsets, similar to riverbeds in a river-delta. A close-up of the riverbed-like crack structures and the objects constituting the dendrites can be seen in Fig. 5.11.

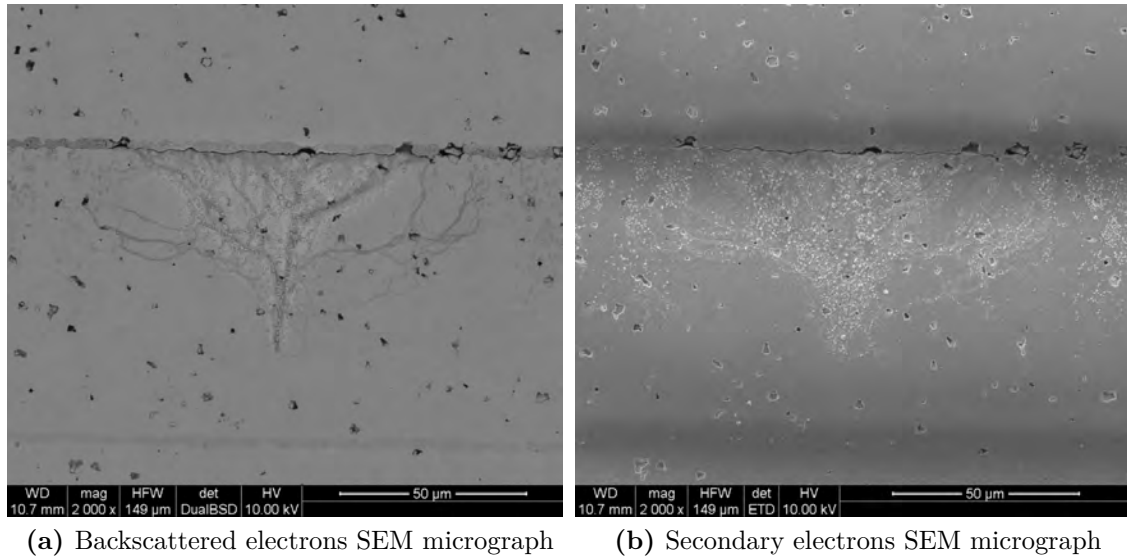


Figure 5.10: SEM micrograph of a dendrite/crack structure. In the middle of the pictures a formerly dendrite structure has transformed into a river-delta crack structure. On the left and right borders of the pictures pure dendrite structures (constituted of droplets) can be seen.

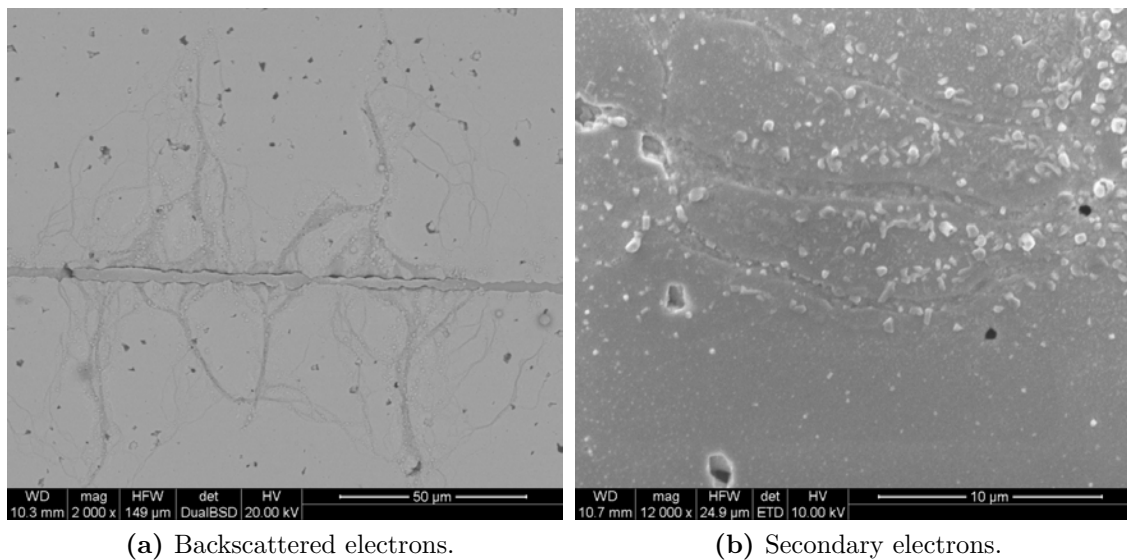


Figure 5.11: Riverbed / river-delta structure of a crack.

Close-ups of the edge of a crack are depicted in Fig. 5.12. On some edges of the riverbed-like cracks, structures resembling molten mass were found.

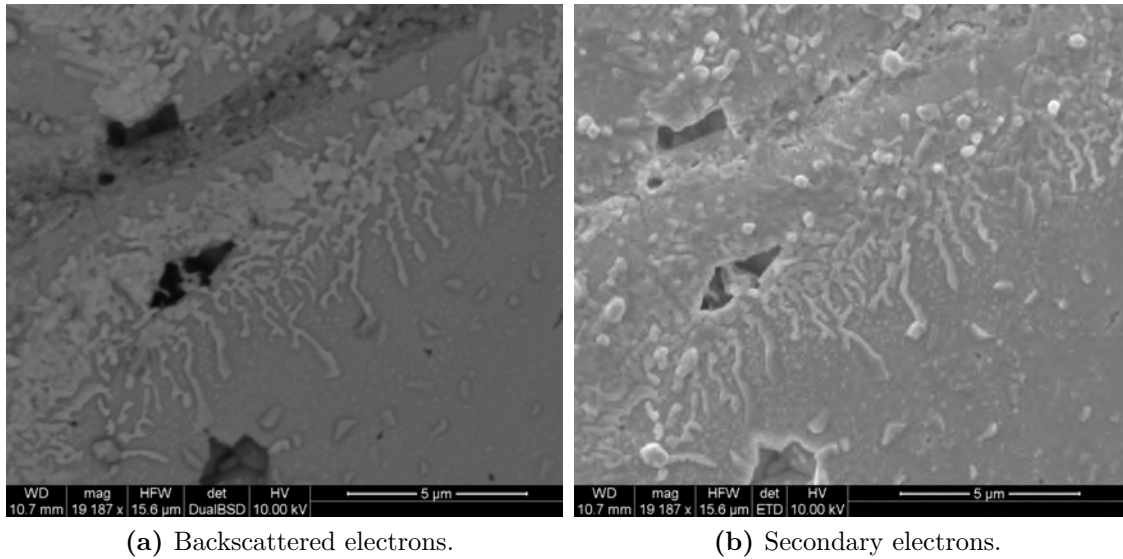


Figure 5.12: Molten mass at the edge of some riverbed-like cracks

EDX microprobing was also applied to various objects in or close to the riverbed structure of the cracks. The corresponding EDX spectra are illustrated in Fig. 5.13. The “molten mass” turned out to be most probably molten PZT.

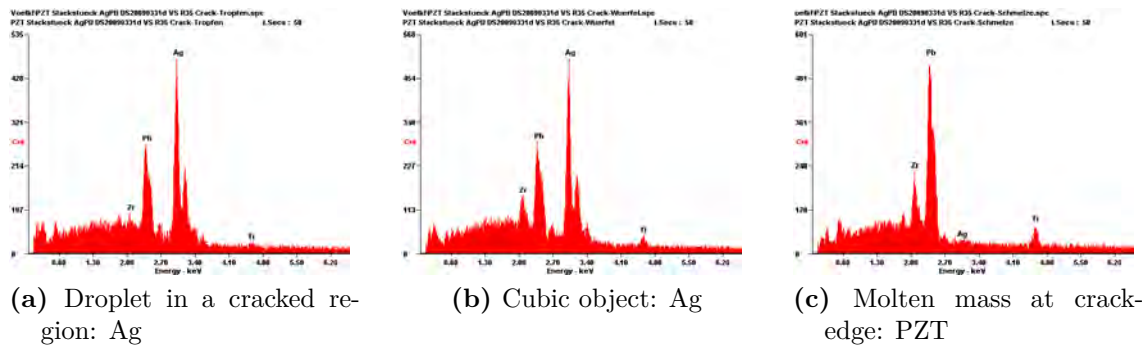


Figure 5.13: EDX spectrographs of objects in the crack area.

However, no chemical difference between virgin (unstressed) and blackened but otherwise dendrite/crack/crater-free Nd:PZT(AgPd)-layers could be found. Various drops and cubic objects in non-cracked dendrite areas and similar drops and cubic objects within the crack-area turned out to be silver (Ag). The EDX-spectra

of the crack-constituting features (riverbeds) did not show any difference to virgin Nd:PZT(AgPd).

5.1.1.5 Breakdown

The (preliminary) end of the degradation experiments on Nd:PZT(AgPd) in air was always determined by a sudden *current peak into the current limit* of the Source-Measure-Unit accompanied by the formation of *craters* similar to those on Nd:PZT(Cu), see sec. 4.3.3. At 400 °C, breakdowns of Nd:PZT(AgPd) layers occurred for 100 V *dc*-load after 1 800 s ... 3 200 s, one layer subjected to 160 VDC load broke down after 800 s.

Subsequent impedance measurements showed quasi-short-circuited resistivities in the order of 11 Ω ... 70 Ω , even at room-temperature, cf. Fig. 5.14.

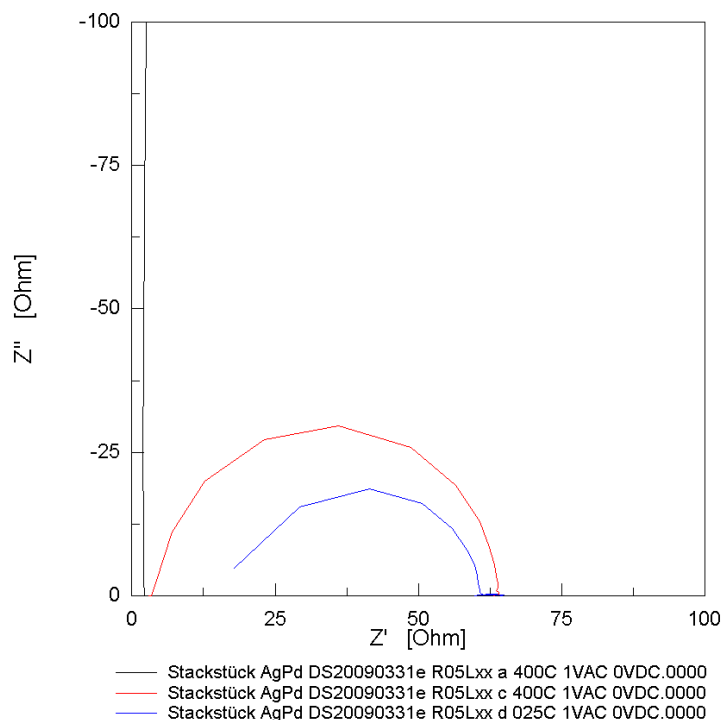


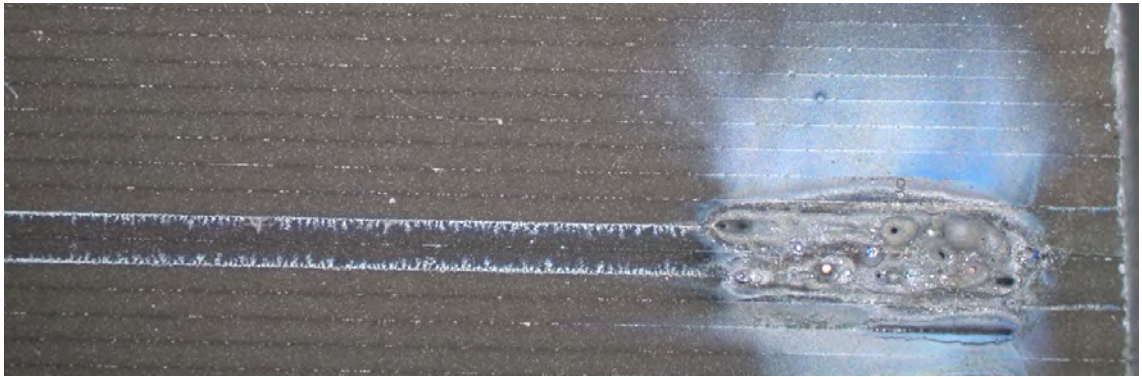
Figure 5.14: Impedance spectra (NYQUIST-plot) of a 100 V stressed Nd:PZT(AgPd)-layers at 400 °C before the experiment started (black) and after breakdown (red). The blue semicircle was recorded at room temperature after breakdown.

Two micrographs of breakdown craters on Nd:PZT(AgPd) are depicted in Fig. 5.15. Note the random distribution of dendrites along the interdigit anodes. The crack structures close to the threefold crater in Fig. 5.15c might indicate, that craters are formed at previous cracks.

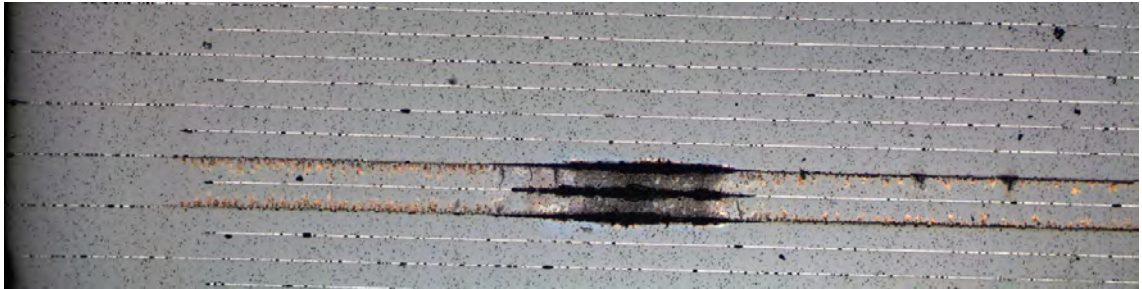
After grinding-off some μm of the damaged top-side of samples after breakdown, a



(a) Bright field.



(b) Dark field.



(c) Threefold crater in the region of (previous) cracks.

Figure 5.15: Breakdown craters on Nd:PZT(AgPd). Air, 400 °C, 100 V.

change also in morphology of the stressed Nd:PZT(AgPd) layer was found below the craters, cf. Fig. 5.16. The initially porous PZT obviously transformed into an ultimately dense state of matter beneath the section of the anode, closely under the (former) crater. Possibly the PZT melted at the time of breakdown and at the site of the crater, leaking into adjacent pores.

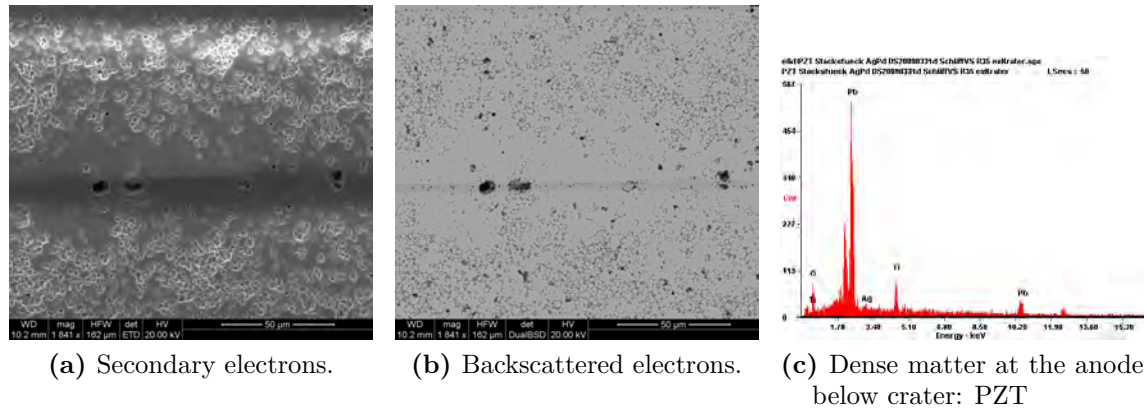
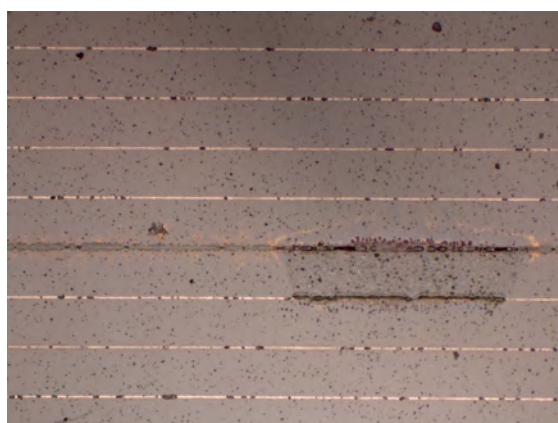


Figure 5.16: Densification of PZT close to the anode (+100 V) straight below the breakdown crater (polished-off).

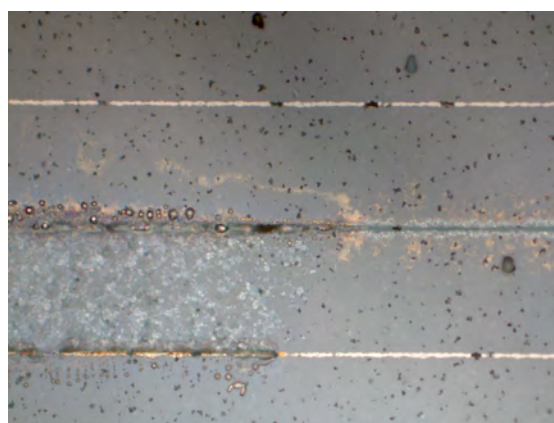
On one sample (400 °C; +160 VDC) not only a crater was formed on the downwarded bottom-side of a sample, but on the same stressed Nd:PZT(AgPd)-layer a strange section of changed morphology was found, cf. Fig. 5.17. However, since this was a single finding, this kind of structure was not further investigated.



(a) Dark field, 5 ×



(b) Bright field, 20 ×



(c) Bright field, 50 ×

Figure 5.17: Exceptional grainy structure found in addition to a typical breakdown crater. Anodic (+160 V) interdigit electrode between two cathodically charged (0 V) electrodes. 400 °C.

5.1.2 Low-voltage

One Nd:PZT(AgPd)-layer was subjected only to 10 VDC, but for a longer period of time. Similar to the high-voltage experiment with 100 V the conductivity did also increase at 10 V, but on a much longer time scale. In the first hour of the experiment no dendrites could be observed. After ~15 hours the experiment was aborted without any breakdown, however. At this time very extended dendritic structures were found, but no blackening and no cracks were visible. The development of the conductivity in this long-term low-voltage experiment is illustrated in Fig. 5.18.

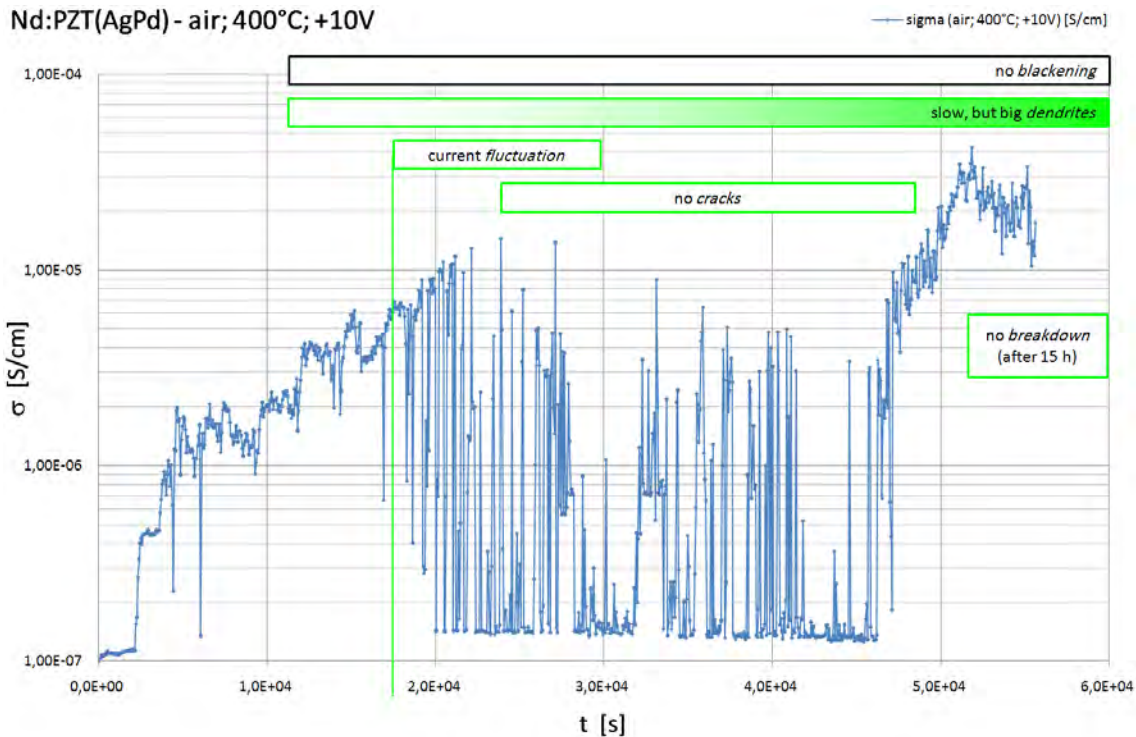


Figure 5.18: Behavior of a Nd:PZT(AgPd) layer at 400 °C in air, under a reduced voltage load of 10 VDC for ~1 000 min.

Before and after the 10 V have been applied, impedance spectra were recorded and showed semicircles in good agreement with an R//C equivalent-circuit CNLS-fitting method, cf. Fig. 5.19. However, it was not possible to determine a definite *ac*-resistivity value after the 10 VDC-phase, because a normal (bias-free) impedance measurement yielded much higher resistivities (red semicircle in Fig. 5.19a), than an additional EIS-measurement with +2 VDC bias, (blue line in Fig. 5.19b). The discrepancy between the two impedance measurements conducted after switching-off the 10 V *dc*-load might either be explained by a pronounced nonlinear response

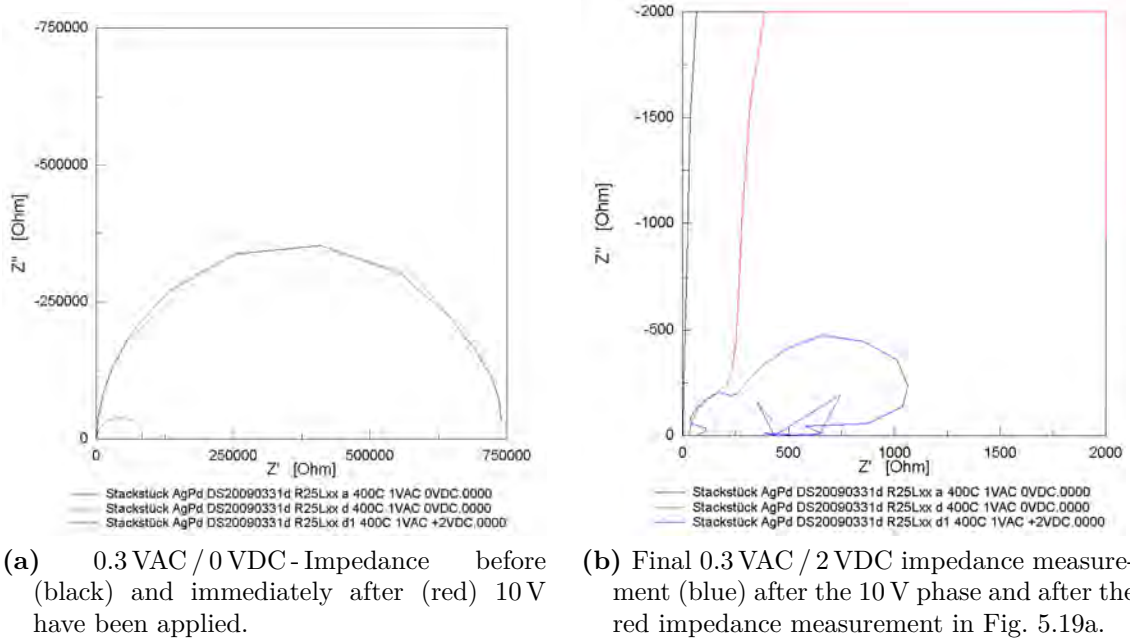
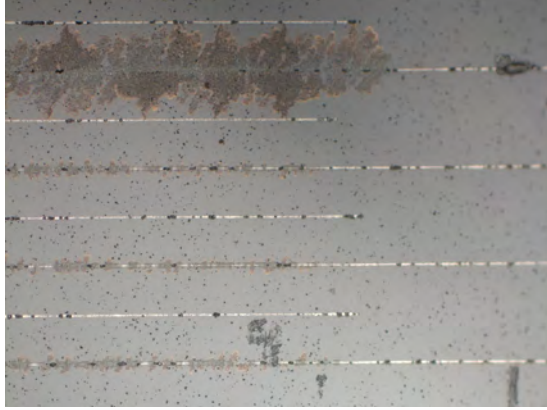


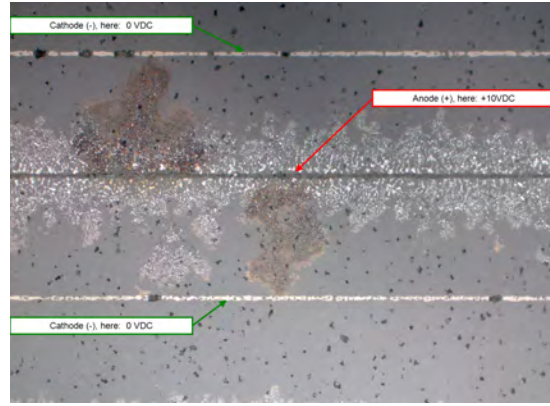
Figure 5.19: Three NYQUIST-plots of a Nd:PZT(AgPd)-layer stressed by 10 VDC for ~100 min without breakdown.

(already at 2 VDC) due to the 10 VDC stress or by a very rapid resistance degradation effect already due to the 2 VDC impedance-bias offset-voltage. However, such a rapid resistance degradation from $\sim 80 \text{ k}\Omega$ to $\sim 500 \Omega$ during one and the same EIS-measurement seems quite unlikely, especially at only 2 V *dc*-load and 400°C .

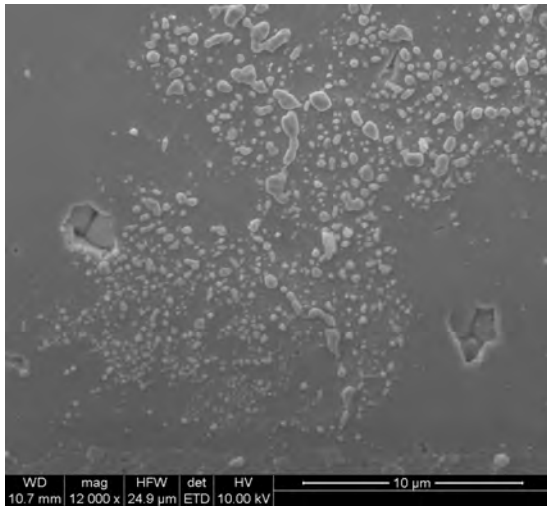
Since in this experiment the voltage (10 V) was much smaller than in all other experiments conducted on Nd:PZT(AgPd), a breakdown did not occur even after $\sim 60\,000 \text{ s}$ and the dendrite forming process got more time. Hence, this degraded layer showed the *most pronounced dendrites*, cf. Fig. 5.20a and Fig. 5.20b. A SEM micrograph of the dendrites is given in Fig. 5.20c and the EDX-analysis again confirmed that the superficial droplets consist of Ag (Fig. 5.20d).



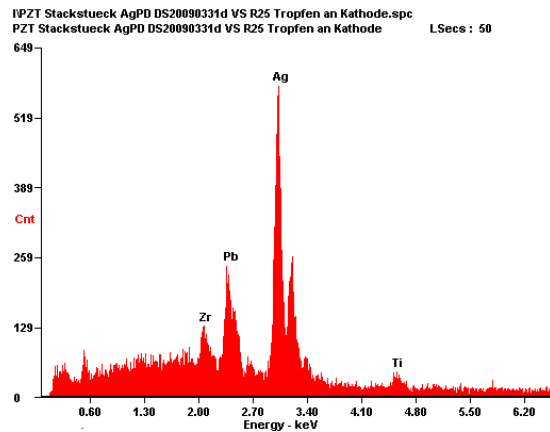
(a) Comparison of 10 V long-term dendrites (top bilayer) with dendrites from normal high-field (100 V) experiments (three bilayers below).



(b) Droplets grow from the anode (\oplus) up to the cathode (\ominus).



(c) SEM micrograph of 10 V induced dendrites reaching the cathode.



(d) EDX-microprobe of a 10 V induced dendrite close to the cathode: Ag

Figure 5.20: Extraordinarily big dendrite growth on a Nd:PZT(AgPd)-layer at 400 °C in air, stressed for ~60 000 s with 10 VDC-load.

5.2 Degradation behavior of Nd:PZT(AgPd) in Ar

To reduce the oxygen partial pressure, a continuous flow of 99.999 % Ar gas through the gas-tight measurement chamber was used. The leaking-rate of the whole system lead to stationary partial oxygen pressure values in the range from $p(\text{O}_2) = \sim 10 \text{ ppm O}_2$ to $\sim 1\,000 \text{ ppm O}_2$ ($= 0.1 \% \text{ O}_2$).

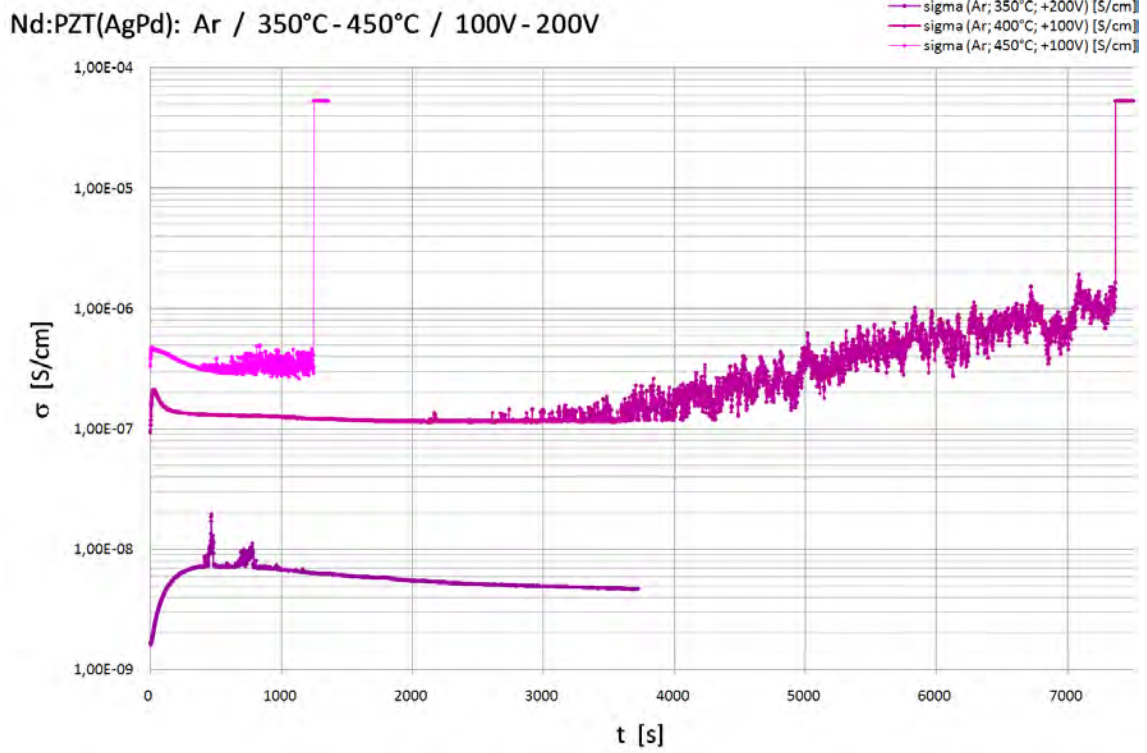


Figure 5.21: Nd:PZT(AgPd) layers in Ar ambiance at 350 °C (violet), 400 °C (magenta) and 450 °C (pink). The 350 °C measurement was aborted before any breakdown.

In this argon environment, three measurements at three different temperatures (350 °C, 400 °C, 450 °C) have been conducted, cf. Fig. 5.21.

- At 350 °C and even under 200 V Nd:PZT(AgPd) turned out to be surprisingly stable in argon-gas: After an initial conductivity increase the conductivity slowly decreased again. When the measurement was aborted after $\sim 4\,000 \text{ s}$ without any dendrites, blackening, cracks or breakdown, the conductivity had nevertheless suffered an overall increase by a factor of ~ 4 .
- At 400 °C and 100 V *dc*-load the conductivity of a Nd:PZT(AgPd)-layer showed similar features as the high-voltage experiments in air: After a fluctuation-

phase an overall increasing current lead into a breakdown. However, the conductivity increase turned out to be not as monotonous as in air: A steep initial increase was followed by a less pronounced decrease. Neither dendrites or cracks nor blackening were detected.

- At 450 °C and 100 VDC the the features of the experiment turned out to be similar to those at 400 °C , but faster. However, also at this temperature neither dendrites or cracks nor blackening were detected.

At any temperature Nd:PZT(AgPd)-layers in Ar displayed single semicircles in NYQUIST-impedance-plots (before and after high-voltage was applied), cf. Fig. 5.22a. No dendrites, blackening or other optical phenomena were found during or after high-field stress, cf. Fig. 5.22b.

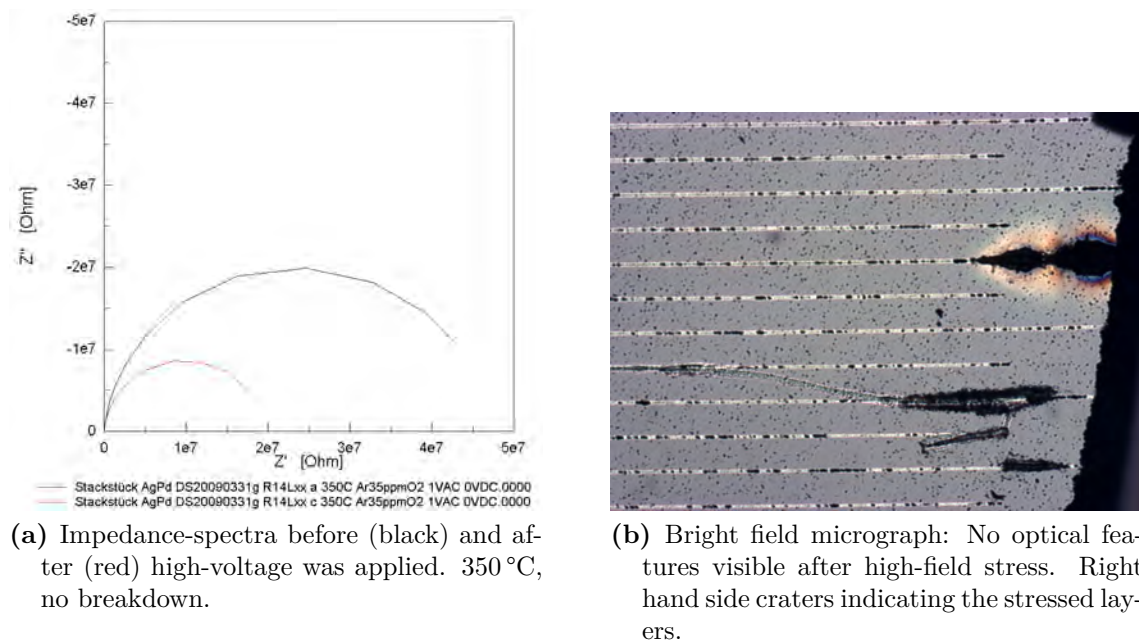


Figure 5.22: Nd:PZT(AgPd) in Ar-atmosphere

Analog to the breakdowns in air, the small-signal impedance values immediately after breakdown were actually much smaller ($<100 \Omega$) than the corresponding resistance of the current-limit of the Source-Measure-Unit. A further investigation of the conductivity after high-field stress (with or without breakdown) was not conducted.

5.3 Degradation behavior of Nd:PZT(AgPd) in H₂

Ten experiments have been conducted in the gas-tight measurement chamber, under a controlled hydrogen atmosphere: A flow of a gas mixture of 2.5 vol% H₂ in Ar was used. Depending on the flow rate of the gas-mixture and the (possibly temperature dependent) leaking-rate of the vessel, the oxygen partial pressure could be reduced to values in the range from $p(\text{O}_2) = \sim 10^{-19}$ to $\sim 10^{-14}$ ppm O₂.

The typical development of the conductivity of 10 V-stressed Nd:PZT(AgPd)-layers in H₂-atmosphere ($p(\text{O}_2) = \sim 10^{-19}$ ppm O₂) at 400 °C is illustrated in Fig. 5.23. The similarity to the development of the conductivity in the same experiment in air (Fig. 5.18) is striking.

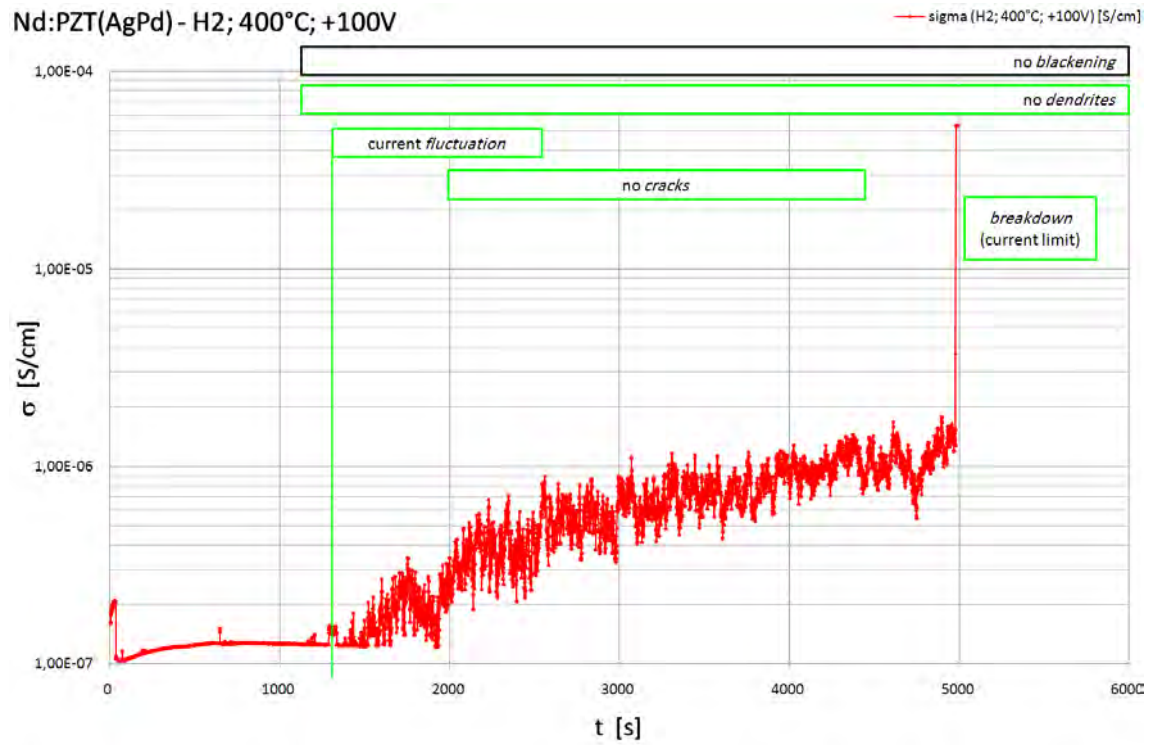


Figure 5.23: Behavior of a Nd:PZT(AgPd)-layer in H₂, at 400 °C and under 100 VDC load.

Prior to any measurement in H₂-atmosphere a first reference measurement was conducted in *air* after heating the hot-stage to $T_{\text{set}} = 400$ °C (black semicircle in Fig. 5.24a). Then the gas-tight chamber was evacuated and a further impedance spectrum was recorded at 400 °C in *vacuum* (red semicircle in Fig. 5.24a). After a stationary flow-through of the H₂-gas-mixture (2.5 vol% H₂ in Ar - $p(\text{O}_2) < 10^{-17}$ ppm O₂)

had established, a third NYQUIST-plot was recorded in this *hydrogen* atmosphere (blue semicircle in Fig. 5.24a). A *reference* measurement on an unstressed Nd:PZT(AgPd)-layer after ~ 6000 s in H₂-atmosphere ($p(\text{O}_2) = \sim 10^{-19}$ ppm O₂) is also plotted in Fig. 5.24a (green semicircle). Obviously the change from air to hydrogen resulted in a bigger increase of conductivity, than the mere exposition of the sample to hydrogen-atmosphere for the duration of one or two experiments. Hence, any temporal change of the behavior in different gases was not related to the small-signal conductivity variations due to the switch from air to H₂-ambiance.

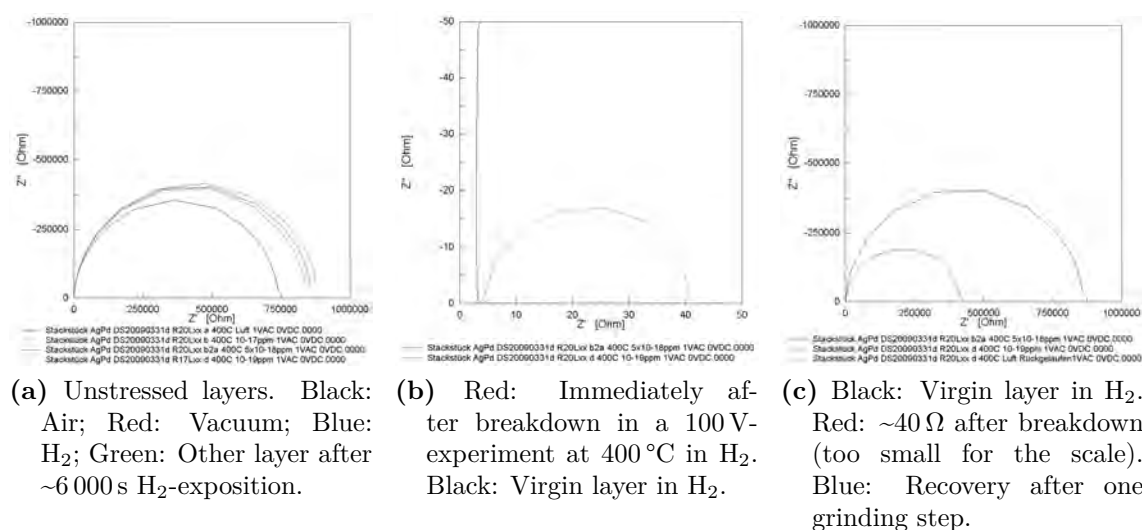


Figure 5.24: Impedance spectra (NYQUIST-plots) of Nd:PZT(AgPd)-layers in H₂-atmosphere at 400 °C.

After a high-voltage experiment had ended with a breakdown, a small-signal *ac*-impedance measurement was conducted to detect the true resistance of the broken Nd:PZT(AgPd)-layer, red semicircle ($\sim 40 \Omega$) in Fig. 5.24b.

However, similar to the Nd:PZT(Cu)-samples, it turned out, that this breakdown was (partially) reversible: After an unknown time at elevated temperature and *one polishing step* the resistance of the formerly short-circuited layer had partially recovered (blue semicircle in Fig. 5.24c). While the resistance of the layer at the beginning of the experiment in H₂ was in the range of $\sim 900 \text{ k}\Omega$, and immediately after breakdown about only 40Ω , finally $450 \text{ k}\Omega$ were measured (all at 400 °C). Since the investigation of post-breakdown conductivity was not the main task of this thesis, no further systematic investigations have been conducted. So the partial conductivity recovery could be *either* due to the grinding step *or* due to thermal

relaxation.

As mentioned already before, in H₂-atmosphere high-voltage stressed Nd:PZT(AgPd)-layers did not show any recognizable optical features on the top-side, like dendrites, cracks, blackening or craters (Fig. 5.25a). The (downwarded) bottom-side of the sample showed an undefined structure along the anodic interdigit electrode (Fig. 5.25b, Fig. 5.25c) and some dendritic droplet structures only at one single end of the anodic interdigit electrode (Fig. 5.25d).



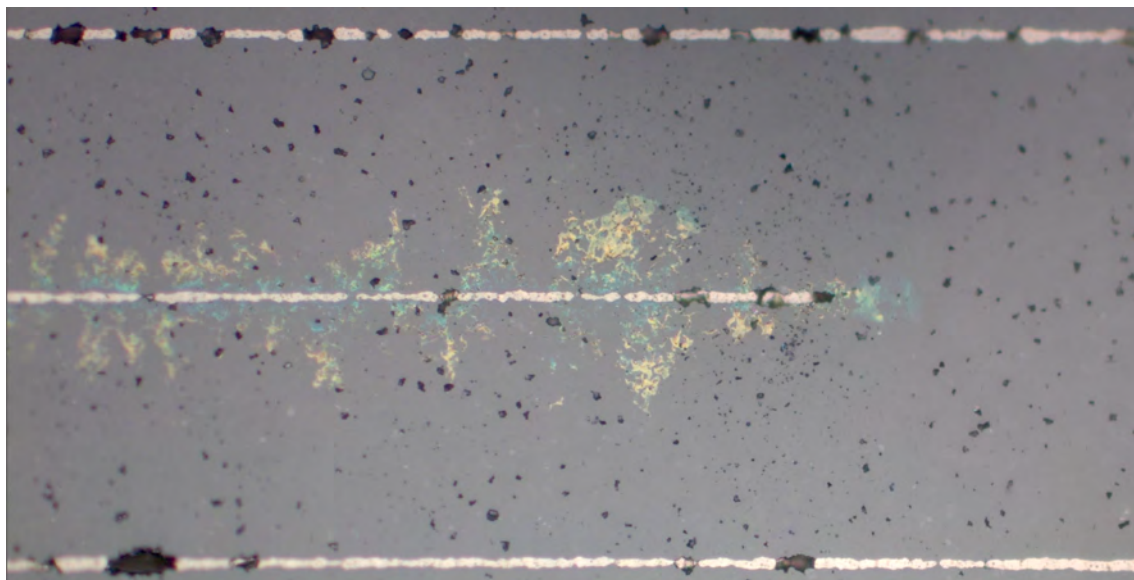
(a) Top-side



(b) Bottom-side (left), undefined structure along the anode.



(c) Bottom-side (right), undefined structure along the anode and dendrites at its end.



(d) Bottom side (right), dendrites at the end of anodic interdigit electrode.

Figure 5.25: Optical features of a Nd:PZT(AgPd) layer stressed with +100 VDC at 400 °C in H₂-atmosphere.

A SEM/EDX analysis on the unpolished bottom-side of the sample again identified the droplets at the end of the anode to be silver (Ag), cf. Fig. 5.26.

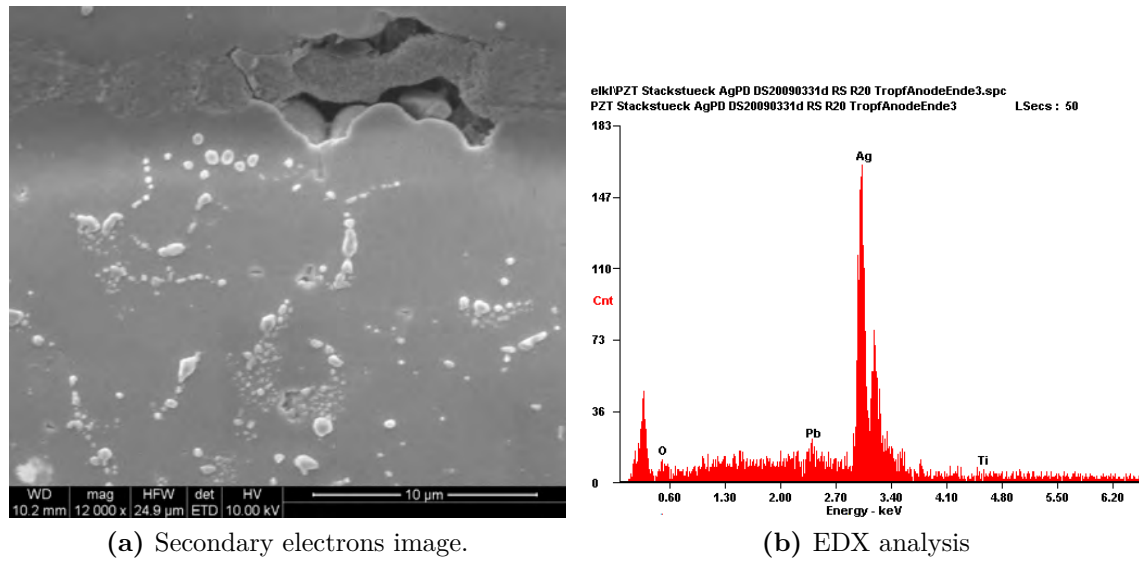


Figure 5.26: Droplets at only one end of the anodic interdigit electrode constitute a dendritic structure on a 100 V stressed Nd:PZT(AgPd) at 400 °C in H₂.

5.3.1 Pb-precipitates

However, a closer look with the scanning electron microscope (SEM) revealed features unique for the H₂-experiment: Offside the dendrites at the end of the anode, *lead (Pb) precipitates* were found between anode and cathode on the top-side and on the bottom-side of the sample. An example of the top-side is depicted in Fig. 5.27.

On the top-side of the sample Pb-precipitates were also found *within* the formerly stressed Nd:PZT(AgPd)-layer: After grinding-off some μm white dot structures were found in the SEM and subsequently identified by EDX microprobing as to be Pb, cf. Fig. 5.28.

However, although Pb-precipitates were primarily found on Nd:PZT(AgPd) layers in H₂-atmosphere, it can not be excluded, that the same Pb-precipitates also exist on (and in) high-field stressed Nd:PZT-layers in other atmospheres, but then - especially in air - they might have been concealed by stronger pronounced effects, such as dendritic droplets, cracks or craters.

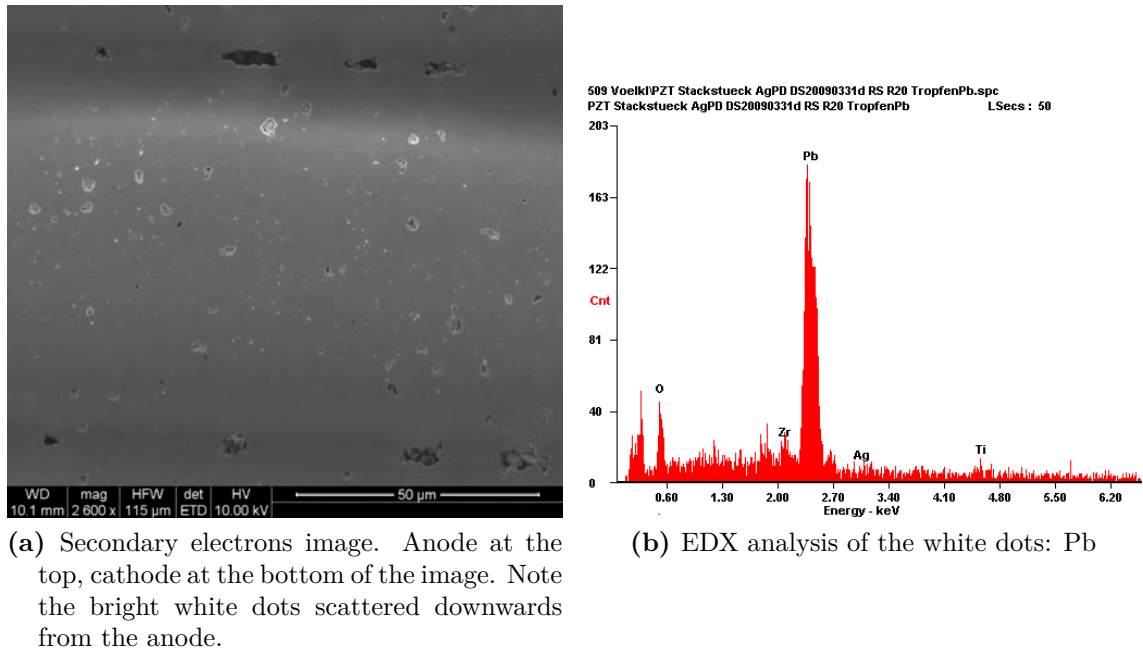


Figure 5.27: Superficial Pb-precipitates on a Nd:PZT(AgPd)-layer, stressed by 100 V at 400 °C in H₂-atmosphere.

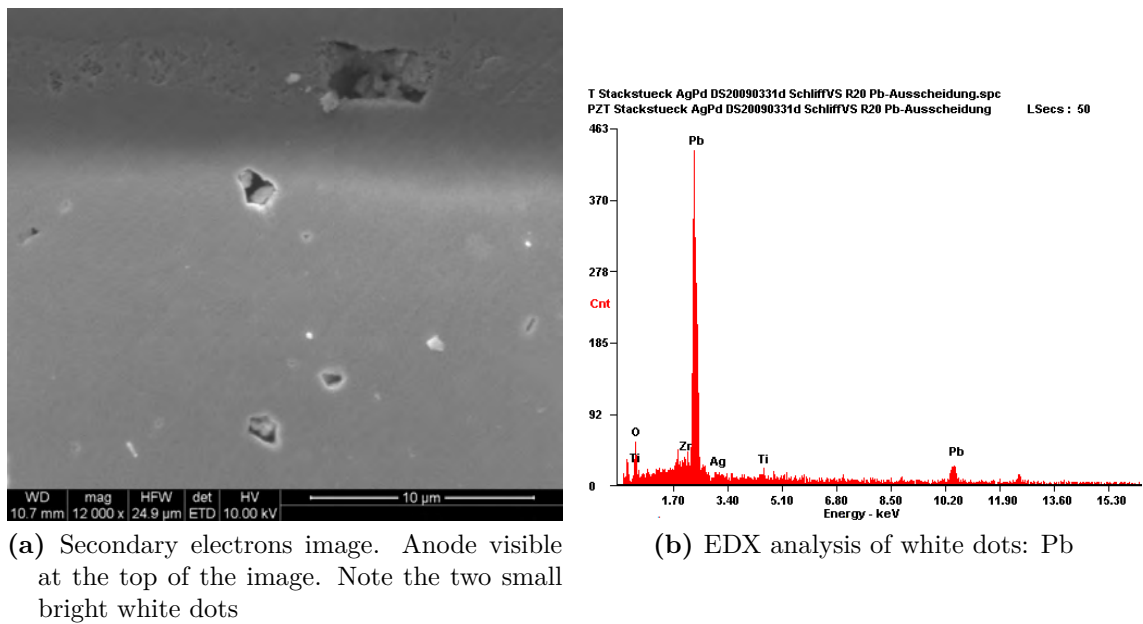


Figure 5.28: Pb-precipitates inside a Nd:PZT(AgPd)-layer, stressed by 100 V at 400 °C in H₂-atmosphere.

5.3.2 Long-term recovery

One Nd:PZT(AgPd)-layer on another sample was investigated at only 350 °C in H₂-atmosphere ($p(\text{O}_2) = \sim 10^{-15}$ ppm O₂). For long-term observation a voltage ramp was programmed, reducing the voltage stepwise from initial +100 VDC to +10 VDC and finally to +1 VDC after each 10 hours (36 000 s), respectively.

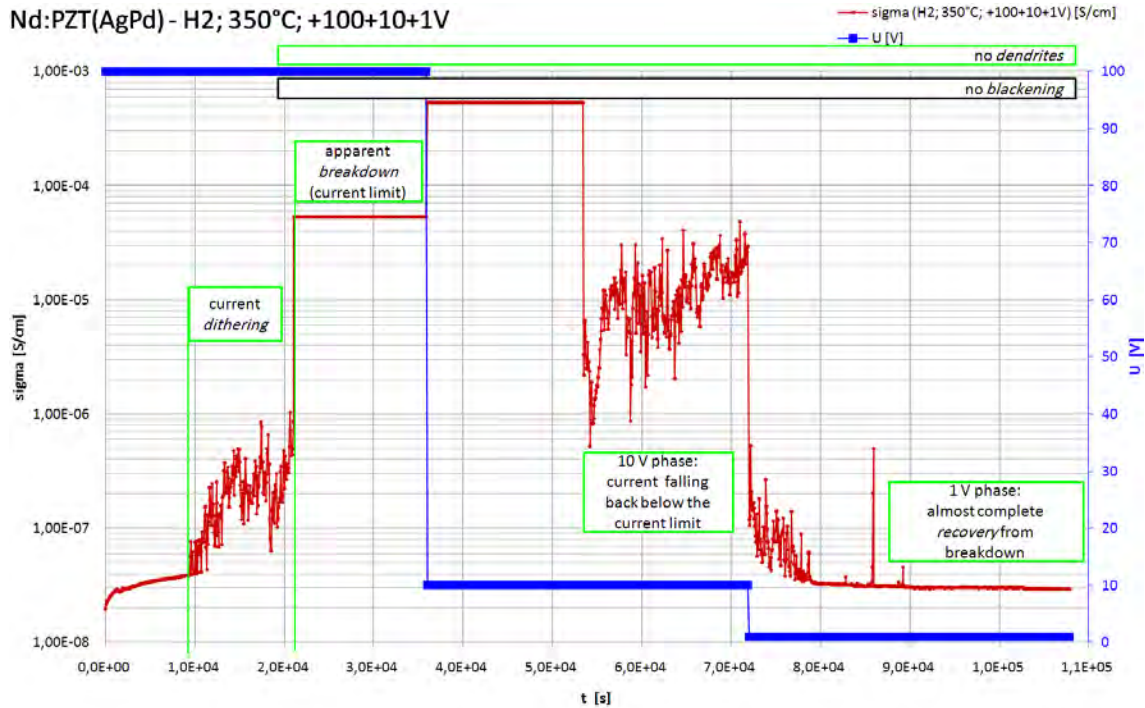


Figure 5.29: Almost complete recovery of an apparent breakthrough on Nd:PZT(AgPd) at 350 °C after 100 V *dc*-load.

The beginning of the conductivity curve, illustrated in Fig. 5.29, is quite similar to those at 400 °C, of course on a longer time-scale. As the experiment took place in H₂-atmosphere, dendrite-like silver droplets and craters were not expected. Although at only 350 °C, within the first high-voltage phase (at ~20 000 s) an apparent breakdown did occur after a period of current fluctuations. Due to the quasi short-circuited character of the breakdown the current-limit of the Source-Measure-Unit was exceeded until the end of the 100 V-phase, and even for some hours in the subsequent 10 V-phase (with a 10× higher current limit). But after ~55 000 s a measurable current suddenly appeared again, followed by heavy fluctuations still within the 10 V-phase. After a total of 20 hours (72 000 s) the voltage was reduced to +1 VDC. Since then the current fluctuation weakened and clearly gave way to a complete

recovery of the conductivity, close to its initial value before any high-voltage was ever applied ($\sim 85\,000\text{ s}$).

Before and after this $> 30\text{ h}$ -experiment impedance spectra of the layer under investigation were recorded, cf. Fig. 5.30. Since this experiment was an uninterrupted (pre-programmed) “auto-run”, no impedance spectra immediately after breakdown could have been obtained, hence the actual resistance value at the time of breakdown is unknown, but it is assumed to be $< 100\,\Omega$.

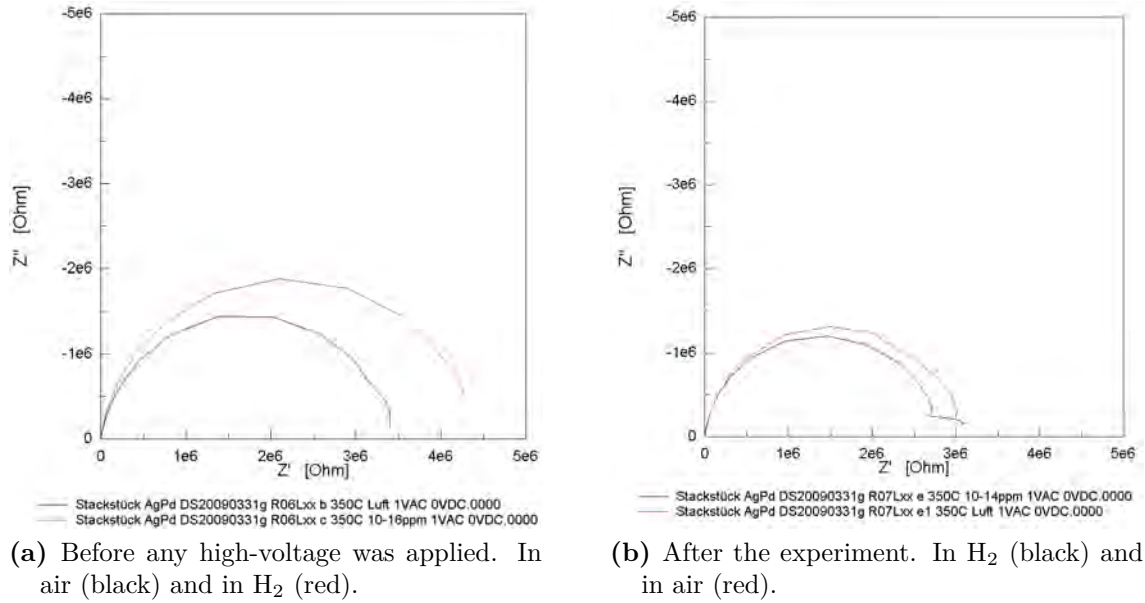


Figure 5.30: NYQUIST-plots of the Nd:PZT(AgPd)-layer of the experiment from Fig. 5.29. $350\,^\circ\text{C}$. Before (a) and after (b) 100 V *dc*-load

Obviously the apparent breakdown occurring at 100 VDC and $350\,^\circ\text{C}$ in H_2 turned out to recover almost completely at low-voltage after multiples of the degradation time period.

5.4 Nd:PZT(AgPd): Comparison and Discussion

A comparison of the conductivity variations of Nd:PZT(AgPd) under high-field stress at 400 °C and under different oxygen partial pressure (air: 21 % O₂; Ar: ~100 ppm O₂; H₂: ~10⁻¹⁹ ... ~10⁻¹⁴ ppm O₂) is given in Fig. 5.31.

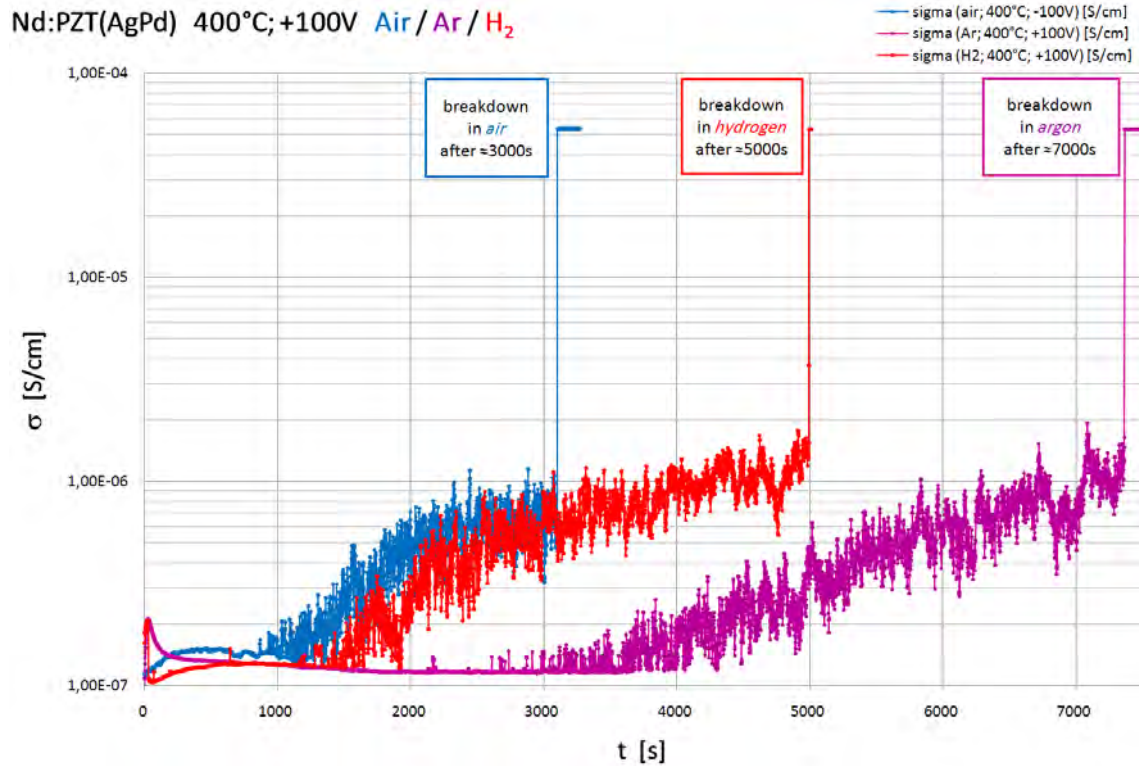


Figure 5.31: Comparison of 100 V stressed Nd:PZT(AgPd)-layers at 400 °C: In air (blue), in Ar (magenta) and in H₂ (red).

Although the current-behavior of Nd:PZT(AgPd) layers at high-field is quite similar, in Ar- and H₂-atmosphere virtually no Ag-droplets were found. The experiment on a Nd:PZT(AgPd)-layer in air under low-voltage (10 V) did prove that dendrites reaching even from the anode up to the cathode are not triggering any breakdown. Dendrite formation on PZT at humid conditions below 100 °C is well known [91]. Under the presence of water, silver ions (Ag⁺) dissolve electrochemically from the anode (⊕) and migrate in the field to the cathode (⊖), where they precipitate in the form of well-known dendrites. In our experiments at much higher temperatures (>300 °C) water was not expected to play a role as an electrolyte. Furthermore, the deposition of the Ag droplets at the anode (rather at the cathode) does not fit

to conventional electrochemical migration. Regarding these dendrites, a model can not be suggested yet.

The phases of suddenly starting current-fluctuations were observed in air, Ar- and H₂-atmosphere and those fluctuations cannot be directly assigned to the dendrites or other optically observed phenomena.

Since blackening of stressed Nd:PZT(AgPd)-layers did occur only in air (and not in Ar-/H₂-atmosphere), this darkening feature might be a result of stoichiometry changes within the layer. From a top-side view, the blackening seemed quite homogeneously, but maybe blackening “grows” from the top- and bottom-side into the layer. Hence, a lateral resolution of blackening by grinding-off blackened layers step-wise could enlight such a surface dependency. However, this was not systematically done within this work.

Another phenomenon not understood so far is the sudden appearance of cracks (riverbed structures) at some former locations of Ag-dendrites in air. Phenomenologically it might be concluded, that cracks are precursors of breakdowns, but in Ar-/H₂-atmosphere breakdowns occurred without any crack.

Finally, virtually all high-voltage experiments on Nd:PZT(AgPd) ended in an electrical breakdown. Although the very small resistance immediately after breakdown suggested an electrical short-circuiting, a long-term experiment in air (Fig. 5.29) proved this apparent short-circuit to be almost completely recovering after several hours at 350 °C.

The temperature dependent conductivity behavior of Nd:PZT(AgPd)-layers in Ar-atmosphere at 350 °C, 400 °C and 450 °C (Fig. 5.21) might give rise to a hypothesis of interlinked multiple temperature activated processes: Not only the first steep rise of conductivity seems to be temperature dependent, but also the subsequent conductivity decrease and the time until breakdown as well.

ANDREJS continued this work with extensive investigations on long-term degradation behavior and post-breakdown analysis on identically Nd:PZT(AgPd) samples [168].

6 Results and discussion: Other PZT-samples

6.1 Macroscopic PZT samples

6.1.1 W- and Sr-doped PZT discs (W/Sr:PZT)

Alkaline earth elements, are usually expected to isovalently substitute Pb on the A-site in PZT, e. g. $(\text{Sr}^{2+})_{(\text{Pb})^{2+}}^{\times}$ [122]. Tungsten on the other hand acts as a positive donor $((\text{W}^{6+})_{(\text{Ti}, \text{Zr})^{4+}}^{\cdot\cdot})$. However, in more complex doping systems of PZT involving alkaline earth metals (like Sr) together with tungsten, Sr might also be situated on B-sites adjacent to B-sites occupied by W. A similar situation was proven for strontium niobate in Ref. [134]. Then Sr would also act as a negative acceptor $((\text{Sr}^{2+})_{(\text{Ti}, \text{Zr})^{4+}}^{\prime\prime})$. For the publication “Piezoelectric properties and conductivity of $\text{Pb}(\text{Zr}, \text{Ti})\text{O}_3$ with SrO-WO_3 additive” by REICHMANN et al. [158], capacitance and conductivity measurements have been conducted on macroscopic PZT disc samples ($1.2 \text{ mm} \times \varnothing 10 \text{ mm}$). Undoped $\text{Pb}(\text{Zr}_{0.525}\text{Ti}_{0.475})\text{O}_3$ was compared to 0 % SrO and 1.5 % SrO doped samples with an increasing WO_3 fraction (0.5 %, 1.0 %, 1.5 %), respectively, cf. Tab. 6.1. For this purpose metallic bilayer electrodes (20 nm Ti, $\sim 200 \text{ nm Au}$) were sputtered on both sides of the PZT discs and impedance spectra were recorded while the sample in a glass sample-holder was heated in a cylindrical oven to set-temperatures between 275 °C and 550 °C.

Since the NYQUIST-plots of those macroscopic samples did show sufficient fractions of semicircles (at least above 300 °C), the conductivity could be easily calculated by CNLS fitting with a simple R//CPE-element, cf. Fig. 6.1. Analysis was thus similar to that employed to PZT-layers in stack segments, cf. sec. 3.2. Predominantly a Newtons4th PSM1735 impedance analyzer (plus IAI-interface) was used instead of the Novocontrol instrument. The frequency range was 0.01 Hz to 500 kHz at true

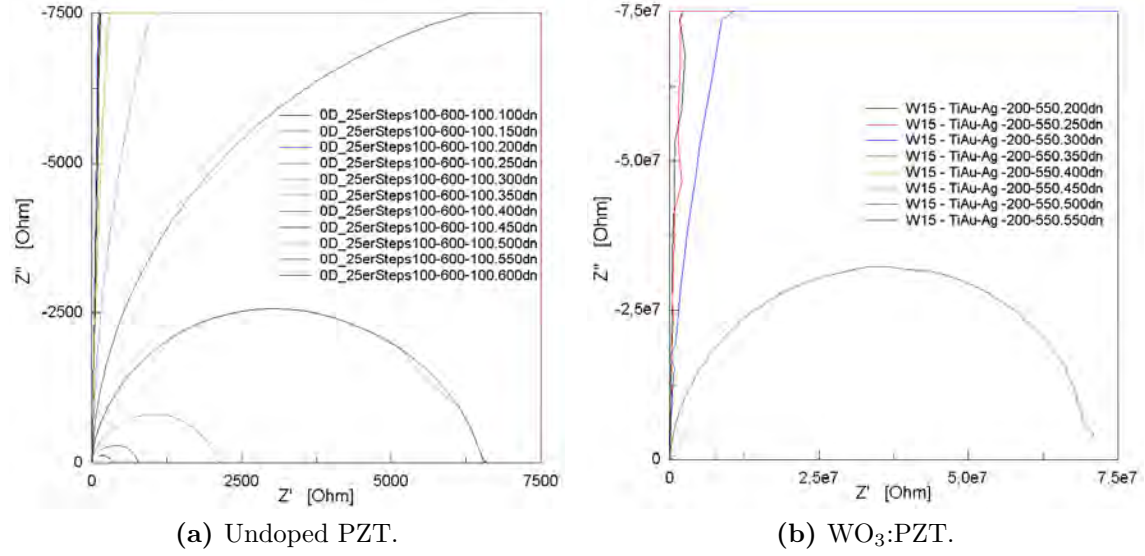


Figure 6.1: Impedance spectra of some macroscopic PZT samples in the temperature range of 100 °C to 600 °C.

sample temperatures between 265 °C and 520 °C.

The temperature dependency of conductivity σ and capacitance C enabled the calculation of activation energies E_a (due to Eq. (2.61)), cf. Fig. 6.2 and CURIE-temperatures T_C , cf. Fig. 6.3.

Owing to

$$C = \epsilon_r \cdot \epsilon_0 \cdot \frac{A}{d} \quad (6.1)$$

the absolute permittivity $\epsilon = \epsilon_r \cdot \epsilon_0$ could be calculated from given capacitance C , area A and distance d of the parallel-plate capacitor, established by the two electrodes on the PZT disc. In this case the capacitance C was neither calculated from the relaxation frequency ($\omega_r = \frac{1}{RC}$) nor with a CNLS fitting procedure. Rather the 1 kHz value of the real part of the capacitance was used to calculate the corresponding value of the relative permittivity ϵ_r .

Because of the phase transition between the paraelectric and ferroelectric state, a peak of ϵ is expected at the CURIE-temperature T_C , cf. sec. 2.3.2 (CURIE-WEISS-law, Eq. (2.81)). Several $1/\epsilon$ vs. T plots for the samples without SrO are shown in Fig. 6.3a, with the minima indicating the CURIE-temperature T_C . The actual values of T_C were determined from the temperature at which the linear fits of the descend-

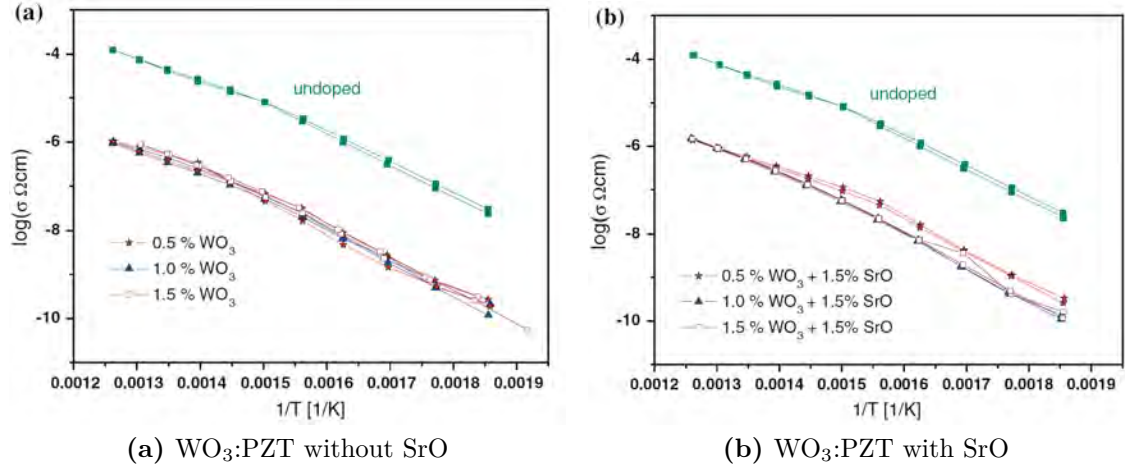


Figure 6.2: Conductivity vs. reciprocal temperature plots of undoped and SrO- and WO_3 -doped PZT

ing and ascending $1/\epsilon$ -branches for each composition intersect. The dependency of the CURIE-temperature for varying WO_3 -concentration is illustrated in 6.3b for the samples without SrO additive. In Tab. 6.1 the calculated activation energies E_a of the conductivities and CURIE-temperatures T_C are summarized.

The addition of WO_3 to the PZT decreased the conductivity by approximately two orders of magnitude (Fig. 6.2), which can be explained by the donor effect of W^{6+} substituting Ti^{4+} and thus reducing hole-conductivity in the PZT [122]. From the sample series with 1.5 % SrO the PZT with 0.5 mol% WO_3 exhibited a significantly higher conductivity below T_C ($\sim 373^\circ\text{C} = 1.55 \cdot 10^3/\text{K}$) compared to Sr-doped samples with higher WO_3 content (Fig. 6.2b) and the samples without any SrO (Fig. 6.2a). Obviously, SrO counteracts the donor effect of WO_3 in this molar ratio, which might suggest, that a part of Sr^{2+} indeed acts as an acceptor on B-sites (Zr, Ti) thus compensating the conductivity limiting donor effect of W^{6+} .

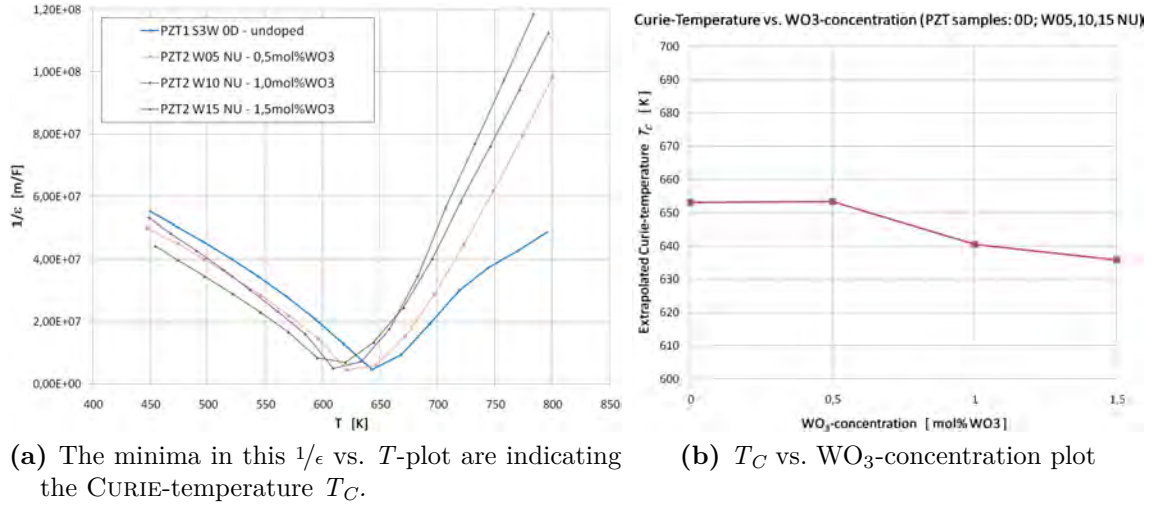


Figure 6.3: Evaluation of WO_3 -doped PZT samples without SrO additive.

Sample	E_a (below T_C) [eV]	T_C [°C]	E_a (above T_C) [eV]
Pb(Zr _{0.525} Ti _{0.475})O ₃ (PZT)	1.43	381	0.98
PZT + 0.5 % WO ₃	4.45	379	1.05
PZT + 1.0 % WO ₃	1.44	379	1.08
PZT + 1.5 % WO ₃	1.41	374	1.22
PZT + 1.5 % SrO + 0.5 % WO ₃	1.50	376	1.00
PZT + 1.5 % SrO + 1.0 % WO ₃	1.50	362	1.21
PZT + 1.5 % SrO + 1.5 % WO ₃	1.50	363	1.21

Table 6.1: Activation energies E_a and CURIE-temperatures T_C of PZT samples with WO_3 and SrO additive.

6.1.2 Nd-doped PZT discs

The impedance of macroscopic 2 % Nd-doped $\text{Pb}(\text{Zr}_{0,5515}\text{Ti}_{0,4485})\text{O}_3$ -discs without any interdigit electrodes was investigated with respect to voltage and temperature. The samples of the dimension $\sim 2\text{ mm} \times \varnothing 12\text{ mm}$ were supplied by the EPC-TDK Corporation, Deutschlandsberg. Some of them were already prepared for electrical measurements with a thin (sputtered) layer of Ag on both sides. For our experiments 20 nm Cr and $\sim 200\text{ nm}$ Au were (cold-) sputtered on both PZT-surfaces. NYQUIST-plots of the macroscopic samples showed almost perfect semicircles (at least above 300°C), similar to those of the W/Sr-doped samples illustrated in Fig. 6.1. Hence, the resistance R could easily be gained by extrapolating the semicircle to its low-frequency intersection with the (real) x -axis, or by CNLS fitting with an R//CPE equivalent circuit.

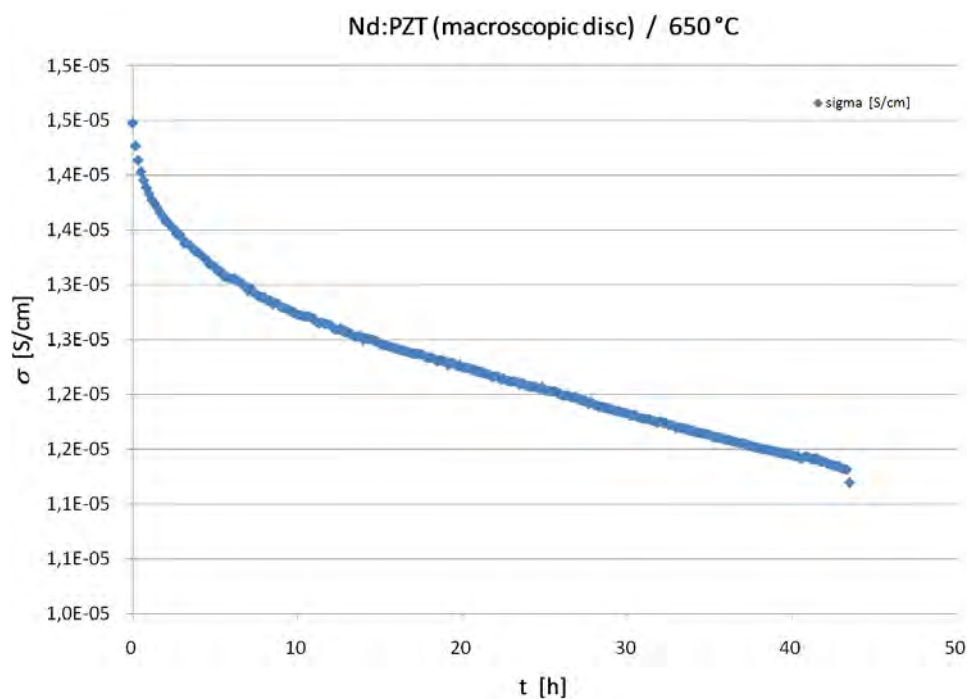


Figure 6.4: Macroscopic Nd:PZT at 650°C without any dc -load. Confer with the 450°C -equilibration curve in Fig. 4.7.

One sample was held at 650°C without any dc -load for more than 40 hours, to investigate a possible equilibration effect in air. Actually the conductivity σ showed a decrease (Fig. 6.4) resembling the equilibration behavior (conductivity loss) of the $75\text{ }\mu\text{m}$ Nd:PZT(Cu)-layers, illustrated in Fig. 4.7, though less pronounced. Since at 450°C (Nd:PZT(Cu)) and 650°C (2 % Nd-doped $\text{Pb}(\text{Zr}_{0,5515}\text{Ti}_{0,4485})\text{O}_3$ -disc) the

first major drop seems to be completed within similar time scales (~ 50 h), it is suggested, that in the latter case (at 650°C) cation vacancy (V_{Pb}'') motion rather than oxygen (vacancy) equilibration is involved.

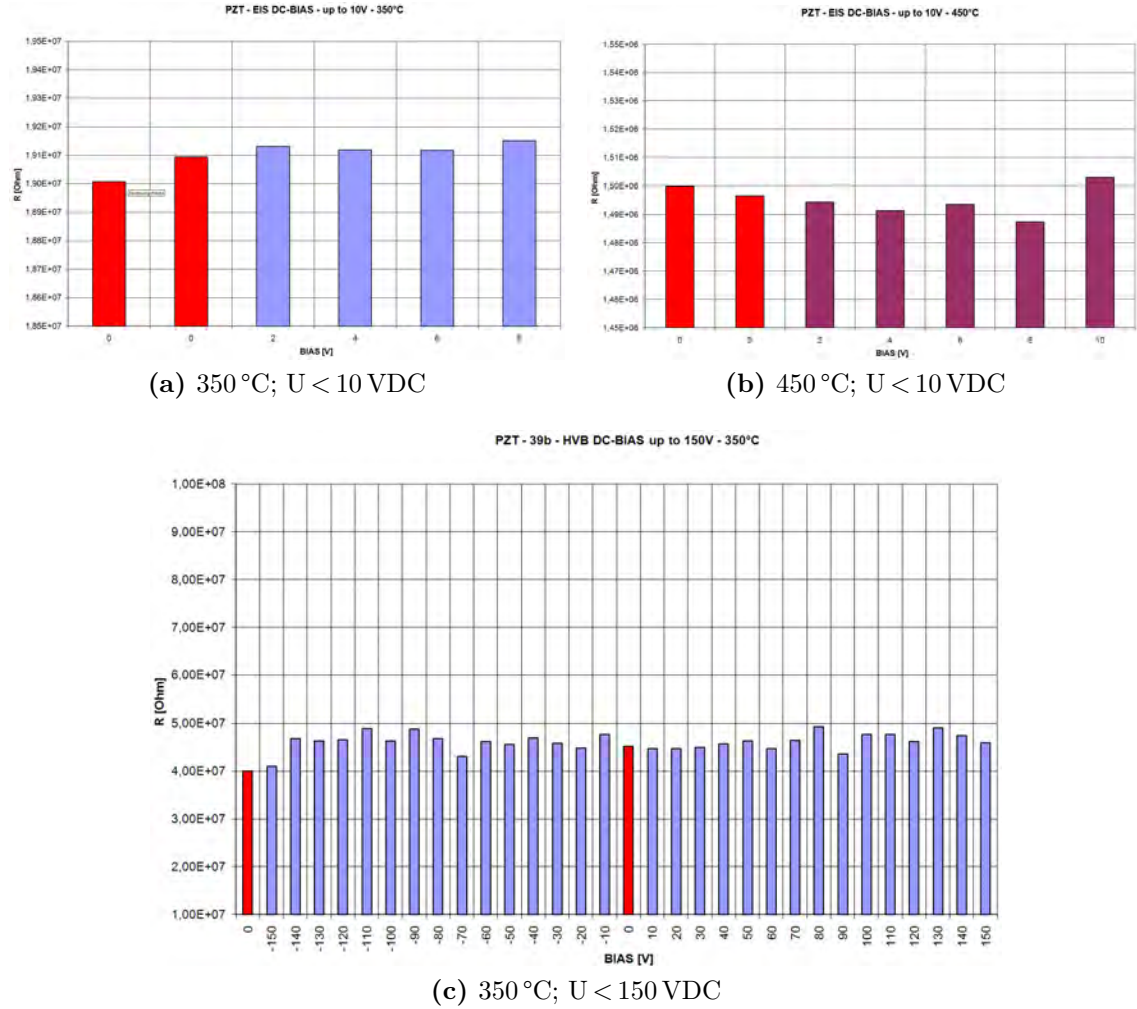


Figure 6.5: Resistance of macroscopic Nd:PZT vs. dc -bias-voltage, measured by ac -EIS with dc -offset.

On other samples a possible nonlinear I - U -behavior was probed, but neither at small voltages (< 10 V) nor at high voltages (< 150 V) a significant deviation from the zero- dc value of the impedance could be found, cf. Fig. 6.5. Since at the $75\ \mu\text{m}$ PZT layers of multilayer stacks only the highest fields induced (small) nonlinear behavior, it is not surprising that similar voltages at much thicker (~ 2 mm) samples cannot cause comparable effects. Measurements were done by EIS with a dc -bias offset.

6.2 Complete (full)stacks

Fullstacks are those complete functional multilayer stacks, from which the stack segments for the single-layer measurements in chapter 4 were cut. Accordingly *fullstacks* are of exactly the same composition, but as already explained in sec. 3.1, they consist of ~ 350 single layers of Nd:PZT, hard-wired via Cu or Ag/Pd interdigit electrodes in a parallel connection. Hence, when applying a voltage between the two current collectors (contact stripes), each layer is stressed by the same voltage as when the experiment is performed on a single layer (like in chapter 4 and chapter 5). So, the voltage drop per layer is still the same as in Tab. 3.1, but due to the changed geometry the electrode area is increased to $350 \times \sim 6 \times 6 \text{ mm}^2$. An example of a virgin multilayer stack is illustrated in Fig. 6.6.

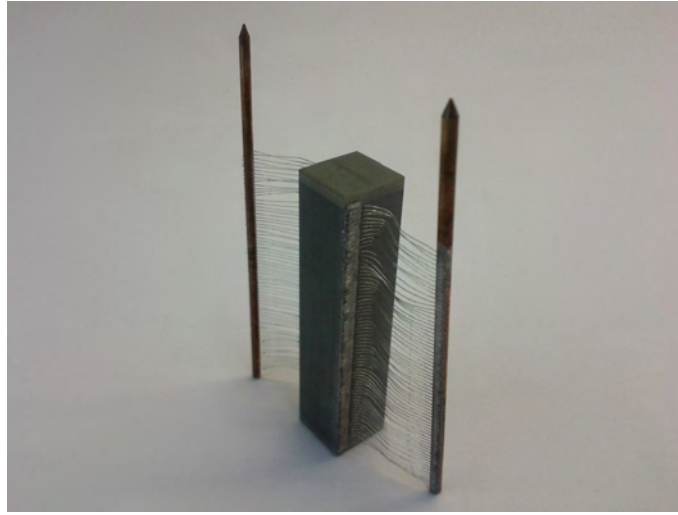


Figure 6.6: A Nd:PZT(AgPd)-fullstack

Since the resistance R of 350 parallel wired layers of Nd:PZT due to

$$\frac{1}{R} = \sum_{i=1}^{350} \frac{1}{R_i} = 350 \cdot \frac{\sigma \cdot A}{l} \quad (6.2)$$

is much smaller than the resistance of a single layer R_i , measurements at significantly lower temperatures are possible, and thus much smaller conductivities σ can still be investigated (l ... distance between interdigit two electrodes ($75 \mu\text{m}$); A ... overlapping area of interdigit electrodes).

Nd:PZT(Cu)- and Nd:PZT(AgPd)-fullstacks did show rather ideal semicircles in

the NYQUIST-plots in the temperature range between 200 °C and 530 °C, cf. Fig. 6.7. CNLS fitting with an R//CPE equivalent circuit allowed the calculation of resistance and conductivity. Due to the rapid conductivity change at high-fields it was difficult to measure a stationary *ac*-impedance value with an offset *dc*-load. However, the resistance turned out to be only slightly voltage-dependent for temperatures below T_C and voltages from 0 VDC to 130 VDC, cf. Fig. 6.7c.

From the temperature dependent conductivities activation energies E_a were calculated, cf. Fig. 6.8. The resulting values are $E_a = 1.26$ eV above the CURIE-temperature and $E_a = 1.57$ eV below T_C for the Nd:PZT(Cu)-fullstack. Since no clear bend was found at the temperature dependent conductivity of the Nd:PZT(AgPd)-fullstack the whole temperature range was fitted, leading to an activation energy of $E_a = 0.98$ eV.

On Nd:PZT(Cu)-fullstacks reversible degradation phenomena could be observed only within a small temperature range and the (early reached) current-limit rendered the investigation of significant conductivity variations impossible. Accordingly the focus of this thesis was on single-layer measurements as described in chapter 4. Nd:PZT(AgPd)-fullstacks turned out to be even less stable under high-field *dc*-load. Most breakdowns on AgPd-fullstacks occurred already immediately after switching on a voltage >50 VDC in the temperature range between 250 °C and 300 °C, regularly accompanied by heavy disintegration (multiple craters and stack-fractures) of the fullstack. Hence, single-layer measurements were the preferred way to analyze the Nd:PZT(AgPd) composition, as described in chapter 5.

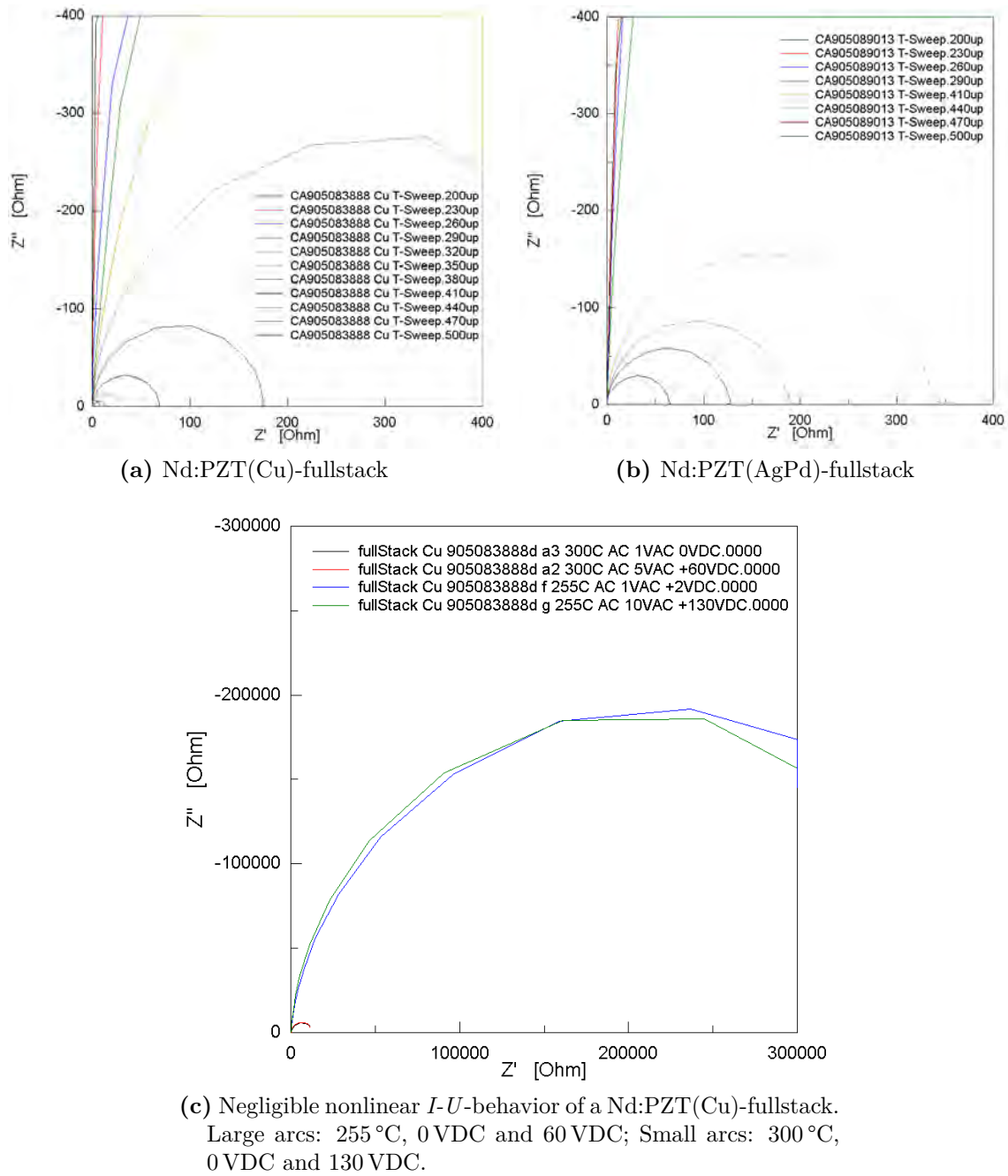


Figure 6.7: Impedance spectra of fullstacks in the temperature range from 200 °C to 530 °C: (a)-(b); The temperature is indicated in the labels. Voltage dependence of the impedance (c).

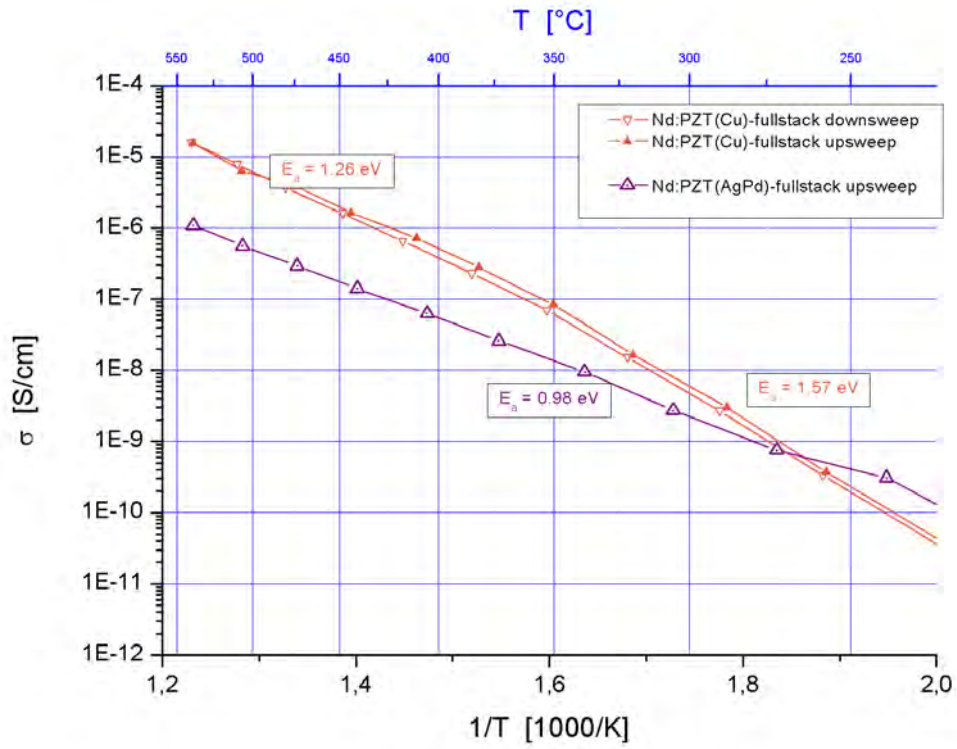


Figure 6.8: ARRHENIUS-plots Nd:PZT(Cu)-fullstacks (orange) and Nd:PZT(AgPd)-fullstacks (violet).

6.3 PZT samples with microelectrodes

For spatially resolved impedance measurements microelectrodes - lithographically applied to the surface - can be utilized, cf. Fig. 6.9. Evaluation is then performed by the spreading resistance formula (Eq. (3.4)). See also Ref. [59]. Such highly spatially resolved experiments were performed on many PZT samples with and without interdigit electrodes, e. g. for the purpose of locating inhomogeneities or inducing locally very high electric fields. Nd:PZT top-face cover plates (german: “*Deckplatten*”) from Nd:PZT(AgPd)-fullstacks, but without interdigit electrodes (see sec. 3.1) were delivered by EPC-TDK Corporation, Deutschlandsberg (Austria). 20 nm Cr / 200 nm Au bilayers sputtered on the surface were microstructured by a negative photoresist lift-off procedure. Circular microelectrodes with diameters in the range of 10 μm and 200 μm were created.

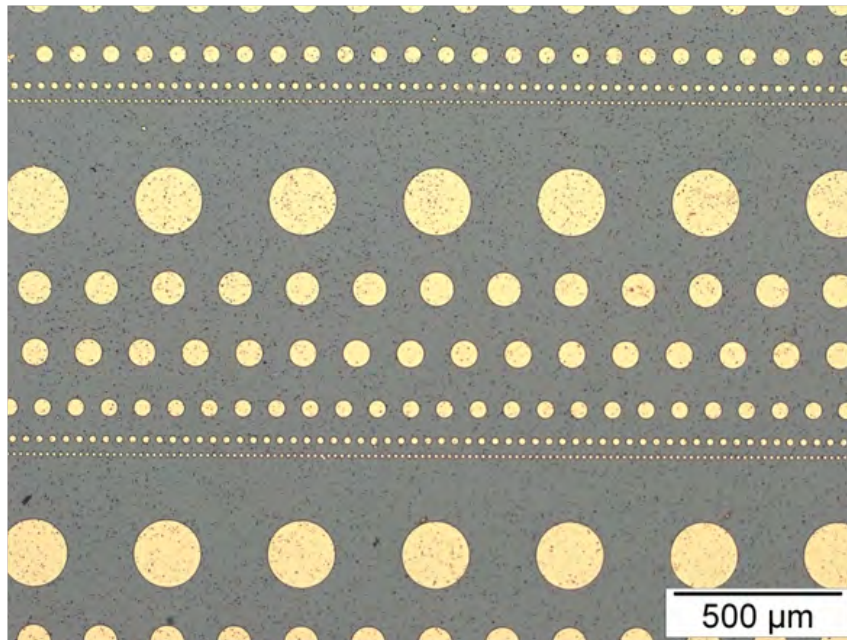
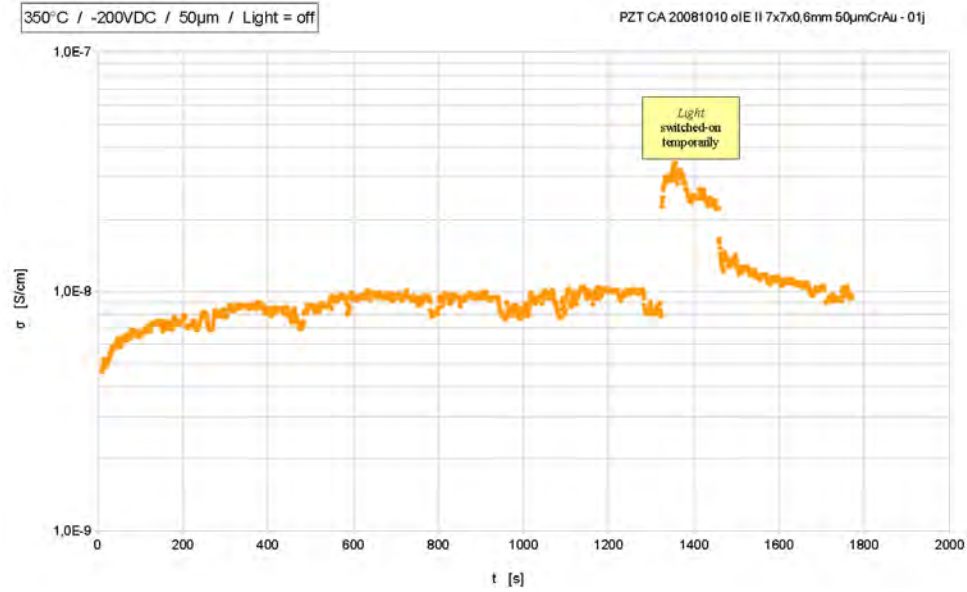


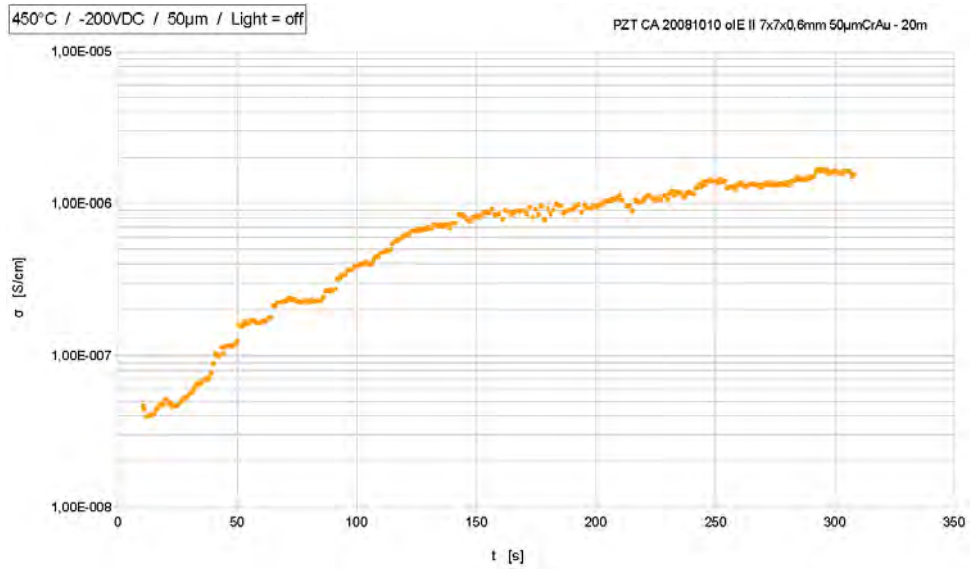
Figure 6.9: Bilayer (20 nm Cr / 200 nm Au) microelectrodes with diameters from 10 μm to 200 μm on the surface of a PZT sample.

6.3.1 High-voltage experiments on microelectrodes

High-voltage conductivity measurements were conducted at elevated temperatures between 350 $^{\circ}\text{C}$ and 450 $^{\circ}\text{C}$.



(a) 350 °C



(b) 450 °C

Figure 6.10: Conductivity variation of Nd:PZT top-face cover plates with superficial microelectrodes of 50 μm diameter polarized by −200 VDC vs. a pseudo-infinite counter-electrode at 350 °C (a) and 450 °C (b). Note the coincidence of switching-on the microscope-light and simultaneous increase of conductivity at the measurement at 350 °C (a).

Already at 350 °C, but becoming more pronounced at 450 °C, an *increase* of conductivity could be observed after applying -200V *dc*-load to the microelectrode. An increase of leakage current was also observed at single Nd:PZT(AgPd)-layers, cf. chapter 5. At 450 °C the conductivity during the high-field phase *increases* from $4 \times 10^{-8} \text{ S/cm}$ ($2.5 \text{ G}\Omega$) to $2 \times 10^{-6} \text{ S/cm}$ ($60 \text{ M}\Omega$).

In Fig. 6.11 the impedance spectra *before* and *after* the high-voltage experiment of Fig. 6.10b are illustrated.

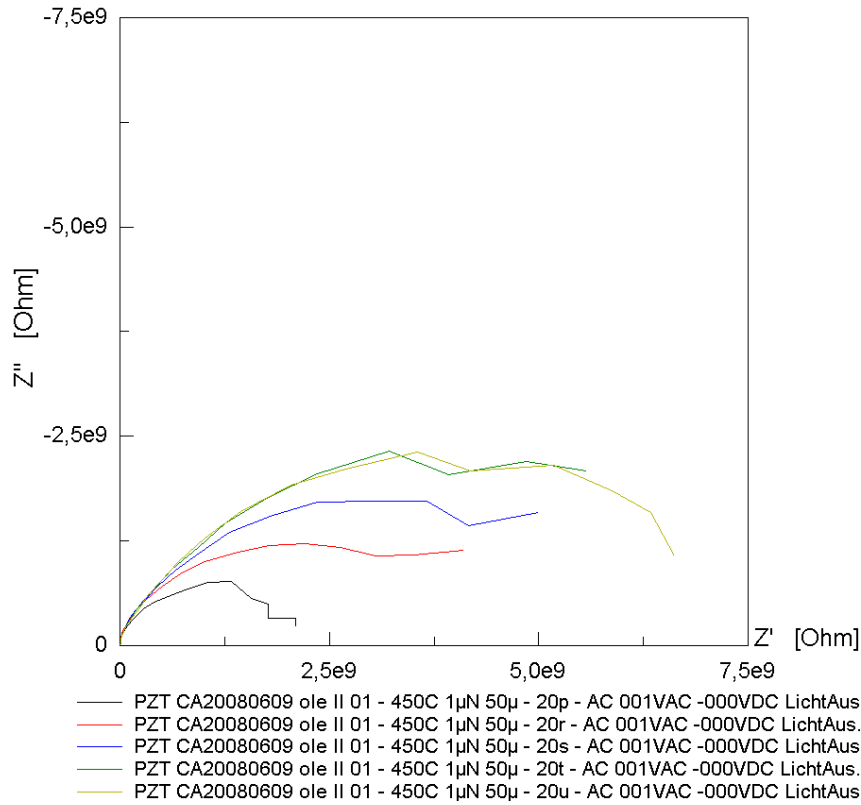


Figure 6.11: 1VAC / 0VDC impedance spectra before (black) and after (red, blue, green, yellow) the exposure of a $\varnothing 50 \mu\text{m}$ CrAu-microelectrode to -200 VDC (450 °C). After the red spectra the blue, green and finally the yellow one has been recorded with one minute in between, respectively. Microscope light was switched-off.

Surprisingly, small-signal *ac*-impedance measurements indicated a conductivity *decrease* by the high-voltage stress. Obviously the small-signal *ac*-investigation shows the very opposite conductivity behavior, compared with the high-voltage experiment in Fig. 6.10b: While the latter displays a pronounced resistance degradation from $2.50 \text{ G}\Omega$ to $0.06 \text{ G}\Omega$ under high-field load, the former clearly shows a small-signal resistance increase from $2.10 \text{ G}\Omega$ to $>7 \text{ G}\Omega$.

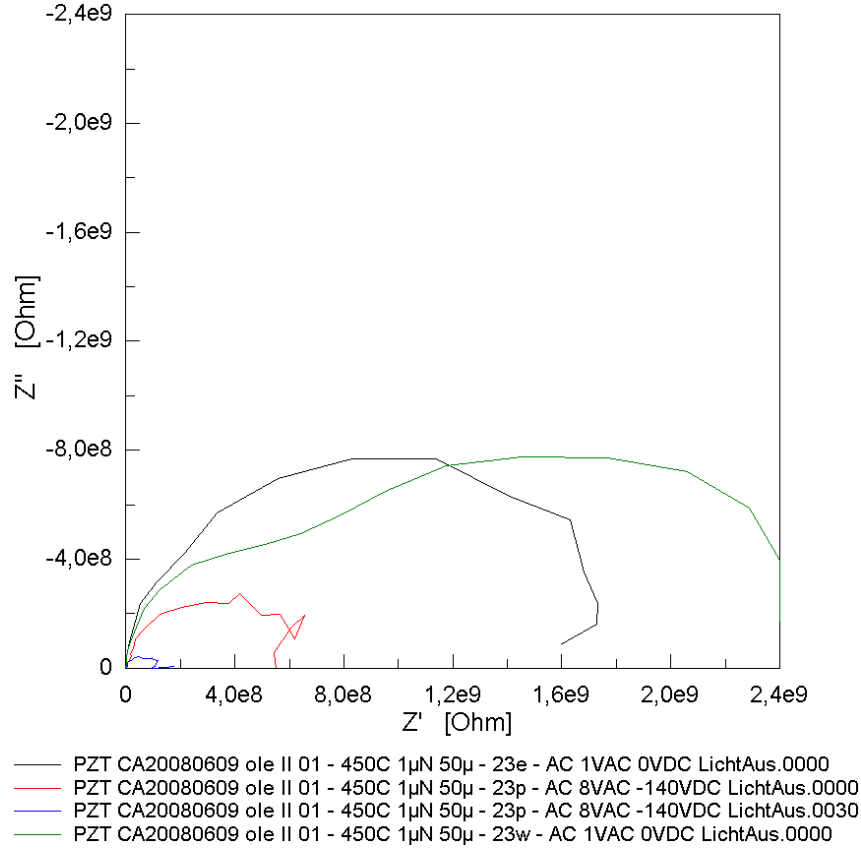


Figure 6.12: NYQUIST-plots of 50 μm microelectrodes under 0 VDC (black, green) and 140 VDC (red, blue) at 450 $^{\circ}\text{C}$. Prior to any high-field stress a first 0 VDC impedance was recorded (black): 1.8 $\text{G}\Omega$. Immediately after applying -140 VDC a high-field Nyquist-plot was recorded (red): 0.6 $\text{G}\Omega$. After 80 min -140 VDC-load the last high-field impedance spectra was recorded (blue): 0.1 $\text{G}\Omega$. After the high-voltage stress a final 0 VDC impedance was recorded (green): 2.5 $\text{G}\Omega$.

The same result was obtained for a high-voltage experiment fully monitored by *ac*-impedance measurements, cf. Fig. 6.12: While the *conductivity* during the high-field phase (-140 VDC) *increased* (0.6 $\text{G}\Omega \rightarrow 0.1 \text{ G}\Omega$), zero-bias (0 VDC) *ac*-impedance measurements before and after the high-voltage period indicated an overall *conductivity decrease* (1.8 $\text{G}\Omega \rightarrow 2.5 \text{ G}\Omega$). Since this might be due to a heavily pronounced current-voltage nonlinearity, *I-U*-plots of microelectrodes on PZT have been recorded, cf. Fig. 6.13.

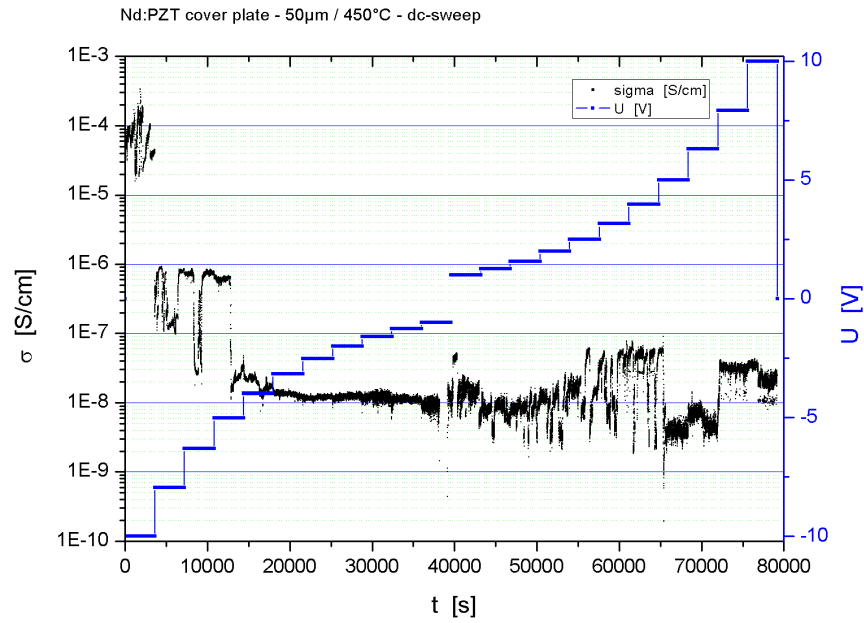
With respect to the quite unconventional conductivity-voltage dependencies in Fig. 6.13, two remarks have to be made:

1. Although single NYQUIST-plots did show quite good semicircles, the scattering of the conductivity-values of continuous *dc*-measurements is very pronounced.

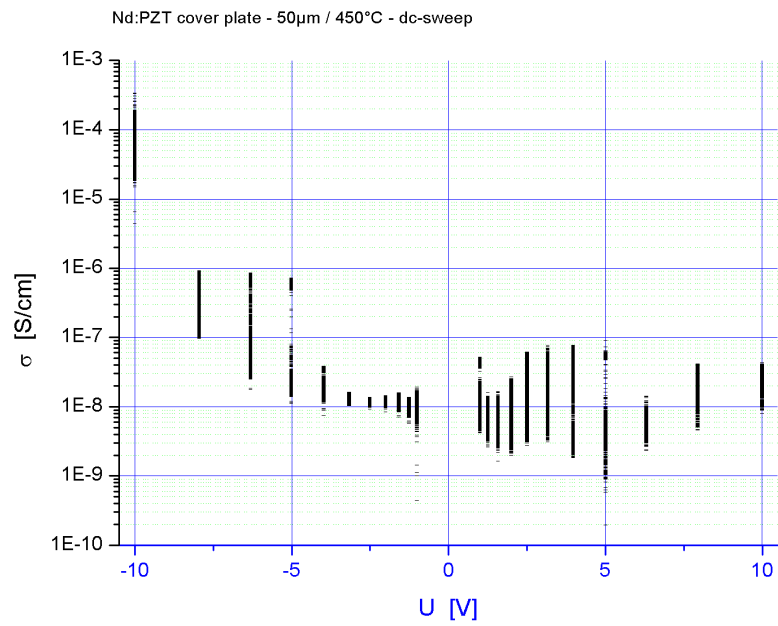
This scattering may explain the discrepancy between pre- and post-high-field impedance measurements.

2. Besides the pronounced scattering, one can recognize an asymmetric tendency in the conductivity vs. voltage plot: Obviously the *cathodically* (<0 VDC) polarized microelectrode displays much higher conductivities, than the same microelectrode in an *anodic* state (>0 VDC). This is not surprising, since the geometry of a small microelectrode versus a pseudo-infinite counterelectrode is asymmetric by definition. Hence, the overall conductivity is necessarily more determined by the polarization state of the microelectrode than by changes at the counterelectrode). It has to be clarified in future whether this asymmetry can fully explain the mentioned difference between *ac*- and *dc*-conductivity during/after high-voltage load.

Despite these highly interesting observations, such microelectrode measurements were not continued in this work. However, the results mentioned in this section may be an inspiration for a more systematic investigation using microelectrodes on PZT.



(a) Conductivity σ (black) and voltage U (blue) versus time t .



(b) Conductivity σ vs. voltage U .

Figure 6.13: Probing of nonlinear I - U -behavior of Nd:PZT cover-plates with 50 μm microelectrodes at 450 $^{\circ}\text{C}$ in the voltage range from -10 VDC to $+10$ VDC.

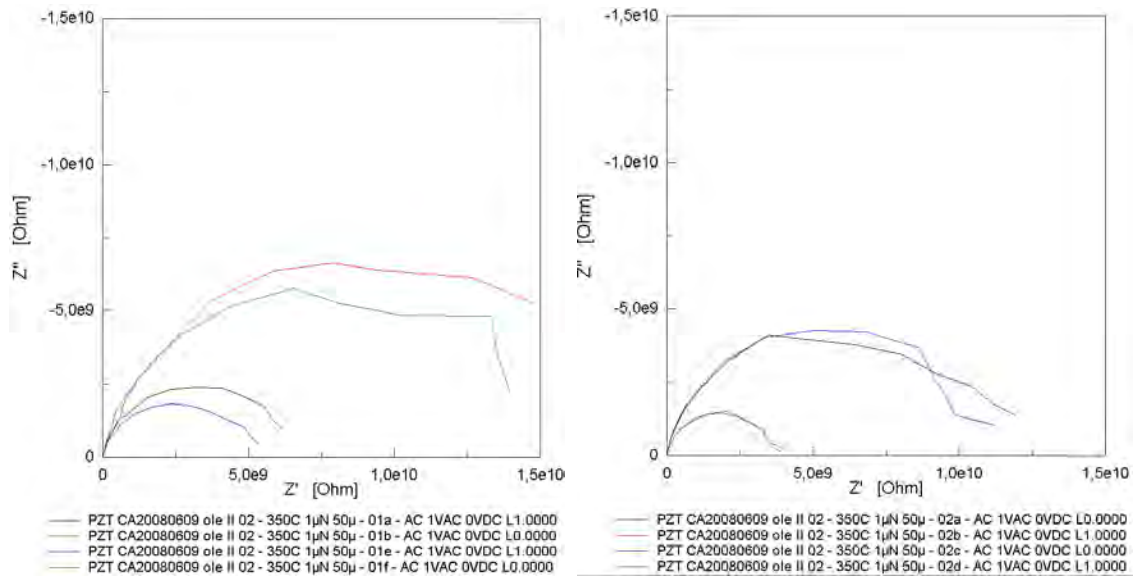
6.3.2 Light-effect

Since microelectrode measurements were performed under a reflected-light microscope, it could be investigated how far local conductivity measurements are sensitive to the microscope light. Indeed, already in Fig. 6.10a a significant light sensitivity can clearly be recognized.

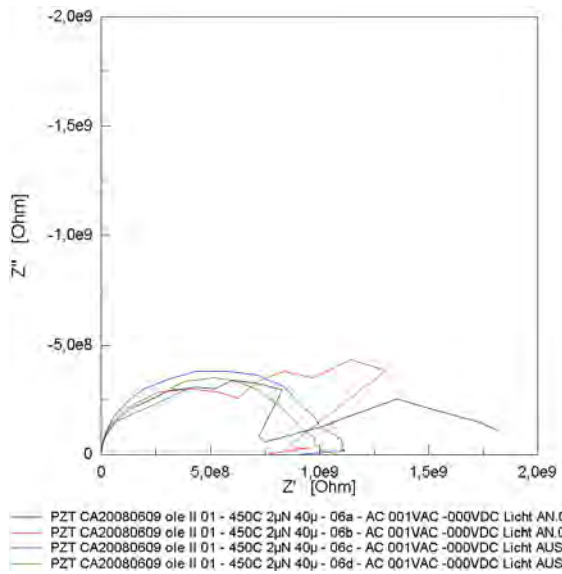
Just by switching-on the microscope light and thus illuminating the very microelectrode under investigation, the resistance R decreased down to $\sim 30\%$ of the value measured with the microscope-light switched-off, cf. Fig. 6.14. This phenomenon could be easily reproduced at 350°C . At 450°C , however, the only significant effect of the microscope-light being switched-on seems to be a more pronounced scattering of the impedance data.

These measurements indicate that most probably electronic (e' or h') conduction prevails at 350°C : Additional charge carriers are generated by the photoelectric effect and thus enhance the electronic conductivity. Modification of ionic conduction by light is on no account expected.

At 450°C either all possibly light-generated charge carriers are already thermally excited and any effect is too small to be measured by our experimental setup or ionic conduction begins to dominate the total conductivity or the conductivity is now governed by any other unknown effect not sensitive to light, e. g. if grain boundary conductivity is involved.



(a) 350 °C. Light off (red, green) vs. light on (blue, black). (b) 350 °C. Light off (blue, black) vs. light on (red, green).



(c) 450 °C. Light off (blue, green) vs. light on (red, black).

Figure 6.14: Light-sensitivity of PZT, determined with superficial Cr/Au micro-electrodes at 350 °C (a,b) and 450 °C (c).

7 Conclusions

Short- and long-term conductivity measurements on individual 75 μm thick layers of positively (Nd-donor) doped PZT piezoactuator stack segments were investigated in the temperature range from 350 °C to 500 °C. The setup allowed the application of high-electrical fields (up to 2.67 V/m) on the material and made numerous experiments on nominally identical PZT compositions possible.

Nd:PZT(Cu) In *air*, samples with Cu interdigit electrodes (Nd:PZT(Cu)) showed in a first short-term high-voltage phase a significant thermally activated conductivity *decrease* down to a conductivity minimum: The higher the voltage, the faster the *ARRHENIUS*-activated conductivity decrease. Switching-off the high-field at the minimum leads to a slower, but also thermally activated, *increase* of the conductivity.

Without any external voltage load the concentration of oxygen vacancies ($V_{\text{O}}^{\bullet\bullet}$) is expected to be homogeneously distributed within the (nonstoichiometric) PZT. For (at least partially) ionically blocking electrodes, oxygen vacancies accumulate at the cathode (\ominus) and deplete at the anode (\oplus). Such a voltage-triggered gradient of spatial defect distribution is well-known as *stoichiometry polarization*. A quantitative comparison of the activation energies and time constants of the conductivity variations in Nd:PZT(Cu) with that of other stoichiometrically polarized materials, such as negatively (acceptor) doped SrTiO_3 , suggested that $V_{\text{O}}^{\bullet\bullet}$ -driven stoichiometry polarization indeed takes place in our Nd:PZT(Cu) layers under *dc*-field stress. Calculated *chemical diffusion coefficients of oxygen* (D_{O}^{δ}) and *self-diffusion coefficients of oxygen vacancies* ($D_{V_{\text{O}}^{\bullet\bullet}}^{\sigma}$) fit well between those of similar materials. Although Nd:PZT is positively (donor) doped and accordingly positive oxygen vacancies are *prima facie* not expected to compensate the positive $(\text{Nd}^{3+})_{\text{Pb}^{2+}}$ -donor charge, the unquantified - but in any case significant - PbO evaporation during sintering, clearly boosts oxygen removal despite donor doping. Hence, the observed conductivity de-

crease under high-field fits well to an V_{O} -induced electron conductivity variation due to stoichiometric polarization. The subsequent field-free conductivity relaxation is assumed to correspond to the chemical diffusion of the oxygen vacancies back to equilibrium. However, it is an open question whether the suggested V_{O} -motion (between 350 °C and 500 °C) mainly occurs along/near grain boundaries or in the grain interior.

Keeping the high-voltage switched-on beyond the conductivity minimum, a long-term resistance degradation (conductivity increase) behavior was observed, which mostly ended with an electrical breakdown. Also this degradation rate was thermally activated and voltage-dependent. If long-term high-field degradation was interrupted before any breakdown occurred, an immediate conductivity relaxation could be observed. Some evidence was found, that most layers that have suffered an electrical breakthrough thermally recovered from their quasi-short-circuit conductivity immediately after breakdown. However, some few layers did not display such a recovery behavior after breakdown; furthermore, they showed high conductivities not only at elevated temperatures, but also at room-temperature. Since grinding-off ca. $\sim 100\text{ }\mu\text{m}$ from the surface restored the initial conductivity, it is assumed that locally separated conduction-paths might cause the long-term resistance degradation process. Indeed, after polishing-off the breakdown-triggered “craters” on some samples, Cu-precipitates were found in some distance of the (former) Cu interdigit electrode region. Already during the short-term high-field phase (before the conductivity minimum) a darkening of the stressed layer was observed. Long-term experiments revealed that this “blackening” intensifies mostly with time (and only to a less degree with voltage). No blackened front, moving from one electrode to the other, was ever observed. Also the blackening was not a superficial effect. Annealing the sample at elevated temperatures ($\geq 500\text{ }^{\circ}\text{C}$) for longer times again bleached the darkened layer, at least on the surface.

Nd:PZT(AgPd) Samples with interdigit electrodes made of 80 % Ag and 20 % Pd (Nd:PZT(AgPd)) showed a conductivity *increase* under high-field stress until an electrical breakdown determined the end of the high-voltage phase. During long-term *dc*-load in *air*, characteristic phenomena such as dendritic droplet growth, blackening, current-fluctuations, cracks and finally crater-accompanied breakdowns occurred. Current (conductivity) fluctuations started in the last two thirds of the degradation curve before breakdown. Approximately in the last third of the degrada-

tion process of Nd:PZT(AgPd) in air, sudden “cracks” appeared within the dendritic structures, which turned out to be riverbed-like planar offsets and may be precursors of breakdown-craters. Finally, the stressed Nd:PZT(AgPd)-layers exhibited an electrical breakdown, accompanied by crater formation. In Ar- and H₂-atmosphere neither blackening, dendritic droplet-growth nor blackening was observed. However, the conductivity behavior under high-field stress was still almost completely identical to that of Nd:PZT(AgPd) in air.

The structures termed “dendrites” turned out to consist of Ag-droplets. The structures grew with proceeding time under *dc*-voltage from the anode (\oplus) to the cathode (\ominus) (and not backwards, as one would expect for electrochemical dendrite-growth). However, the dendrites did not seem to be responsible for the final breakdown, since firstly, breakdowns did also occur in the very same way in low $p(\text{O}_2)$ -atmospheres, where almost no dendritic growth has been observed, and secondly, breakdowns did not necessarily occur even at the time when the dendrites had already reached the cathode (at low *dc*-voltages). In air, a blackening of *dc*-stressed layers was observed, similar to the blackening of Nd:PZT(Cu). After degradation in H₂, SEM/EDX analysis revealed Pb-precipitates within *dc*-stressed layers, offside the interdigit-electrode region, which might play a role in the breakdown process. Long-term monitoring of a Nd:PZT(AgPd)-layer after breakdown in H₂ gave evidence for a purely thermal recovery from the quasi short-circuit post-breakdown conductivity.

Exact degradation mechanisms can not be suggested yet, based on these studies. Defect chemical changes and defect motion may cause precipitates as well as relaxation processes and are thus believed to play a major role, however.

Outlook Since almost all results discussed in this work supported the relevance of oxygen-vacancies dominated defect chemistry of even positively (Nd-donor) doped PZT, further research with a more detailed focus on equilibration behavior in different atmospheres is necessary to approach a quantitative BROUWER-diagram of Nd:PZT. Also the conductivity mechanism of PZT is far from being understood: The role of grain boundaries and the transference number of ionic vs. electronic conductivity is still unclear. Very important, but though also insufficiently understood, is the degradation/breakdown mechanism of Nd:PZT(Cu) and Nd:PZT(AgPd) multi-layer piezostacks. More detailed long-term degradation experiments with subsequent

post-breakdown observations have to be done. In this context the possibility of a local highly conductive breakdown path has to be checked.

Acknowledgments

As this thesis grew under extraordinary adverse circumstances, exceptional acknowledge owns to Jürgen Fleig, whose conduct supported me for more than four years and who made a finalization of this research project possible.

Of course I also have to thank all members of the (most likely) best research group of the world: Any of them helped me with his or her specific kind of support to finish my thesis: Martin Ahrens, David Glück, Alex Opitz, Till Frömling, Matthias Gerstl, Lukas Andrejs, Judith Januschewsky, Philipp Hillebrand, Christian Maurer, Markus Kubicek, Susi Strobl, Tobias Huber, Arno Schintlmeister and a lot of other researchers and employees of the Institute of Chemical Technologies and Analytics (CTA). Especially Elisabeth Eitenberger from the scanning electron microscopy (SEM) unit and Wolfgang “*Tschilp*” Tomischko from the same CTA-department always helped me when needed, with good and quick advice.

Klaus Reichmann, from the Graz University of Technology also supported me occasionally with inspiring discussions.

Finally I have to thank TDK-EPC (formerly: EPCOS), Deutschlandsberg, the Vienna University of Technology and the Graz University of Technology who set up the necessary organizational and financial research framework in the name of the Christian Doppler Laboratory of Ferroic Materials.

This thesis was designed by L^AT_EX, with the help of L^YX 2.0.0 and *zotero*-plugin for Mozilla Firefox.

Bibliography

- [1] R. W. Schwartz, J. Ballato, and G. H. Haertling, “Piezoelectric and electro-optic ceramics,” *Ceramic Materials for Electronics*, p. 207–315, 2004.
- [2] R. N. Torah, S. P. Beeby, M. J. Tudor, and N. M. White, “Thick-film piezoceramics and devices,” *Journal of Electroceramics*, vol. 19, pp. 97–112, Feb. 2007.
- [3] G. H. Haertling, “Ferroelectric ceramics: History and technology,” *Journal of the American Ceramic Society*, vol. 82, pp. 797–818, Apr. 1999.
- [4] D. M. Smyth, “Defect structure in perovskite titanates,” *Current Opinion in Solid State and Materials Science*, vol. 1, pp. 692–697, Oct. 1996.
- [5] I. Denk, W. Münch, and J. Maier, “Partial conductivities in SrTiO₃: bulk polarization experiments, oxygen concentration cell measurements, and Defect-Chemical modeling,” *Journal of the American Ceramic Society*, vol. 78, no. 12, p. 3265–3272, 1995.
- [6] R. Merkle and J. Maier, “Oxygen incorporation into Fe-doped SrTiO₃: mechanistic interpretation of the surface reaction,” *Physical Chemistry Chemical Physics*, vol. 4, pp. 4140–4148, Aug. 2002.
- [7] R. A. De Souza, J. Fleig, R. Merkle, and J. Maier, “SrTiO₃: a model electroceramic,” *Zeitschrift für Metallkunde / Materials Research and Advanced Techniques*, vol. 94, no. 3, pp. 218–225, 2003.
- [8] R. A. Souza, J. Fleig, J. Maier, O. Kienzle, Z. Zhang, W. Sigle, and M. Rühle, “Electrical and structural characterization of a Low-Angle tilt grain boundary in Iron-Doped strontium titanate,” *Journal of the American Ceramic Society*, vol. 86, pp. 922–928, June 2003.
- [9] M. Vollmann, R. Hagenbeck, and R. Waser, “Grain-Boundary defect chemistry of Acceptor-Doped titanates: Inversion layer and Low-Field conduction,” *Journal of the American Ceramic Society*, vol. 80, pp. 2301–2314, Sept. 1997.

-
- [10] R. Waser, "Bulk conductivity and defect chemistry of Acceptor-Doped strontium titanate in the quenched state," *Journal of the American Ceramic Society*, vol. 74, pp. 1934–1940, Aug. 1991.
- [11] R. Meyer, R. Waser, J. Helmbold, and G. Borchardt, "Cationic surface segregation in donor-doped SrTiO₃ under oxidizing conditions," *Journal of electroceramics*, vol. 9, no. 2, p. 101–110, 2002.
- [12] J. Daniels and R. Wernicke, "New aspects of an improved PTC model," *Philips Res. Repts*, vol. 31, no. 5, p. 544–559, 1976.
- [13] S. Rodewald, J. Fleig, and J. Maier, "Microcontact impedance spectroscopy at single grain boundaries in Fe-Doped SrTiO₃ polycrystals," *Journal of the American Ceramic Society*, vol. 84, pp. 521–530, Mar. 2001.
- [14] H. Kwon, H. Yoo, C. Kim, and K. Hur, "Semiconductor-to-insulator transition of undoped-BaTiO₃ in quenched state," *Journal of Applied Physics*, vol. 107, pp. 083702–083702–5, Apr. 2010.
- [15] C. Shin, H. Yoo, and C. Lee, "Al-doped SrTiO₃: part i, anomalous oxygen nonstoichiometry," *Solid State Ionics*, vol. 178, pp. 1081–1087, June 2007.
- [16] H. Yoo and C. Lee, "Two-Fold diffusion kinetics of oxygen Re-Equilibration in Donor-Doped BaTiO₃," *Journal of the American Ceramic Society*, vol. 88, pp. 617–623, Mar. 2005.
- [17] R. Moos and K. H. Hardtl, "Defect chemistry of Donor-Doped and undoped strontium titanate ceramics between 1000° and 1400°C," *Journal of the American Ceramic Society*, vol. 80, pp. 2549–2562, Oct. 1997.
- [18] G. M. Choi and H. L. Tuller, "Defect structure and electrical properties of Single-Crystal Ba_{0.03}Sr_{0.97}TiO₃," *Journal of the American Ceramic Society*, vol. 71, pp. 201–205, Apr. 1988.
- [19] J. Maier, J. Jamnik, and M. Leonhardt, "Kinetics of oxygen stoichiometry changes," *Solid State Ionics*, vol. 129, pp. 25–32, Apr. 2000.
- [20] K. Sasaki and J. Maier, "Low temperature defect chemistry of oxides," *Journal of the European Ceramic Society*, vol. 19, pp. 741–745, June 1999.
- [21] K. Becker, M. Schrader, H. Kwon, and H. Yoo, "Electrical and optical characterization of undoped BaTiO₃ in the quenched state," *Physical Chemistry Chemical Physics*, vol. 11, no. 17, p. 3082, 2009.

- [22] G. Y. Yang, E. C. Dickey, C. A. Randall, D. E. Barber, P. Pinceloup, M. A. Henderson, R. A. Hill, J. J. Beeson, and D. J. Skamser, "Oxygen nonstoichiometry and dielectric evolution of BaTiO₃. part i—improvement of insulation resistance with reoxidation," *Journal of Applied Physics*, vol. 96, no. 12, p. 7492, 2004.
- [23] I. J. Clark, F. B. Marques, and D. C. Sinclair, "The influence of grain boundary impedances on the p-type conductivity of undoped BaTiO₃ ceramics," *Journal of the European Ceramic Society*, vol. 22, pp. 579–583, Apr. 2002.
- [24] W. Preis and W. Sitte, "Electronic conductivity and chemical diffusion in n-conducting barium titanate ceramics at high temperatures," *Solid State Ionics*, vol. 177, pp. 3093–3098, Nov. 2006.
- [25] Y. Tsur and C. A. Randall, "Point defect concentrations in barium titanate revisited," *Journal of the American Ceramic Society*, vol. 84, pp. 2147–2149, Sept. 2001.
- [26] F. D. Morrison, A. M. Coats, D. C. Sinclair, and A. R. West, "Charge compensation mechanisms in la-doped BaTiO₃," *Journal of electroceramics*, vol. 6, no. 3, p. 219–232, 2001.
- [27] Y. Chiang and T. Takagi, "Grain-Boundary chemistry of barium titanate and strontium titanate: I, High-Temperature equilibrium space charge," *Journal of the American Ceramic Society*, vol. 73, pp. 3278–3285, Nov. 1990.
- [28] Y. Tsur, T. D. Dunbar, and C. A. Randall, "Crystal and defect chemistry of rare earth cations in BaTiO₃," *Journal of electroceramics*, vol. 7, no. 1, p. 25–34, 2001.
- [29] B. A. Boukamp, M. T. N. Pham, D. H. A. Blank, and H. J. M. Bouwmeester, "Ionic and electronic conductivity in lead-zirconate-titanate (PZT)," *Solid State Ionics*, vol. 170, pp. 239–254, May 2004.
- [30] M. V. Raymond and D. M. Smyth, "Defect chemistry and transport properties of pb (Zr_{1/2}Ti_{1/2}) o₃," *Integrated Ferroelectrics*, vol. 4, no. 2, p. 145–154, 1994.
- [31] M. V. Raymond and D. M. Smyth, "Defects and charge transport in perovskite ferroelectrics," *Journal of Physics and Chemistry of Solids*, vol. 57, pp. 1507–1511, Oct. 1996.

- [32] R. Wang and P. C. McIntyre, "18O tracer diffusion in Pb(Zr,Ti)O₃ thin films: A probe of local oxygen vacancy concentration," *Journal of Applied Physics*, vol. 97, pp. 023508–023508–8, Jan. 2005.
- [33] T. Izaki, H. Haneda, A. Watanabe, J. Tanaka, S. I. Shirasaki, and K. Tsuji, "Self-Diffusion of oxygen in PLZT ceramics," *Nippon Seramikkusu Kyokai Gakujutsu Ronbunshi (Journal of the Ceramic Society of Japan) (Japan)*, vol. 101, p. 133–138, 1993.
- [34] R. L. Holman and R. M. Fulrath, "Intrinsic nonstoichiometry in the lead zirconate-lead titanate system determined by knudsen effusion," *Journal of Applied Physics*, vol. 44, pp. 5227–5236, Dec. 1973.
- [35] S. Zhao, S. J. Zhang, W. Liu, N. J. Donnelly, Z. Xu, and C. A. Randall, "Time dependent dc resistance degradation in lead-based perovskites: 0.7 Pb(Mg_{1/3}Nb_{2/3})O₃-0.3 PbTiO₃," *Journal of Applied Physics*, vol. 105, pp. 053705–053705–7, Mar. 2009.
- [36] M. F. Zhang, Y. Wang, K. F. Wang, J. S. Zhu, and J. M. Liu, "Characterization of oxygen vacancies and their migration in ba-doped Pb(Zr_{0.52}Ti_{0.48})O₃ ferroelectrics," *Journal of Applied Physics*, vol. 105, pp. 061639–061639–6, Mar. 2009.
- [37] V. V. Prisedsky, V. I. Shishkovsky, and V. V. Klimov, "High-temperature electrical conductivity and point defects in lead zirconate-titanate," *Ferroelectrics*, vol. 17, no. 1, p. 465, 1978.
- [38] B. Guiffard, E. Boucher, L. Eyraud, L. Lebrun, and D. Guyomar, "Influence of donor co-doping by niobium or fluorine on the conductivity of mn doped and mg doped PZT ceramics," *Journal of the European Ceramic Society*, vol. 25, no. 12, pp. 2487–2490, 2005.
- [39] D. Kobor, B. Guiffard, L. Lebrun, A. Hajjaji, and D. Guyomar, "Oxygen vacancies effect on ionic conductivity and relaxation phenomenon in undoped and mn doped PZN-4.5PT single crystals," *Journal of Physics D: Applied Physics*, vol. 40, pp. 2920–2926, May 2007.
- [40] R. Alvarez Roca, E. R. Botero, F. Guerrero, J. D. S. Guerra, D. Garcia, and J. A. Eiras, "Effect of the sintering conditions on the electrical properties of nd³⁺ modified PLZT ceramics," *Journal of Physics D: Applied Physics*, vol. 41, p. 045410, Feb. 2008.

- [41] J. J. Dih and R. M. Fulrath, “Electrical conductivity in lead Zirconate-Titanate ceramics,” *Journal of the American Ceramic Society*, vol. 61, pp. 448–451, Sept. 1978.
- [42] J. G. Burt and R. A. Krakowski, “Oxygen concentration cell and electrical conductivity measurements on PZT ferroelectrics,” *Journal of the American Ceramic Society*, vol. 54, pp. 415–419, Sept. 1971.
- [43] A. Peláiz Barranco, F. Calderón Piñar, O. Pérez Martínez, J. De Los Santos Guerra, and I. González Carmenate, “AC behaviour and conductive mechanisms of 2 · 5 mol% La₂O₃ doped PbZr_{0.53}Ti_{0.47}O₃ ferroelectric ceramics,” *Journal of the European Ceramic Society*, vol. 19, pp. 2677–2683, Nov. 1999.
- [44] R. W. Whatmore, O. Molter, and C. P. Shaw, “Electrical properties of sb and cr-doped PbZrO₃-PbTiO₃-PbMg_{1/3}Nb_{2/3}O₃ ceramics,” *Journal of the European Ceramic Society*, vol. 23, pp. 721–728, Apr. 2003.
- [45] A. Ezis, J. G. Burt, and R. A. Krakowski, “Oxygen concentration cell measurements of ionic transport numbers in PZT ferroelectrics,” *Journal of the American Ceramic Society*, vol. 53, pp. 521–524, Sept. 1970.
- [46] N. J. Donnelly and C. A. Randall, “Mixed conduction and chemical diffusion in a Pb(Zr_{0.53},Ti_{0.47})O₃ buried capacitor structure,” *Applied Physics Letters*, vol. 96, pp. 052906–052906–3, Feb. 2010.
- [47] T. Frömling, *Oxide Ion Transport in Donor Doped Lead Zirconate Titanate*. Ph.D. thesis, Vienna University of Technology, Vienna, June 2011.
- [48] S. Gottschalk, H. Hahn, S. Flege, and A. G. Balogh, “Oxygen vacancy kinetics in ferroelectric PbZr_{0.4}Ti_{0.6}O₃,” *Journal of Applied Physics*, vol. 104, no. 11, p. 114106, 2008.
- [49] D. C. Lupascu, Y. A. Genenko, and N. Balke, “Aging in ferroelectrics,” *Journal of the American Ceramic Society*, vol. 89, pp. 224–229, Jan. 2006.
- [50] S. W. Gotmare, S. O. Leontsev, and R. E. Eitel, “Thermal degradation and aging of High-Temperature piezoelectric ceramics,” *Journal of the American Ceramic Society*, vol. 93, pp. 1965–1969, July 2010.
- [51] A. J. Moulson and J. M. Herbert, *Electroceramics: materials, properties, applications*. John Wiley and Sons, 2003.

-
- [52] R. Waser, T. Baiatu, and K. Härdtl, “dc electrical degradation of Perovskite-Type titanates: I, ceramics,” *Journal of the American Ceramic Society*, vol. 73, pp. 1645–1653, June 1990.
- [53] R. Waser, T. Baiatu, and K. Härdtl, “dc electrical degradation of Perovskite-Type titanates: II, single crystals,” *Journal of the American Ceramic Society*, vol. 73, pp. 1654–1662, June 1990.
- [54] T. Baiatu, R. Waser, and K. Härdtl, “dc electrical degradation of Perovskite-Type titanates: III, a model of the mechanism,” *Journal of the American Ceramic Society*, vol. 73, pp. 1663–1673, June 1990.
- [55] J. Rödel and G. Tomandl, “Degradation of mn-doped BaTiO₃ ceramic under a high d.c. electric field,” *Journal of Materials Science*, vol. 19, pp. 3515–3523, Nov. 1984.
- [56] M. H. Hebb, “Electrical conductivity of silver sulfide,” *The Journal of Chemical Physics*, vol. 20, no. 1, p. 185, 1952.
- [57] C. Wagner, “Galvanic cells with solid electrolytes involving ionic and electronic conduction,” in *Proceedings of the 7th Meeting of the International Committee on Electrochemical Thermodynamics and Kinetics (CITCE)*, (Lindau, Germany 1955), pp. 361–377, Butterworth, London, 1957.
- [58] I. Yokota, “On the theory of mixed conduction with special reference to conduction in silver sulfide group semiconductors,” *Journal of the Physical Society of Japan*, vol. 16, pp. 2213–2223, 1961.
- [59] J. Fleig, *Electrical and Electrochemical Investigations of Inhomogeneities in Solid State Ionics*. Habilitation thesis, Fakultät für Naturwissenschaften der Universität Ulm and Max-Planck-Institut für Festkörperforschung Stuttgart, Stuttgart/Ulm, 2002.
- [60] S. Rodewald, J. Fleig, and J. Maier, “Resistance degradation of Iron-Doped strontium titanate investigated by spatially resolved conductivity measurements,” *Journal of the American Ceramic Society*, vol. 83, pp. 1969–1976, Aug. 2000.
- [61] S. Rodewald, N. Sakai, K. Yamaji, H. Yokokawa, J. Fleig, and J. Maier, “The effect of the oxygen exchange at electrodes on the High-Voltage electrocoloration of Fe-Doped SrTiO₃ single crystals: A combined SIMS and microelec-

- trode impedance study,” *Journal of Electroceramics*, vol. 7, pp. 95–105, Nov. 2001.
- [62] J. B. MacChesney, P. K. Gallagher, and F. V. DiMarcello, “Stabilized barium titanate ceramics for capacitor dielectrics,” *Journal of the American Ceramic Society*, vol. 46, pp. 197–202, May 1963.
- [63] D. Zheng, J. Swingler, and P. M. Weaver, “Electrical conduction mechanisms in piezoelectric ceramics under harsh operating conditions,” *Sensors and Actuators A: Physical*, vol. 167, pp. 19–24, May 2011.
- [64] N. J. Donnelly and C. A. Randall, “Refined model of electromigration of Ag/Pd electrodes in multilayer PZT ceramics under extreme humidity,” *Journal of the American Ceramic Society*, vol. 92, pp. 405–410, Feb. 2009.
- [65] I. Lipscomb, P. Weaver, J. Swingler, and J. McBride, “The effect of relative humidity, temperature and electrical field on leakage currents in piezo-ceramic actuators under dc bias,” *Sensors and Actuators A: Physical*, vol. 151, pp. 179–186, Apr. 2009.
- [66] J. Thongrueng, T. Tsuchiya, and K. Nagata, “Lifetime and degradation mechanism of multilayer ceramic actuator,” *Japanese Journal of Applied Physics*, vol. 37, pp. 5306–5310, Sept. 1998.
- [67] J. Pritchard, C. Bowen, and F. Lowrie, “Multilayer actuators: review,” *British Ceramic Transactions*, vol. 100, pp. 265–273, 2001.
- [68] I. P. Lipscomb, P. M. Weaver, J. Swingler, and J. W. McBride, “Micro-computer tomography—An aid in the investigation of structural changes in lead zirconate titanate ceramics after temperature-humidity bias testing,” *Journal of Electroceramics*, vol. 23, pp. 72–75, Aug. 2008.
- [69] H. C. Ling and A. M. Jackson, “Correlation of silver migration with temperature-humidity-bias (THB) failures in multilayer ceramic capacitors,” *Components, Hybrids, and Manufacturing Technology, IEEE Transactions on*, vol. 12, pp. 130–137, Mar. 1989.
- [70] H. Kanai, O. Furukawa, S.-i. Nakamura, M. Hayashi, M. Yoshiki, and Y. Yatsushita, “Effects of silver doping on the reliability of $(\text{Pb}_{0.875}\text{Ba}_{0.125})[(\text{Mg}_{1/3}\text{Nb}_{2/3})_{0.5}(\text{Zn}_{1/3}\text{Nb}_{2/3})_{0.3}\text{Ti}_{0.2}]\text{O}_3$ relaxor dielectric ceramics,” *Journal of the American Ceramic Society*, vol. 78, pp. 1173–1178, May 1995.

-
- [71] H. Kanai, O. Furukawa, S.-i. Nakamura, and Y. Yamashita, "Effect of stoichiometry on the dielectric properties and life performance of $(\text{Pb}_{0.875}\text{Ba}_{0.125})[(\text{Mg}_{1/3}\text{Nb}_{2/3})_{0.5}(\text{Zn}_{1/3}\text{Nb}_{2/3})_{0.3}\text{Ti}_{0.2}]\text{O}_3$ relaxor dielectric ceramic: Part i, dielectric properties," *Journal of the American Ceramic Society*, vol. 76, pp. 454–458, Feb. 1993.
- [72] J. L. Cao, L. T. Li, N. X. Zhang, and Z. L. Gui, "Direct Current-Voltage failure in lead magnesium Niobate-Based multilayer ceramic capacitors," *Journal of Materials Research*, vol. 17, no. 04, pp. 779–783, 2002.
- [73] S. Yang, J. Wu, and A. Christou, "Initial stage of silver electrochemical migration degradation," *Microelectronics and Reliability*, vol. 46, no. 9-11, pp. 1915–1921, 2006.
- [74] S. J. Krumbein, "Metallic electromigration phenomena," *Components, Hybrids, and Manufacturing Technology, IEEE Transactions on*, vol. 11, pp. 5–15, Mar. 1988.
- [75] J. Lin and J. Chan, "On the resistance of silver migration in Ag-Pd conductive thick films under humid environment and applied d.c. field," *Materials Chemistry and Physics*, vol. 43, pp. 256–265, Mar. 1996.
- [76] S. A. Yang and A. Christou, "Failure model for silver electrochemical migration," *Device and Materials Reliability, IEEE Transactions on*, vol. 7, pp. 188–196, Mar. 2007.
- [77] G. T. Kohman, H. W. Hermance, and G. H. Downes, "Silver migration in electrical insulation," *Bell System Technical Journal*, vol. 34, p. 1115, 1955.
- [78] C. Dominkovics and G. Harsányi, "Fractal description of dendrite growth during electrochemical migration," *Microelectronics Reliability*, vol. 48, pp. 1628–1634, Oct. 2008.
- [79] G. Harsanyi, "Electrochemical processes resulting in migrated short failures in microcircuits," *Components, Packaging, and Manufacturing Technology, Part A, IEEE Transactions on*, vol. 18, pp. 602–610, Sept. 1995.
- [80] R. C. Benson, B. M. Romenesko, J. A. Weiner, B. H. Nall, and H. K. Charles, "Metal electromigration induced by solder flux residue in hybrid microcircuits," *Components, Hybrids, and Manufacturing Technology, IEEE Transactions on*, vol. 11, pp. 363–370, Dec. 1988.

- [81] M. Chentir, E. Bouyssou, L. Ventura, and C. Anceau, "Leakage current evolution versus dielectric thickness in lead zirconate titanate thin film capacitors," *Journal of Applied Physics*, vol. 105, pp. 061605–061605–7, Mar. 2009.
- [82] B. Nagaraj, S. Aggarwal, T. K. Song, T. Sawhney, and R. Ramesh, "Leakage current mechanisms in lead-based thin-film ferroelectric capacitors," *Physical Review B*, vol. 59, p. 16022, June 1999.
- [83] P. Zubko, D. J. Jung, and J. F. Scott, "Electrical characterization of $\text{PbZr}_{0.4}\text{Ti}_{0.6}\text{O}_3$ capacitors," *Journal of Applied Physics*, vol. 100, pp. 114113–114113–7, Dec. 2006.
- [84] J. Maier, *Physical Chemistry of Ionic Materials - Ions and Electrons in Solids*. Wiley-VCH, 2005.
- [85] P. W. Atkins and J. d. Paula, *Physikalische Chemie*. Wiley-VCH Weinheim, Germany, 4 ed., 2006.
- [86] A. R. West, *Grundlagen der Festkörperchemie*. Wiley-VCH Weinheim, Germany, 1992.
- [87] L. Smart and E. Moore, *Einführung in die Festkörperchemie*. London, Braunschweig, Wiesbaden: Vieweg, 1997.
- [88] Y. Chiang, D. P. Birnie, and W. D. Kingery, *Physical Ceramics: Principles for Ceramic Science and Engineering*. MIT Series in Materials Science & Engineering, Wiley-VCH, 1997.
- [89] B. Boddenberg, "Zur definition und zum gebrauch der größe "Partialdruck",", *Bunsenmagazin*, vol. 13, pp. 81–82, Mar. 2011.
- [90] F. Kröger, H. Vink, F. Seitz, and D. Turnbull, "Relations between the concentrations of imperfections in crystalline solids," in *Advances in Research and Applications*, vol. Volume 3, pp. 307–435, Academic Press, 1956.
- [91] P. Hillebrand, *Conductivity variations in donor doped PZT under high field stress*. Diploma thesis, Vienna University of Technology, Institute for Chemical Technologies and Analytics, Research group Electrochemistry, Vienna, 2010.
- [92] S. Rodewald, *Lokale elektrochemische Charakterisierung von Leitfähigkeitsinhomogenitäten in Fe-dotiertem SrTiO_3* . Ph.D. thesis, Universität Stuttgart; Max-Planck Institut für Festkörperforschung, Stuttgart, 1999.

- [93] S. Rodewald, J. Fleig, and J. Maier, "Measurement of conductivity profiles in acceptor-doped strontium titanate," *Journal of the European Ceramic Society*, vol. 19, pp. 797–801, June 1999.
- [94] C. H. Hamann and W. Vielstich, *Elektrochemie*. Wiley-VCH, 4 ed., 2005.
- [95] K. Lautenschläger, W. Schröter, and A. Wanninger, *Taschenbuch der Chemie*. Frankfurt am Main, Germany: Harri Deutsch Verlag, 20 ed., 2005.
- [96] D. Glück, *Die Untersuchung von spannungsinduzierter Elektronenleitfähigkeit in Yttrium stabilisiertem Zirkoniumdioxid*. Diploma thesis, Vienna University of Technology, Vienna University of Technology, 2008.
- [97] Y. Chiang and T. Takagi, "Grain-Boundary chemistry of barium titanate and strontium titanate: II, origin of electrical barriers in Positive-Temperature-Coefficient thermistors," *Journal of the American Ceramic Society*, vol. 73, pp. 3286–3291, Nov. 1990.
- [98] J. Fleig and J. Maier, "The impedance of ceramics with highly resistive grain boundaries: validity and limits of the brick layer model," *Journal of the European Ceramic Society*, vol. 19, pp. 693–696, June 1999.
- [99] J. Fleig and J. Maier, "Microcontact impedance measurements of individual highly conductive grain boundaries: General aspects and application to AgCl," *Physical Chemistry Chemical Physics*, vol. 1, pp. 3315–3320, 1999. Phys. Chem. Chem. Phys., 1999, 1, 3315 - 3320, DOI: 10.1039/a902839k.
- [100] J. Fleig, S. Rodewald, and J. Maier, "Microcontact impedance measurements of individual highly resistive grain boundaries: General aspects and application to acceptor-doped SrTiO₃," *Journal of Applied Physics*, vol. 87, no. 5, p. 2372, 2000.
- [101] T. van Dijk and A. J. Burggraaf, "Grain boundary effects on ionic conductivity in ceramic Gd_xZr_{1-x}O_{2-(x/2)} solid solutions," *physica status solidi (a)*, vol. 63, pp. 229–240, Jan. 1981.
- [102] M. Verkerk, B. Middelhuis, and A. Burggraaf, "Effect of grain boundaries on the conductivity of high-purity ZrO₂—Y₂O₃ ceramics," *Solid State Ionics*, vol. 6, pp. 159–170, Mar. 1982.
- [103] U. Brossmann, R. Würschum, U. Södervall, and H. Schaefer, "Oxygen diffusion in ultrafine grained monoclinic ZrO₂," *Journal of Applied Physics*, vol. 85, no. 11, p. 7646, 1999.

- [104] J. Fleig, "Microelectrodes in solid state ionics," *Solid State Ionics*, vol. 161, pp. 279–289, Aug. 2003.
- [105] "Thermionic emission - schottky emission; wikipedia, the free encyclopedia." http://en.wikipedia.org/wiki/Thermionic_emission#Schottky_emission, May 2011.
- [106] A. K. Opitz and J. Fleig, "Investigation of o₂ reduction on Pt/YSZ by means of thin film microelectrodes: The geometry dependence of the electrode impedance," *Solid State Ionics*, vol. 181, pp. 684–693, June 2010.
- [107] J. L. Hertz and H. L. Tuller, "Measurement and finite element modeling of triple phase boundary-related current constriction in YSZ," *Solid State Ionics*, vol. 178, no. 13-14, pp. 915–923, 2007.
- [108] J. Nielsen and T. Jacobsen, "Three-phase-boundary dynamics at Pt/YSZ microelectrodes," *Solid State Ionics*, vol. 178, no. 13-14, pp. 1001–1009, 2007.
- [109] Z. Stoyanov and D. Vladikova, *Differential impedance analysis*. Marine Drinov Academic Publishing House, Sofia, 2005.
- [110] H. Stöcker, *Taschenbuch der Physik*. Harri Deutsch, 3 ed., 1998.
- [111] J. R. MacDonald, *Impedance Spectroscopy – Emphasizing Solid Materials and Systems*. Wiley-Interscience, John Wiley and Sons, 1987.
- [112] B. A. Boukamp, "A linear Kronig-Kramers transform test for immittance data validation," *Journal of the Electrochemical Society*, vol. 142, no. 6, pp. 1885–1894, 1995.
- [113] G. Shirane and K. Suzuki, "Crystal structure of Pb(Zr-Ti)O₃," *Journal of the Physical Society of Japan*, vol. 7, p. 333, June 1952.
- [114] B. Jaffe, "Piezoelectric properties of lead Zirconate-Lead titanate Solid-Solution ceramics," *Journal of Applied Physics*, vol. 25, no. 6, p. 809, 1954.
- [115] S. Gansberger, *Piezoaktoren mit Kupfer-Innenelektroden*. Diploma thesis, University Graz, Graz, Deutschlandsberg; Austria, Feb. 2000.
- [116] U. Dibbern, "Elektrochemische materialien. grundlagen und anwendungen," in *Piezoelektrische Keramiken. Eigenschaften und Anwendungen*, Jülich: Forschungszentrum Jülich, 1995.
- [117] T. Corporation, "Piezo-Aktuatoren für einspritzsysteme in kupfer-technologie: Mehr leistung und längere lebensdauer - EPCOS AG."

- <http://www.epcos.de/web/generator/Web/Sections/Components/Page,locale=nn,r=247996>
May 2011.
- [118] J. D. Patterson and B. C. Bailey, *Solid-State Physics: Introduction to the Theory*. Springer, 2007.
 - [119] P. Skalicky, “Einführung in die Festkörperphysik - Skriptum für den Studiengebrauch v1.3.” 1991.
 - [120] “Piezoelectric effect in quartz.” <http://www.creationscience.com/onlinebook/Radioactivity3.h>
June 2011.
 - [121] N. W. Ashcroft and N. D. Mermin, *Festkörperphysik*. Oldenbourg, 2001.
 - [122] B. Jaffe, W. R. Cook, and H. Jaffe, *Piezoelectric ceramics*, vol. 3 of *Non-Metallic Solids*. London: Academic Press, 1971.
 - [123] “Perovskite ABO₃ unit cell.” <http://www.physics.ohio-state.edu/~trivedi/groupresearchb.html>, May 2011.
 - [124] “Perovskite structure and derivatives - SrTiO₃ cubic perovskite.” <http://www.princeton.edu/~cavalab/tutorials/public/structures/perovskites.html>,
June 2011.
 - [125] “PZT unit cell.” <http://www.physikinstrumente.com/en/products/primages.php?sortnr=400>
June 2011.
 - [126] “Tetragonal PZT - two polar directions.” <http://encyclopedia2.thefreedictionary.com/F-RAM>, June 2011.
 - [127] W. Cao and L. E. Cross, “Theoretical model for the morphotropic phase boundary in lead zirconate - lead titanate solid solution,” *Physical Review B*, vol. 47, p. 4825, Mar. 1993.
 - [128] M. Hammer, *Herstellung und Gefüge-Eigenschaftskorrelationen von PZT-Keramiken. Dissertation*. Dissertation, Universität Karlsruhe, Universität Karlsruhe, Germany, 1996.
 - [129] H. Ibach and H. Lüth, *Solid-State Physics: An Introduction to Principles of Materials Science*. Springer, July 2009.
 - [130] W. Heywang, K. Lubitz, and W. Wersing, *Piezoelectricity: Evolution and Future of a Technology*. Berlin Heidelberg, Germany: Springer, 2008.
 - [131] C. Auer, “Polarisation; stackstücke [email],” Mar. 2009.

- [132] D. L. Polla and L. F. Francis, "Processing and characterization of piezoelectric materials and integration into microelectromechanical systems," *Annual Review of Materials Science*, vol. 28, pp. 563–597, Aug. 1998.
- [133] T. Ishihara, *Perovskite Oxide for Solid Oxide Fuel Cells*. Springer, June 2009.
- [134] A. Feltz, P. Schmidt-Winkel, M. Schossmann, C. H. Booth, and J. H. Albring, "Remarkable strontium B-Site occupancy in ferroelectric $\text{Pb}(\text{Zr}_{1-x}\text{Ti}_x)\text{O}_3$ solid solutions doped with Cryolite-Type strontium niobate," *Journal of the American Ceramic Society*, vol. 90, pp. 3959–3967, Dec. 2007.
- [135] N. J. Donnelly and C. A. Randall, "Pb loss in $\text{Pb}(\text{Zr,Ti})\text{O}_3$ ceramics observed by in situ ionic conductivity measurements," *Journal of Applied Physics*, vol. 109, no. 10, p. 104107, 2011.
- [136] X. J. Lou, "Polarization fatigue in ferroelectric thin films and related materials," *Journal of Applied Physics*, vol. 105, pp. 024101–024101–24, Jan. 2009.
- [137] W. L. Warren, D. Dimos, B. A. Tuttle, G. E. Pike, R. W. Schwartz, P. J. Clews, and D. C. McIntyre, "Polarization suppression in $\text{Pb}(\text{Zr,Ti})\text{O}_3$ thin films," *Journal of Applied Physics*, vol. 77, no. 12, p. 6695–6702, 1995.
- [138] Y. A. Genenko and D. C. Lupascu, "Drift of charged defects in local fields as aging mechanism in ferroelectrics," *Physical Review B*, vol. 75, p. 184107, May 2007.
- [139] Y. A. Genenko, J. Glaum, O. Hirsch, H. Kungl, M. J. Hoffmann, and T. Granzow, "Aging of poled ferroelectric ceramics due to relaxation of random depolarization fields by space-charge accumulation near grain boundaries," *Physical Review B*, vol. 80, p. 224109, Dec. 2009.
- [140] D. Dimos, H. N. Al-Shareef, W. L. Warren, and B. A. Tuttle, "Photoinduced changes in the fatigue behavior of $\text{SrBi}_2\text{Ta}_2\text{O}_9$ and $\text{Pb}(\text{Zr,Ti})\text{O}_3$ thin films," *Journal of Applied Physics*, vol. 80, no. 3, p. 1682, 1996.
- [141] P. Mokřý, Y. Wang, A. K. Tagantsev, D. Damjanovic, I. Stolichnov, and N. Setter, "Evidence for dielectric aging due to progressive 180° domain wall pinning in polydomain $\text{Pb}(\text{Zr}_{0.45}\text{Ti}_{0.55})\text{O}_3$ thin films," *Physical Review B*, vol. 79, p. 054104, Feb. 2009.
- [142] N. Balke, T. Granzow, and J. Rödel, "Degradation of lead-zirconate-titanate ceramics under different dc loads," *Journal of Applied Physics*, vol. 105, pp. 104105–104105–7, May 2009.

-
- [143] S. Pöykkö and D. J. Chadi, “Dipolar defect model for fatigue in ferroelectric perovskites,” *Physical Review Letters*, vol. 83, no. 6, p. 1231, 1999.
- [144] D. C. Lupascu and U. Rabe, “Cyclic cluster growth in ferroelectric perovskites,” *Physical Review Letters*, vol. 89, p. 187601, Oct. 2002.
- [145] Q. Jiang, W. Cao, and L. E. Cross, “Electric fatigue in lead zirconate titanate ceramics,” *Journal of the American Ceramic Society*, vol. 77, pp. 211–215, Jan. 1994.
- [146] M. D. Hill, G. S. White, C. Hwang, and I. K. Lloyd, “Cyclic damage in lead zirconate titanate,” *Journal of the American Ceramic Society*, vol. 79, pp. 1915–1920, July 1996.
- [147] X. J. Lou, M. Zhang, S. A. T. Redfern, and J. F. Scott, “Local phase decomposition as a cause of polarization fatigue in ferroelectric thin films,” *Physical Review Letters*, vol. 97, p. 177601, Oct. 2006.
- [148] X. J. Lou, M. Zhang, S. A. T. Redfern, and J. F. Scott, “Fatigue as a local phase decomposition: A switching-induced charge-injection model,” *Physical Review B*, vol. 75, p. 224104, June 2007.
- [149] A. K. Tagantsev, I. Stolichnov, E. L. Colla, and N. Setter, “Polarization fatigue in ferroelectric films: Basic experimental findings, phenomenological scenarios, and microscopic features,” *Journal of Applied Physics*, vol. 90, no. 3, p. 1387, 2001.
- [150] R. Ramesh, J. Lee, T. Sands, V. G. Keramidas, and O. Auciello, “Oriented ferroelectric La-Sr-Co-O/Pb-La-Zr-Ti-O/La-Sr-Co-O heterostructures on [001] Pt/SiO₂ si substrates using a bismuth titanate template layer,” *Applied Physics Letters*, vol. 64, pp. 2511–2513, May 1994.
- [151] D. Lupascu and J. Rödel, “Fatigue in bulk lead zirconate titanate actuator materials,” *Advanced Engineering Materials*, vol. 7, pp. 882–898, Oct. 2005.
- [152] R. Zuo, L. Li, X. Hu, and Z. Gui, “Effect of silver dopant on electrical properties of PMN-PNN-PZT piezoelectric ceramics by complex impedance spectroscopy,” *Materials Letters*, vol. 54, pp. 185–190, May 2002.
- [153] M. V. Slinkina, G. I. Dontsov, and V. M. Zhukovsky, “Diffusional penetration of silver from electrodes into PZT ceramics,” *Journal of Materials Science*, vol. 28, no. 19, pp. 5189–5192, 1993.

- [154] F. Zheng, J. Xu, L. Fang, M. Shen, and X. Wu, "Separation of the schottky barrier and polarization effects on the photocurrent of pt sandwiched $\text{Pb}(\text{Zr}_{0.20}\text{Ti}_{0.80})\text{O}_3$ films," *Applied Physics Letters*, vol. 93, pp. 172101–172101–3, Oct. 2008.
- [155] F. Chen, R. Schafrank, W. Wu, and A. Klein, "Formation and modification of schottky barriers at the PZT/Pt interface," *Journal of Physics D: Applied Physics*, vol. 42, p. 215302, Nov. 2009.
- [156] J. Xu, D. W. Cao, L. Fang, F. G. Zheng, M. R. Shen, and X. L. Wu, "Space charge effect on the photocurrent of pt-sandwiched pb ($\text{Zr}_{0.20}\text{Ti}_{0.80}$) o₃ film capacitors," *Journal of Applied Physics*, vol. 106, p. 113705, 2009.
- [157] E. Völkl, P. Hillebrand, and J. Fleig, "Resistance variation in donor-doped PZT stacks with cu inner electrodes under high field stress," *Journal of Electroceramics*, 2011. accepted.
- [158] K. Reichmann, E. Völkl, M. Ahrens, J. Fleig, and J. Vötsch, "Piezoelectric properties and conductivity of $\text{Pb}(\text{Zr,Ti})\text{O}_3$ with SrO-WO_3 additive," *Journal of Materials Science*, vol. 45, pp. 1473–1477, Dec. 2009.
- [159] F. Llewellyn-Jones, *The physics of electrical contacts*. Oxford, UK: Clarendon Press, 1957.
- [160] R. Holm, *Electric Contacts Handbook*. Springer, Berlin, 3rd edition ed., 1958.
- [161] J. Newman, "Resistance for flow of current to a disk," *Journal of The Electrochemical Society*, vol. 113, no. 5, p. 501, 1966.
- [162] J. Maier, "On the conductivity of polycrystalline materials," *Berichte der Bunsengesellschaft für physikalische Chemie*, vol. 90, pp. 26–33, Jan. 1986.
- [163] P. Balaya, J. Jamnik, J. Fleig, and J. Maier, "Mesoscopic electrical conduction in nanocrystalline SrTiO_3 ," *Applied Physics Letters*, vol. 88, no. 6, p. 062109, 2006.
- [164] P. Balaya, J. Jamnik, J. Fleig, and J. Maier, "Mesoscopic hole conduction in nanocrystalline SrTiO_3 ," *Journal of The Electrochemical Society*, vol. 154, pp. P69–P76, June 2007.
- [165] T. Frömling, A. Schintlmeister, H. Hutter, and J. Fleig, "Oxide ion transport in Donor-Doped $\text{Pb}(\text{Zr}_x\text{Ti}_{1-x})\text{O}_3$: the role of grain boundaries," *Journal of the American Ceramic Society*, vol. 94, pp. 1173–1181, Apr. 2011.

-
- [166] A. Khodorov, S. A. S. Rodrigues, M. Pereira, and M. J. M. Gomes, “Impedance spectroscopy study of a compositionally graded lead zirconate titanate structure,” *Journal of Applied Physics*, vol. 102, no. 11, p. 114109, 2007.
- [167] V. A. Chaudhari and G. K. Bichile, “Structural and impedance spectroscopic studies on $\text{PbZr}_x\text{Ti}_{1-x}\text{O}_3$ ceramics,” *Physica B: Condensed Matter*, vol. 405, pp. 534–539, Jan. 2010.
- [168] L. Andrejs, *in preparation*. Ph.D. thesis, Vienna University of Technology, Institute for Chemical Technologies and Analytics, Research group Electrochemistry, Vienna, 2011.
- [169] C. Ayraancioglu, *in preparation*. Master thesis, Vienna University of Technology, Institute for Chemical Technologies and Analytics, Research group Electrochemistry, Vienna, 2011.
- [170] R. Waser, R. Dittmann, G. Staikov, and K. Szot, “Redox-Based resistive switching memories – nanoionic mechanisms, prospects, and challenges,” *Advanced Materials*, vol. 21, pp. 2632–2663, July 2009.
- [171] C. Schindler, X. Guo, A. Besmehn, and R. Waser, “Resistive switching in $\text{Ge}_{0.3}\text{Se}_{0.7}$ films by means of copper ion migration,” *Zeitschrift für Physikalische Chemie*, vol. 221, pp. 1469–1478, Dec. 2007.
- [172] R. Waser and M. Aono, “Nanoionics-based resistive switching memories,” *Nat Mater*, vol. 6, pp. 833–840, Nov. 2007.
- [173] K. Szot, W. Speier, G. Bihlmayer, and R. Waser, “Switching the electrical resistance of individual dislocations in single-crystalline SrTiO_3 ,” *Nat Mater*, vol. 5, pp. 312–320, Apr. 2006.
- [174] R. Wernicke, “The kinetics of equilibrium restoration in barium titanate ceramics,” *Philips Research Report*, vol. 31, no. 6, p. 526–543, 1976.
- [175] R. Wernicke, “The influence of kinetic processes on the electrical conductivity of donor-doped BaTiO_3 ceramics,” *physica status solidi (a)*, vol. 47, pp. 139–144, May 1978.
- [176] K. Gömann, G. Borchardt, M. Schulz, A. Gömann, W. Maus-Friedrichs, B. Lesage, O. Kaitasov, S. Hoffmann-Eifert, and T. Schneller, “Sr diffusion in undoped and La-doped SrTiO_3 single crystals under oxidizing conditions,” *Physical Chemistry Chemical Physics*, vol. 7, no. 9, p. 2053, 2005.

- [177] S. Koerfer, R. A. De Souza, H. Yoo, and M. Martin, “Diffusion of sr and zr in BaTiO₃ single crystals,” *Solid State Sciences*, vol. 10, pp. 725–734, June 2008.
- [178] W. Preis and W. Sitte, “Modelling of grain boundary resistivities of n-conducting BaTiO₃ ceramics,” *Solid State Ionics*, vol. 177, pp. 2549–2553, Oct. 2006.
- [179] W. Heywang, “Resistivity anomaly in doped barium titanate,” *Journal of the American Ceramic Society*, vol. 47, pp. 484–490, Oct. 1964.
- [180] G. V. Lewis, C. R. A. Catlow, and R. E. W. Casselton, “PTCR effect in BaTiO₃,” *Journal of the American Ceramic Society*, vol. 68, pp. 555–558, Oct. 1985.
- [181] “Defect chemistry and electrical conductivity of doped barium titanate ceramics,” vol. 31, pp. 487–559, Eindhoven, Netherlands: Philips Research Reports, 1976.

This is a BibT_EX Bibliography.

List of abbreviations

3PB	Three phase boundary
<i>ac</i>	alternating current
BT	Breakthrough (Breakdown)
BNT	$\text{Bi}_x\text{Na}_{1-x}\text{TiO}_3$ ($0 \leq x \leq 1$)
CB	Conduction Band (electrons)
CNLS	Comple non-linear least square (fitting procedere)
CPE	Constant phase element
<i>dc</i>	direct current
delta	normalized magnitude of conductivity change, $\text{delta} = \frac{\sigma^\infty(\text{HV})}{\sigma^0(\text{HV})} \cdot 100\%$
EDX	Energy-dispersive X-ray spectroscopy
EIS	Electrochemical impedance spectroscopy
fullstacks	complete multilayer piezoactuator stacks
gb	Grain boundary
HV	High-voltage
IE, IEIE	interdigit electrode (contacting mode)
LST	LYDDANE-SACHS-TELLER (transformation)
LV	Low-voltage
macro	Macroscopically contacted samples in a normal furnace
micro	Microscopically needle-contacted samples on the hot-stage
MPB	Morphotropic phase boundary
Nd:PZT(XY)	Nd-doped PZT multilayer stack with interdigit electrodes of the composition XY
Phase 1	First high-voltage phase of conductivity experiments
Phase 2	Small-signal relaxation phase after the conductivity minimum of Phase 1 was reached
Phase 2LT	High-voltage phase exceeding the conductivity minimum of Phase 1

PLZT	(Pb,La)(Zr,Ti)O ₃
ppm	Parts per million
R//C	Parallel circuit of resistor and capacitor
R//CPE	Parallel circuit of resistor and constant phase element
SEM	Scanning electrode microscope
SOFC	Solid oxide fuel cell
ToF-SIMS	Time-of-flight mode in secondary ion mass spectrometry
VAC	Alternating current voltage
VDC	Direct current voltage
PZT	Lead-zirconate-titanate Pb(Zr _x Ti _{1-x})O ₃ (0 ≤ x ≤ 1)
YSZ	Yttria (Y ₂ O ₃) stabilized zirconia (ZrO ₂) (cubic crystal structure at room-temperature)

List of constants

ϵ_0	Electric constant (vacuum permittivity), $\epsilon_0 = 8.854 \times 10^{-12} \text{ F/m}$
π	Pi, $\pi = 3.142$
e	Elementary charge, $e = 1.602 \times 10^{-19} \text{ C}$
e	EULER's number, $e = 2.718$
F	FARADAY constant, $F = e \cdot N_A = 96.485 \text{ kC/mol}$
G_O^{Veg}	Number of animals slaughtered worldwide every day, $G_O^{Veg} = 411 \times 10^6$
N_A	AVOGADRO constant, $N_A = 6.022 \times 10^{23} \text{ mol}^{-1}$
k_B	BOLTZMANN constant, $k_B = \frac{R}{N_A} = 8.617 \times 10^{-5} \frac{\text{eV}}{\text{K}} = 1.381 \times 10^{-23} \frac{\text{J}}{\text{K}}$
R	Ideal gas constant, $R = 5.189 \times 10^{19} \frac{\text{eV}}{\text{mol} \cdot \text{K}} = 8.314 \frac{\text{J}}{\text{mol} \cdot \text{K}}$

List of symbols

\oplus	Anode (plus-pole)
\ominus	Cathode (minus-pole)
∇	Vacancy (KRÖGER-VINK notation)
i	Interstitial (KRÖGER-VINK notation)
$'$, \times , \cdot	KRÖGER-VINK indicators for negative, zero and positive (relative) charge, respectively
$h\cdot$	Holes (electron-holes, typically in the valence band)
e'	Electrons (typically in the conduction band)
nil	Defect-free lattice structure
$[...]$	Concentrations, denoted by squared brackets
d	1-dim. differential operator
∂	Partial differential operator
∇	<i>Nabla</i> vector, differential operator, $\nabla := \begin{pmatrix} \partial_x \\ \partial_y \\ \partial_z \end{pmatrix}$
Δ	LAPLACE operator, $\Delta := \nabla^2 = \partial_x^2 + \partial_y^2 + \partial_z^2$
Δ, δ	Delta, finite differential indicator
$\Re(Z)$	Real part of a complex number $Z \in \mathbb{C}$
$\Im(Z)$	Imaginary part of a complex number $Z \in \mathbb{C}$
$\mathcal{L}[f]$	LAPLACE-transformation of the function f
$\mathcal{F}[f(t)]$	FOURIER-transformation of $f(t)$, $\mathcal{F}[f(t)] := \int_0^\infty f(t) \cdot \exp(-j\omega t) dt$
a	Symmetry factor for an enthalpy barrier, $[-]$
β	CURIE-WEISS constant

ϵ	Absolute permittivity, $\epsilon = \epsilon_0 \cdot \epsilon_r = \epsilon_0 \cdot (1 + \chi_e)$, $[F/m]$
$\epsilon_r, \{\epsilon_r\}_{ij}$	Relative permittivity (2 nd -order-tensor), $[-]$
λ	Wave length of an electromagnetic wave, $[m]$
η	(Local) potential drop (voltage difference), $[V]$
ν	Stoichiometric index (of a chemical reaction), $[-]$
μ	Chemical potential, $\mu(c) := \mu^0 + RT \cdot \ln(a(c))$, $[J/mol]$
$\tilde{\mu}$	Electrochemical potential, $\tilde{\mu} = \mu + z \cdot F \cdot \phi$, $[J/mol]$
ϕ	Electrical potential, $[V] = [J/C]$
$\rho(x)$	Charge distribution
ρ	Resistivity, specific electrical resistance, $[\Omega m]$
σ	Electric conductivity, $\sigma = \frac{1}{\rho}$, $[S/m]$
ω	Angular frequency, $[rad/s]$
χ_e	Electric susceptibility, $[-]$
a	Chemical activity
c	Chemical concentration
d	Distance, length, $[m]$
d	Diameter, $[m]$
d, d_{ijk}	Piezoelectric charge constant (3 rd -order-tensor), $[m/V] = [C/N]$
f	Frequency, $[Hz]$
g, g_{ijk}	Piezoelectric voltage constant (3 rd -order-tensor), $g := \frac{1}{\epsilon} \cdot d$, $[V/m] = [N/m^2]$
g	Specific GIBBS free enthalpy, $[J]$
\mathbf{i}	Charge current density
$i(t)$	Electrical current, $[A]$
j	Imaginary unit, $j^2 := -1$
k	Wave number of an electromagnetic wave, $k = \frac{2\pi}{\lambda}$, $[1/m]$

k	Electromechanical coupling factors, [-]
l	Length, distance, [m]
n	Mole number, [mol]
n	Non-ideality exponent for CPE-elements, $Z_{CPE} = \frac{1}{(j\omega)^n \cdot A}$, [-]
p	Pressure; partial pressure, [Pa]
q	Heat, [J]
\vec{q}	Wave vector
s_{ijkl}	Stiffness; compliance (4 th -order-tensor), [N/m]
t	Time, [s]
u	Electrical mobility, $u := \frac{v}{E}$, $m^2/V \cdot s$
$u(t)$	Electrical voltage, [V]
v	Velocity, [m/s]
w	Specific work (electrical, mechanical)
z	Charge number, [-]
A	Area, [m^2]
\vec{B}	Magnetic field, magnetic flux density (vector), [T]
C	Capacitor, capacity, [F]
D^*	Isotope tracer diffusion coefficient, [m^2/s]
D^δ	Chemical diffusion coefficient, [m^2/s]
D^σ	Self-diffusion coefficient, [m^2/s]
\vec{D}, D_i	Electric displacement field, [C/m^2]
E	Energy, [J]
E	Electric field, [V/m]
\vec{E}, E_i, \mathbf{E}	Electric field (1 st -order-tensor; vector), [V/m]
F	(Mechanical) force, [N]
G	GIBBS free enthalpy, $G = U + p \cdot V - T \cdot S$, [J]

\vec{H}	Magnetic field strength (vector), $[A/m]$
I	Electrical current, $[A]$
\mathbf{J}	Particle flux density
$\overleftarrow{K}, \overrightarrow{K}$	Equilibrium constant of chemical reactions, $[-]$
L	Inductivity, inductance, $[H]$
M	Abbr. for the metallic cation in a binary compound MX
\vec{M}	Magnetization (vector), $[A/m]$
P	Power-law exponent, e. g. $\tau \propto U^P$, $[-]$
\vec{P}	Dielectric polarization (vector), $[C/m^2]$
R	Electrical resistance; real part of the impedance Z , $X = Z'$, $[\Omega]$
\mathbf{R}	Rate of a chemical reaction
S	Entropy, $[J/K]$
S, S_{ij}	Mechanical strain (2 nd -order-tensor), $[-]$
T	Temperature, $[K]$
T, T_{ij}	Mechanical stress, $[N/m^2]$
T_C	CURIE-temperature, $[K]$
U	Internal Energy, $[J]$
U	Electrical Voltage (potential difference), $[V]$
V	Volume, $[m^3]$
W	Work (electrical, mechanical), $[J]$
X	Electrical reactance; imaginary part of the impedance Z , $X = Z''$, $[\Omega]$
X	Abbr. for the anion in a binary compound MX
Z	Complex impedance, $Z = Z' + jZ''$, $[\Omega]$
Z'	Real part of the complex impedance Z , $Z' = R$, $[\Omega]$
Z''	Imaginary part of the complex impedance Z , $Z'' = X$, $[\Omega]$

Lebenslauf



Ich wurde am 11. Februar 1977 in Mödling, als Sohn des Musikprofessors Walter Völkl und seiner Gattin Herta, geb. Strommer, geboren.

Nach dem Besuch der Volksschule in Traiskirchen (1984 bis 1988) und der Unterstufe (naturwissenschaftlicher Zweig) der AHS Baden Frauengasse (1988 bis 1992) entschied ich mich für ein Studium an einer Höheren Technischen Lehranstalt.

Mein Entschluss fiel auf die Höhere Abteilung für Kraftfahrzeugbau der HTBLuVA Mödling. Meine Ausbildung an dieser Schule habe ich im Juni 1997 mit der Reifeprüfung erfolgreich beendet. Seit Februar 1995 besitze ich den Führerschein der Gruppe B. Anschließend habe ich für die Dauer von acht Monaten meinen Präsenzdienst im

Vorschriften- und Versuchsstab der Heereskraftfahrerschule Baden abgeleistet (IX.1997 bis V.1998).

Im September 1998 inskribierte ich Technische Physik an der TU-Wien. Im Juni 2002 habe ich den ersten der beiden Studienabschnitte dieses Diplomstudiums erfolgreich abgeschlossen. Meine Diplomarbeit habe ich 2005 bei *DaimlerChrysler* in Stuttgart/Nabern zum Thema „Alterung und Wasserstoffemissionen eines Brennstoffzellenfahrzeuges“ verfasst. Am 04. Oktober 2006 habe ich das Physikstudium mit der Diplomprüfung auch formal beendet. Seitdem arbeite ich an einer Doktorarbeit am Institut für Chemische Technologien und Analytik / Elektrochemie an der TU-Wien im Bereich Piezokeramiken.

Mit Einführung der Studiengebühren im Jahr 2000 arbeitete ich für drei Jahre nebenbei in der Firma *SOJAREI* Traiskirchen.

In meiner Freizeit engagiere ich mich bei Tierrechtsvereinen und betreibe gerne Sport.

Ich bin Vegetarier und Nichtraucher.

Meine Computerkenntnisse umfassen *Linux*, *MS-Windows & Office*, *etwas CAD*, *LabVIEW*, *LyX/Latex* und *MacOS* sowie diverse Mathematik-Programme.

Ich bin österreichischer Staatsbürger und ledig.



Elmar VÖLKL